UNIVERSIDAD CATOLICA DEL NORTE
FACULTAD DE INGENIERIA Y CIENCIAS GEOLÓGICAS
departamento de Ciencias Geológicas

EFECTOS DE FLUIDOS HIDROTERMALES EN EL DESARROLLO DE FALLAS: PETROGRAFÍA Y PROPIEDADES MECÁNICAS

Tesis para optar al grado de Doctor en Ciencias Mención Geología

ERIK ARTURO JENSEN SILES

Profesor Guía:
Dr. Gabriel González López
Universidad Católica del Norte

Tutor Externo:
Dr. Daniel Faulkner
University of Liverpool
Rock Deformation Laboratory

1 de Ocubre, 2018

TABLA DE CONTENIDOS

INDICE DE FIGURAS

AGRADECIMIENTOS

Agradecimientos a la Comisión Nacional de Ciencias y Tecnología **CONICYT**, del gobierno de Chile, por financiar totalmente la investigación científica y parcialmente la manutención del estudiante de postgrado e investigador responsable de esta tesis. En específico, se agradecen las becas: **24091112**: Beca de Apoyo de Tesis Doctoral (Gastos de Investigación). **21090074**: Beca de Doctorado Nacional (Manutención).

Agradecimientos a **CODELCO Chile** por apoyarme completamente con la logística del trabajo realizado en la mina Radomiro Tomic. Al Sr. Manuel Vergara y al Sr. Gabriel Leiva, por todas sus gestiones e incondicional apoyo. A Mario Carrasco y Dr. Jorge Skarmeta por las importantes conversaciones sobre las fallas de RT.

Gracias al **Departamento de Ciencias Geológicas** de la Universidad Católica del Norte, que me ha apoyado y formado como geólogo desde mis inicios profesionales. Por aconsejarme y motivarme a ingresar Programa de Doctorado para desarrollar mi investigación y desarrollarme como geocientífico. Por apoyarme logística, económica y administrativamente cuando fue necesario, durante el desarrollo de mi doctorado, en el ámbito humano y profesional: Marisol Bembow, Andrew Menzies, Arturo Jensen, Shoji Kojima, Eduardo Medina, Rodrigo Riquelme, Iván Soto, Hans-Gerhard Wilke, Fernando Álvarez, Xeomara Soto, Gladys Vidal, Cinthia Peñaloza.

A mis mentores profesionales. Profesor Guía, **Gabriel González**, por motivarme ingresar al programa para iniciar este proyecto científico y apoyarme a desarrollarlo durante todo su transcurso. *To my external advisor, **Dan Faulkner**, special thanks for receiving me in your lab, trusting in me, teaching to me and freely allowing me to use your beloved creations (rigs) and the coffee machine.*

A **mi familia**: Padres, hermanas e hijo. Gracias por entregarme su amor, apoyo y paciencia, durante todas las inesperables situaciones que he pasado para lograr cumplir con este difícil proyecto.

RESUMEN GENERAL

Se expresa aquí el resultado de la investigación desarrollada con el objetivo de responder a la pregunta: ¿Cómo afectan los fluidos hidrotermales en la mecánica y desarrollo de fallas en rocas graníticas? Usando dos casos de estudios: Duplex Caleta Coloso (Sistema de Fallas Atacama) y Fallas en Radomiro Tomic (Sistema de Fallas Domeyko). El primero, entrega información sobre el desarrollo de fallas en un sistema hidrotermal de condiciones químicas alcalinas (dominado por clorita y epidota). El segundo, entrega información acerca del desarrollo de fallas en un sistema hidrotermal de menor profundidad (2-3 km), que evoluciona de acidez intermedia a ácida, (alteración potásica, fílica y argílica), cercano a una importante fuente de fluidos (yacimiento de cobre porfídico). Las observaciones indican que tanto la presión de fluidos como la química de éstos afectan a la mecánica y al estilo de deformación (en el sentido de la arquitectura interna de las fallas). Fluidos a alta presión, esperable en sistemas porfídicos, promueven el inicio de la deformación frágil de forma localizada en vetas, por hidrofracturamiento. En tanto, bajas presiones de fluido permiten inicio de la deformación frágil de forma distribuida, como una red de fracturas, eventualmente con geometría autosimilar. Fluidos hidrotermales de acides alcalina a intermedia (alteración propilítica y potásica) tienden a fortalecer los sistemas de fracturas desarrollados en rocas félsicas (granito-diorita). En estos ambientes se sellan fracturas por precipitación de minerales (epidota o cuarzo), mientras que en la roca de caja circundante solo se debilitan los escasos minerales máficos por alteración a biotita o clorita. Fluidos ácidos (alteración fílica y argílica) tienden a debilitar los sistemas de fallas en rocas félsicas. A pesar de que las fracturas también se pueden sellar por precipitación de minerales (cuarzo, sulfuros y sulfatos de metales) los feldespatos son fuertemente hidrolizados tanto dentro como alrededor de las fallas. Resultando en grandes cantidades de arcillas y rocas con baja resistencia al stress.

En rocas graníticas, la hidrólisis de feldespatos puede producir una disminución de resistencia tensional de hasta un 60% y una pérdida de resistencia triaxial (Fricción interna) de hasta un 40%. Adicionalmente puede aumentar la porosidad hasta en un 100%. En salbandas la hidrolisis de los feldespatos puede producir una pérdida de coeficiente de fricción de hasta un 45% y una reducción de su potencial para propagar terremotos (haciéndose más estables a los cambios de velocidad).

GENERAL ABSTRACT

The present thesis is the result of the scientific research focused the general question: “How do the hydrothermal fluids affect in the mechanics and the internal structure of faults in crystalline rocks?”. Faults from two fault systems have been used: Bolfin Fault (Atacama Fault System) and Faults of Radomiro Tomic Deposit (Domeyko Fault System). The first case consists of faults developed under the influence of alkaline hydrothermal fluids (Propilitic Alteration). The faults in the second case developed under the influence of a hydrothermal system that evolved, while cooling, from intermediate to aciditic conditions and from lithostatic to hydrostatic fluid pressure. This hydrothermal system is related to an important porphyritic ore deposit (Radomiro Tomic Deposit) with potassic alteration, metric length quartz veins, phyllic alteration and argillic alterations. Both systems show microstructure suggesting deformation during plastic to brittle transition.

The petrography and internal structure of the faults here described suggest that both the pressure and acidity of the fluids affect to the mechanics and deformation style of the faults. High fluid pressure (Case 1) localizes the initiation of the brittle deformation in large extension fractures (cm-thick veins), as transient pulses of hydrofracturing during long-term and slow rate plastic deformation. Later, when the system is fully brittle, theses veins are reactivated as cataclastic faults. In turn, low fluid pressure (Case 2) allows the brittle deformation to initiate as homogeneously distributed fractures (shear and extension), forming a self-similar network. This fractures later link each other and form fault cores of banded cataclasites.

With respect to the chemistry, we found that the acidity of the fluids has an important control in the texture, mineralogy and mechanical properties of fault rocks. Fluids of alkaline to intermediate acidity, that form propilitic and potassic mineralogical alteration assemblages and are found to strengthen a brittle fault developed in quartz-feldespatic crystalline rocks. In this environment, fractures tend to be sealed with new minerals: Epidote and chlorite in propilitic alteration or quartz in the potassic alteration. Simultaneously, the surrounding rocks are only altered by the break-down of the scarce mafic minerals.

In turn, more aciditic fluids, that form phyllic and argillic alteration, tend to weaken a fault system developed quartz-feldespatic rocks. Even though fractures are also partially sealed by precipitation (of quartz, sulphides or sulphates) the feldspars in the surrounding rocks and comminuted fragments are strongly hydrolyzed, resulting in large amounts of clay that weakens the rocks in both friction and resistance to fracturing.

In granitic rocks the hydrolysis can produce a loss of tensile strength up to 60% and loss of compressive triaxial strength (internal friction) up to 40%. Additionally, it can increase the porosity in up to 100%. In gouges, the hydrolysis of feldspar can produce a loss of frictional coefficient up to 45% and a reduction of their potential to propagate earthquakes (becoming more velocity stable).

I. INTRODUCCIÓN DE LA TESIS

I.1. PROBLEMA DE INVESTIGACIÓN

El agua es el componente más importante del planeta y se encuentra como fluido poral en toda la parte frágil de la corteza terrestre: "*schizosphere can be assumed to be universally permeated fluids" (*Scholz, 2002*).*

Las fallas también se encuentran en toda la corteza frágil, por lo tanto, son de extrema importancia en el control del flujo de fluidos porales. El control que ejercen las fracturas sobre el flujo de fluidos corticales ha sido ampliamente estudiado, es conocido que las redes de fracturas tienden a canalizar los fluidos a lo largo de la corteza (Brown & Bruhn, 1998; Caine *et al.,* 1996; Faulkner & Rutter, 2003; Sibson, 1990). Sin embargo, la interacción entre fallas y fluidos consiste en una compleja retroalimentación de procesos en la que los fluidos también afectan a la deformación frágil, controlando la reología y las propiedades mecánicas de las rocas. Por lo que no se puede llegar a comprender un proceso sin estudiar el otro. Además, la distribución de depósitos metálicos de origen hidrotermal, típicamente asociados a sistemas de fallas (Curewitz & Karson, 1997; Charrier *et al.*, 2007; Eisenlohr *et al.*, 1989, Yang *et al.*, 2003), indica que el mencionado efecto reológico se puede esperar de manera común en las grandes fallas de la corteza.

Entender como los fluidos corticales que circulan por las fallas modifican las propiedades mecánicas de las rocas y de fallas es de fundamental importancia para cualquier tipo de modelo que intente predecir la propagación de nuevas fallas y/o el deslizamiento de las existentes (Jaeger and Cook ,1979; Handy, 2001; Zahng *et al.*, 2008).

Por una parte, se sabe que, con el incremento de la temperatura y presión, el agua activa mecanismos de deformación cristalina que debilitan la roca. A escala cristalina, una variación de 0.0015% a 0.13% de agua en la estructura del cuarzo puede bajar la temperatura de activación de mecanismos de deformación plástica de 1070 a 380 °C (Griggs & Blacic, 1965; Griggs, 1967). Este mecanismo es identificado como "*hydrolitic weakening*" y consta del deslizamiento (*glide*) de dislocaciones por la destrucción enlaces Si-O-Si. Puede ocurrir también en otros minerales formadores de roca y al combinarse con otros mecanismos asociados a difusión, debilitar rocas félsicas y máficas, incluso en zonas no cizalladas, disminuyendo la profundidad del límite frágil-plástico (Mei & Kohlstedt, 2000a, b)

Por otra parte, en condiciones donde predomina la deformación frágil, los fluidos facilitan el deslizamiento de fallas, al reducir los esfuerzos normales en planos de cizalle. Este fenómeno

físico produce una aparente pérdida de resistencia friccional y se encuentra muy bien explicado por la Ley de Esfuerzos Efectivos (Nur & Byerlee, 1971; Robin, 1973).

Sin embargo, la influencia de los fluidos en la deformación de fallas frágiles no se restringe a efectos transitorios (deformación bajo el efecto inmediato de fluidos), sino que también existen mecanismos de transferencia de masa asistidos por fluidos (difusión), que tienen efectos permanentes en la mineralogía de las rocas y salbandas y, por lo tanto, en la mecánica de la deformación frágil.

Una forma de entender estos procesos es a través de experimentos mecánicos de laboratorio imitando condiciones hidrotermales. Experimentos de cizalle directo intermitente, en salbandas simuladas inyectadas con agua destilada, indican que las salbandas son cementadas por procesos químicos durante los periodos de reposo y que su reactivación se dificulta con el tiempo de reposo. Esto, indica las condiciones de stress cíclico son controladas por cambios en las propiedades mecánicas de cohesión y fricción. (Olsen *et al.,* 1998; Muhuri *et al.,* 2003). Este fenómeno ha sido atribuido a mecanismos de disolución por presión y sutura entre partículas, favorecida por condiciones hidrotermales (Giger *et al.,* 2008; Niemeijer *et al.,* 2008).

Estos experimentos de laboratorio buscan imitar la deformación bajo condiciones hidrotermales, pero se encuentran restringidos a las condiciones de temperatura y actividad química que los materiales de construcción puedan resistir. Esto, dificulta el estudio de procesos alteración mineralógica. Una forma de compensar científicamente este problema es complementar los resultados de laboratorio con observaciones petrográficas de fallas reales, exhumadas, que indiquen la naturaleza y secuencia de los cambios producidos por fluidos en las fallas corticales; para posteriormente poder simular y cuantificarlos en laboratorio.

Al respecto, todos los estudios petrográficos de rocas de falla desarrollados en rocas cristalinas (estructura interna y análisis mineralógico) enfocados en entender la interacción fallas-fluidos, se han realizado en sistemas de fallas con débil actividad hidrotermal, comparados con sistemas hidrotermales relacionados a depósitos minerales. (Braathen *et al.*, 2009; Chester & Chester 1998; Chester *et al.*, 2004; Evans & Chester, 1995; Faulkner *et al.*, 2003; Janssen *et al.*, 2004; Wibberley & Shimamoto, 2003).

En la siguiente tesis, se presenta una combinación de análisis petrográficos y experimentos de laboratorio en rocas de fallas de dos casos de estudios, ubicados en dos grandes sistemas de fallas corticales exhumados de diferentes edades. Uno es el Sistema de Falla Atacama, (Duplex Caleta Coloso) en el que se describen fallas con alteración hidrotermal moderada. El segundo caso de estudio está conformado por el sistema de fallas del depósito de cobre Radomiro Tomic, en el Sistema de Falla Domeyko.

Se combina petrología de sistemas de falla reales con datos de laboratorio buscando responder a la pregunta de investigación: ***"Cómo afectan los fluidos hidrotermales en la mecánica y la estructura interna de las fallas en rocas cristalinas?".***

I.2. OBJETIVOS

Para responder a la pregunta de investigación, se ha planteado el siguiente Objetivo Principal:

"Comprender cómo los fluidos de alteración afectan al desarrollo de fallas en rocas graníticas, mediante la modificación de su petrografía, estructura interna, y propiedades mecánicas".

Objetivos Específicos:

- Entender la propagación y evolución de los casos de estudio
- Deducir procesos que controlan la estructura interna y petrografía de fallas asociados a diferentes ambientes hidrotermales
- Diferenciar cambios petrográficos consecuentes del fallamiento de aquellos resultantes de la alteración por fluidos.
- Cuantificar los efectos de la alteración mineralógica en las propiedades mecánicas de rocas de falla y rocas cristalinas circundantes.

I.3. DISTRIBUCIÓN DE LA TESIS

La siguiente tesis se divide en 3 capítulos (identificados con números romanos) cada uno con su propio capítulo de introducción, fundamentando sus correspondientes objetivos, y de conclusión, entregando un resultado aplicable de los análisis y datos obtenidos.

El primer capítulo, reporta la investigación desarrollada en las ramas subsidiarias de la Falla Bolfín, Sistema de Falla Atacama. Se basa en la observación y análisis de elementos estructurales y mineralógicos, multiescalar, de fallas, en terreno y cortes transparentes al microscopio. Aporta en el entendimiento de la arquitectura y rocas de fallas desarrolladas en sistemas químicamente alcalinos (dominado por clorita y epidotas) y lejos de grandes fuentes de fluidos hidrotermales. Este capítulo ha sido publicado en la revista Journal of Structural Geólogy, capítulo 33, año 2011.

El segundo capítulo, reporta la investigación desarrollada en las fallas expuestas en la mina Radomiro Tomic durante el 2010 y 2011; en el Sistema de Falla Domeyko. Se basa en la observación y análisis estructural y mineralógico, de fallas en terreno y cortes transparentes al microscopio. Representa el desarrollo de fallas en sistemas químicamente intermedios a ácidos (dominado por cuarzo, illita, caolinita y pirita) y cercanos a fuentes importantes de fluidos (yacimiento porfídico). Este capítulo se encuentra aceptado (con correcciones mayores) en el Journal of Structural Geology.

El tercer capítulo, reporta la investigación desarrollada en el Rock Deformation Laboratory, Liverpool, durante el 2011 y 2012 en muestra tomada de las mismas fallas expuestas en la mina Radomiro Tomic del capítulo anterior. Se basa en la medición de propiedades mecánicas de rocas con diferentes niveles de alteración como proxy de una falla desarrollada bajo esas condiciones y la posterior comparación con rocas de fallas reales del mismo sistema. Representa la cuantificación de los efectos de la interacción roca-fluido en fallas desarrolladas en sistemas químicamente intermedios a ácidos, cercanos a fuentes importantes de fluidos.

Todos los capítulos han sido redactados en inglés y en formato de artículo científico con el objetivo de ser posteriormente publicados en revistas ISI especializadas en el tema correspondiente.

I.4. MARCO TEÓRICO

I.4.1. Estructura Interna de Fallas

Las fallas, son zonas relativamente planares, a lo largo de las cuales ha ocurrido desplazamiento opuesto de las paredes, es decir, cizalle. Los materiales que se puedan encontrar dentro de estas zonas son en general rocas y minerales deformadas por dicho cizalle y se denominan Rocas de Falla. La distribución y tipo rocas de falla, por ende, la estructura interna de las fallas varia por con la profundidad a la cual ha ocurrido el cizalle, principalmente controlado por la temperatura y mecanismos de deformación de cuarzo y feldespato (Scholz 1988), (Figura I-1). Por la naturaleza de los casos de estudio aquí presentado y la necesidad de fracturas de los sistemas hidrotermal (para su movilización), esta tesis se enfoca principalmente en el desarrollo de fallas en la zona de deformación frágil (zona de cataclasitas).

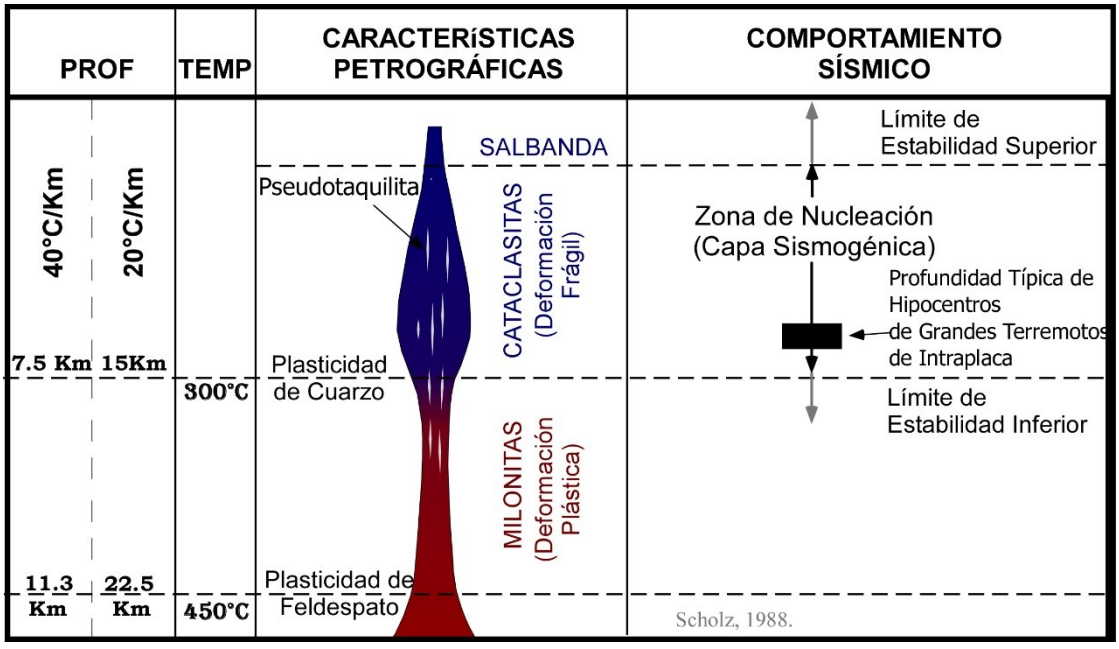

Figura I-1. Diagrama de la variación de la estructura interna de fallas en el límite plástico-frágil (Modificado de Scholz, 1988).
Los límites de mecanismos de deformación, características petrográficas y comportamiento sísmico de las fallas en la corteza continental se muestran en función de la temperatura de activación de la plasticidad del cuarzo y el feldespato. Las profundidades equivalentes son calculadas para dos gradientes geotérmicos.

Para describir la estructura interna de zonas de fallas en zona de deformación frágil, el modelo más conocido y difundido en la literatura científica es modelo simplificado de Chester *et al.,* (1993). En su trabajo describe ramas inactivas exhumadas del Sistema de Falla San Andrés

(Punchbowl Fault y San Gabriel Fault) que cortan principalmente rocas cristalinas cuarzo-feldespáticas y tienen movimientos de rumbo de decenas de kilómetros.

Todas las fallas descritas por Chester en el sistema de Falla San Andrés constan de una delgada lámina simple y continua de ultracataclasita, de entre 10 y 20 cm de espesor, rodeada de una zona de cataclasita foliada de algunos metros de espesor (Figura I-2). Estas cataclasitas se encuentran a su vez rodeadas por una, mucho más gruesa, zona de protocataclasitas y protolito fracturado (~100 m). A partir de estas observaciones de campo, define Zona de Falla como el volumen de roca que exhibe una intensidad de deformación frágil significativamente mayor que la típica en la roca circundante y separa dicha zona en dos subzonas: Núcleo y Zona de Daño (Figura I-3). Se considera como Núcleo de falla tanto la lámina de ultracataclasita como la zona de cataclasita foliada circundante y como Zona de Daño la zona de protolito fracturado (y proto cataclasitas) que rodea las cataclasitas (Chester *et al*., 2004).

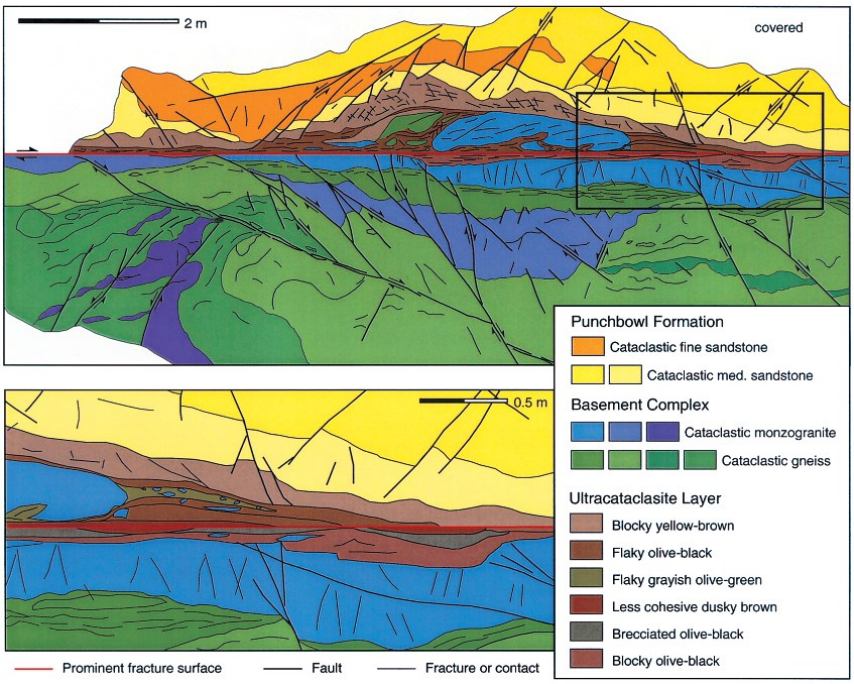

Figura I-2. Mapa de la estructura interna de la Punchbowl Fault una rama exhumada del Sistema de Falla San Andreas (Chester *et al*., 2004).
Esta falla se caracteriza por estar formada de un solo núcleo de bordes irregulares, compuesto de ultracataclasitas corta rocas (metamórficas) ricas en filosilicatos y muestra un núcleo compuesto de múltiples bandas de salbanda anastomosadas.

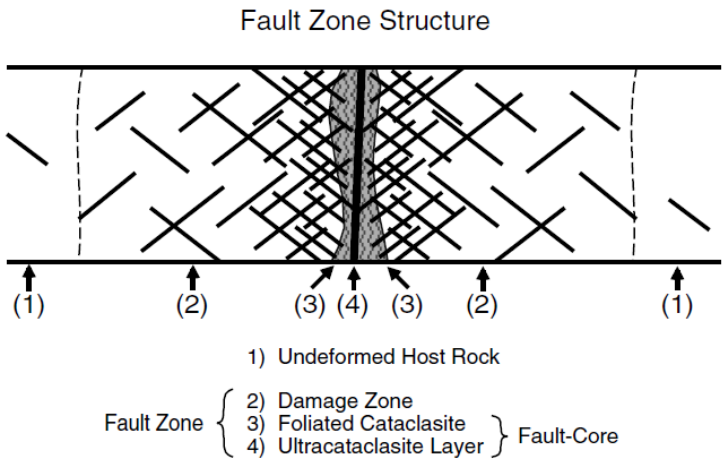

Figura I-3. Modelo simplificado de la estructura interna para el Sistema falla San Andrés. (Chester *et al*., 2004).
Este modelo es el más difundido y aplicado en la literatura científica para estudiar estructura interna en zonas de deformación frágil (zona sismogénica) en rocas cristalinas cuarzo-feldespáticas.

A pesar de aplicar muy bien para muchas zonas de fallas descritas en el mundo, este modelo no aplica para todas de las fallas de rumbo observadas en el mundo y se han observado variaciones según la mineralogía del protolito o las condiciones fisicoquímicas de los fluidos circundantes. La Falla Carboneras (España), parte de una zona de cizalle regional, corta principalmente rocas metamórficas ricas en filosilicatos y dolomitas, y presenta diferente estructura interna (Faulkner *et al.,* 2003). Esta falla ha sido descrita como "una zona de falla compuesta de múltiples láminas de salbanda rica en filosilicatos (cada una típicamente de menos de 5 m de espesor) separadas por lentes de protolito de variadas condiciones de fracturamiento" (Figura I-4). Estas láminas de salbanda son consideradas en conjunto como un Núcleo Múltiple, con un espesor total de 1km (considerando tanto las láminas de salbanda como los lentes de protolito) y que se encuentra rodeado de una, mucho más delgada, Zona de Daño de unos 100 m de espesor.

La estructura interna de la Falla Carboneras ha sido explicada por la propiedad de los filosilicatos (contenidos en la salbanda) de endurecerse en respuesta al aumento de la tasa de deformación. Sin embargo, un Núcleo Múltiple también puede desarrollarse en fallas que cortan rocas cuarzo-feldespáticas, como es el caso de la Falla Caleta Coloso, en el norte de Chile. La Falla Caleta Coloso es una falla exhumada siniestral inactiva, perteneciente al Sistema de Falla Atacama, que corta rocas volcánicas, sedimentarias y plutónicas. Se observa que desarrolla un grueso Núcleo Múltiple compuesto de láminas de cataclasita, protocataclasita y ultracataclasita

separadas por lentes de protolito fracturado, que en total suman un espesor de ~500m, Figura I-5 (Cembrano *et al.,* 2005, Faulkner *et al*., 2008).

Según lo visto en estos tres ejemplos (Punchbowl, Carboneras y Caleta Coloso) se puede determinar que no existe un modelo que describa de manera precisa la estructura interna de todas zonas de falla de rumbo. Sin embargo, puede mantenerse la idea de que una Zona de Falla está compuesta por un Núcleo, y una Zona de Daño, y que su arquitectura está determinada, entre otros, por la mineralogía del protolito y las condiciones fisicoquímicas a las que se forma. Por esta razón se ha definido un modelo de estructura interna dual, que describe los casos de núcleo simple y múltiple (Figura I-6).

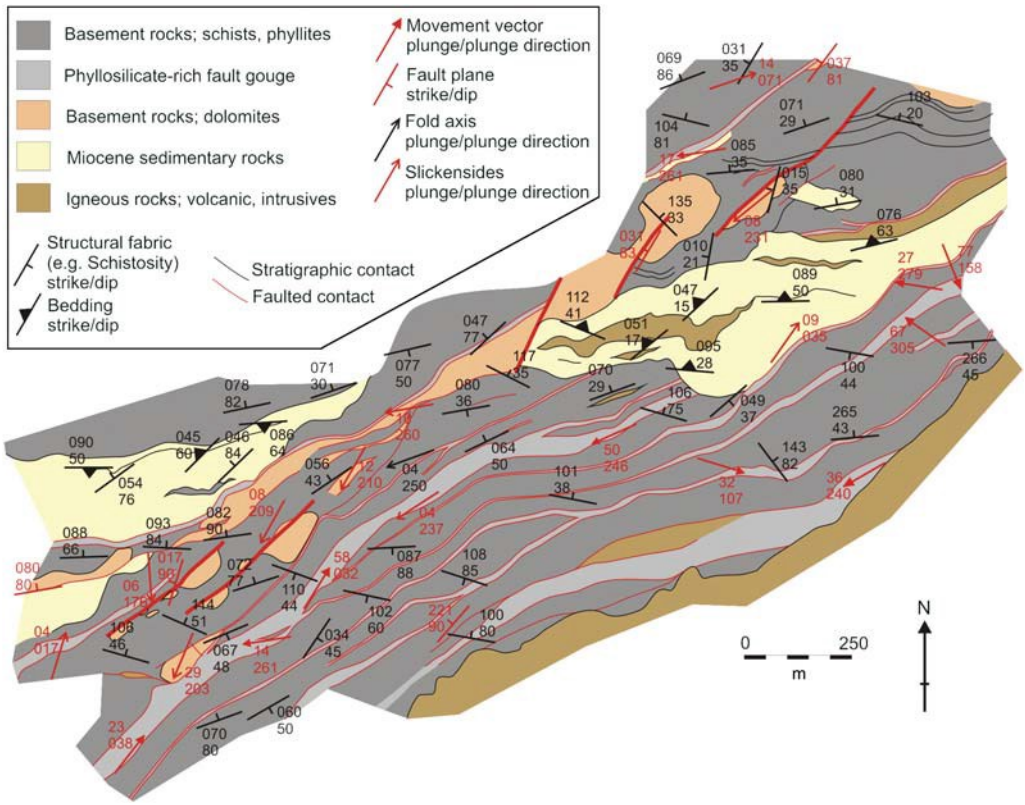

Figura I-4. Mapa de la estructura interna de la falla Carboneras, España. (Faulkner et al., 2008).
Esta falla corta rocas ricas en filosilicatos (metamórficas) y muestra un núcleo compuesto de múltiples bandas de salbanda anastomosadas.

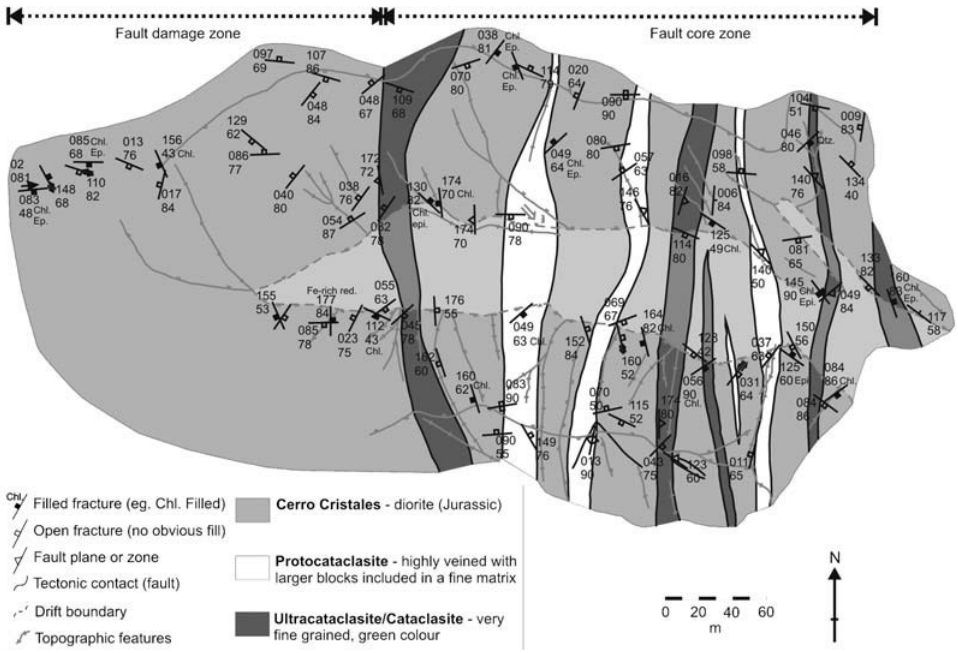

Figura I-5. Mapa de la estructura interna de la Falla Caleta Coloso (Faulkner *et al*., 2008).
Esta falla corta rocas cuarzo feldespáticas y muestra un núcleo compuesto de múltiples bandas de cataclasita anastomosadas.

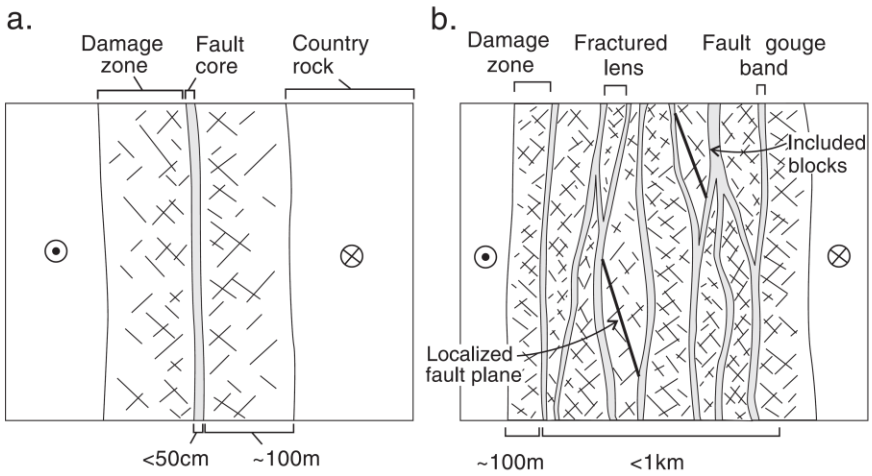

Fig. 6. Conceptual models for large strike slip fault zones compared. The models are drawn as cross-sections. (a) The conceptual model commonly used for the structure of large strike-slip fault zones as developed by a number of previous workers (see text). (b) A conceptual model for the type of fault zone described in this work, containing a large proportion of phyllosilicate-rich material. The fault is much wider and contains anastomosing strands of fault gouge which contain lenses of country rock. The fault may also contain blocks of rock that are more competent than the country rock, and this material may respond differently to the deformation, developing localized fault planes.

Figura I-6. Comparación de modelos conceptuales de estructura interna de grandes fallas de rumbo (Faulkner et al., 2008).
(a) Modelo de núcleo simple definido para la falla Punchbowl, San Andreas. (b) Modelo de núcleo múltiple definido en la falla Carboneras y aplicable para la falla Caleta Coloso (Ambos en sección vertical).

I.4.2. Formación de Rocas de Falla

Las rocas molidas y trituradas han sido relacionadas con fallas durante varios siglos, sin embargo, la primera descripción detallada de esto fue hecha por Lapworth (1885), quien acuñó el término milonita para describir rocas dentro de los sistemas de cabalgamiento escoceses. Sin una clara idea de los procesos genéticos, el llamó “roca molida (“mylonite = milled rock”) a las rocas que actualmente son reconocidas como producto de procesos de deformación plástica (Scholz, 2002) y no molienda o abrasión friccional.

Desde entonces, muchos términos han sido usados para rocas de falla, cómo “cataclasitas” “salbanda” (“gouge”), brechas y areniscas cataclásticas (Engelder, 1974), sin embargo, estos también han sido usados sin una clasificación general comprensiva por el desconocimiento de los procesos genético.

La primera clasificación textural de rocas de fallas que incluye a la mayoría de los términos usados y que permite una amplia correlación entre procesos de deformación y rocas resultantes fue hecha por Sibson (Sibson, 1977) (ver Figura I-7 para una versión levemente modificada). Ésta se basa principalmente en la cohesión y anisotropía, y ha sido la clasificación más usada en investigaciones sobre fallas.

Sibson, sobre la base de observaciones de laboratorio previas, clasificó los procesos que producen roas de falla en dos regímenes principales: Elástico-friccional (EF) y Quasi-plástico (QP) Figura I-8.

El régimen EF, ocurre a profundidades someras y en él, las partículas de roca se comportan de una manera casi elástica frente al fallamiento y no pueden absorber grandes cantidades de strain por plasticidad cristalina (o difusión de masas), así la deformación de masas de rocas es dominada por fricción. Se incluyen los procesos de fracturamiento frágil, desgaste friccional y abrasivo (“*abrasive and frictional wear*”) y flujo cataclástico.

En el régimen QP, un constituyente mayor de las rocas (usualmente cuarzo) puede fácilmente deformarse por plasticidad cristalina” acomodando la deformación. Se incluyen varios procesos de difusión y solución, como “*dislocation creep*” con recristalización y rotación de subgranos asociada.

El principal punto débil de la clasificación de tal clasificación es que asume que bajo régimen EF solo se pueden producir rocas de fábrica aleatoria o isótropas. Esto ha sido refutado por observaciones posteriores, tanto en salbandas naturales como en reproducciones de laboratorios (Chester *et al.,* 1985; Chester & Logan, 1987; Lin, 1999). En ellas se ha observado que el flujo

cataclástico en condiciones de deformación puramente frágil también puede desarrollar foliaciones en el material fragmentado. Parte de este problema ha sido reparado por Scholz (2002) agregando “salbanda foliada” a la clasificación original de Sibson (como se muestra en la **Figura I-7**)

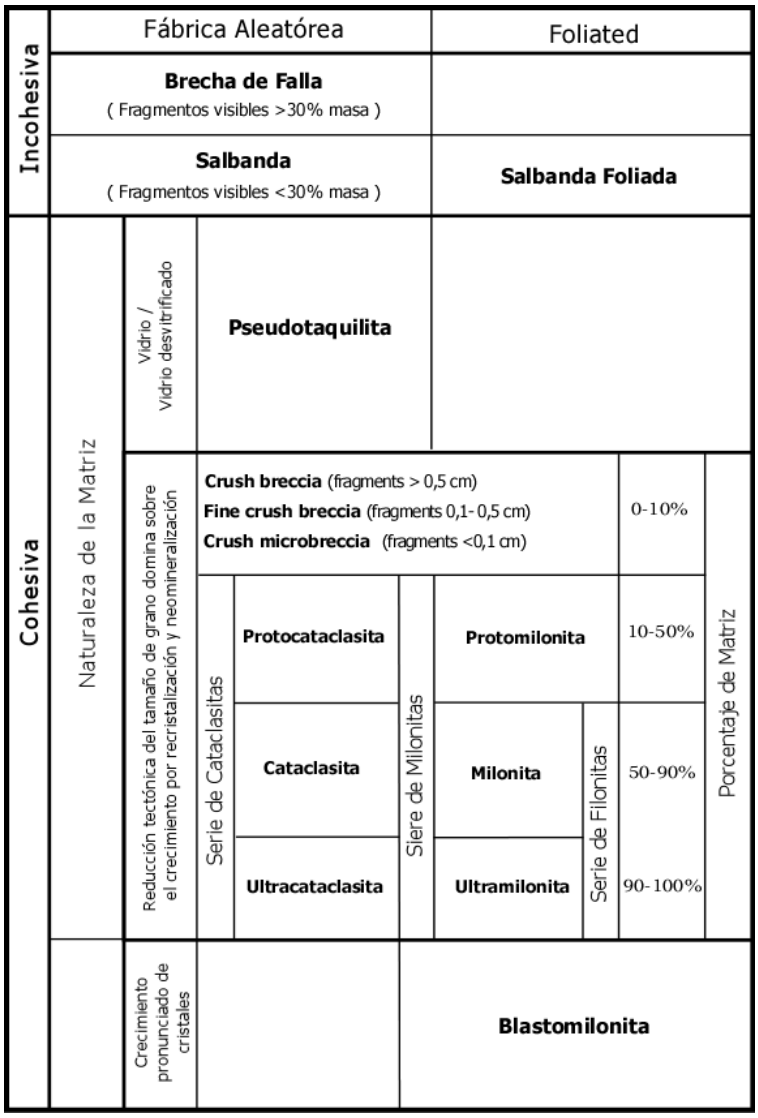

Figura I-7. Tabla de clasificación para rocas de falla (Sibson, 1977; Scholz, 2002).
Creada por Sibson y posteriormente modificada agregando “salbanda foliada”

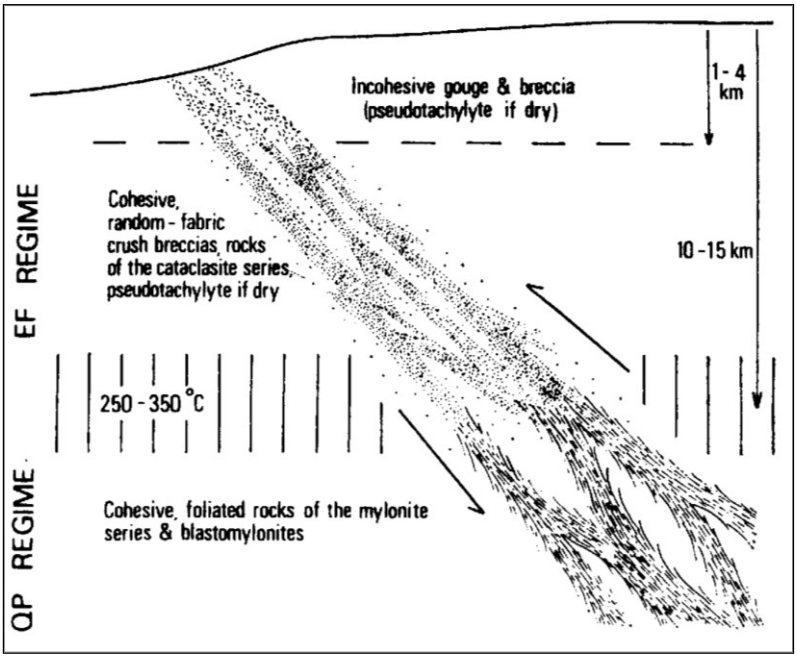

Figura I-8. Perfil estructural esquemático representando una falla inversa. Muestra distribución de rocas de fallas y regímenes de mecanismos de deformación. (Tomado de Sibson, 1977)

I.4.3. Propiedades Texturales

Uno de los primeros trabajos dedicados a caracterizar y medir propiedades texturales de rocas de fallas ha sido el realizado por Engelder (1974), quien tamizó salbandas de cuarzo tanto experimentales como naturales y documentó que, en ambos casos, el tamaño de grano promedio y grado de selección decrecen con los incrementos de presión confinante y el desplazamiento.

Los principales procesos a escala cristalina inferidos de ser responsables de dicha reducción de tamaño han sido el microfracturamiento y la rotación de cuerpo rígido que, a escala mayor, son usualmente considerados ser parte de un proceso llamado "desgaste friccional" ("*frictional wear*"). Al respecto, Scholz (1987) ha documentado una relación linear de 10^{-2} entre desplazamiento y espesor de salbandas en fallas cortando rocas plutónicas, y lo ha interpretado cómo el resultado de este desgaste progresivo con el incremento del strain.

Por otra parte, esta reducción de fragmentos no es el único cambio textural registrado por salbandas como resultado del desgaste friccional progresivo, sino que también cambios de forma, como la redondez han sido medidos (Cladouhos, 1999; Heilbronner & Keulen, 2006). de manera que, a condiciones físicas similares, la redondez puede ser usada para distinguir salbandas maduras de otras recientemente formadas.

Además, las relaciones obtenidas de estas investigaciones experimentales han sido utilizadas para realizar modelos numéricos de desarrollo cinemático (Guo & Morgan 2007; Mair & Abe; 2008).

I.4.4. Fricción

La ficción es la resistencia al movimiento de un cuerpo que se desliza tangencialmente a una superficie de contacto con otro cuerpo. Juega un importante role en una gran variedad de procesos. La fricción controla procesos naturales y funcionamiento de maquinarias, por lo que se pueden encontrar registros de investigación científica al respecto desde el siglo XV, por Leonardo Davinci (Scholz, 2002). Matemáticamente la fricción se define como (μ) la relación entre las fuerzas tangencial (τ) y normal (N) a una superficie, necesarias para que un cuerpo se deslice a lo largo de esta superficie y la propiedad constitutiva que determina esta fuerza se llama Coeficiente de Fricción: $\mu = \tau/N$.

Diferentes métodos y configuraciones se han usado para medir la fricción de los materiales, algunos ejemplos se muestran en la Figura I-9. La configuración de carga triaxial es la más apta para teste de alta presión confinante, sin embargo, tiene limitaciones en el deslizamiento friccional. Por esta razón, las pruebas de fricción para la presente investigación han sido realizados con una nueva configuración experimental de vanguardia que es una combinación entre carga triaxial y cizalle directo. Ésta se explica con detalle en la sección IV.3.3.2 “Direct Shear in a Triaxial Apparatus“ de la presente tesis.

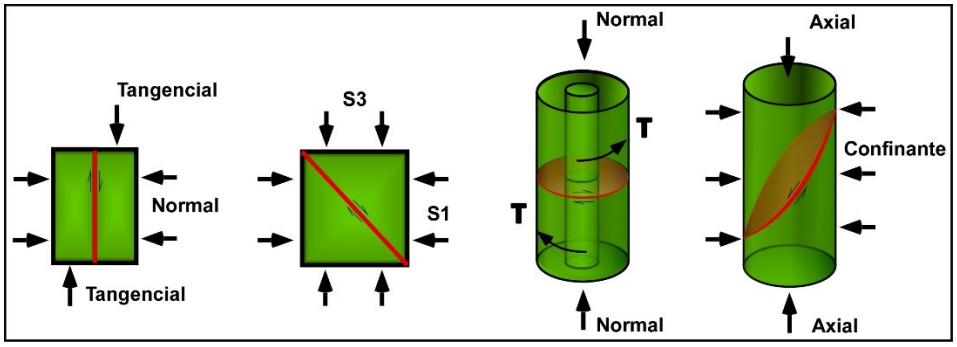

Figura I-9. Tipos de configuraciones experimentales más comunes en estudios de fricción. (Editado de Scholz, 2002)
Las flechas indican la dirección de aplicación de esfuerzos, la lámina roja representa la superficie de medición de fricción (Frecuentemente reemplazada por salbanda). De izquierda a derecha, se conocen con los siguientes nombres: Cizalle Directo, Carga Biaxial, Test Rotatorio y Compresión Triaxial.

Según la relación empírica conocida como Ley de Byerlee (Byerlee, 1978) el coeficiente de fricción es casi igual para todos los tipos de roca (no lubricados) tanto para superficies como para material fragmentado o salbandas (μ= 0.85 (<200Mpa) y 0.6 (>200Mpa)), excepto en presencia de arcillas, que muestran comportamiento anómalo. El efecto que las arcillas producen en la fricción de las salbandas ha sido estudiado por Crawford *et al.* (2008) quienes han medido la resistencia de cizalle ("*shear strength*") de salbandas simuladas con diferentes cantidades de arcilla y cuarzo Figura I-10. En dichos experimentos, las arcillas han mostrado debilitar las salbandas mediante la disminución del coeficiente de fricción.

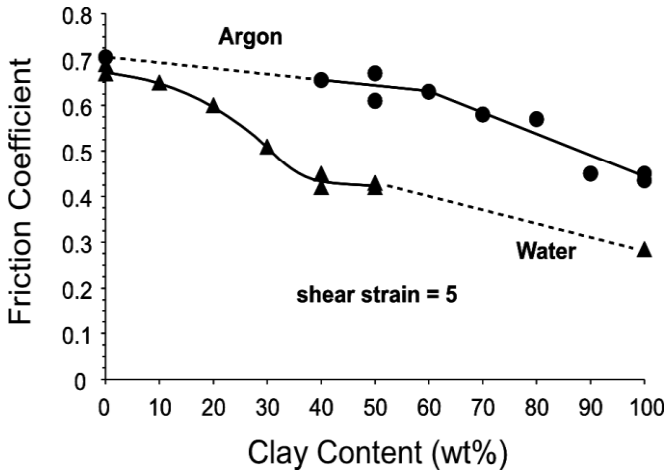

Figura I-10. Coeficiente de fricción vs arcilla en salbanda.
Reducción del coeficiente de fricción como función del aumento de contenido de kaolinita en la salbanda. (Crawford *et al.,* 2008)

Estas diferencias de resistencia friccional mostradas por salbandas de arcilla sugieren fuertemente que las diferencias mineralógicas producidas por los fluidos porales tanto en ambiente hidrotermal como supérgeno también pueden afectar a su comportamiento mecánico. La alteración de feldespatos y otros minerales a arcillas ocurre frecuentemente en la naturaleza, así como otras alteraciones que pueden alterar mecánicamente a las fallas.

I.4.5. Permeabilidad

Muchas de las investigaciones experimentales en desarrollo de rocas de falla se han enfocados en medir su permeabilidad y los factores que la controlan. En este contexto, Faulkner (2004) resume la información disponible sobre la permeabilidad de salbandas ricas en filosilicatos y la incorpora dentro de un modelo de variación de permeabilidad respecto la profundidad. Concluye con esto que el control más importante sobre la permeabilidad esta dado por cambios

en la presión y en naturaleza química de los fluidos porales (fuerza iónica). La permeabilidad decrece con el aumento de la presión (Figura I-11) de acuerdo con la ecuación: $k = k_0 \exp(-\gamma \Delta\sigma)$ y decrece con el aumento de la fuerza iónica de los fluidos. Se han registrado diferencias de ~1 orden de magnitud de permeabilidad en salbandas de arcillas entre el uso de argón o agua como fluido poral. Este efecto es atribuido a la absorción de agua en minerales de arcilla muy finas que crecen y se aglomeran en los espacios porales (Faulkner & Rutter, 2003).

Por otra parte, cuando las salbandas presentan una foliación bien desarrollada se registra una notable anisotropía de la permeabilidad. Mediciones realizadas en salbandas naturales de arcilla (Faulkner & Rutter, 1998) muestran anisotropía de 3 órdenes de magnitud, con el mayor valor orientado en dirección paralela a la intersección de las foliaciones (P y R_1) y el menor perpendicular al plano de falla (Figura I-12). La razón sugerida para esta anisotropía ha sido la orientación de los filosilicatos (Solum *et al.,* 2003).

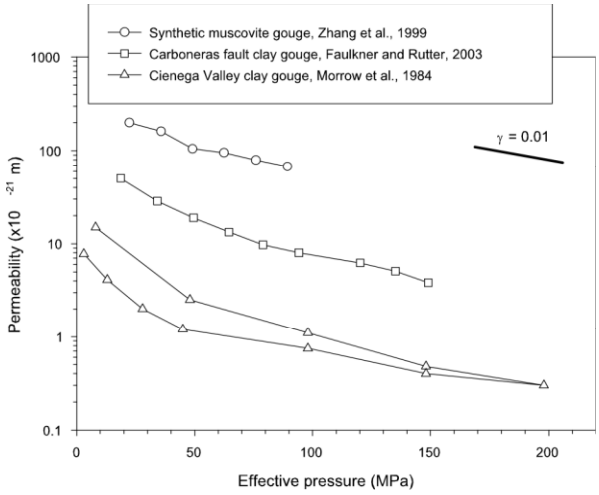

Figura I-11: Gráfico de dependencia de permeabilidad a la presión (Faulkner, 2004).
Obtenido de estudios experimentales en salbanda de filosilicatos, natural y sintética.

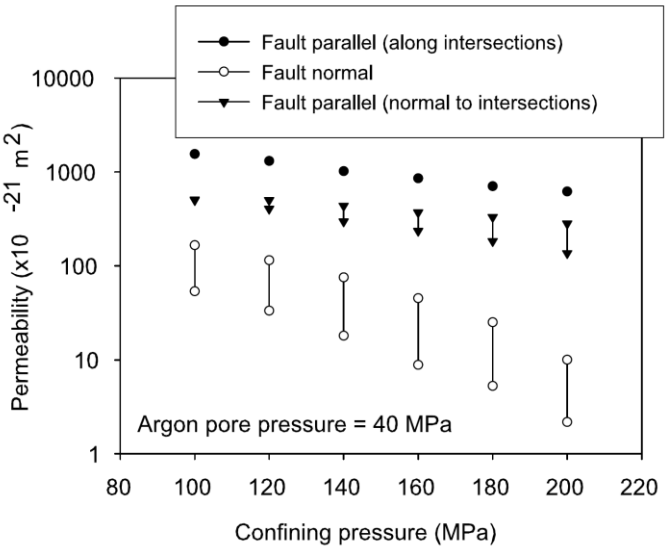

Figura I-12. Anisotropía de la permeabilidad en salbandas naturales ricas en filosilicatos. Usando argón y agua como fluidos porales (Faulkner & Rutter, 1998).

I.4.6. Alteraciones Mineralógicas

El agua es el fluido más versátil y reactivo que fluye por la corteza y dependiendo de sus condiciones fisicoquímicas, en especial temperatura y pH, interactúa de diferentes formas con la roca. Los diferentes fluidos acuosos resultantes de las variaciones de esas condiciones pueden producir a su paso grandes alteraciones mineralógicas en la roca que los hospeda.

En general, dependiendo de la temperatura y profundidad a la que los fluidos actúan, sus efectos se pueden separar en Alteración Hidrotermal o Hipógenas y Alteraciones Supérgenas o Meteorización (Rakovan, 2003).

I.4.6.1. Alteración Hidrotermal

"La distribución de los minerales de alteración en sistemas hidrotermales es controlada por la temperatura, química del fluido, concentraciones, composición de la roca hospedante y permeabilidad" (Browne, 1978). de los cuales la temperatura y pH son los factores más importantes" (Corbett & Leach, 1998).

Aunque es considerado preferible usar paragénesis minerales para definir estilos de alteración (Corbett & Leach, 1998) y consecuentemente esta investigación se hará de dicha forma, puede ser útil una clasificación de tipos de alteración para describir las características

generales de los sistemas. Los modelos de tipos de alteración entregan una buena idea sobre que esperar de un sistema hidrotermal.

Los tipos de alteración hidrotermal, producidos en rocas graníticas de aluminosilicatos, han sido clasificados en: Argílica Intermedia, Argílica Avanzada, Sericítica y Potásica (Meyer & Hemley, 1967). Posteriormente la alteración Sericítica fue llamada Fílica (Rose & Burt, 1979). Su mineralogía, se resume en:

Argílica (O Argílica Intermedia): Minerales formados a relativamente bajas temperaturas (>200º-250ºC) y con fluidos moderadamente ácidos (pH de 4 a 6). Minerales de los grupos caolinita, esméctica, halloysita e illita. También puede haber minerales del grupo de la clorita subordinados a la illita (Corbett & Leach, 1998).

Argílica Avanzada: Minerales formados por fluidos ácidos (pH menor a 4), como minerales de sílice y del grupo alunita además de paragénesis minerales de los grupos alunita y caolinita combinados (Corbett & Leach, 1998).

Fílica: Rangos de pH similares a alteración argílica intermedia, pero mayores temperaturas (200-350ºC) y se caracteriza por la presencia de sericita (illita). Puede también incluir minerales de más alta temperatura del grupo caolinita y clorita subordinados a la sericita (Corbett & Leach, 1998).

Propilítica**:** Se forma bajo condiciones alcalinas a neutras y se caracterizan por la presencia de epidota y clorita, a temperaturas relativamente bajas (200-250ºC). Donde es dominada por zeolitas en lugar de epidota, el término sub-propilítica debe ser aplicado. La ocurrencia de anfíboles secundarios (actinolita), albita y feldespato potásico es común en con esta alteración (Corbett & Leach, 1998).

Potásica**:** Forma a altas temperaturas, bajo condiciones neutrales a alcalinas y se caracteriza por biotita y/o feldespático potásico. En rocas hospedantes calcáreas (skarn) es común la presencia de granate, clinopiroxeno y tremolita (Corbett & Leach, 1998).

Un resumen de las paragénesis minerales que se pueden esperar para cada tipo de alteración hidrotermal se puede encontrar en la Figura I-13, que muestra esquemáticamente los rangos de estabilidad relativos de los minerales hidrotermales más comúnmente encontrados en campos geotermales activos del anillo del pacífico y en sistemas hidrotermales relacionados a depósitos minerales oro y cobre. Los datos se presentan en función de la acidez y temperatura relativa de estabilidad. Este esquema deriva de la compilación de datos obtenidos de Filipinas, Japón, U.S.A., Islandia y Nueva Zelanda, en combinación de resultados experimentales termodinámicos de varias fases minerales (Corbett & Leach, 1998).

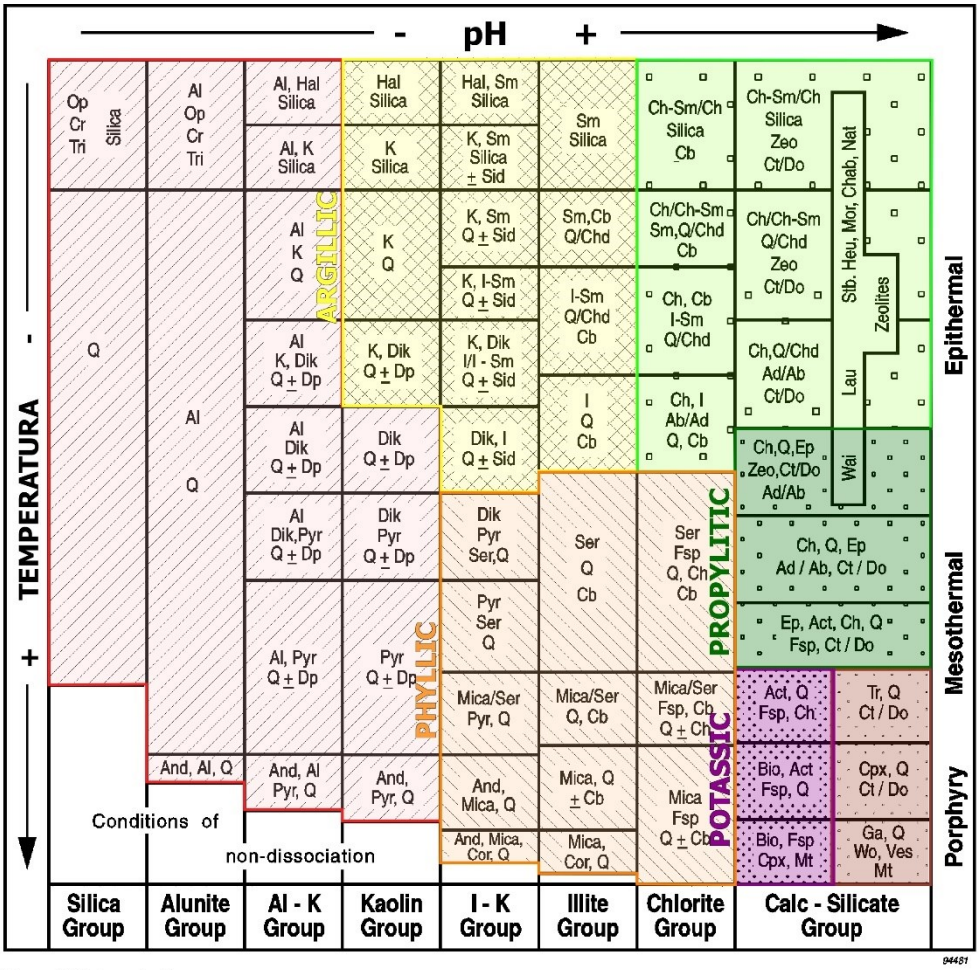

Mineral Abbreviations :

Ab - albite; Act - actinolite; Ad - adularia; Al - alunite; And - andalusite; Bio - biotite; Cb - carbonate (Ca, Mg, Mn, Fe); Ch - chlorite; Chab - chabazite; Chd - chalcedony; Ch-Sm - chlorite-smectite; Cor - corundum; Cpx - clinopyroxene; Cr - cristobalite; Ct - calcite; Do - dolomite; Dik - dickite; Dp - diaspore; Ep - epidote; Fsp - feldspar; Ga - garnet; Hal - halloysite; Heu - heulandite; I - illite; I-Sm - illite-smectite; K - kaolinite; Lau - laumontite; Mt - magnetite; Mor - mordenite; Nat - natrolite; Op - opaline silica; Pyr - pyrophyllite; Q - quartz; Ser - sericite; Sid - siderite; Sm - smectite; Stb - stilbite; Tr - tremolite; Tri - tridymite; Ves - vesuvianite; Wai - wairakite; Wo - wollastonite; Zeo - zeolite

Potásica | Propilítica | Sub-Propilítica
Skarn | Argílica | Argílica Avanzada
Fílica

Figura I-13. Temperatura y pH de asociaciones minerales en sistemas hidrotermales relacionados a depósitos de cobre-oro (Corbett & Leach, 1998)

En general, los sistemas hidrotermales porfídicos de cobre-oro muestran un patrón de distribución de alteraciones mineralógicas zonado como se muestra en la Figura I-14 (Sillitoe, 2010). En las partes más profundas del depósito, la alteración potásica tiende a ser las

predominante. Hacia arriba, en un depósito típico, las alteraciones fílica y argílica van tomando una creciente importancia a expensas de la alteración potásica. Alrededor de estas alteraciones se encuentra la alteración que cubre más áreas y alcanza zonas más lejanas a la fuente, la alteración propilítica.

Dataciones de K/Ar medidas en minerales de alteración y paleo salinidades analizadas en inclusiones fluidas indican que la alteración potásica y argílica pueden ocurrir al mismo tiempo y que la alteración argílica ocurre por fluidos ácidos livianos y ácidos que se exsuelven de los densos fluidos de menor acides (*brines*) que producen alteración potásica. (Hedenquist, 1998; Sibson 2010). La alteración fílica o sericítica, puede ocurrir en uno varios eventos posteriores, por el ascenso de fluidos de menor temperatura y salinidad intermedia, estos fluidos también pueden exsolver fluidos ácidos y producir alteración argílica avanzada (Ver **Figura I-14** tomada de Sillitoe, 2010). La alteración argílica ("intermedia") puede producirse en cualquier momento (incluso muy posterior al sistema hidrotermal) por descenso de aguas meteóricas o meteorización.

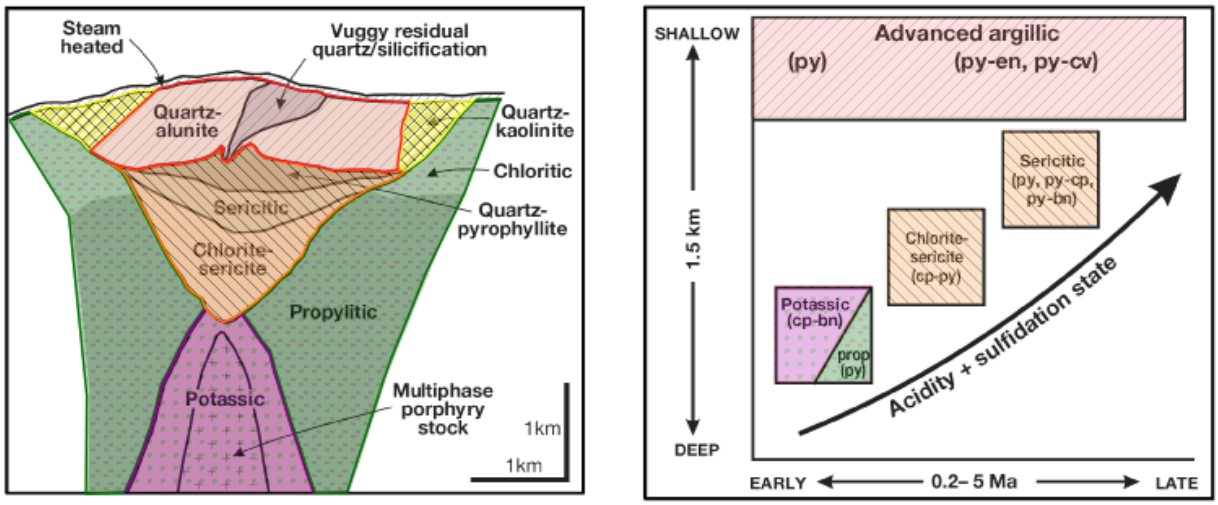

Figura I-14. Distribución y temporalidad de alteraciones mineralógica en un pórfido cuprífero (Sillitoe, 2010).
Izquierda: Dibujo esquemático de las zonas de alteración y mineralización en un modelo generalizado para depósitos tipo pórfido cuprífero. Derecha: Evolución temporal de un sistema porfídico mostrando alteraciones mineralógicas cada vez más someras, con mayor acides y mayor estado de sulfuración.

Para tener una idea del periodo de tiempo durante el cual los fluidos hidrotermales pueden haber afectado a las rocas del sistema porfídico se pueden usar como referencia dataciones radiométricas realizadas en sistemas de múltiples intrusiones porfídicas, con el método de U-Pb en zircones. Estas dataciones indican que un sistema porfídico (y las alteraciones mineralógicas relacionadas) pueden desarrollarse completamente en periodos tan pequeños como 80 mil años. (Baty Hijau, Indonesia, Garwin, 2002). Sin embargo, similares dataciones muestran que el

emplazamiento de stock porfídicos en los Andes ha ocurrido en periodos de 2 a 5 millones de años, indicando importantes periodos de tiempo (0.5-1.5 m.y.) entre emplazamientos de diferentes eventos intrusivos. (Ballard et al., 2001 (Chuquicamata); Maksaev et al., 2004 (El Teniente); Padilla-Garza et al., 2004 (La Escondida); Perelló et al., 2007(Esperanza); Harris et al., 2008 (Bajo de la Alumbrera)). Por otra parte, no se ha podido observar una relación entre el tamaño de los depósitos porfídicos y la duración de la actividad hidrotermal, por lo que se determina un rango de tiempo entre 0.2 y 5 millones de años para la actividad hidrotermal relacionada a intrusiones porfídicas (Sibson, 2010).

I.4.6.2. Alteración Supérgena

La alteración supérgena o meteorización, es el resultado de la interacción entre rocas y fluidos freáticos. Ocurre a mucha menor temperatura (0-50ºC) que la alteración hidrotermal y a bajas profundidades (0-1km), fuertemente controlada por el nivel freático y la mineralogía del protolito (Chávez, 2000). Los procesos más importantes en este tipo de alteración son la hidrólisis, hidratación y los cambios en el estado de oxidación, que resultan principalmente en la formación de zonas argílicas, migración vertical de elementos y oxidación in situ (Chávez, 2000). Debido a que la mayoría de los depósitos de mena se caracterizan por tener metales bases combinados con Fe y S reducido", los procesos de oxidación resultan en cambios químicos muy significativos, con zonas de alteración supérgena mucho más desarrolladas que en otros ambientes geológicos.

Zona	Domina la lixiviación de Fe y Cu	Domina la Oxidación in Situ
Fuente	Sulfuros reactivos con jarosita, goetita >>hematita Pirita residual, calcopirita, alunita, sulfatos de Al y Fe.	Poco volumen de sulfuros (metálicos o total) Oxidación casi in situ y precipitación de hematita, hematita>>gohetita, jarosita
Precipitación	Chalcantita, bonatita, anttlerita, brocantita, posnjakita, cobre nativo en pocas caniidades. Calcocina, covelina, pirita, calcopirita. Posiblemente; Alunita, Oxidos de As y Fe, arseinatos.	Atacamita, brocantita, cobre nativo, calcosiderita, cuprita, tenorita, paramelaconita, malaquita, fosfatos, alunita, calcopirita residual, bornita, pirita.
Protolito	Pirita , calcosina, trazas de borbita, pirrotina	Bornita, calcocina, calcopirita, ± pirita.

Figura I-15. Paragénesis en zonas de alteración supérgena (Chávez, 2000).

Un ambiente de alteración supérgena, cuando se encuentra bien desarrollado, puede ser separado en 3 dominios geoquímicos:

(1) Zona Fuente, que comprende el volumen de roca en el que ocurre o ha ocurrido oxidación y pérdida de masa.

(2) Zona de Precipitación ("*Sink Zone*"), donde la masa perdida en la zona fuente es acumulada por precipitación química, dependiendo de la fugacidad de oxígeno, controlada por el nivel freático, pueden desarrollarse minerales metálicos tipo óxidos o sulfuros.

(3) Protolito, normalmente se encuentra debajo de la zona de precipitación, y se trata de la roca no afectada por alteración supérgena (Chávez, 2000).

El tamaño de estas zonas depende de la relación entre la acidez de los fluidos percolantes y la acidez del protolito. La acidez de los fluidos aumenta principalmente por la alteración de minerales de fierro, que al oxidarse generan goethitas que consumen grupos hidroxilo (OH^-) provenientes del agua y liberan protones hidrógeno. La pirita es el principal generador de acidez en los medios bajo alteración supérgena, sin embargo, no es el único mineral de hierro que colabora con protones al medio y los silicatos de hierro como piroxeno y biotitas también se oxidan a goethita y H^+.

En los depósitos hidrotermales de cobre, debido a que originalmente tienen altos contenidos de pirita, la alteración supérgena ocurre muy intensamente y como resultado se encuentra una zonación muy bien desarrollada. Las paragénesis minerales que se pueden encontrar en las distintas zonas han sido resumidas por Chávez (2000) en la tabla de la Figura I-15, en esta tabla las paragénesis son separadas según el proceso que ha dominado más, transporte de masa por lixiviación u oxidación in situ.

Esta investigación se enfoca en efectos principalmente de fluidos hidrotermales (hipógenos) por lo que se han seleccionado los afloramientos con el menor efecto de alteración supérgena posible, es decir en la zona "protolito" de la figura I-15.

I.5. MARCO TECTÓNICO-ESTRUCTURAL DE LOS CASOS DE ESTUDIO

Los 2 casos de estudio de esta tesis se encuentran en diferentes sistemas de fallas pero ambos dentro del mismo antearco de los Andes Centrales, como se muestra en las Figura I-16 y Figura I-17**,** ubicados en latitudes cercanas (a escala continental). Este segmento de los Andes se encuentra sobre una transición de subducción de la placa oceánica entre el Ridge de Nazca, al norte, y el Ridge de Juan Fernández, al sur. (Tassara & Yañez, 2003). En los Andes Centrales,

el orógeno andino se caracteriza por estar curvado y un presentar un mayor ancho (extensión E-W) que otros segmentos. Esto incluye una serie de unidades morfoestructurales sub-paralelas con tendencia N-S (a NW-SE) entre el arco volcánico actual que, de oeste a este, se denominan: (1) Cordillera de la Costa, (2) Valle longitudinal (3) Precordillera (con Depresión Pre-Andina), (4) Cordillera Occidental o Arco Magmático Actual, (5) Altiplano o Puna, (6) Cordillera Oriental y (7) Sierras Sub-Andinas o Antepaís Deformado (Amilibia et al., 2008). Los casos de estudio de la presente tesis son fallas ubicadas en dos unidades morfoestructurales diferentes: Cordillera de la Costa (Duplex Caleta Coloso, dentro del Sistema de Falla Atacama) y Precordillera (Fallas de Radomiro Tomic, en el Sistema de Falla Domeyko).

La deformación y evolución de las unidades morfoestructurales arriba mencionadas y, por ende, la ubicación y los casos de estudio, se muestra en los perfiles transversales de la Figura I-18. El Sistema de Falla Atacama, ha iniciado como una zona de deformación plástica (milonitas) asociada al emplazamiento de plutones y a volcanismo en la cordillera de la costa durante el Jurásico Tardío (Taylor *et al.*, 1998). Posteriormente, durante el cretácico, el enfriamiento de la cordillera de la costa por la migración del arco magmático hacia el Este habría marcado el paso de deformación dúctil a frágil, desarrollándose las fallas que se pueden observar hoy en superficie. Por su parte, el Sistema de Falla Domeyko, habría iniciado mucho después, durante el Terciario (ver Figura I-18 y Figura I-19) durante el emplazamiento de magmas porfídicos en cuencas invertidas de rift, en la actual Pre-Cordillera Andina.

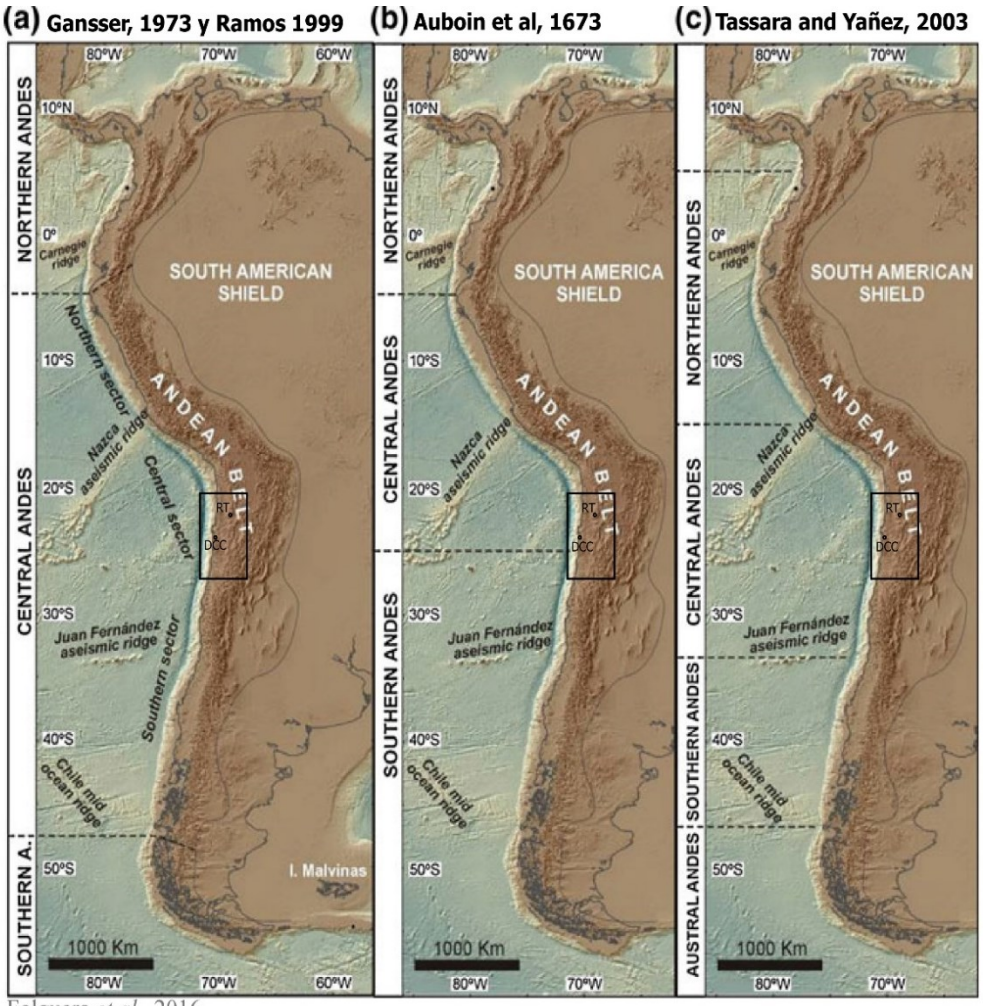

Folguera *et al*., 2016

Figura I-16. Ubicación de los casos de estudio en contexto de la segmentación de los Andes. Editado de Folguera *et al.*, 2016)

Cada uno de los tres mapas muestra una diferente clasificación de segmentos de los Andes, según el (los) autores que se citan sobre estas. El rectángulo negro indica la posición de la Figura I-17 y los puntos dentro de éste indican la posición de los casos de estudio DCC: Duplex Caleta Coloso y RT: Radomiro Tomic.

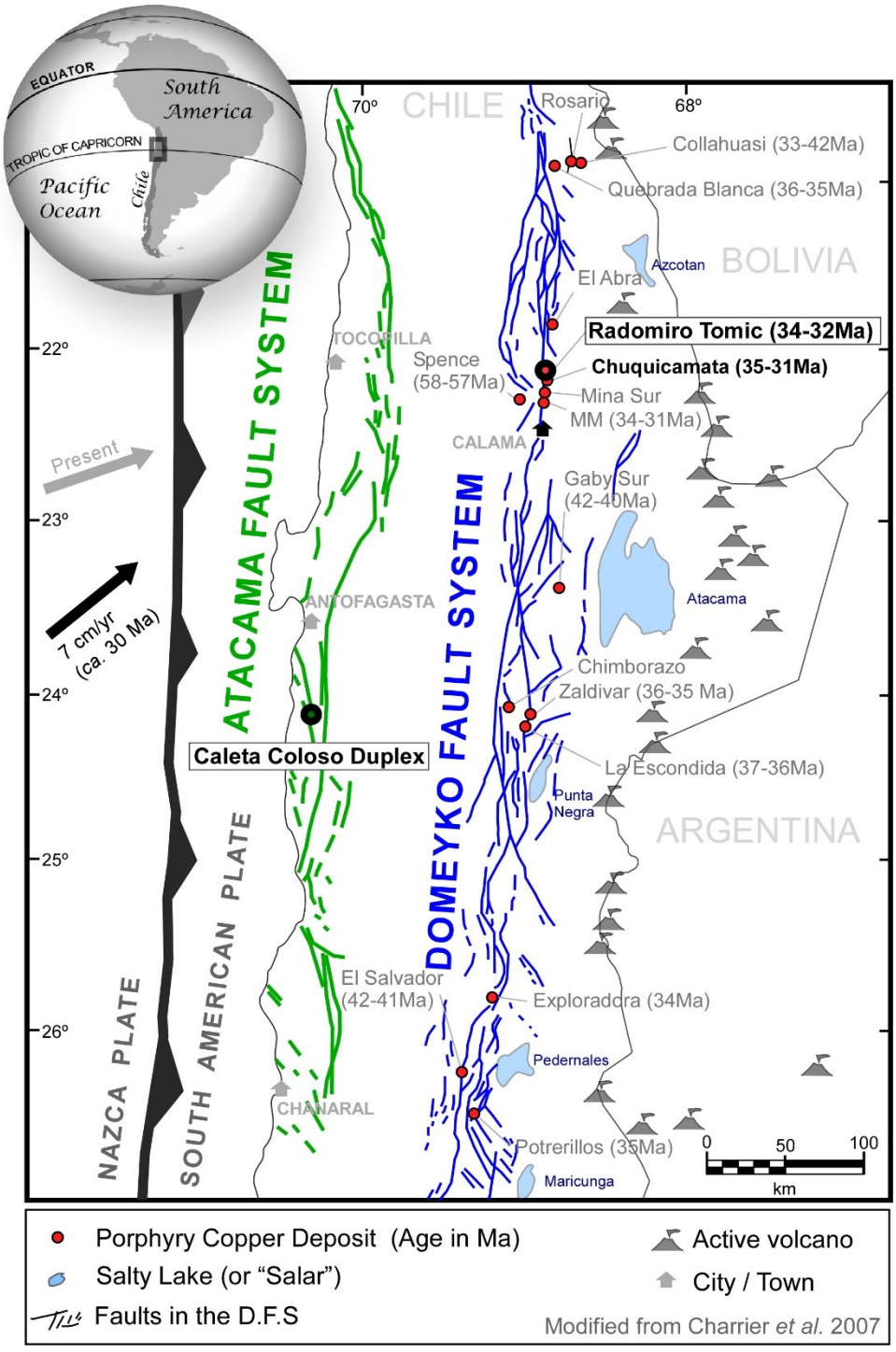

Figura I-17. Mapa estructural del norte de Chile entre los 21º y 27ºS. (Charrier *et al.*, 2007)
Se muestra el Sistema de Falla Atacama y el Sistema de Falla Domeyko. Se indican los depósitos de pórfido cuprífero y sus edades de emplazamiento. Se destaca el Duplex Caleta Coloso (DCC) el depósito metalífero Radomiro Tomic por ser los casos de estudio.

I.5.1. Sistema de Falla Domeyko (SFD)

El Sistema de Falla Domeyko, en adelante llamado SFD, se extiende desde el 20ºS hasta los 27ºS, y se compone de muchas fallas frágiles de rumbo e inversas de escala métrica a kilométrica. Este sistema se encuentra localizado a lo largo del eje de arcos volcánicos previos (Cretácico tardío a Eoceno) y se han reportado evidencias de inversión de fallas normales y de movimientos de rumbo dextrales y siniestrales (Charrier *et al.,* 2007; Charrier & Reutter, 1994; Mpodozis & Allmendinger, 1993; Tomlinson & Blanco, 1997a, 1997b).

A la fecha pocos trabajos han documentado la estructura interna de las fallas del SFD. Niemeyer *et al.,* (2004) han realizado una muy detallada descripción de una banda cataclástica en Sierra de Varas. Se trata de cataclasita y protocataclasita mineralizada con clorita y calcita. Es importante destacar que dichas cataclasitas actualmente se encuentran desplazadas por la traza más reciente de la falla Sierra de Varas, por lo que se trata de la estructura interna en etapas previas a la correspondiente al actual SFD.

La Falla Oeste o “West Fissure” ha sido estudiada a través de lineamientos en fotografías aéreas y perfiles geofísicos hasta los 3 km de profundidad en la quebrada Guatacondo y Sierra Limón Verde (Janssen *et al.,* 2002). Esta investigación concluye en que la falla tiene una zona de daño de 4 a 7 km de ancho caracterizada por zonas de mayor fracturamiento al promedio regional. El núcleo de la Falla Oeste no ha sido encontrado en superficie por los autores y a partir de zonas de baja resistividad eléctrica en perfiles audiomagnetotelúricos se interpreta que estos solo consisten en zonas de mayor densidad de fracturas de entre 100 y 200 m. Sin embargo, se describe un afloramiento de una falla subsidiaria compuesta de un núcleo de cataclasitas de 10-20cm, con matriz muy fina (<10 μm) rodeando algunos pequeños fragmentos de protolito, principalmente de cuarzo.

Una característica muy importante del Sistema de Falla Domeyko es su relación espacial con los yacimientos tipo pórfido cuprífero. Numerosos depósitos hidrotermales de edad Eoceno (medio) a Oligoceno (temprano) del orden de los kilómetros cuadrados de extensión se encuentran distribuidos a lo largo su traza (Figura I-17). Esta evidencia sugiere fuertemente que tanto las cataclasitas y salbandas en los núcleos de fallas cómo los protolitos en las paredes circundantes han sido alterados hidrotermalmente y esta interacción se ha interpretado que podría haber producido un debilitamiento cortical que favorece el desarrollo del SFD (McElderry *et al.,* 1996).

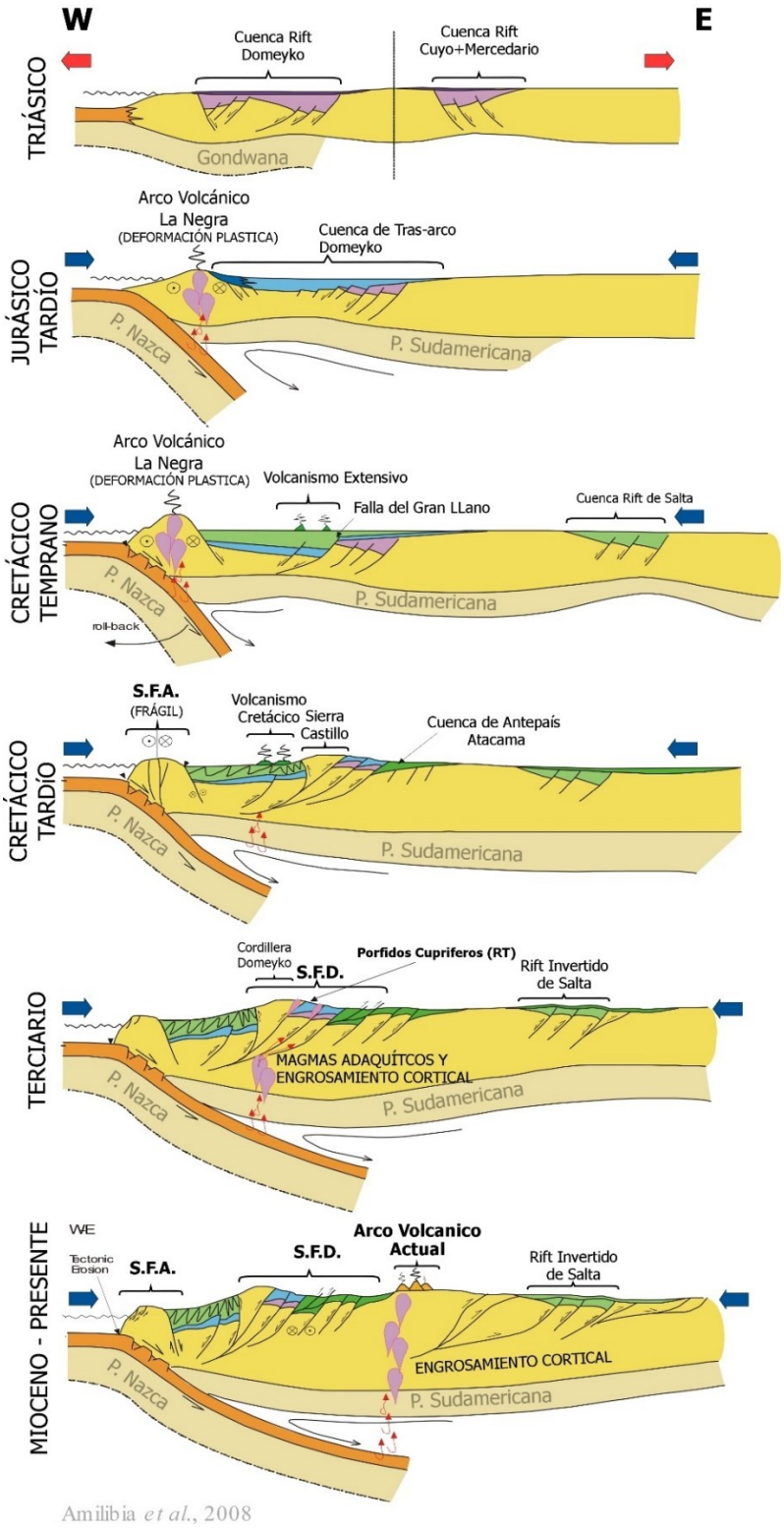

Figura I-18. Perfiles mostrando la evolución tectono-estratigráfica de los Andes Centrales
Modificado de Amilibia et al., (2008) para destacar la formación del Sistema de Falla Atacama (SFA) y Sistema de Falla Domeyko (SFD). Historia cinemática del SFA se ha modificado de acuerdo con Scheuber et al. (1995) y Taylor et al. (1998).

I.5.2. Sistema de Falla Atacama (SFA) y Dúplex Caleta Coloso (DCC)

El Sistema de Falla Atacama (SFA) es el elemento tectónico más importante de la Cordillera de la Costa en el antearco de los Andes Centrales (Arabasz, 1971; Brown *et al.,* 1993, Grocott & Taylor, 2002; Scheuber & Andriessen, 1990). Se trata de un sistema de falla paralelo a la fosa compuesto de varios segmentos sub-verticales con rumbos entre N-S y NW-SE y longitudes entre kilómetros y decenas de km. En total, el SFA tiene una longitud de unos 1000 km de longitud y unos 100 km de ancho, afectando al arco magmático entre Iquique (21ºS) y La Serena (30ºS) (Arabasz, 1971, Brown *et al.,* 1993, González, 1996) (Figura I-17).

La propagación de este sistema de fallas ha ocurrido durante la última etapa de deformación de la Cordillera de la Costa, cuando el enfriamiento progresivo del arco permitió un cambió en el régimen de deformación: desde deformación plástica, representada por zonas de milonitas kilométricas, con facies mineralógicas de anfibolitas (150-143 Ma) y esquistos verdes (139-125 Ma) (Scheuber *et al.,* 1995), a deformación frágil, representada por fallas con núcleos de anchos métricos con cataclasitas ricas en clorita y epidota (125-118 Ma) (Cembrano *et al.,* 2005) que conforman la geometría principal del actual SFA en el segmento Paposo Figura I-18.

Las estructuras frágiles del SFA muestran principalmente movimientos siniestrales con una pequeña componente extensional. Esta cinemática ha sido atribuida al ángulo de convergencia altamente oblicuo de la subducción predominante en la época, de la placa Aluk bajo la Sudamericana (Grocott & Taylor, 2002; Scheuber & Andriessen, 1990; Scheuber & González, 1999).

Una estructura muy importante dentro del SFA, por su tamaño, significado cinemática y por la gran cantidad de estudios realizados en el Dúplex Caleta Coloso. Este es un dúplex de rumbo siniestral ubicado a 20 km al sur de la ciudad de Antofagasta. Está formado por dos, fallas maestras de rumbo NNW y manteo sub-vertical que se ramifican de la falla Caleta Coloso. Estas dos fallas son la falla Bolfín y la Falla Jorgillo, las cuales, a su vez, se encuentran conectadas por un set de fallas imbricadas de segundo orden (NW-SE) y tercer orden (E-W).

El DCC ha sido interpretado como de haber sido formado en un codo dilatacional entre las fallas Jorgillo y Bolfín (Cembrano *et al.,* 2005). Las condiciones físicas bajo las cuales este codo fue desarrollado pueden ser inducidas a partir de las paragénesis minerales asociadas. Tanto las cataclasitas en los núcleos de las fallas como las vetas geométrica- y espacialmente relacionadas muestran asociaciones mineralógicas de epidota y clorita con menor cuarzo y albita, correspondientes a alteración propilítica, sugiriendo un fuerte vínculo con transporte de fluidos en

condiciones Pº y Tº de esquistos verdes (Cembrano *et al.,* 2005; Olivares, 2004). La profundidad desde donde las rocas falladas han sido posteriormente levantadas hasta su presente posición ha sido estimada entre 3 y 10 km (Cembrano *et al.,* 2005; Faulkner *et al.,* 2006).

La relación entre las fallas del Duplex Caleta Coloso (en el SFA) y fluidos hidrotermales magmáticos, evidenciada por precipitación de clorita, epidota y calcita, contribuirá al entendimiento de procesos de deformación frágil bajo el efecto de fluidos hidrotermales de diferentes naturaleza y características químicas que los fluidos asociados a depósitos porfídicos. Para posteriormente comparar con el complejo sistema de alteración hidrotermal mostrado por las fallas de Radomiro Tomic, en el Sistema de Falla Domeyko.

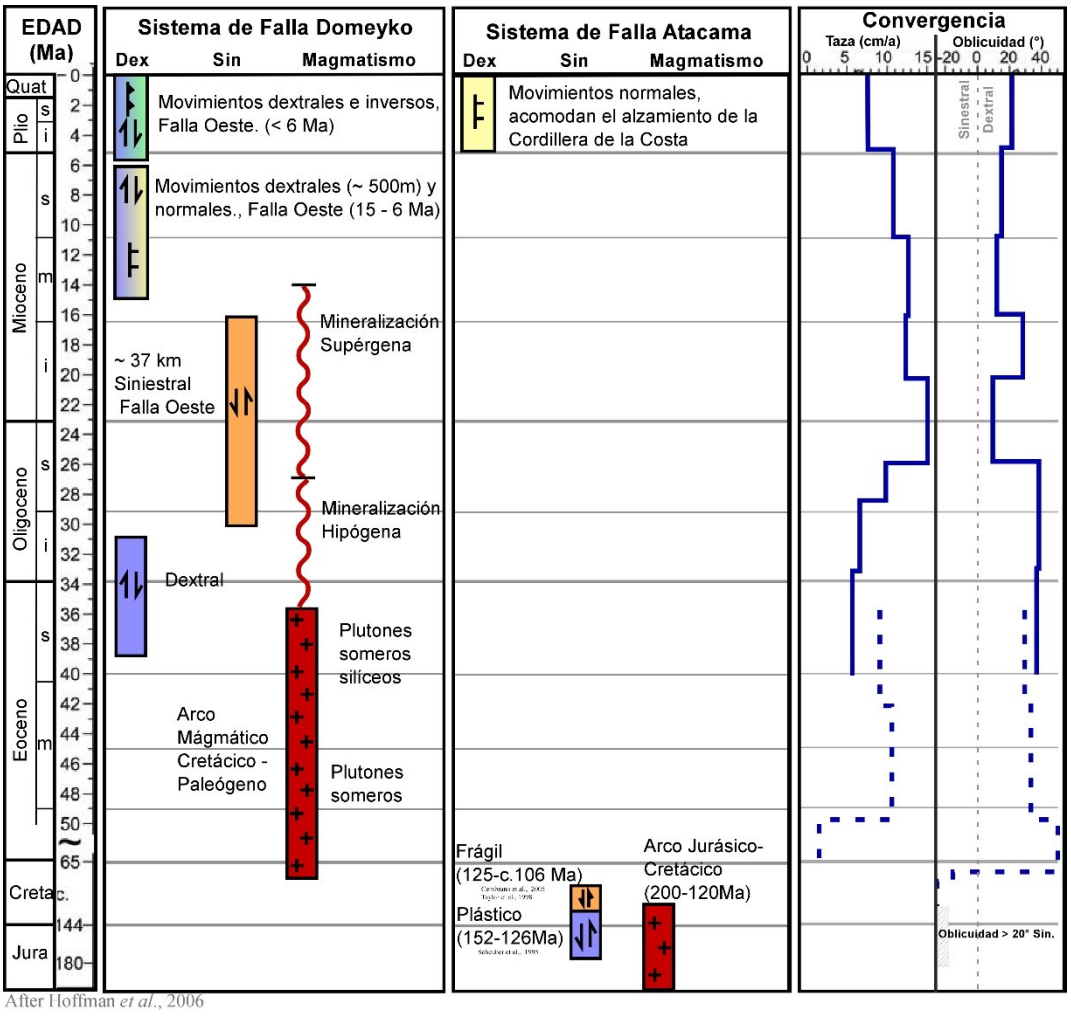

Figura I-19. Esquema temporal de la actividad magmática y cinemática del SFA y SFD. (Modificado de Hoffmann-Rothe *et al*., 2006).
Recopilación de los principales modos de fallamiento a lo largo de los sistemas de fallas paralelos al margen más prominentes del Norte de Chile. Las tasas y oblicuidad de la convergencia están de acuerdo con Somoza (1998) y a Pardo-Casas & Molnar (1987).

I.6. REFERENCIAS

Alpers, C. N. & Brimhall, G. H. (1998). Middle Miocene climatic change in the Atacama desert, northern Chile: Evidence from supergene mineralization at La Escondida. Geological Society of America Bulletin 100(10), 1640-1656.

Amilibia, A., Sàbat, F., McClay, K. R., Muñoz, J. A., Roca, E. & Chong, G. (2008). The role of inherited tectono-sedimentary architecture in the development of the central Andean mountain belt: Insights from the Cordillera de Domeyko. Journal of Structural Geology 30(12), 1520-1539.

Arabasz, Walter Joseph, Jr. (1971). Geological and Geophysical Studies of the Atacama Fault Zone in Northern Chile. Dissertation (Ph.D.), California Institute of Technology.

Auboin, J. (1973). Présentation de la Cordillère des Andes. Revue de Géographie physique et de Géologie Dynamique 15, 5–10.

Ballard, J.R., Palin, J.M., Williams, I.S., Campbell, I.H., and Faunes, A., (2001). Two ages of porphyry intrusion resolved for the super-giant Chuquicamata copper deposit of northern Chile by ELA-ICP-MS and SHRIMP. Geology, v. 29, p. 383−386.

Braathen, A., Tveranger, J., Fossen, H., Skar, T., Cardozo, N., Semshaug, S. E., Bastesen, E. & Sverdrup, E. (2009). Fault facies and its application to sandstone reservoirs. AAPG Bulletin 93(7), 891-917.

Brown, M., Diaz, F. & Grocott, J. (1993). Displacement History of the Atacama Fault System 25º00'S-27º00'S, Northern Chile. Geological Society of America Bulletin 105(9), 1165-1174.

Brown, S. R. & Bruhn, R. L. (1998). Fluid permeability of deformable fracture networks. Journal of Geophysical Research-Solid Earth 103(B2), 2489-2500.

Browne, P. R. L. (1978). Hydrothermal Alteration in Active Geothermal Fields. Annual Review of Earth and Planetary Sciences 6(1), 229.

Byerlee, J.D. (1978). Friction of rocks. Pure & Applied Geophysics 116, 615–626.

Caine, J. S., Evans, J. P. & Forster, C. B. (1996). Fault zone architecture and permeability structure. Geology 24(11), 1025-1028.

Campos, E. A. (2002). Metal origin and fluid evolution in the Zaldívar porphyry copper deposit, Chile: an orthomagmatic model, Vrije Universiteit Amsterdam.

Cembrano, J., Gonzalez, G., Arancibia, G., Ahumada, I., Olivares, V. & Herrera, V. (2005). Fault zone development and strain partitioning in an extensional strike-slip duplex: A case study from the Mesozoic Atacama fault system, Northern Chile. Tectonophysics 400(1-4), 105-125.

Cladouhos, T. T. (1999). Shape preferred orientations of survivor grains in fault gouge. Journal of Structural Geology 21(4), 419-436.

Corbett & Leach. (1998). Controls on hydrothermal alteration and mineralization. Society of Economic Geologist. Special Publication No.6, 13.

Crawford, B. R., Faulkner, D. R. & Rutter, E. H. (2008). Strength, porosity, and permeability development during hydrostatic and shear loading of synthetic quartz-clay fault gouge. Journal of Geophysical Research-Solid Earth 113(B3).

Charrier, R. & Reutter, K.-J. (1994). The Purilactis Group of Northern Chile: Boundary between arc and backarc from late Cretaceous to Eocene. In: Tectonics of the Southern Central Andes (edited by Scheuber, E. & Wigger, P.). Springer-Verlag, Beriln, 189-202.

Charrier, R., Pinto, L. & Rodrigues, M. (2007). Tectonostratigraphic evolution of the Andean Orogen in Chile. In: The Geology of Chile (edited by Moreno, T. & Gibbons, W.). The Geological Society, London, 21–114.

Chester, F. M., Chester, J. S., Kirschner, D. L., Schulz, S. E. & Evans, J. P. 2004. Structure of large-displacement, strike-slip fault zones in the brittle continental crust. In: Rheology and Deformation in the Lithosphere at Continental Margins (edited by Karner, G. D., Taylor, B., Driscoll, N. W. & Kohlstedt, D. L.). Columbia Univ. Press, New York.

Chavez, W. X. (2000). Supergene Oxidation of Copper deposits: Zoning and Distribution of Copper Oxide Minerals. Society of Economic Geologist Newsletter 41, 13.

Chester, F. M., Friedman, M. & Logan, J. M. (1985). Foliated cataclasites. Tectonophysics 111(1-2), 139-146.

Chester, F. M. & Logan, J. M. (1987). Composite Planar Fabric of Gouge from the Punchbowl Fault, California. Journal of Structural Geology 9(5-6), 621-634.

Chester, F. M., Evans, J. P. & Biegel, R. L. (1993). Internal Structure and Weakening Mechanisms of the San-Andreas Fault. Journal of Geophysical Research-Solid Earth 98(B1), 771-786.

Engelder, J. T. (1974). Cataclasis and Generation of Fault Gouge. Geological Society of America Bulletin 85(10), 1515-1522.

Evans, J. P. & Chester, F. M. (1995). Fluid-rock interaction in faults of the San Andreas system: Inferences from San Gabriel fault rock geochemistry and microstructures. Journal of Geophysical Research: Solid Earth 100(B7), 13007-13020.

Faulkner, D. R. & Rutter, E. H. (1998). The gas permeability of clay-bearing fault gouge at 20ºC. In: Faults, Fault Sealing and Fluid Flow in Hydrocarbon Reservoirs (edited by Jones, G., Fisher, Q. & Knipe, R. J.) 147. Geological Society of London Special Publication, 147-156.

Faulkner, D. R. & Rutter, E. H. (2003). The effect of temperature, the nature of the pore fluid, and subyield differential stress on the permeability of phyllosilicate-rich fault gouge. Journal of Geophysical Research-Solid Earth 108(B5).

Faulkner, D. R., Lewis, A. C. & Rutter, E. H. (2003). On the internal structure and mechanics of large strike-slip fault zones: field observations of the Carboneras fault in southeastern Spain. Tectonophysics 367(3-4), 235-251.

Faulkner, D. R. (2004). A model for the variation in permeability of clay-bearing fault gouge with depth in the brittle crust. Geophysical Research Letters 31(19), 5.

Faulkner, D. R., Mitchell, T. M., Healy, D. & Heap, M. J. (2006). Slip on 'weak' faults by the rotation of regional stress in the fracture damage zone. Nature 444(7121), 922-925.

Faulkner, D. R., Mitchell, T. M., Rutter, E. H. & Cembrano, J. (2008). On the structure and mechanical properties of large strike-slip faults. Geological Society, London, Special Publications 299(1), 139.

Fischer, G. J. (1992). The determination of permeability and storage capacity: Pore pressure oscillation method. In: "Fault Mechanics and Transport Properties of Rocks" Evans, B. and Wong, T.-F (eds). Academic Press Ltd, 187-212.

Folguera, Andres & Naipauer, Maximiliano & Sagripanti, Lucía & Ghiglione, Matias & Orts, Darío & Giambiagi, Laura. (2016). Growth of the Southern Andes. 10.1007/978-3-319-23060-3.

Gansser A (1973) Facts and theories on the Andes. J Geol Soc London 129:93–131

Garwin, S., (2002). The geologic setting of intrusion-related hydrothermal systems near the Batu Hijau porphyry copper-gold deposit, Sumbawa, Indonesia. Society of Economic Geologists Special Publication 9, p. 333−366

Giger, S. B., Cox, S. F. & Tenthorey, E. (2008). Slip localization and fault weakening as a consequence of fault gouge strengthening -- Insights from laboratory experiments. Earth and Planetary Science Letters 276(1-2), 73-84.

González, G. (1996). Evolución tectónica de la Cordillera de la Costa de Antofagasta (Chile): Con especial referencia a las deformaciones sinmagmáticas del Jurásico-Cretácico Inferior, Freïe Universität Berlin

Griggs, D. T. & Blacic, J. D. (1965). Quartz: Anomalous Weakness of Synthetic Crystals. Science 147(3655), 292-295.

Griggs, D. (1967). Hydrolytic Weakening of Quartz and Other Silicates. Geophysical Journal of the Royal Astronomical Society 14(1-4), 19-31.

Hoffmann-Rothe, A., Kukowsky, N., Dresen, D., Helmut, E., Oncken, O. J., K., Scheuber, E. & Kellner, A. 2006. Oblique Convergence along the Chilean Margin: Partitioning, Margin-Parallel

Faulting and Force Interaction at the Plate Interface. In: The Andes: Active Subduction Orogeny (edited by Oncken, O., Gotze, H., Chong, G., Ramos, V., Franz, G., Strecker, M., Giese, P. & Wigger, P.). Springer London, Limited.

Harris, A.C., Dunlap, W.J., Reiners, P.W., Allen, C.M., Cooke, D.R., White, N.C., Campbell, I.H., and Golding, S.D., (2008). Multimillion year thermal history of a porphyry copper deposit: Application of U-Pb, 40Ar/39Ar and (U-Th)/He chronometers, Bajo de la Alumbrera copper-gold deposit, Argentina: Mineralium Deposita, v. 43, p. 295−314.

Grocott, J. & Taylor, G. K. (2002). Magmatic arc fault systems, deformation partitioning and emplacement of granitic complexes in the Coastal Cordillera, north Chilean Andes (25º30'S to 27º00'S). Journal of the Geological Society 159(4), 425-443.

Guo, Y. & Morgan, J. K. (2007). Fault gouge evolution and its dependence on normal stress and rock strengthâ€"Results of discrete element simulations: Gouge zone properties. J. Geophys. Res. 112.

Hedenquist, J.W., Arribas, A., Jr., and Reynolds, T.J. (1998). Evolution of an intrusion-centered hydrothermal system: Far Southeast-Lepanto porphyry and epithermal Cu-Au deposits, Philippines: Economic Geology, v. 93, 373−404.

Heilbronner, R. & Keulen, N. (2006). Grain size and grain shape analysis of fault rocks. Tectonophysics 427(1-4), 199-216.

Herrera, V., Cembrano, J., Olivares, V., Kojima, S. & Arancibia, G. (2005). Precipitation by depressurization and boiling in veins hosted in an extensional strike-slip duplex: microstructural and microthermometric evidence. Revista Geologica de Chile 32(2), 207-227.

Jaeger, J. C. & Cook, N., (1979). Fundamentals of Rock Mechanics, 3rd edn. Chapman and Hall, London.

Janssen, C., Hoffmann-Rothe, A., Tauber, S. & Wilke, H. (2002). Internal structure of the Precordilleran fault system (Chile) - insights from structural and geophysical observations. Journal of Structural Geology 24(1), 123-143.

Lapworth, C. (1885). The Highland controversy in British geology: its causes, course and consequences. Nature 32, 2.

Lin, A. (1999). S-C cataclasite in granitic rock. Tectonophysics 304(3), 257-273.

Mair, K. & Abe, S. (2008). 3D numerical simulations of fault gouge evolution during shear: Grain size reduction and strain localization. Earth and Planetary Science Letters 274(1-2), 72-81.

Maksaev, V., Munizaga, F., McWilliams, M., Fanning, M., Mathur, R., Ruiz, J., and Zentilli, M., (2004). New chronology for El Teniente, Chilean Andes, from U-Pb, 40Ar/39Ar, Re-Os, and

fission track dating: Implications for the evolution of a supergiant porphyry Cu-Mo deposit: Society of Economic Geologists Special Publication 11, p. 15−54.

McElderry, S., Chong, G., Prior, D. & Flint, S.)(1996). Structural styles in the Domeyko range, northern Chile. In: Symposium International sur la Géodynamique Andine, 17-19 septembre, 1996, Saint Malo, 439-442.

Mei, S. & Kohlstedt, D. L. (2000a). Influence of water on plastic deformation of olivine aggregates 1. Diffusion creep regime. J. Geophys. Res. 105(B9).

Mei, S. & Kohlstedt, D. L. (2000b). Influence of water on plastic deformation of olivine aggregates 2. Dislocation creep regime. J. Geophys. Res. 105(B9).

Meyer, C. & Hemley, J. (1967). Wall rock alteration. In: Geochemistry of Hydrothermal Ore deposits (edited by Barnes, H.). Holt, Rinehart, and Winston., New York, 166-235.

Mpodozis, C. & Allmendinger, R. W. (1993). Extensional tectonics, Cretaceous Andes, northern Chile (27ºS). Geological Society of America Bulletin 105(11), 1462-1477.

Muhuri, S. K., dewers, T. A., Scott, T. E., & Reches, Z. (2003). Interseismic fault strengthening and earthquake-slip instability: Friction or cohesion? Geology 31(10), 881-884.

Niemeijer, A. R., Spiers, C. J. & Peach, C. J. (2008). Frictional behaviour of simulated quartz fault gouges under hydrothermal conditions: Results from ultra-high strain rotary shear experiments. Tectonophysics 460(1-4), 288-303.

Niemeyer, H., Berrios, H. & Ruiz Cruz, M. D. (2004). Temperaturas de formación en cataclasitas triásicas de la Cordillera Domeyko, Antofagasta. Revista Gologica de Chile 31(1), 3-18.

Nur, A. & Byerlee, J. D. (1971). An Exact Effective Stress Law for Elastic deformation of Rock with Fluids. Journal of Geophysical. Research. 76(26).

Olivares, V. (2004). Geometría y cinemática del sistema de fallas y vetas de la porción sur del Duplex Caleta Coloso, región de Antofagasta. Universidad Católica del Norte.

Olsen, M. P., Scholz, C. H. & Leger, A. (1998). Healing and sealing of a simulated fault gouge under hydrothermal conditions: Implications for fault healing. Journal of Geophysical Research-Solid Earth 103(B4), 7421-7430.

Padilla-Garza, R.A., Titley, S.R., and Eastoe, C.J., (2004). Hypogene evolution of the Escondida porphyry copper deposit, Chile: Society of Economic Geologists Special Publication 11, p. 141−165.

Padilla, R. A., Titley, S. R. & Pimentel B, F. (2001). Geology of the Escondida Porphyry Copper deposit, Antofagasta Region, Chile. Economic Geology 96(2), 307-324.

Pardo-Casas F. & Molnar P. (1987). Relative motion of the Nazca (Farallon) and South American plates since late Cretaceous time. Tectonics 6, 233–248

Perelló, J., Brockway, H., and Martini, R., (2004), Discovery and geology of the Esperanza porphyry copper-gold deposit, Antofagasta Region, northern Chile: Society of Economic Geologists Special Publication 11, 167−186.

Rakovan, J. (2003). A Word to the Wise: Hypogene & Supergene. Rocks & Minerals 78(6), 419-419.

Ramos VA (1999) Plate tectonic setting of the Andean Cordillera. Episodes 22(3):183–190

Robin, P. (1973). Note on Effective Pressure. Journal of Geophysical Research 78(14), 4.

Rose, A. W. & Burt, D. M. 1979. Hydrothermal alteration. In: Geochemistry of hydrothermal ore deposits. (edited by Barnes, H. L.). Wiley, New York, 173-235.

Scheuber, E. & Andriessen, P. A. M. (1990). The Kinematic and Geodynamic Significance of the Atacama Fault Zone, Northern Chile. Journal of Structural Geology 12(2), 243-257.

Scheuber, E. & González, G. (1999). Tectonics of the Jurassic- Early Cretaceous magmatic arc of the north Chilean Coastal Cordillera (22 degrees-26 degrees S): A story of crustal deformation along a convergent plate boundary. Tectonics 18(5), 895-910.

Scheuber, E., Hammerschmidt, K. & Friedrichsen, H. (1995). Ar-40/Ar-39 and Rb-Sr Analyses from Ductile Shear Zones from the Atacama Fault Zone, Northern Chile - the Age of deformation. Tectonophysics 250(1-3), 61-87.

Scholz, C. H. (1987). Wear and Gouge Formation in Brittle Faulting. Geology 15(6), 493-495.

Scholz, C. H. (1988). The brittle-plastic transition and the depth of seismic faulting. Geol. Runds. 77: 319–328.

Scholz, C. H. (2002). The mechanics of Earthquakes and Faulting. 2nd edition, Cambridge University Press, Cambridge.

Sibson, R. H. (1977). Fault rocks and fault mechanisms. Journal of the Geological Society of London 133, 22.

Sillitoe, R. H. (1973). The tops and bottoms of porphyry copper deposits. Economic Geology 68(6), 799-815.

Sibson, R. H. (1990). Conditions for fault-valve behaviour. Geol. Soc. Lond. Spec. Pub 54(1), 15-28.

Solum, J. G., van der Pluijm, B. A., Peacor, D. R. & Warr, L. N. (2003). Influence of phyllosilicate mineral assemblages, fabrics, and fluids on the behavior of the Punchbowl fault, southern California. Journal of Geophysical. Research. 108.

Somoza, R. (1998). Updated Nazca (Farallon)-South America relative motions during the last 40 My: implications for mountain building in the central Andean region. Journal of South American Earth Sciences 11(3), 211–215

Tomlinson & Blanco. (1997a). Structural evolution and displacement history of West Fissure fault system. Precordillera, Chile. Part 1, Synmineral Hystory In: 8º Congreso Geológico Chileno, Antofagasta, 1873-17877.

Tomlinson & Blanco. (1997b). Structural evolution and displacement history of West Fissure fault system. Precordillera, Chile. Part 1, Postmineral Hystory. 8º Congreso Geológico Chileno, Antofagasta, 1873-17877.

Tassara, A. & Yáñez, G. (2003). Relación entre el espesor elástico de la litósfera y la segmentación tectónica del margen andino (15–47°S). Rev Geol de Chile 30(2):159–186

Taylor, G., Grocott, J., Pope, A. & Randall D,. (1998). Mesozoic fault systems, deformation and fault block rotation in the Andean forearc: a crustal scale strike-slip duplex in the Coastal Cordillera of northern Chile. Tectonophysics 299:93–109

Tichelaar, B. & Ruff, L. (1991). Seismic coupling alongTullis, J. & Yund, R. A. (1980). Hydrolytic weakening of experimentally deformed Westerly granite and Hale albite rock. Journal of Structural Geology 2(4), 439-451.

Zhang, Y., Schaubs, P. M., Zhao, C., Ord, A., Hobbs, B. E. & Barnicoat, A. C. 2008. Fault-related dilation, permeability enhancement, fluid flow and mineral precipitation patterns: numerical models. *Geological Society, London, Special Publications* **299**(1), 239-255.

II. DEVELOPMENT OF A SELF-SIMILAR STRIKE-SLIP DUPLEX SYSTEM IN THE ATACAMA FAULT SYSTEM, CHILE

(*Publicado en Journal of Structural Geology, N 33, 2011*)

ABSTRACT

Fault development models are crucial to predict geometry and distribution of fractures at all scales. We present here structures related to the development of the Bolfín fault in the Atacama Fault System (AFS), covering a range of scales of 7 orders of magnitude. The AFS is a 1000 km-long trench-parallel fault system located in the Andean Forearc. The Bolfín fault is a first-order fault of the Caleta Coloso Duplex, has a trend ~170° and length >45 km. It cuts mainly meta-diorites and exhibits a 100-200m thick core of subvertical bands of altered fractured host rock and of foliated cataclasites. This foliation is made up of several trend-parallel cm-thick shear bands, composed of plagioclase fragments (>0.1mm) surrounded by epidote.

In the compressive quadrant around the tip point of Bolfín Fault, the lower strain faults exhibit an unusual internal structure consisting fractures arranged in a multi-duplex pattern. This pattern can be observed from meters to millimetres scale. The fractures in the strike-slip duplex pattern can be separated into 2 types: *Main Faults*: Trend-parallel, longer and with larger offsets; and *Secondary Fractures*: sigmoid-shape fractures distributed in the regions between Main Faults, all oriented between 15° and 75° with respect to the Main Faults, measured in the sinistral sense of shear (i.e. in P–dihedra).

On the basis of the distribution of the 2 types of recognized fractures, the relative sequence of propagation can be inferred. The Main Faults, the more widely distributed, were propagated earlier. The Secondary Fractures, in turn, distributed in thinner areas between the larger Main Faults, were propagated later as linking fractures.

The duplex pattern is self-similar: Multiple-Core Faults with internal structure of multiple-duplex are itself in turn secondary faults in a larger km-scale duplex (Caleta Coloso Duplex).

The duplex width (W) and the length (L) of the Main Faults forming the duplex show an almost linear relationship, for duplexes observed from micro to regional scale. For a scale range of seven orders of magnitude, the length of the master strike-slip faults is about ten times the width of the overlapping duplex area. This relationship evidences the self-similar nature of the structural system under study and suggests that the same fundamental mechanical processes that build up the small strike-slip duplexes operate also at the regional scale.

II.1. INTRODUCTION

The progressive development of the geometric arrangement of faults in the upper crust is of fundamental importance for a host of applications such as ore deposit exploration, hydrocarbon reservoir production and for the understanding of intra-plate seismicity. Faults localize ore bodies through their fundamental control of fluid flow (Sibson 1987; Sibson *et al.*, 1975; Barton, *et al.,* 1995; Connolly and Cosgrove, 1999; Cox, 1999; Sanderson and Zhang, 2004; Sibson, 1994; Wibberley *et al.*, 2008) and the displacement of pre-existing ore bodies (Sillitoe, 1973; Tomlinson & Blanco, 1997a; 1997b). In hydrocarbon fields, faults transport and trap oil and gas (Gibson, 1994; Smith, 1980). In seismology, in turn, the geometry of faults systems controls the distribution of the intra-plate seismicity by rupturing and fracturing (Lange *et al.*, 2008; Sibson, 1985; Sylvester, 1988). Therefore, conceptual models about how faults propagate and develop in the upper crust are crucial for studying those topics that demand knowledge of fault geometry.

Models of fault propagation and growth have been constructed from the observations and analysis of faulted laboratory samples (Lockner *et al.,*1991; Scholz *et al.*, 1993; Wibberley *et al.*, 2000) to the observation and measurement of mesoscopic- to regional-scale faults (Cembrano *et al.*, 2005; Flodin & Aydin, 2004; Martel *et al.*, 1988; Moir, 2010; Swanson, 2006). Nonetheless, they are based on observations over a small-scale range and models including structures from micro- to regional-scale, are very scarce (*e.g*. Martel *et al.*, 1988), mainly because of the lack of fault zones exhibiting well exposed fractures at all scales.

Here, we present and analyse structures related to the propagation and evolution of the Atacama Fault System (AFS) in the Coastal Cordillera of Northern Chile (Arabasz, 1971; Scheuber & Andriessen, 1990) exhumed from seismogenic depths (6-10 km) and observed over a range of scale of 9 orders of magnitude (10^{-4} -10^{4}m). An excellent exposure of faults results from very slow erosion in the coastal-desert climate (Fuenzalida, 1965) and allows a rigorous analysis of structures from micro- to regional-scale. All of the faults analysed here cut essentially the same protolith, and hence direct comparisons can be made over the range of scales. We are then able to present excellent millimetric-scale structures that provide data about the fault geometry evolution at small scale, and structural maps, showing the medium (meter-scale) and large (km-scale) scale fault arrangements. These multi-scale observations and measurements are analysed, in terms of orientation, size and displacement, to construct a model of propagation and development of a strike-slip duplex fault system. The observations are compared with previously published works from other natural fault systems.

In this paper, the term *fracture* is used to refer any petrographic or crystallographic planar and relatively narrow discontinuity, disrupting the original physical properties of a rock. This term is used regardless of the relative movement of the volumes of solid separated by the fracture, and hence it includes ex*tensional fractures* (also *cracks* or *joints*) and *shear fractures* (or *faults,* defined below). If some other material is filling a fracture, the structure is named according to the nature of this material (*e.g*. dyke or vein).

The term *fault* is used specifically to refer to *shear fractures*, that is, a relatively narrow discontinuity with observable shear offset. An oriented group of faults with a preferred orientation concentrated in a narrow planar zone is referred as a single fault if the scale of observation means that it can be represented only with a line.

II.2. REGIONAL STRUCTURAL SETTING

II.2.1. The Atacama Fault System (AFS)

The Atacama Fault System or AFS (Figure II-1) is the most important tectonic feature of the Coastal Cordillera in the Central Andes forearc (Arabasz, 1971; Brown *et al.*, 1993; Grocott & Taylor, 2002; Scheuber & Andriessen, 1990). It is a trench-parallel fault system (Scheuber & González 1999) composed of several sub-vertical and NS to NW -striking, fault segments ranging up to tens of kilometres in length. These segments are organized into a ~1000 km-long and ~50 km-thick fault system, affecting the Jurassic magmatic arc between Iquique (21ºS) and La Serena (30ºS) (Arabasz, 1971; Brown *et al.*, 1993; González, 1996).

The deformation in the Coastal Cordillera has been interpreted to be strongly controlled by the magmatic activity of the Jurassic-Early Cretaceous arc, from 200-120 Ma ago (Scheuber & Reutter, 1992). The AFS *sensu stricto* propagated in the last stages of deformation, when the progressive cooling of the arc led to a change in the mode of deformation from a plastic regime represented by kilometric shear zones of amphibolite (150-143 Ma) to greenschist facies (139-125 Ma) (Scheuber *et al.*, 1995) and finally to a brittle regime represented by meter-thick fault cores of chlorite- and epidote-rich cataclasites (125 – 118 Ma) that form the main structure of the AFS (Cembrano *et al.*, 2005). Crosscutting relationship plus these common alteration products indicate that these brittle structures formed under the same physical conditions and during the same deformation episode. This paper focuses on the progressive development of small- to large-scale structures during the brittle propagation stage of a segment of the AFS.

The kinematics of the brittle structures of the AFS is mainly left-lateral strike-slip with a minor extensional component. This kinematics have been attributed to the highly oblique convergence in the subduction of the Aluk plate under the South American plate during the Mesozoic (Grocott & Taylor, 2002; Scheuber & Andriessen, 1990; Scheuber & González, 1999).

Cenozoic normal movements have also been recorded in the AFS, attributed to elastic rebound of the forearc co-seismically with large magnitude subduction earthquakes (Gonzalez & Carrizo, 2003). These are easy to recognize in the field as localized sub-vertical brittle structures that do not greatly overprint the earlier, more widespread brittle deformation. The structures temporally associated with these later movements will not be described as they are not on the focus of this paper.

II.2.2. The Caleta Coloso Duplex (CCD)

The Caleta Coloso Duplex is a strike-slip structure located 20km south from Antofagasta (Figure II-1, A). It is formed by two, NNW striking, sub-vertical master faults that splay off the Coloso Fault, a major structure of the AFS. These two master faults are the Bolfin and Jorgillo fault (Figure II-1, B), which are in turn joined by a set of second-order NW-striking and third-order EW-striking, imbricate splay faults. The CCD has been interpreted to be formed in a dilatational jog between Jorgillo and Bolfin Faults (Cembrano *et al.*, 2005; González, 1996).

According to previous work, the second order faults in the CCD have south-westward steep dips and left-lateral/normal kinematics; they have minimum net displacements varying between 10 and 100 m and show variable internal structure. Low-displacement faults (in the order of 1-10m) consist of straight decametre–long faults linked by hybrid/extensional fractures, and high displacement faults (of the order of >10m) show well-developed layers of cataclasites and gouge (Cembrano *et al.*, 2005).

The third order faults, in turn, are steeply to shallowly dipping both to the south and north with mainly normal kinematics; they have centimetric thickness and vertical separations between 1 and 10 cm (Herrera *et al.*, 2005; Olivares 2004).

The physical conditions under which the CCD was developed can be inferred from the associated mineral assemblages. Both the cataclasites from the fault cores and spatially and geometrically related hydrothermal veins show mineral assemblages of epidote, chlorite and quartz, suggesting a strong link between faulting and fluid transport under low-greenschist facies conditions (Cembrano *et al.*, 2005; Olivares, 2004). The depths from which the rocks have been

passively exhumed have been estimated between 3 km and 10 km (Faulkner *et al.*, 2006; Herrera *et al.*, 2005).

II.3. METHODOLOGY

For characterizing the geometry of regional-scale faults (1-10km long), our observations are based on detailed maps (1:250,000 to 1:100,000 scale) and descriptions made by several previous studies in the AFS and Caleta Coloso Duplex (Arabasz, 1971; Cembrano *et al.*, 2005; González, 1996; Olivares, 2004). For meter- to hundred-meters scale faults (101-102m long), mapping at 1:10000 scale was carried out at the tip point of one segment of a regional-scale fault, the Bolfin Fault. The tip point was selected because of good exposure and the occurrence of several spatially related faults, which at larger scale appear to form a horsetail structure (Figure II-1, B) (Cembrano *et al.*, 2005; Herrera *et al.*, 2005; Olivares, 2004). The tip point is thought to represent a zone of possible static and dynamic fracturing resulting from fault propagation and/or arrest (Faulkner *et al.*, 2010).

The outcrop-scale fractures (10^{-3}-10^{1}m long), which constitute the internal structure of larger-scale faults, were characterized and measured by means of detailed outcrop-scale maps, made at the scale of 1:20 and 1:5. These maps were produced directly in the field, based on structural measurements and on digital camera imaging. For the case of the internal structure of the Parulo Fault (Figure II-2), the map (10^{-1}-10^{1}m) was constructed onto an ortho-rectified photomosaic, composed of 196 images with a spatial resolution of 10mm. These images were obtained with a 5.36 MP camera mounted on a structure consisting of 4 fixed legs connected by 4 metallic cables, forming a 7m horizontal square. The images where rectified and stitched together with the Orthobase application of Erdas Imagine, considering the distance of the camera, the position, focal distance, and some reference points previously marked in the outcrop before the imaging.

The microscopic-scale deformation (10^{-5}-10^{-3}m long fractures) was characterized by fracture counting and mapping on oriented thin sections, taken both from the core of the main regional-scale fault (Bolfin Fault) of the studied area and from the damage zones of the surrounding outcrop-scale faults (Palmera Fault).

In the Palmera Fault, the microanalysis was conducted directly in the M plane (a plane orthogonal to the fault and parallel to the striae). This configuration allows measuring the real angles between the main shear plane (the faulting plane in this case) and the spatially related fractures. Then, the real orientation of the related fractures can easily be traced on a stereographic projection as a lineation contained in the known M-plane.

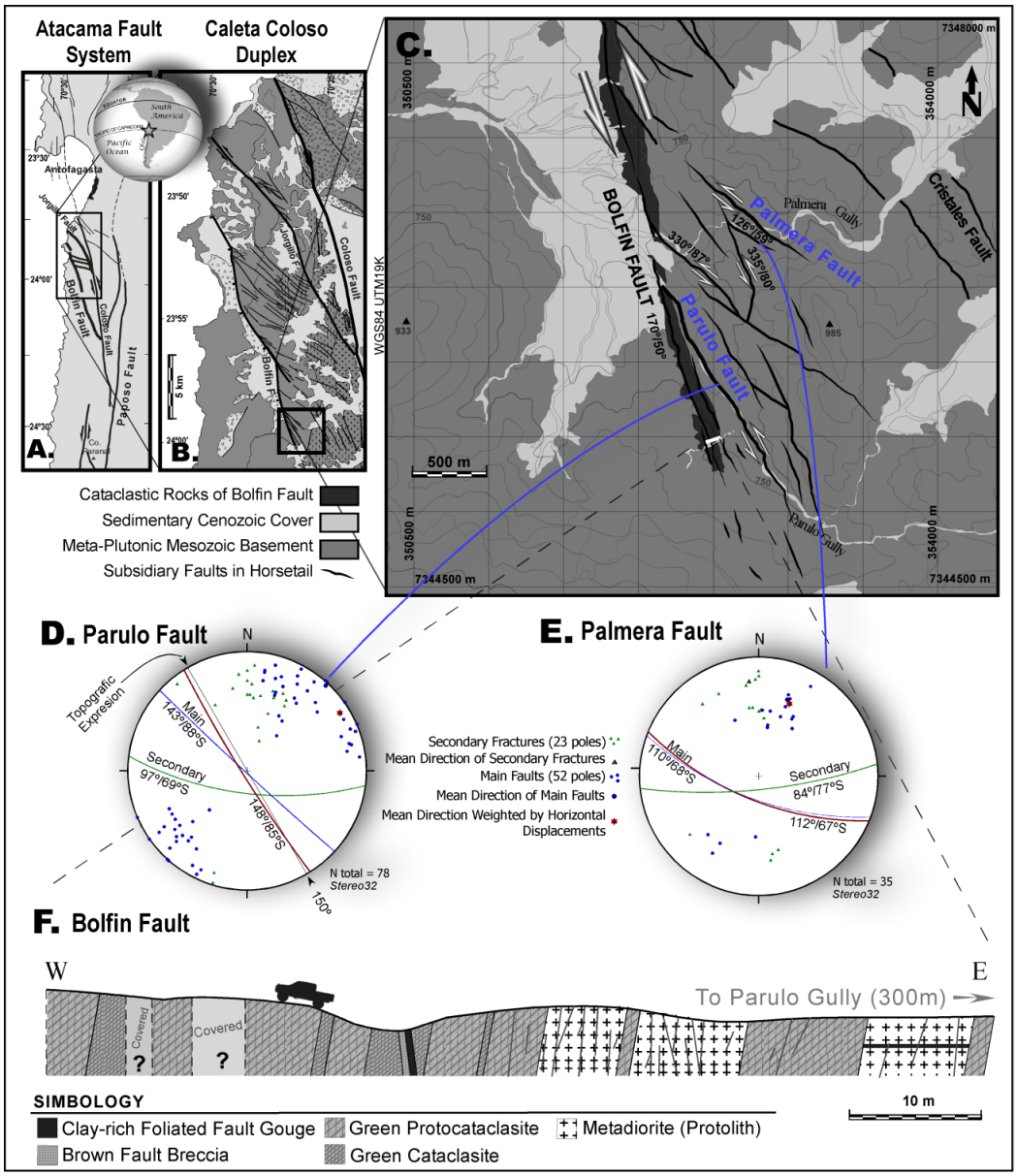

Figure II-1. Kilometric-scale structural maps and metric -scale internal structure.
(A) Regional scale map showing the geometry of Atacama Fault System in Antofagasta Region, Chile (Simplified from (Brown *et al.,*1993)). (B) Map of the Duplex Caleta Coloso, redrawn from (Cembrano *et al.,*2005). (C) Map of the horsetail structure in a termination (tip-point) of Bolfin Fault. Parulo and Palmera faults are described in the text. (D) and (E) Equal-area projection diagrams of fractures measured within the Parulo and Palmera fault, respectively (Data in tables 1and 2). Triangles and dots are the poles of Secondary Fractures and Main Faults respectively, and the lines represent the great circles of the calculated mean directions (blue: Main Faults, green: Secondary Fractures). Weighted mean orientation is plotted in dark red and was calculated weighting the fracture orientations by the horizontal displacement of them. (F) Vertical section perpendicular to the strike of the Bolfin Fault close to the tip.

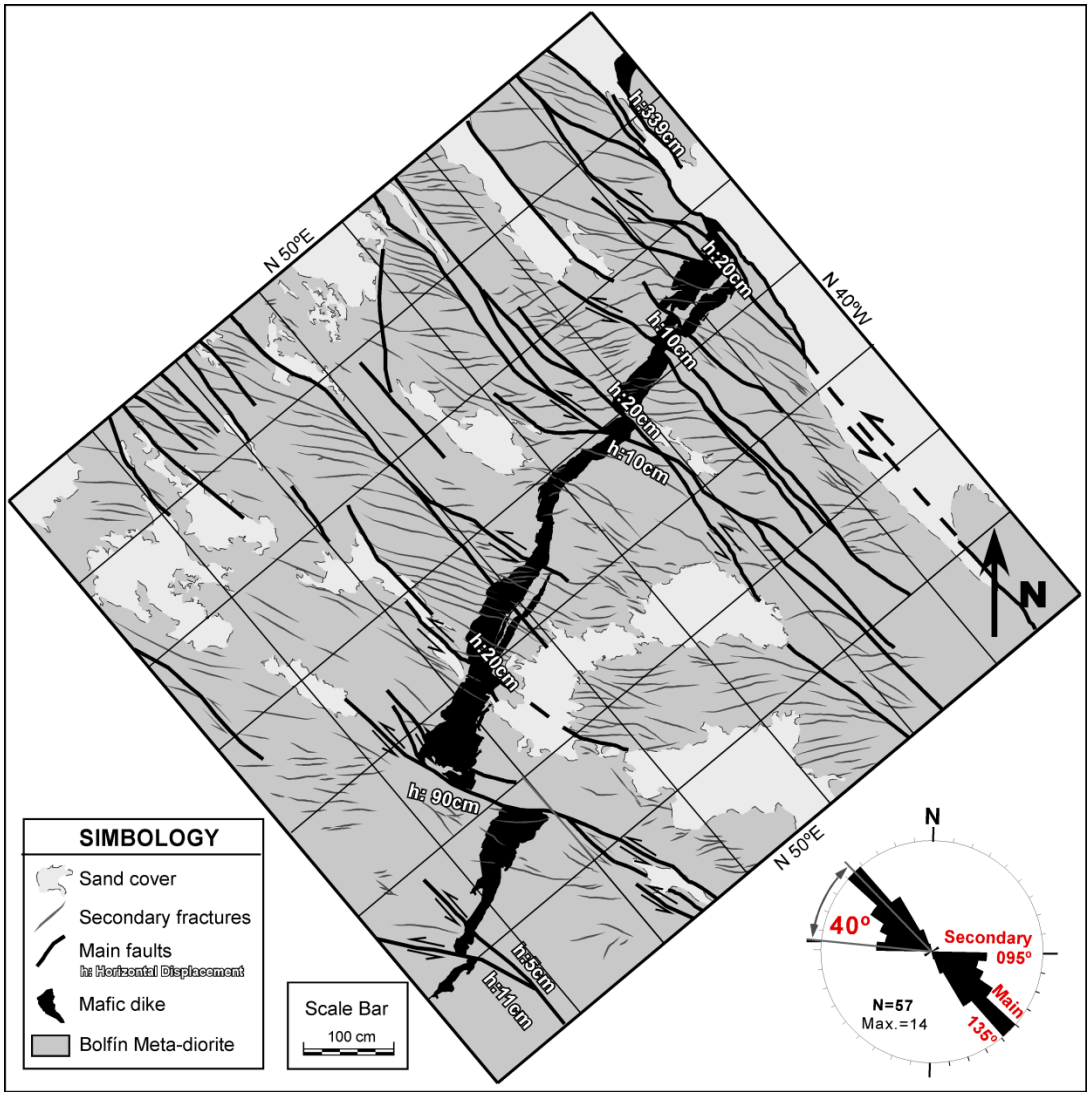

Figure II-2. Outcrop-scale structural map in Parulo Fault.
Performed over the orthorectified photomosaic of Figure II-3. The black band is a displaced dike. White numbers are horizontal offsets (h). The protolith, or host rock, is metadiorite of the Bolfin Complex. The rose diagram made in portion of the map shows that the Secondary Fractures have an average trend 40º deflected from Main Faults.

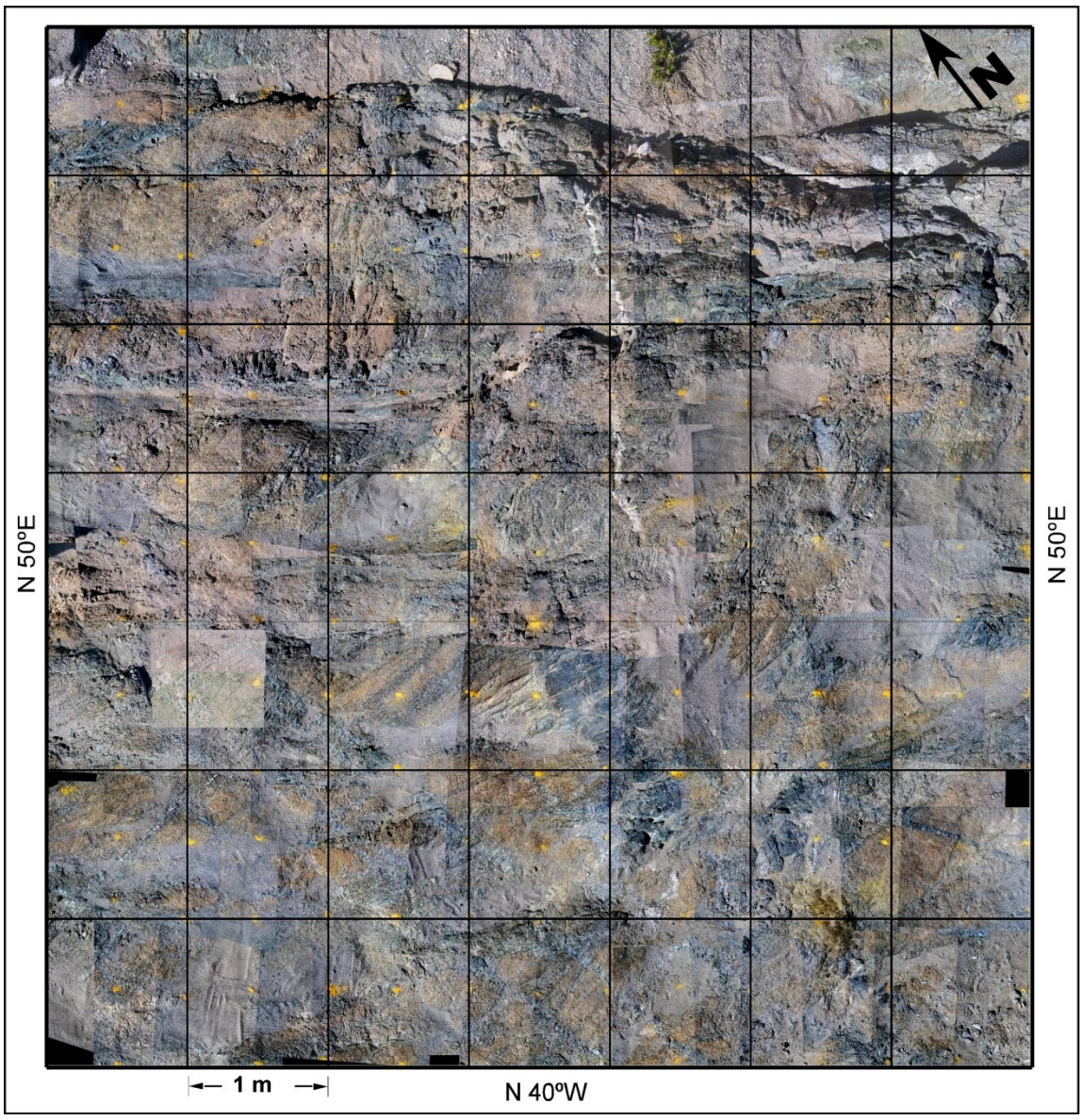

Figure II-3. Ortho-rectified photomosaic.
Ortho-rectified photomosaic of a sub-horizontal outcrop in the internal structure of Parulo Fault. Base of mapping to build the map on Figure II-2.

II.4. FAULT SYSTEM DESCRIPTION

The Bolfin Fault splays off the Coloso Fault at 70º23' 24º10', with an average strike of 162º and an exposed length of at least 45 km. It has a 50 to 100 m-thick core, with an internal structure characterized by subvertical meter-thick zones of cohesive fault rocks and of some fractured host rock, very similar to that described for the Coloso Fault (Cembrano *et al.*, 2005; Faulkner *et al.*, 2006; Faulkner *et al.*, 2008). Fault rocks are mainly dark green cataclasite and protocataclasite (according to classification by Sibson 1977) with 2 discrete strands, 2 – 50 to 80 cm thick of brown/red foliated gouge. The dark green colour of the cohesive rocks is given by the epidote-chlorite mineral association, mainly cementing rock fragments and in veins, but also altering original minerals in the host rock. The red colour of the gouge is due to oxidized iron-bearing minerals such as hematite.

The Bolfin Fault is segmented into three main sections; the southern termination of the central fault segment is the focus of this study, as it shows the best developed small-to-large-scale fault zone structure (Figure II-1, B).

In this region, the Bolfin Fault exhibits several related smaller faults arranged in a horsetail structure consistently orientated with the kilometric geometry of the Caleta Coloso Duplex (Cembrano *et al.*, 2005; Herrera *et al.*, 2005; Olivares, 2004).

All faults mapped in this termination area are located to the East of Bolfin Fault, are NW-striking, have subvertical dips (between 70ºSW and 70ºNE) and trace lengths between 300m and 3km (Figure II-1, C).

Two types of faults can be identified according their internal structure at the outcrop-scale: *Single Core Faults* and *Multiple Strand Faults.*

II.4.1. Single-Core Faults

The traces of these faults are easy to recognize in the high-resolution satellite images and can be seen as continuous straight lines. These are the most frequently mapped faults in previous works and a good example of one of these faults is the Cristales Fault (Figure II-1, C and see also Mitchell & Faulkner, 2009)

The single-core faults show a single green cataclastic cores similar to that of Bolfin Fault but thinner, generally 0.5 - 2m total thick, and with less bands. The cores exhibit two sets of different planar structures (foliations), one defined by compositional and textural bands, and another

defined by discrete preferentially-oriented discontinuities (fractures). The former set is sub-parallel to the core boundaries and consist of layers of different colours and different fabric (matrix/fragments ratios) that can be classified as different fault rocks. The latter, in turn, show a systematic preferred orientation between 20º and 75º counterclockwise with respect to the core boundaries and to the banded structure. These fractures cut both the cataclasites in the core and the surrounding host rock (damage zone); however, the majority is in the core like a cataclastic foliation.

II.4.2. Multiple Strand Faults

This name is given to faults consisting of several sub-parallel, cm-m long and mm-cm thick faults, bearing cataclastic cores and separated by domains of systematically fractured protolith (Figure II-4). They can also be named Compound Faults as in Martel (1990). Most of the shear in the multiple strand faults is accommodated in sub-parallel faults that are separated by distances of about one order of magnitude smaller than their lengths, and here are named *Main Faults*. These Main Faults are connected by several smaller fractures with much smaller to none displacement on them, that here named *Secondary Fractures*. It should be noted that the terms ‘main’ and ‘secondary’ are relative names used to differentiate between fractures that are distinguishable at the same scale of observation and can be applied at any scale of observation. They relate only to the relative orientation, length, and offset on these structures, and not to the timing of propagation; this issue will be addressed in the discussion.

The geometrical and spatial distribution of these two types of fractures results in a meter-scale strike-slip duplex arrangement to the multiple strand faults.

Two examples of these multiple-core faults with a duplex arrangement are Parulo and Palmera faults, described below. Both are located around the tip-point of Bolfin Fault and have left-lateral total horizontal displacement of a few meters (exceptionally some of the Main Faults show dextral displacements).

The Main Faults show only shear displacements and the Secondary Fractures show much smaller shear displacements (down to 0) and extensional movements, with the larger opening in the centre of the fractures (filled with epidote). They have a smooth sigmoidal shape, where they tend to become sub asymptotic to the Main Faults as they approach them (Figure II-5).

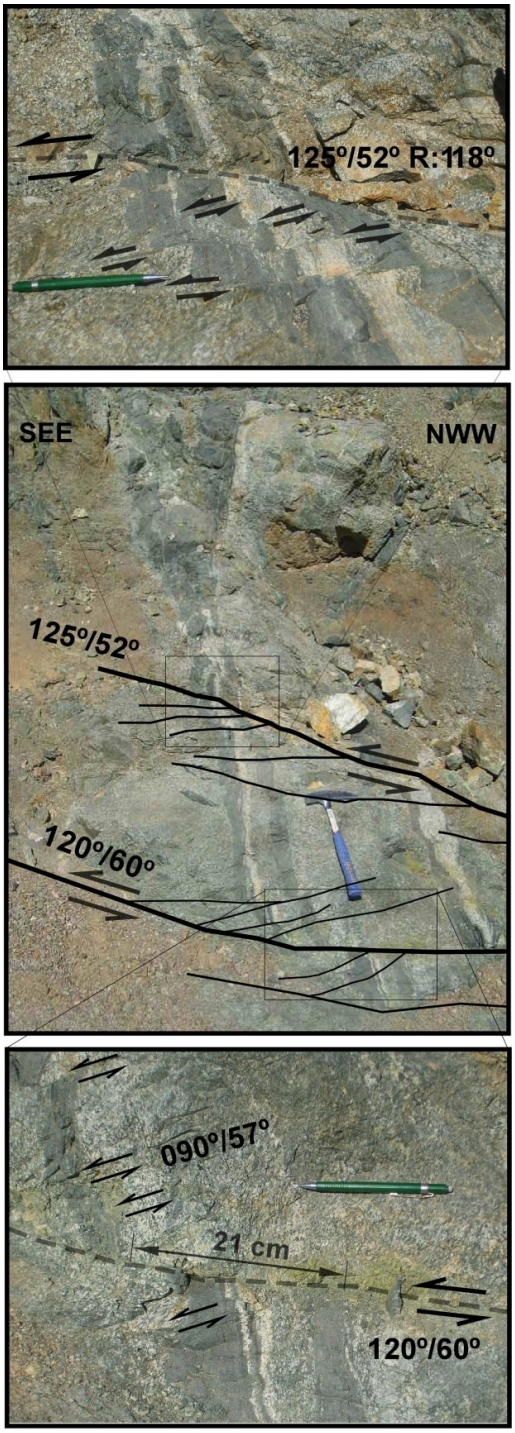

Figure II-4. Field photos of Palmera fault.
This is a representative case of a Multiple-core Fault (or Compound Faults). Note that the faults can be separated by size and orientation in two types (Main Faults, Secondary Fractures).
The photographies were taken oblique to the highly irregular surface of the outcrop and (unlike Figure II-2) photos are not orthorectified. This can produce distortion on the scale and the real shape of the features exposed.
Hammer: 40cm-long; Pencil: 15cm-long

II.4.2.1. Parulo Fault

The Parulo Fault outcrops along the Parulo Gully (Figure II-1, C) and is one of the second-order faults defining the horsetail structure of the tip point of the Bolfin Fault (Olivares 2004). It shows a general NNW strike of 150º, has a length of about 2km and its total thickness is ~17m.

Figure II-2 shows an outcrop-scale structural map from part of the internal structure of Parulo Fault. In this map, the Main Faults and the Secondary Fractures can easily be identified.

The Main Faults within Parulo Fault are 3-10 m long and 3-11 mm thick. They exhibit millimetric cores of clay-rich light-green gouge layers that have sub-horizontal striae and show centimetric –to metric horizontal displacements as evidenced by offsets of a mafic dike.

The Secondary Fractures, in turn, are 0.1-1.0 m long and 0.1-3.0 mm thick. Their strikes vary between 090º and 100º, with a statistical mean deflected 40º counterclockwise from the strike of the Main Faults (Rose diagram in Figure II-2). These thin fractures are mostly extensional, however small left-lateral/extension hybrid movements can be identified in the central segment of some of them. They are filled by very a thin (<1mm) layer of chlorite and epidote, and no-striation was identified.

The orientation of the fractures within Parulo Fault is expressed in the equal-area diagram in the Figure II-1 , D, it exhibits the poles of 75 fractures (see table 1) including main and secondary fractures measured within the fault. The mean orientation of the Secondary Faults is 097º/69º and of the Main Faults is 143º/88ºS. Weighting the orientations by the sinistral horizontal displacements measured on the field (i.e.: Giving more importance to highest displacement faults and voiding fractures without displacement) the weighted mean direction is 148º/85º. This strike is closer to the topographic expression of the fault, given by the Parulo Gully, and this suggest that its surface expression may be controlled mostly by the larger fractures.

Both Main and Secondary Fractures exhibit felsic halos of alteration minerals. Most of the halos are made of albite and epidote, this gives them a characteristic white/green coloration that strongly contrasts with the oxide orange colour of the weathering of the amphiboles in the meta-diorites host rock. They have variable mm to cm thickness and their scaling with the displacement is discussed in Faulkner *et al.,*(2010).

The total horizontal displacement of the Parulo Fault was calculated by adding up the offsets of the Main Faults on transects across the fault in two different locations. The data indicate this fault exhibits an extremely low localization of the strain: Varies from 40 to 50 cm of shear displacement per meter of fault-thickness. However, it is worth noting that this is a highly heterogeneous and discrete strain distribution at outcrop scale (*i.e.* Brittle).

II.4.2.2. Palmera Fault

The Palmera Fault runs along the Palmera Gully, in the central area around the tip point of Bolfin Fault (see Figure II-1 , C) and has a general strike 120º. Its length cannot be determined in satellite or aerial imagery; however, from field observations it can be estimated to be *ca*. 1000 m long. Its minimum total thickness is 4 m, including all the decimetric to metric-long faults of which Palmera Fault is made up.

The Main Faults within this fault are mostly 1 to 5 m long and 1 to 3 mm thick. In general, their trends vary between 90º-130º, and their dips: 50ºNE – 50ºSW. All of them exhibit shear displacement as evidenced by the offset of markers (*e.g*. subvertical dikes) or the presence of wear material (cataclastic layers) without offset markers, in which case the shear sense cannot be determined. Ridge-and-groove striae onto epidote + chlorite assemblages and dike offsets of Main Faults within Palmera Fault indicate a predominantly left-lateral strike-slip displacement, with a vertical component less than 40% of the horizontal movement.

Secondary Fractures, in turn, are 5 - 500 mm long and between 10 and 100 µm thick. These small fractures show smooth sigmoidal shapes with an average trend deflected 30º counterclockwise from the average trend of the Main Faults. Microscopic analysis shows that some of these fractures are tensional, but most of them are small shear fractures or “microfaults” with hybrid movement (see Figure II-5 and Figure II-6). Millimetric displacements in these microfaults produce thin cataclasite layers or displaced crystal boundaries.

The orientation of the fractures within Palmera Fault is expressed in the equal-area diagram in the Figure II-1, E, it exhibits the poles of 35 fractures (see table 2) including main and secondary fractures measured within the fault. The mean orientation of the Secondary Faults is 084º/77º and of the Main Faults is 110º/68ºS. The horizontal displacement weighted mean direction is 112º/67º.

Figure II-5 shows a microstructural map made from a thin section of the M-plane or “plane of movement” (*i.e*. the plane parallel to striation and perpendicular to the fault plane) of a metric fault, oriented 120º/66ºNE and a striation with rake 020º NW (a Main Fault).

Main and Secondary Fractures are easily identified in this thin section, they form a millimetric-scale strike-slip duplex structure (similar to hosting, kilometric-scale Caleta Coloso Duplex), and decrease in density away from the largest fault.

Although all of the microfractures in the map of Figure II-5 exhibit an evident decrease in density away from the largest displacement fault (22.5 cm), Main Faults dominate over Secondary Fractures. The formers are heterogeneously distributed over an area of a 47 cm around the largest

displacement fault. The latter, in turn, are located in a narrower zone (20 cm), only in areas between Main Faults and more concentrated between faults with larger displacements (> 5 cm).

As can be observed in the photo micrograph (Figure II-6, Figure II-7) most the microfaults and fractures are sealed or cemented by the precipitation of neo-formed minerals (epidote, chlorite or phyllosilicates). In their cores, some of the microfaults host fragments of plagioclase from the protolith or restrained neo-formed minerals (Figure II-6, A).

Associated with the microfaults, other straight and narrow shear discontinuities can also be identified producing offsets of the plagioclase twins. These are straight microscopic shear bands, 10 to 400 microns long and left-lateral offsets (synthetic to the main sense of shear). The facts that no crystallographic discontinuity was recognized across them and that twins terminate at this deformation bands and do not follow within them, suggest that these bands represent healed shear fractures (as in Stünitz *et al.,*2003) (Figure II-7, C).

In close spatial and geometrical relationship with the microfaults, also can be recognized some evidences of plastic deformation: deformation twins, undulatory extinction and bending of crystal boundaries can be observed in the plagioclase crystals of the protolith under the petrographic light microscope (Figure II-7, D).

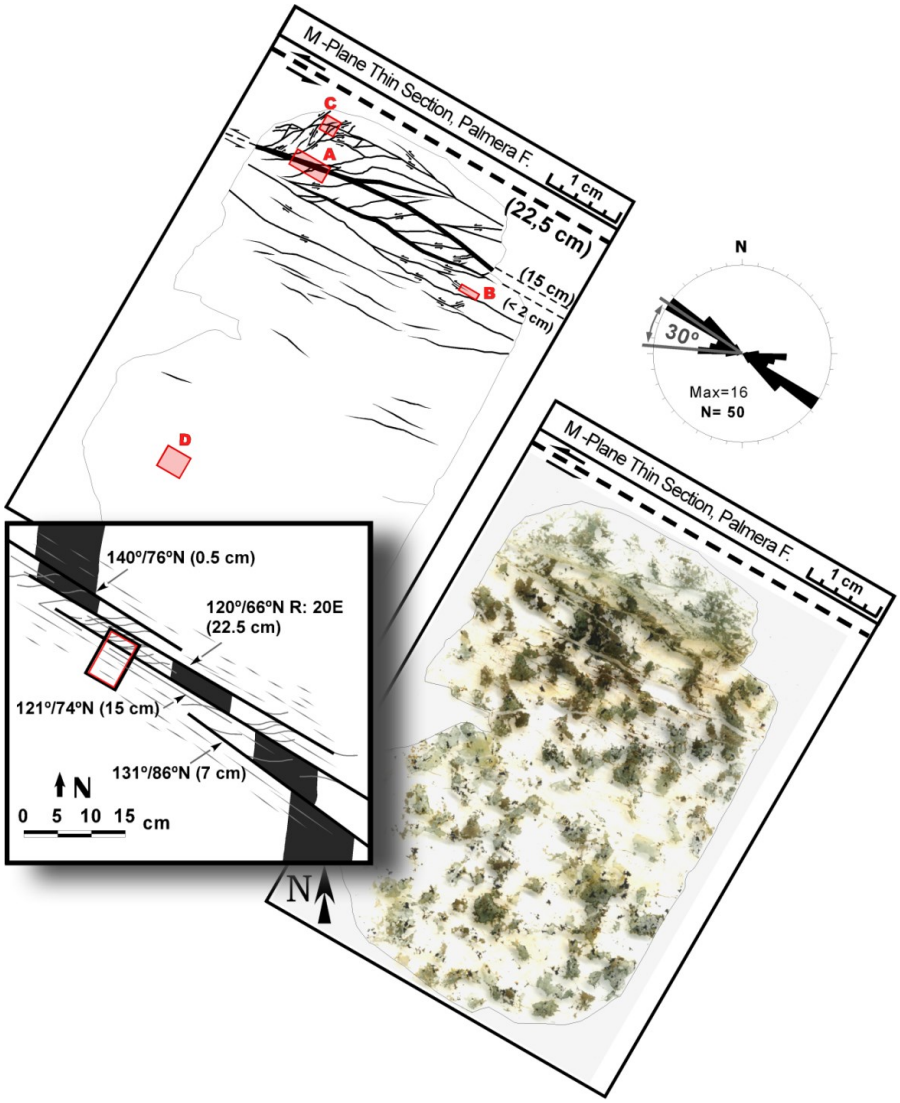

Figure II-5. Microstructure in thin section of Palmera Fault.
Microstructural map performed over a thin section in the M-Plane of a main fault within Palmera fault. (i.e. parallel to the striation and perpendicular to the fault plane). The inset is a small sketch map showing how faults are distributed and how the thin section was oriented. Horizontal left-lateral offsets of larger faults are indicated (h). Small squares with letters indicate the location of the photo micrographs Figure II-6 and Figure II-7.

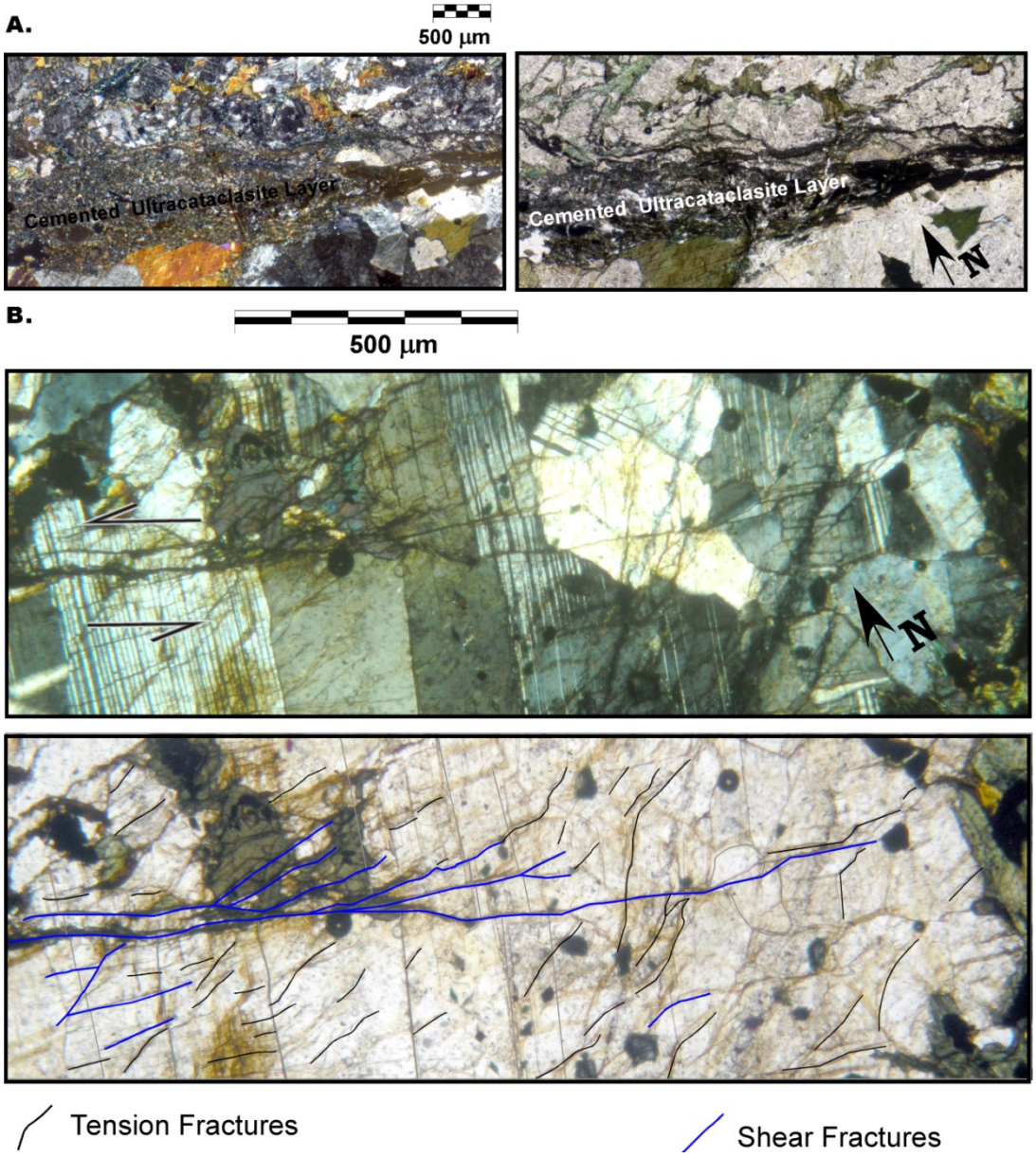

Figure II-6. Microscopic horsetail in thin section.
Microscopic photos made in the thin section on Figure II-5. **A**: Core of a main fault with 15cm of horizontal offset. **B**: Horsetail structure in a small displacement Main Fault.

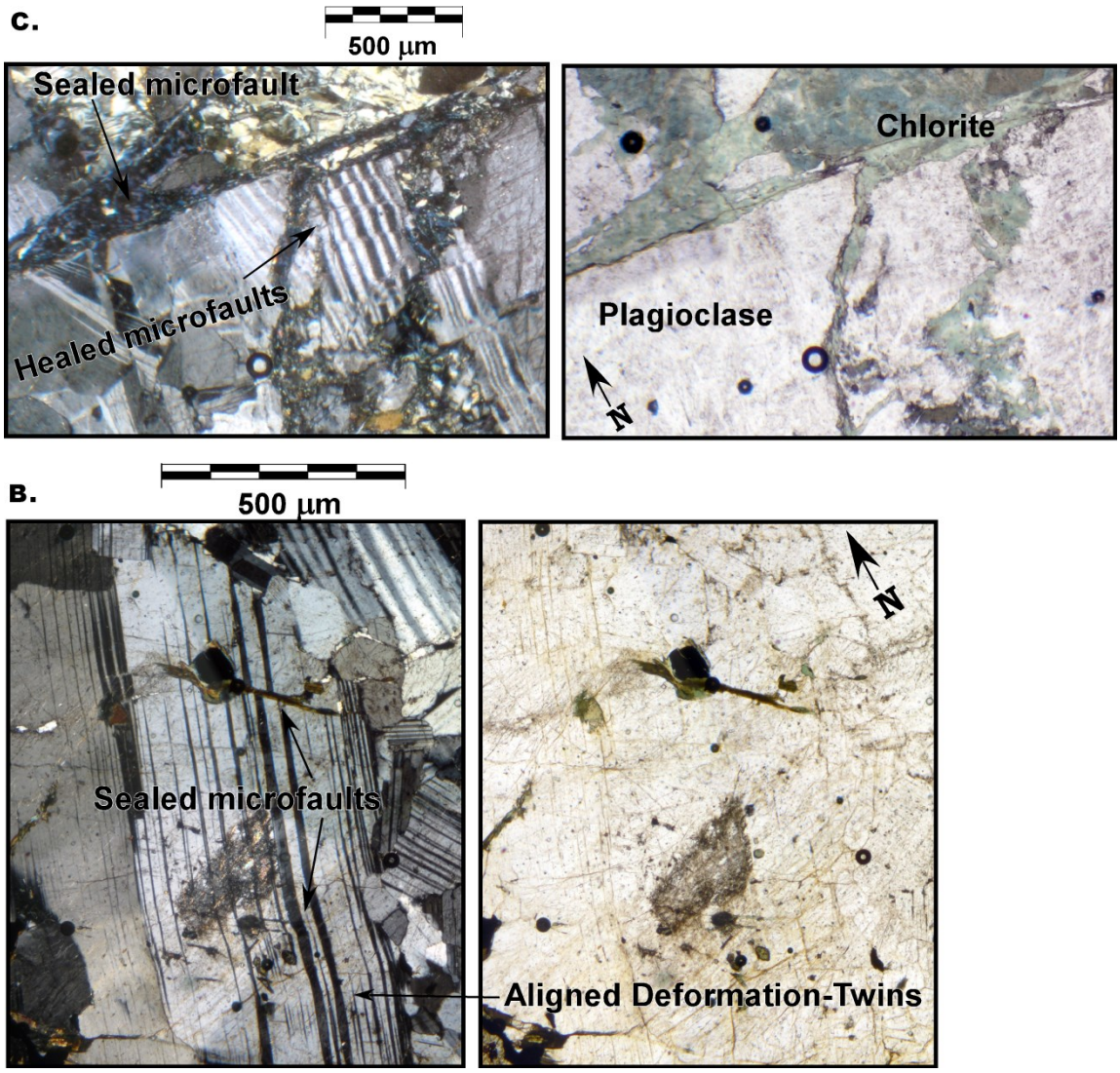

Figure II-7. Microscopic shear fractures.
Microscopic photos made in the thin section on Figure II-5. **C**: Sealed- fractures with hydrothermal chlorite, and healed shear fractures evidenced by plagioclase left-lateral dislocations. **D**: Plagioclase crystal with left-lateral shear-strain. The configuration of the deformational twins and the sealed fractures suggest that it suffered both plastic and brittle deformation.

II.5. DISCUSSION

II.5.1. Multiple Scale Strike-Slip Duplex Geometry

According to the data presented here, the strike-slip duplex pattern is the most characteristic feature in the geometry of the fault arrangements at all scales. This pattern can be observed at the regional scale, in the Atacama Fault System (Caleta Coloso Duplex in Cembrano *et al.,*2005); at outcrop- or metric-scale, in the Parulo and Palmera Fault internal structure; and at millimetric-scale, in the thin section of Palmera Fault (Figure II-8).

The presence of this duplex pattern in fault arrangements has been also previously observed in other metric to kilometric scale fault systems. *e.g.*: Three Pagodas and Mae ping fault zones, western Thailand (Morley 2004; Morley *et al.,*2007); in the Sierra Nevada, California (Flodin & Aydin 2004; Kirkpatrick *et al.,*2008; Martel 1990, Martel *et al.,*1988); and in the Italian Southern Alps (Di Toro & Pennacchioni 2005). However, none of these works include observations from such a wide scale-range, and none describes a strike-slip duplex pattern in the internal structure of a fault that is part of larger duplex. In turn, the duplex fault systems described here are self-similar, as the same structure appears repeated on a range of scales (Mandelbrot 1967). Specifically, the geometry of the Caleta Coloso Duplex is repeated in the geometry of fractures in the Secondary Fractures of the Duplex (Parulo and Palmera Faults). This self-similarity suggests that the same processes control the fault propagation at all scales and, subsequently, are scale-invariant processes.

In mathematics, the term “self-similar” refers to a system that is exactly or approximately similar to a part of itself. Applied to geometrical patterns, self-similar is a shape that is systematically similar to one or more parts of it (Mandelbrot 1967). That is exactly the case of the geometry presented by the structures forming the Caleta Coloso Duplex, over seven orders of magnitude. The duplex pattern is self-similar as can clearly be seen in the log-log plot of the Figure II-9 .

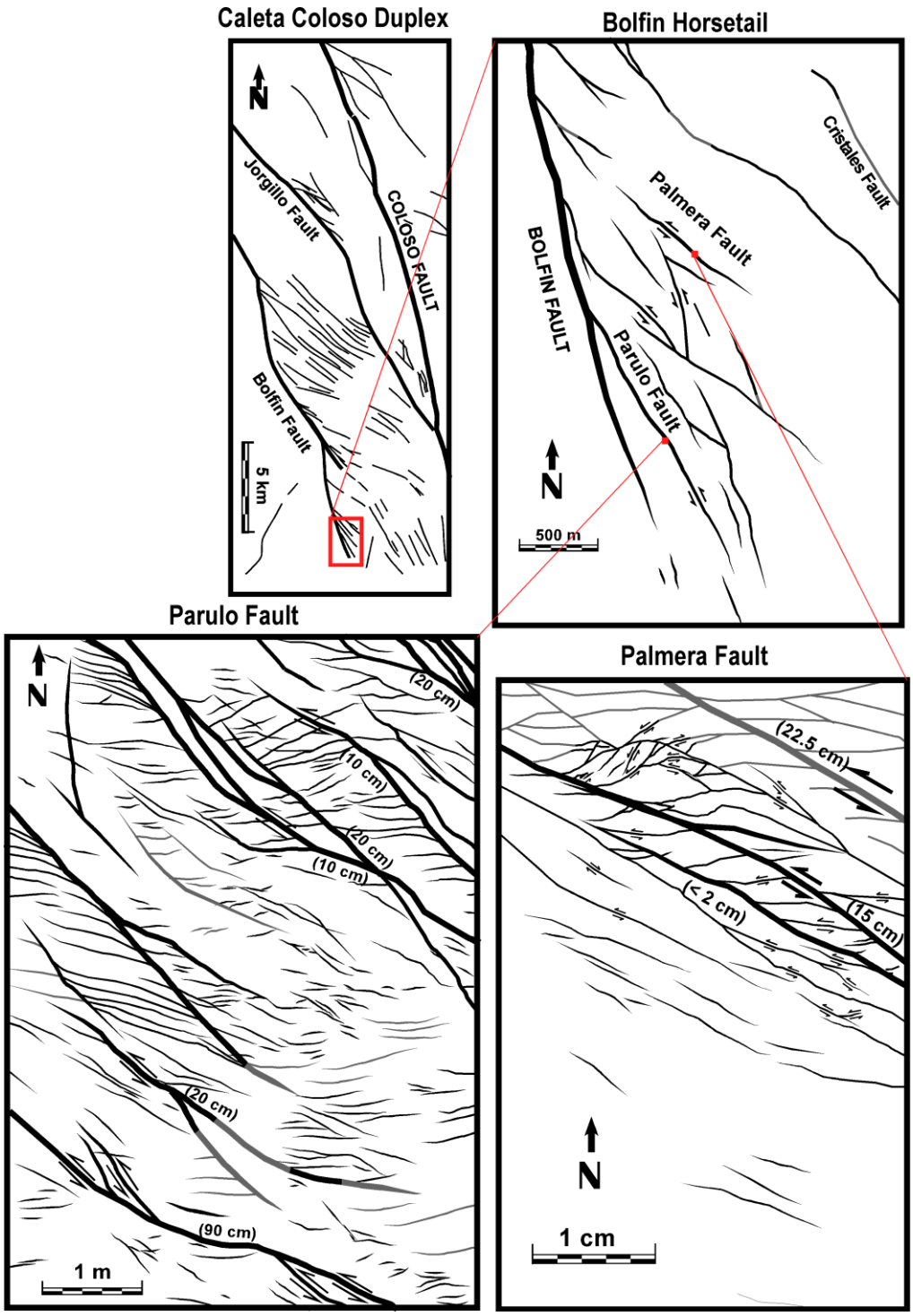

Figure II-8. Multi-scale sketch of the described structural system.
Summary sketch showing the geometry of the described structural system at all the described scales. The structural maps are extracts from the maps shown in figures 1, 2 and 5, slightly modified. Lines were added to fill the covered and not mapped areas based in the surrounding structures, and in the horsetail map some lines where smoothed in order to decrease the strong effect of the topography on the shape of the fault traces. Thicker lines are the largest fault with larger horizontal displacements (marked between parentheses)

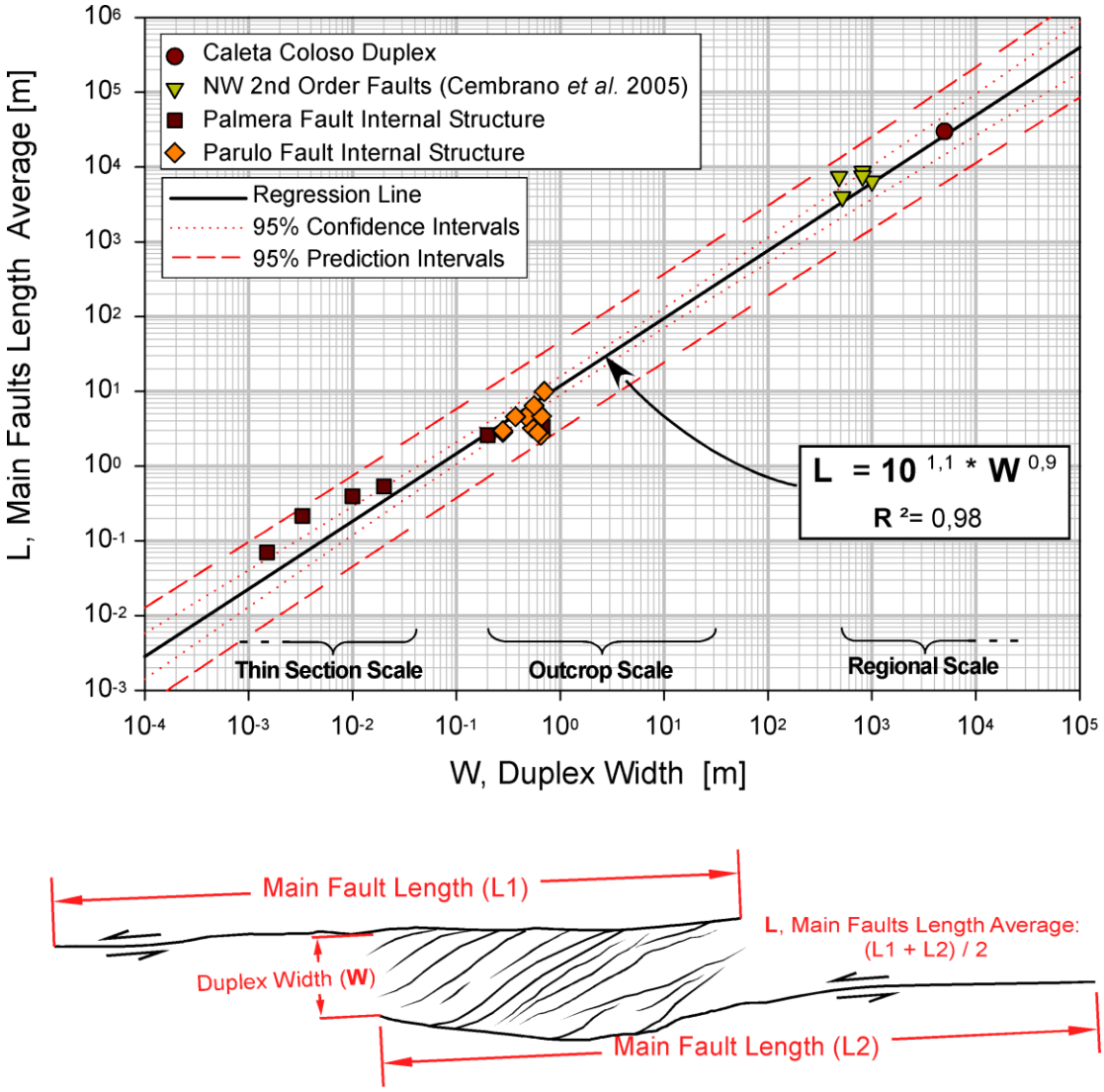

Figure II-9. Log- Log plot of main fault length vs duplex width.
Log- Log plot showing the self-similarity of the duplex pattern in the described structures. The distance between Main Faults represents the duplex size or width, and it scales almost linearly with the length of the faults forming the duplexes (A linear relation would be (A = K * L). The overlapping "Main Faults" within the systems form duplexes almost one order of magnitude smaller than their lengths.

The main fault length (L) and width (W) of 22 duplexes and faults forming them, at several scales, are plotted in the log-log diagram of Figure II-9. The smaller scale data, coming from Palmera and Parulo Fault sites, were obtained from the internal structure of the faults as described in a previous section. The larger scale data was taken from a previously published work in the same area (Cembrano *et al.,*2005). Data in Figure II-9 are best fit by a power law relationship:

$$L = 10^{1.1} \cdot W^{0.9}$$

Where W is the Width of the Duplex and L is the average length between the two Main Faults forming each duplex as represented in the sketch of Figure II-9.

The results are internally consistent and essentially show an almost linear relationship between the mean length of the main duplex faults and the duplex width. In other words, for a scale range of seven orders of magnitude, the length of the master strike-slip faults is about ten times the width of the overlapping duplex area. This relationship, apart from reinforcing the self-similar nature of the structural system under study, suggests that the same fundamental mechanical processes that build up the small strike-slip duplexes operate also at the regional scale.

The distance between the Main Faults of a duplex (or of a multiple duplex fracture pattern) has an important meaning in the propagation of a fault through the linking of sub parallel smaller faults. Each primordial Main Fault can be considered to have its own stress field perturbation around and the propagation of splay and linking faults are expected to be controlled by the size and shape of such stress field, and the interaction between them.

The distance between Main Faults scale with the length of them (Figure II-9) and the stress perturbations are also a function of the fault length (and displacement) (see Homberg *et al.*,1997). This strongly suggests that the interaction between the stress field perturbations around primordial Main Faults controlled the size of the duplexes in the fault system at all scales. Otzuki & Dilov (2005) based on experimental work of fault zone progressive development, demonstrated that fault zones grow keeping a self-similar hierarchical structure, similar to that found on this and other previous field studies of strike-slip faults at various scales (*e.g.* Joussineau & Aydin (2009) and references therein). Furthermore, Otsuki & Dilov (2005) successfully derived the Gutenberg-Richter's law as well as the previously documented relationship of seismic nucleation sizes to seismic moments, suggesting that any seismic rupture nucleates at a smaller jog of a lower hierarchical rank and eventually terminates at a larger jog of a higher rank, which in turn is consistent with the hierarchical fault zone geometry we see in both nature and experiments.

Self-similarity has been also previously documented in structures related to plastic deformation of rocks. S-C fabrics in mylonites show a self-similar relationship in the distance between S planes against the distance between C planes (Hippertt, 1999).

II.5.2. Timing and Mechanism of Fault development

One of the most important topics in the understanding of the development of fault systems in the brittle crust is to deduce the relative timing of recognized structures.

Here, all the faults in the self-similar system (Parulo, Palmera, Bolfín and Jorgillo) are cemented with the same mineral assemblage (epidote-chlorite) and show synthetic displacements, then can be considered to be contemporaneous at geological time scale. However, they were not propagated instantly at the same moment in time, so they have different relative time occurrences at short-term scales. Furthermore, previous researchers (Herrera *et al.,*2005) have postulated that the fault related mineralization occurred by seismic pumping depressurization mechanism (Sibson 1987, Sibson *et al.,*1975), that is an evidence of propagation by discrete events through the time.

A reliable relative timing between the Main Faults and Secondary Fractures can be deduced from the microstructural map made in the thin section on Palmera Fault (Figure II-5). If we consider that the damage area around a fault increases with the increasing total fault displacement (Chester *et al.,*2004; Mitchell & Faulkner 2009; Scholz 1987, Scholz & Aviles 1986) and that the most proximal areas to the Main Faults show more accumulated deformation than the distal ones; then we must consider the proximal areas represent the more mature in terms of accumulated deformation. Accordingly, the deformation occurring away from the largest fault will represent the initial stages of deformation and the evolution can be deduced observing structures at intermediate distances. As seen in the thin section (Figure II-5), both Main Faults and Secondary Fractures decrease away from the largest displacement fault. However, the Secondary Fractures become relatively less common with distance from the high displacement domain. This is evidence that the Main Faults were the first structures to form in the sequence and then the Secondary Fractures started to propagate between them as linking structures. Then, they progressively kept accommodating the bulk displacement together.

Notwithstanding, although the relative timing of the fractures is understood, the mechanism by which the described faults nucleated and propagated through the crystalline rock is still not fully clear. However, a general idea can be obtained from microscopic observations. On Figure II-6, B a microscopic horsetail structure at the tip point of a millimetric-displacement microfault is shown. This horsetail structure consists of very small faults producing micrometric offsets and some of them have extension cracks in their termination. This configuration suggests that the Secondary Fractures were nucleated from the earlier parallel Main Faults to the area between them or away from them. The fact that the Secondary Fractures within the Parulo Fault are mostly extensional and have almost the same orientation than Secondary Fractures within Palmera Fault suggest

that Secondary Fractures have been initially propagated as tensional or “wing” cracks and were sheared later.

The propagation of the Main Faults, in turn, is the most difficult topic to elucidate from the field data. Previous works in fractures system with very similar geometry have proposed that the Main Faults (or “Master Faults”) actually were joints that later become sheared during fault development (Di Toro & Pennacchioni 2005; Flodin & Aydin 2004; Kirkpatrick *et al.,*2008; Martel 1990, Martel *et al.,*1988). However, the data provided here by the thin section made in Palmera fault (Figure II-5) suggests that fractures did not initiate from significant pre-existing joints. In the section, a negative gradient of fracture density and microfault length can be observed with distance from the larger faults. Hence shear fractures become less abundant and smaller in length with distance from the larger structures. This fact, in addition with the fact that the studied outcrops do not display any systematic joint system, indicates that the Main Faults propagated as faults and not as joints.

The propagation of faults through crystalline rocks (*i.e*. Mode II and III fractures) has been strongly studied by laboratory experiments (Cox & Scholz 1988, Petit & Barquins 1988, Wibberley 2000) and field measurements (Cowie & Scholz 1992). The resulting conceptual models agree that faults propagate by nucleation and interaction of tensile fractures arrays ahead of the fault termination. These tensile fractures or cracks should distribute randomly around all the rock but concentrate in areas around the fault plane (as a “damage zone”) and around the edges of the faults or tip lines (as a “process zone”).

The faults observed here under the light microscope show not such important concentrations of cracks, neither in the fault terminations nor around the fault plane. This fact, contrasts with the intense cracking required in the mentioned conceptual models, however, it can be explained in two ways:

(1) The above-mentioned propagation models are based and focused on faulting under pure brittle conditions, through a perfectly elastic material. Instead, the faults described here exhibit mechanical twinning and undulatory extinction coalescing with brittle dilatants fractures (Figure II-7, D), that is an evidence of simultaneous brittle and plastic deformation of the plagioclase (Stünitz *et al.,* 2003). This plasticity involves a ductile deformation of the rock, especially around terminations of shear fractures (Stünitz *et al.,*2003). Then, the ductile bending and shearing accommodating deformation around tip points, in the process zone, will reduce the required cracking. The fault propagation accompanied by permanent ductile deformation must then not be explained by the same models used for complete brittle-elastic conditions.

(2) The observed healed fractures and the intense mineralization activity evidenced by the sealed fractures (Figure II-6, Figure II-7) suggest that the fault system was propagated under hydrothermal conditions (Herrera *et al.,* 2005). These hydrothermal fluids have enhanced the diffusion process favouring healing of fractures. This strong healing may have deleted the possible previous existing cracks.

We propose that the studied Main Faults were propagated by the generation and coalescing of cracks but inhibited by the ongoing coeval plastic processes. Furthermore, the coeval hydrothermal activity probably continuously annihilated the cracks around faults by fracture healing (Stünitz *et al.,* 2003).

II.5.3. Multi-Scale Model of Development

The proposed model of development of the multiple-duplex fault system is shown on Figure II-10 for three scales of observation. In this model, we postulate that the regional scale faults start as families of relatively smaller fractures (extensional and shear) that progressively and heterogeneously concentrate until becoming multiple duplex-fault zones and then become mature fault zones. That evolution through a progressive concentration of fractures, or fault “maturation”, is in complete agreement with previous laboratory observations (Lockner *et al.,* 1991). Furthermore, we propose here that this occurs by the progressive propagation of fractures oriented between 15º and 75º (measured in the sense of slip) from Main Faults. Lately, in the mature fault zones, this fracturing keeps occurring heterogeneously generating cataclastic rocks in the most damaged regions, resulting on a banded cataclastic core with fracture preferred orientation.

Although the evidences to deduce such fault evolution have been mainly observed at microscopic- and metric-scale, it can also be inferred to occur at larger scales, as the system is self-similar.

Then, the banded cataclastic core observed in the internal structure of large scale faults in the AFS (*e.g.*: Bolfin Fault, (Jensen, 2008; and Figure II-1); Coloso Fault (Mitchell, 2007; Mitchell and Faulkner, 2009; and Faulkner *et al.*, 2008) would be the result of the progressive fracturing described above, interacting and mechanically aided by hydrothermal fluids.

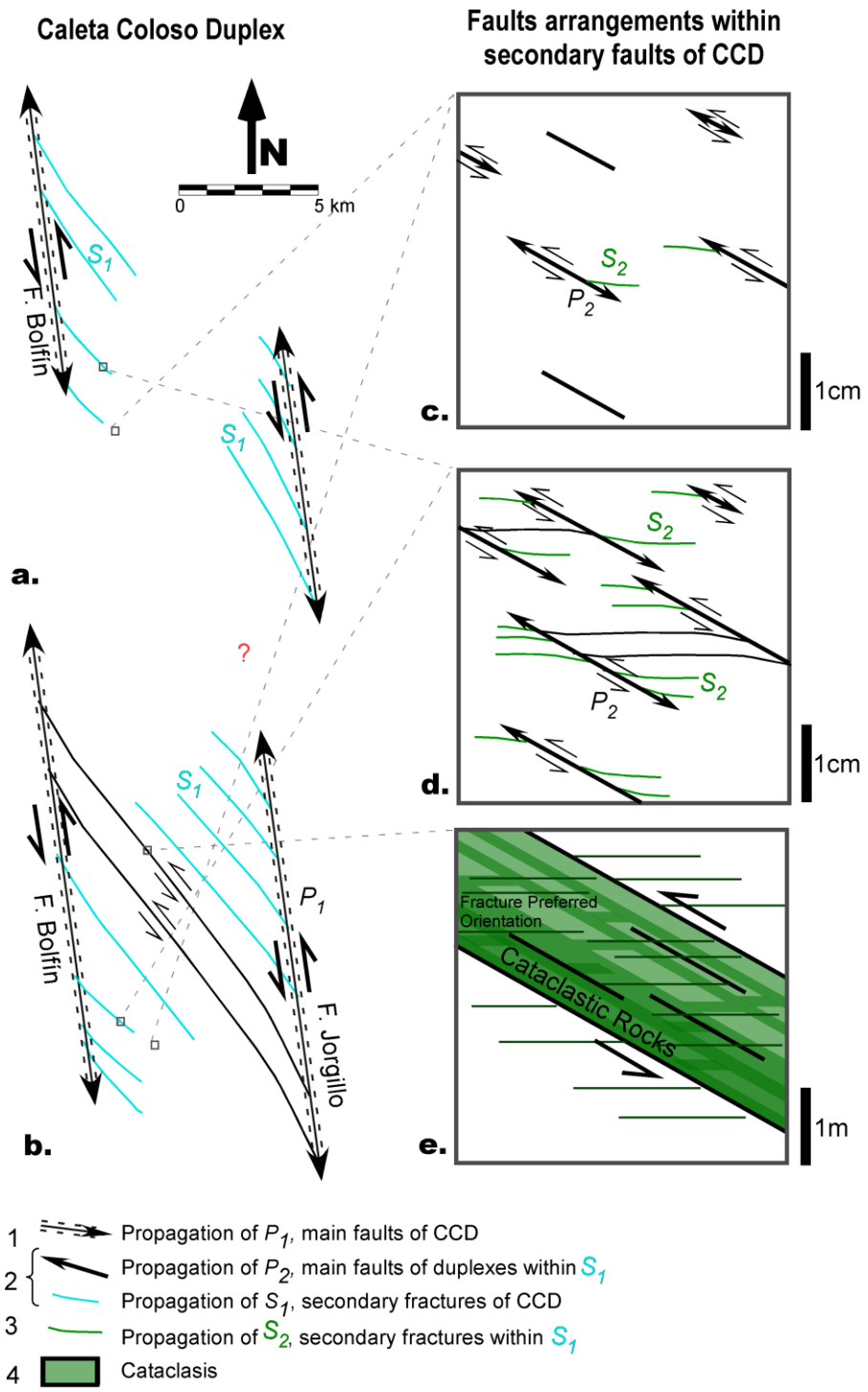

Figure II-10. Development of the fault system
Schematic sketch of the model of development of the whole analysed fault system. A kilometric scale (a, b) and at centimetric to metric-scale (c, d and e)

II.6. CONCLUSIONS

1. The strike-slip duplex pattern is the most characteristic feature in the geometry of the studied fault arrangements at all scales. The presence of this pattern at all scales form a self-similar strike-slip duplex system.
2. The mesoscopic faults in the Duplex Caleta Coloso can be separated according to the internal structure into two types: *Single-Core Faults* and *Multiple Strands Faults* (or Compound Faults)
3. The progressive fracturing oriented between 15º and 75º counterclockwise from the main shear plane (measured in the slip sense) has been the main deformation process building the geometry of the described strike-slip duplex system in the Atacama Fault System. During initial stages, this fracturing linked subparallel faults in slow-strain fault zones (multiple-core faults). Later, with increasing strain, these slow-strain faults evolved to become cataclastic zones where the fracturing continued to occur, producing fracture preferred orientations.
4. The propagation of the fault system occurred under upper-crustal hydrothermal conditions enhancing some crystal-scale processes of fracture sealing and healing and brittle-plastic conditions evidenced by deformation twinning and undulatory extinction around microfaults.
5. The ratio of fault length (L) to duplex width (W) of the studied strike-slip duplexes at a wide range of scales (Figure II-9) is fairly constant and show remarkably well-constrained self-similarity of the system, which in turn appears to be consistent with how earthquake ruptures nucleate and propagate in both experiments and nature.

II.7. ACKNOWLEDGEMENTS

Thanks to all the colleagues at the Departamento de Ciencas Geológicas UCN who help to develop this work. To Pamela Perez, Rodrigo Gomila, Felipe Aron, Pía Ávalos, Tito Álvarez and Rodrigo Carle, for hard working in the field and having essential brainstorm discussions. Special thanks to Professors Gabriel Gonzalez, Eduardo Medina and Hans Wilke.

Thanks to the professor Mark Handy, that kindly help on the recognition of micro-structures from photo micrographs.

Tom Mitchell is thanked for comments and discussion that helped us to improve the manuscript.

Field work was partially financed by a “master thesis development grant, 2007”, given by Universidad Católica del Norte. “*CONICYT Projects FONDECYT 1020439 and 1100464*” and “*AT-24091112*” have also help to fund this work.

II.8. REFERENCES

Arabasz, W.J. 1971: Geological and Geophysical Studies of the Atacama Fault Zone in Northern Chile. Ph. D. Thesis, California Institute of Technology: 275 p.; Passadena.

Barton, C. A., M. D. Zoback, and Moos, D., (1995). "Fluid flow along potentially active faults in crystalline rock." Geology 23(8): 683-686.Brown, M., Diaz, F. and Grocott, J. (1993). Displacement History of the Atacama Fault System 25º00'S-27º00'S, Northern Chile. Geological Society of America Bulletin 105(9), 1165-1174.

Cembrano, J., González, G., Arancibia, G., Ahumada, I., Olivares, V. and Herrera, V. (2005). Fault zone development and strain partitioning in an extensional strike-slip duplex: A case study from the Mesozoic Atacama fault system, Northern Chile. Tectonophysics 400(1-4), 105-125.

Connolly, P. and Cosgrove, J., (1999). "Prediction of static and dynamic fluid pathways within and around dilational jogs." Geological Society, London, Special Publications 155(1): 105-121.

Cowie, P. A. and Scholz, C. H. (1992). Physical Explanation for the Displacement Length Relationship of Faults Using a Post-Yield Fracture-Mechanics Model. Journal of Structural Geology 14(10), 1133-1148.

Cox, S. J. D. and Scholz, C. H. 1988. On the formation and growth of faults: an experimental study. Journal of Structural Geology 10(4), 413-430.

Cox, S. F., (1999). "deformational controls on the dynamics of fluid flow in mesothermal gold systems." Geological Society, London, Special Publications 155(1): 123-140.

Chester, F. M., Chester, J. S., Kirschner, D. L., Schulz, S. E. and Evans, J. P. (2004). Structure of large-displacement, strike-slip fault zones. In: Rheology and deformation , edited by Karner, G. D., Taylor, B., Driscoll, N. W. and Kohlstedt, D. L..

Di Toro, G. and Pennacchioni, G. (2005). Fault plane processes and mesoscopic structure of a strong-type seismogenic fault in tonalites (Adamello batholith, Southern Alps). Tectonophysics 402(1-4), 55-80.

Faulkner, D. R., Mitchell, T. M., Healy, D. and Heap, M. J., (2006). Slip on 'weak' faults by the rotation of regional stress in the fracture damage zone. Nature 444(7121), 922-925.

Faulkner, D.R., Mitchell, T.M., Jensen, E., and Cembrano, J., (2011). The scaling of fault damage zones with displacement and the implications for fault growth processes, Journal of Geophysical Research, 116 B05403 (in review).

Faulkner, D. R., Mitchell, T. M., Rutter, E. H. and Cembrano, J. (2008). On the structure and mechanical properties of large strike-slip faults. Geological Society, London, Special Publications 299(1), 139-150.

Flodin, E. A. and Aydin, A. (2004). Evolution of a strike-slip fault network, Valley of Fire State Park, southern Nevada. Geological Society of America Bulletin 116(1-2), 42-59.

Fuenzalida, V. 1965. Clima In: Geografía Económica de Chile (edited by CORFO), Santiago, 95-152.

Gibson, R. G. (1994). Fault-zone seals in siliciclastic strata of the Columbus Basin, offshore Trinidad. AAPG Bulletin 78(9), 1372-1385.

González, G. (1996). Evolución tectónica de la Cordillera de la Costa de Antofagasta (Chile): Con especial referencia a las deformaciones sinmagmáticas del Jurásico-Cretácico Inferior, PhD Thesis, Freïe Universität Berlin.

Gonzalez, G. and Carrizo, D. (2003). Segmentation, kinematics and relative chronology of the late deformation of Salar del Carmen Fault, Atacama Fault System (23 degrees 40 ' S), northern Chile. Revista Geologica de Chile 30(2), 223-244.

Grocott, J. and Taylor, G. K. (2002). Magmatic arc fault systems, deformation partitioning and emplacement of granitic complexes in the Coastal Cordillera, north Chilean Andes (25º30'S to 27º00'S). Journal of the Geological Society 159(4), 425-443.

Herrera, V., Cembrano, J., Olivares, V., Kojima, S. and Arancibia, G. (2005). Precipitation by depressurization and boiling in veins hosted in an extensional strike-slip duplex: microstructural and microthermometric evidence. Revista Geologica de Chile 32(2), 207-227.

Hippertt, J. (1999). Are S-C structures, duplexes and conjugate shear zones different manifestations of the same scale-invariant phenomenonen? Journal of Structural Geology 21(8), 975-984.Homberg, C., Hu, J., Angelier, J., Bergerat, F., and Lacombe, O., 1997. Characterization of stress perturbations near major fault zones: Insights from 2-D distinct-element modelling and field studies (Jura Mountains). Journal of Structural Geology, 19 (5), 703-718.

Joussineau, G., and Aydin, A. (2009). Segmentation along Strike-Slip Faults Revisited. Pure and Applied Geophysics, 166(19).

Kirkpatrick, J. D., Shipton, Z. K., Evans, J. P., Micklethwaite, S., Lim, S. J. and McKillop, P. (2008). Strike-slip fault terminations at seismogenic depths: The structure and kinematics of the Glacier Lakes fault, Sierra Nevada United States. J. Geophys. Res. 113(B4), B04304.

Lange, D., Cembrano, J., Rietbrock, A., Haberland, C., Dahm, T. and Bataille, K. (2008). First seismic record for intra-arc strike-slip tectonics along the Liquiñe-Ofqui fault zone at the obliquely convergent plate margin of the southern Andes. Tectonophysics 455(1-4), 14-24.

Lockner, D. A., Byerlee, J. D., Kuksenko, V., Ponomarev, A. and Sidorin, A. 1991. Quasi-static fault growth and shear fracture energy in granite. Nature 350(6313), 39-42.

Mandelbrot, B. (1967). How Long Is the Coast of Britain? Statistical Self-Similarity and Fractional Dimension. Science 156(3775), 636-638.

Martel, S. J. (1990). Formation of compound strike-slip fault zones, Mount Abbot quadrangle, California. Journal of Structural Geology 12(7), 869-877, 879-882.

Martel, S. J., Pollard, D. D. and Segall, P. 1988. development of Simple Strike-Slip-Fault Zones, Mount Abbot Quadrangle, Sierra-Nevada, California. Geological Society of America Bulletin 100(9), 1451-1465.

Mitchell. T.M. (2007). PhD Thesis. The Fluid Flow Properties of Fault Damage Zones. (Harold Cohen Library, University of Liverpool).

Mitchell, T. M. and Faulkner, D. R. (2009). The nature and origin of off-fault damage surrounding strike-slip fault zones with a wide range of displacements: A field study from the Atacama fault system, northern Chile. Journal of Structural Geology 31(8), 802-816.

Moir, H., Lunn, R. J., Shipton, Z. K. and Kirkpatrick, J. D.,. (2010). Simulating brittle fault evolution from networks of pre-existing joints within crystalline rock. Journal of Structural Geology, in press.

Morley, C. K. (2004). Nested strike-slip duplexes, and other evidence for Late Cretaceous-Palaeogene transpressional tectonics before and during India-Eurasia collision, in Thailand, Myanmar and Malaysia. Journal of the Geological Society 161(5), 799-812.

Morley, C. K., Smith, M., Carter, A., Charusiri, P. and Chantraprasert, S. (2007). Evolution of deformation styles at a major restraining bend, constraints from cooling histories, Mae Ping fault zone, western Thailand. Geological Society, London, Special Publications 290(1), 325-349.

Olivares, V. (2004). Geometría y cinemática del sistema de fallas y vetas de la porción sur del Duplex Caleta Coloso, región de Antofagasta. , Universidad Católica del Norte.

Otsuki, K., and Dilov, T. (2005). Evolution of hierarchical self-similar geometry of experimental fault zones: Implications for seismic nucleation and earthquake size. Journal of Geophysical Research, 110,(B03303).

Petit, J.-P. and Barquins, M. 1988. CAN NATURAL FAULTS PROPAGATE UNDER MODE II CONDITIONS ? Tectonics 7(6), 1243-1256.

Sanderson, D. J. and Zhang, X., (2004). "Stress-controlled localization of deformation and fluid flow in fractured rocks." Geological Society, London, Special Publications 231(1): 299-314.

Scheuber, E. and Andriessen, P. A. M. (1990). The Kinematic and Geodynamic Significance of the Atacama Fault Zone, Northern Chile. Journal of Structural Geology 12(2), 243-257.

Scheuber, E. and González, G. (1999). Tectonics of the Jurassic- Early Cretaceous magmatic arc of the north Chilean Coastal Cordillera (22 degrees-26 degrees S): A story of crustal deformation along a convergent plate boundary. Tectonics 18(5), 895-910.

Scheuber, E., Hammerschmidt, K. and Friedrichsen, H. (1995). Ar-40/Ar-39 and Rb-Sr Analyses from Ductile Shear Zones from the Atacama Fault Zone, Northern Chile - the Age of deformation. Tectonophysics 250(1-3), 61-87.

Scheuber, E. and Reutter, K. J. (1992). Magmatic Arc Tectonics in the Central Andes between 21ºS and 25ºS. Tectonophysics 205(1-3), 127-140.

Scholz, C., Dawers, N., Yu, J. Z., Anders, M. and Cowie, P. (1993). Fault Growth and Fault Scaling Laws: Preliminary Results. J. Geophys. Res. 98(B12), 21951-21961.

Scholz, C. H. (1987). Wear and gouge formation in brittle faulting. Geology 15(6), 493-495.

Scholz, C. H. and Aviles, C. A. 1986. The fractal geometry of faults and faulting. In: Earthquake Source Mechanics. Academic Press, New York, p. 9. (edited by Das, S., Boatwright, J. and Scholz, C.).

Sibson, R. H. (1977). Fault rocks and fault mechanisms. Journal of the Geological Society 133(3), 191-213.

Sibson, R. H., (1994). . "Crustal stress, faulting and fluid flow." Geological Society, London, Special Publications 78(1): 69-84.

Sibson, R. H. (1985). Stopping of earthquake ruptures at dilational fault jogs. Nature 316(6025), 248-251.

Sibson, R. H. (1987). Earthquake rupturing as a mineralizing agent in hydrothermal systems. Geology 15(8), 701-704.

Sibson, R. H., Moore, J. M. M. and Rankin, A. H. (1975). Seismic pumping--a hydrothermal fluid transport mechanism. Journal of the Geological Society 131(6), 653-659.

Sillitoe, R. H. (1973). The tops and bottoms of porphyry copper deposits. Economic Geology 68(6), 799-815.

Smith, D. A. (1980). Sealing and nonsealing faults in Louisiana Gulf Coast salt basin. Journal Name: Am. Assoc. Pet. Geol., Bull.; (United States); Journal Volume: 64, Medium: X; Size: Pages: 145-172.

Stünitz, H., Fitz Gerald, J. D. and Tullis, J. (2003). Dislocation generation, slip systems, and dynamic recrystallization in experimentally deformed plagioclase single crystals. Tectonophysics 372(3-4), 215-233.

Swanson, M. T. (2006). Late Paleozoic strike-slip faults and related vein arrays of Cape Elizabeth, Maine. Journal of Structural Geology 28(3), 456-473.

Sylvester, A. G. 1988. Strike-slip faults. Geological Society of America Bulletin 100(11), 1666-1703.

Tomlinson and Blanco. (1997a). Structural evolution and displacement history of West Fissure fault system. Precordillera, Chile. Part 1, Synmineral Hystory In: 8º Congreso Geológico Chileno, Antofagasta, 1873-17877.

Tomlinson and Blanco. (1997b). Structural evolution and displacement history of West Fissure fault system. Precordillera, Chile. Part 1, Postmineral Hystory In: 8º Congreso Geológico Chileno, Antofagasta, 1873-17877.

Wibberley, C. A. J., Petit, J. P. and Rives, T. (2000). Micromechanics of shear rupture and the control of normal stress. Journal of Structural Geology 22(4), 411-427.

Wibberley, C. A. J., Yielding, G. and Di Toro, G., (2008). "Recent advances in the understanding of fault zone internal structure: a review." Geological Society, London, Special Publications 299(1): 5-33.

Woodcock N.H. (1977). Specification of fabric shapes using an eigenvalue method. - Bull. geol. Soc. Am., 88, 1231-1236.

III. FAULT-FLUID INTERACTION IN PORPHYRITIC HIDROTHERMAL DEPOSITS: PETROGRAPHIC ANALYSIS OF FAULT-VEINS IN RADOMIRO TOMIC, NORTHERN CHILE

(*Aceptado, con correcciones, en Journal of Structural Geology. Julio 2018*)

ABSTRACT

This contribution aims to unravel the temporal and genetic relationship between hydrothermal fluids, faulting processes and their effect on faulted rock strength. The evolution of the interaction between faults and fluids is studied by observing the petrography of a fault-vein system in the Radomiro Tomic open-pit copper mine. The rocks in and around the faults are grouped into 6 units, according to their spatial relationship to the fault (characterized with detailed mapping), their mineralogy (measured with XRD) and microstructure (described with optical microscopy). The petrography of these units is used to infer the petrogenetic processes and their timing of occurrence. The deformation in RT initiated with hydro-fracturing disrupting low strain crystal plastic deformation. When the system cooled down fractures propagated, increasing its permeability. Phyllic mineral assemblages, concentrated around faults and veins, weakening the rocks and promoting slip along fault-veins. Later, silicification heterogeneously hardened the faults, partially sealing them. Finally, the formation of kaolinite weakened the rocks around the fault cores (haloes), without further deformation.

The petrographic modifications expected for porphyry copper hydrothermal systems are: (1) Growth of K-feldspar and recrystallization of quartz, not related to faults. (2) Recrystallization of K-feldspar and destruction of plagioclase by hydrolysis, restricted to faults (in cores and haloes). (3) Full destruction of K-feldspar by hydrolysis occurred in fault-cores and blocks of protolith surrounded by gouge/cataclasite. (4) Rock cementation by mineral precipitation (quartz and metallic sulphides) and rock comminution were restricted to the fault cores. They combine during the development of a hydrothermal system. Although the cementation tends to strengthen fault cores, the total strength of the faults is reduced for the hydrolysis of plagioclase in the surrounding damage zone, reducing the capacity of faults to accumulate stress.

III.1. INTRODUCTION

Understanding fluid-rock interaction in and around faults in the Earth's crust is important for understanding a wide range of geological processes, such as earthquake generation (Gratier & Gueydan, 2007), crustal rheology (Bos & Spiers, 2002) and the distribution of ore minerals (Curewitz & Karson, 1997). Faults typically consist of a fine-grained, low permeability core surrounded by a fractured and more permeable damage zone. Faults play a fundamental role in the migration of fluids behaving as barriers or conducts, depending on the fluid direction (Caine *et al.*, 1996; López & Smith, 1996; Wibberley & Shimamoto, 2003). The fault core consists of a relatively narrow zone of highly strained rocks, where most of the displacement has been accommodated. In turn, the surrounding damage zone consists of highly fractured rock, which accumulated damage while the fault accumulated displacement. (Braathen *et al.*, 2009; Caine *et al.*, 1996; Chester *et al.*, 1993; Faulkner *et al.*, 2003; Mitchell & Faulkner, 2009).

Many studies over several decades have demonstrated an important feedback relationship between faults and hydrothermal fluids. The mineralogy of fault cores can be highly modified by chemical interaction with fluids. Even though the faults inherit their mineralogy from the protoliths, they are not identical and show significant changes in mineralogy and chemistry (Arancibia *et al.*, 2014; Evans & Chester 1995; Faulkner *et al.*, 2003; Goddard & Evans 1995; Janssen *et al.*, 2004; Schulz & Evans, 1998). Such differences are explained by a combination of brittle deformation and the action of fluid-assisted mass mobilization, caused by hydrothermal fluids, both for closed and open systems (Schulz & Evans, 1998). The channelling of fluids by faults is evidenced by the frequent co-existence of regional-scale fault systems and hydrothermal ore deposits. (Curewitz & Karson, 1997; Charrier *et al.*, 2007; Eisenlohr *et al.*, 1989, Yang *et al.*, 2003). Considering such observations, faulted regions must be considered highly susceptible to petrographic changes induced by the action of fluid-rock interaction, which may subsequently change both their mechanical and hydrodynamic properties (e.g. failure stress, frictional strength, cohesion, seismic stability and permeability). The most characteristic example of this is given by the phyllosilicates, which have been shown to reduce the mechanical strength of faults. (Bos & Spiers, 2002; Wintsch *et al.*, 1995).

In order to better understand the mechanical changes produced by the interaction between faults and fluids affected by hydrothermal activity, both field and petrographic analyses are necessary. However, most of the published petrographic descriptions and mineralogical analysis of fault-rocks which aim to understand fluid-fault relations have been conducted in faults where hydrothermal ore deposits are not found, which express weak evidence of hydrothermal activity,

comparing with hydrothermal systems related to mineral deposits (Braathen *et al.*, 2009; Chester & Chester 1998; Chester *et al.*, 2004; Evans & Chester, 1995; Faulkner *et al.*, 2003; Janssen *et al.*, 2004; Wibberley & Shimamoto, 2003). In this contribution, we present a mineralogical and petrographic description of faults interacting with a crustal-scale hydrothermal system comprising important copper deposits (e.g. Chuquicamata, Radomiro Tomic, El Abra). This contribution aims to unravel the temporal and genetic relationship between hydrothermal fluids, faulting processes and their potential effect in rock strength.

The present study is conducted in the fault branches crossing through the Radomiro Tomic copper deposit (RT), within the Domeyko Fault System in northern Chile (Figure II-1). The location of the faults, within a large-scale hydrothermal deposit, makes it possible to unravel the relationship between faulting and hydrothermal activity. Furthermore, the open pit mining activity which takes place in RT provides direct access to faults for sampling and mapping at deep structural levels, below the water table and away from the atmospheric weathering zone. Firstly, a petrographic description of the faults is reported, grouping their components into fault-related units. For each unit, the textural fabric, distribution, and the crystalline (optical) properties are systematically described, using polarized light microscopy and optical cathodoluminescence. The mineralogy of each unit is identified and quantified using X-ray diffraction (XRD) of both whole-rock “random oriented mounts” and isolated-clay “oriented aggregate mounts” (explained in detail in Text S1, of the section III.6 “Supplementary Information” of the present Thesis). Secondly, the descriptions of the fault-related units are used to infer the timing of formation and the petrogenetic processes, responsible for their formation and distribution. We then discuss these results in the context of the development of faults related to any porphyry copper hydrothermal system.

III.1.1. Geological Setting of Radomiro Tomic Deposit

Radomiro Tomic (RT) is an open-pit copper mine located in northern Chile. It is located at 3000 m.a.s.l., 24 km north of Calama and 6 km from Chuquicamata mine (Figure II-1 a). Tectonically, RT is located in the Central Andes Inner Forearc, in a trench-parallel fault system which has been called both the Domeyko Fault System, DFS (Charrier *et al.*, 2007) and the Precordilleran Fault System, PFS (Reutter, 1986; Janssen, 2002; Hoffman-Rothe *et al.*, 2006); in this article it will be referred to as the DFS. The DFS is comprised of several kilometre-long branches formed during the Eocene Incaic tectonic phase (Charrier *et al.*, 2007; Maksaev, 1978; Maksaev & Zentilli, 1999).

Since its formation the DFS has experienced a complex kinematic history, evolving from right lateral, reversing to left lateral, then dextral-normal and finally dextral-inverse (Hoffmann-Rothe *et al.*, 2006). This fault system demonstrates a primary control on large scale hydrothermal fluid flow, evidenced by the occurrence and distribution of many of the important base metal deposits of the Northern Chile along its trace (Lindsay *et al.*, 1995; Hoffmann-Rothe *et al.*, 2006; Ossandon *et al.*, 2001; Zapettini *et al.*, 2001).

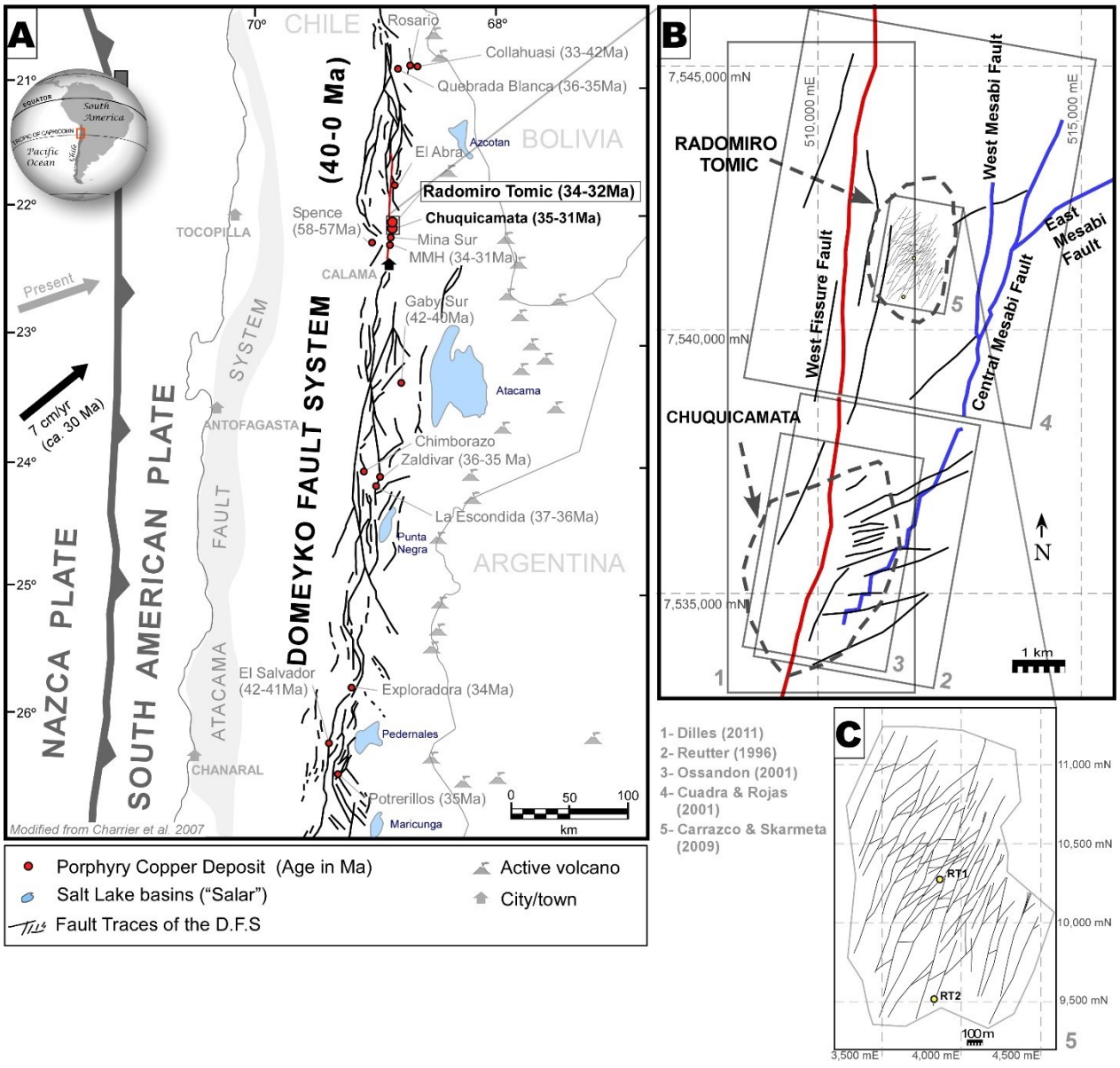

Figure III-1. Structural setting Map
Maps showing the structural settings and location of Radomiro Tomic. A: RT and other main deposits (with ages indicates) and the tectonic setting of Domeyko Fault System. Modified from Charrier *et al.,* (2007). Subduction vector for 30 Ma taken from Somoza (1998). B: District-scale structural map showing the main branches of the DFS around RT. Compiled from structural maps currently available in the published

literature and an internal mine report. The numbered grey rectangles specify their source: 1. (Dilles and Tomlinson H., 2011) 2. Reutter (1996) 3. Ossandon (2001). 4. Cuadra & Rojas (2001). 5. Carrasco & Skarmeta (2009). Segmented lines are the boundaries of the pits in 2009. C: Map of the main structures of RT, mapped in Carrasco & Skarmeta (2009) as VQS (Quartz Sericite Veins).

The most common rock unit in the RT ore deposit is a granitic rock of the East Porphyry unit, part of the Chuquicamata Intrusive Complex. The age of the East Porphyry unit has been dated at 35-36 Ma via the U/Pb technique (Ossandon *et al.*, 2001) and consists of granodioritic to monzogranite intrusive rocks with medium- to coarse-grained phenocrysts of feldspar and minor biotite set in a fine crystalline groundmass. The unit is covered by a 40-to-150m deep layer of Miocene to Pliocene alluvial gravel. (Cuadra & Rojas, 2001; Diaz *et al.*, 2009).

Three hypogene hydrothermal events have been reported for RT, altering the East Porphyry rock unit (Cuadra & Rojas, 2001; Diaz *et al.*, 2009). The occurrence of those three alteration events in RT is consistent with the general alteration sequence described in most porphyry type deposits in the world (Lowell & Guilbert, 1970; Meyer & Hemley, 1967). This sequence is as follows: 1) “K-Silicate Alteration” also called “Background Potassic Alteration”. It is widespread over the entire deposit and is typically represented by biotite crystals replacing hornblende phenocrysts, and by quartz veinlets with K-feldspar haloes (Cuadra & Rojas, 2001). $^{40}Ar/^{39}Ar$ dating on K-feldspar gives an average age of 32.7± 0.3 Ma (Cuadra *et al.*, 1997) suggesting that it forms part of the late-magmatic phase. According to a review of the best-known deposits, this type of alteration typically occurs when the rocks are undergoing crystal-plastic deformation (which occurs at temperatures between 450 and 500 °C) and pulses of high salinity and high temperature (boiling) fluids are injected (Sillitoe, 2010). 2) “Quartz/Sericite Alteration” is imposed over the earlier Background Potassic Alteration, clearly controlled by NE-SW to N-S-striking, subvertical, planar structures. This alteration is represented by fine aggregates of quartz and "sericite" (aggregate of fine-grained phyllosilicates), accompanied by pyrite and chalcopyrite found both in haloes of veinlets (D-type) and selectively replacing feldspar around metre-scale faults (Diaz *et al.*, 2009). $^{40}Ar/^{39}Ar$ dating on sericite yields an average age of 31.8 ± 0.3 Ma and is considered to represent the main hydrothermal phase (Cuadra *et al.*, 1997). Analysis of the same mineral assemblage on other porphyritic deposits indicates a formation temperature of between 250 and 350°C and association with non-boiling fluids of intermediate temperature and intermediate salinity (Sillitoe, 2010). 3) “Supergene Argillic Alteration” is the final alteration event, overprinting (1) and (2) in the upper part of the oxidation zone. This alteration is represented by the replacement of feldspar by smectite and kaolinite replacing feldspar and is related to meteoric water circulation (Cuadra & Rojas, 2001). Operative sections, built from core logging, show that alteration minerals are

homogeneously distributed in the upper 50-150m (ca. 2750m a.s.l.) of the deposit and but are fault-controlled below this depth (Diaz *et al.*, 2009).

The distribution of the products of these alteration events, controlled by structures, defines a deposit-scale vertical anisotropy. However, this is superimposed by a horizontal anisotropy defined by the distribution of minerals with different oxidation states, resulting from a late meteoric leaching, termed supergene enrichment (Cuadra & Rojas, 2001). The alteration mineralogy occurs in two main zones: An Upper Oxide Zone, above 240-360m depth, and a lower Secondary Enrichment Zone, below 240-360 m depth. The Oxide Zone is divided into “Upper” and “Lower” subzones according to their atacamite content (Cu2Cl(OH)3). In turn, the Secondary Enrichment Zone is divided in “Strong” (upper) and “Weak” (lower) according to its sulphide content (Diaz *et al.*, 2009). The research in this work is focussed on the Weak Secondary Enrichment Zone.

III.1.2. The Radomirio Tomic Fault System

RT is structurally located in the middle of an Eocene-Oligocene plutonic block, flanked by two regional scale faults: The West Fissure Fault to the west and the Mesabi Fault to the east (Figure II-1 b). The north-striking West Fissure Fault has been traced in maps for more than 250 km, however it is well exposed as a continuous structure only along 170 km of its length, from Cerro Limon Verde (22°40’S, 10 km to the south of Calama) to Quebrada Blanca mine (21°00’S) (Janssen *et al.*, 2002; Reutter *et al.*, 1996). This fault runs through Chuquicamata mine defining the major limit of mineralization and ore distribution. Mesabi Fault, in turn, has been traced for ca. 18 km from the southernmost wall of Chuquicamata mine towards the north. It strikes N15°E in its southernmost 8 km and smoothly transitions towards a N60°E strike in the north. In its northernmost part the fault separates into three splays - East-Mesabi, Central-Mesabi and West-Mesabi (Cuadra & Rojas, 2001; Ossandon *et al.*, 2001)

Because these two regional faults define the tectonic block where RT is located, neither of them run through the deposit itself (Figure II-1 b). The main fault system within RT is formed by N30-60E-striking subvertical, 100-300 m long-faults, separated by 5-50 meters. These share locus and orientation with quartz and quartz-sericite veins. Locally, these structures are displaced by a few centimetres by post-ore NW-striking faults. (Cuadra & Rojas, 2001; Diaz *et al.*, 2009). This research is then focused only on faults of the NE-striking system. According to the mine maps in the internal operative reports of RT (Carrasco, 2007; Carrasco and Skarmeta, 2009), the largest and thickest structures are those striking N30-40E, with smaller splay faults striking N40-60E (Figure II-1 c). In the internal reports all these faults are considered part of the Kalatche Fault

system and have been also mapped with the name Quartz Sericite Veins ("VQS"), due to the ubiquitous presence of quartz veins and sericite haloes, however, considering the presence of dark fault rocks (described later in this work), in this work they will be referred as "Black Faults", because of their outcrop-scale appearance. Considering their distribution and orientation, the N30-40E striking structures can be considered as master faults, and the N40-60E striking structures as secondary faults, of a multiple dextral strike-slip duplex structure (e.g. Jensen *et al.*, 2011).

At the top, the described fault system is truncated by an unconformity surface, covered by a non-faulted, 50-170 m thick alluvial gravel. A tuff intercalated in the gravels, 2 m below the current surface, was dated in biotite by the K-Ar method at 9.7 ± 0.7 Ma (Cuadra & Rojas, 2001). This indicates that the fault system in RT has been inactive at least for the last 9 My.

III.2. DESCRIPTION OF THE BLACK FAULTS IN RT

III.2.1. Methods

In this study, the main sources of data are outcrop maps of fault internal structure, petrographic descriptions of fault materials, and mineralogical characterization by X-ray diffraction (XRD). A detailed description of the data sources is given in Text 1, of the section III.6 "Supplementary Information" of the present Thesis.

After a first general macroscopic observation of faults on the mine walls of RT, two sites were selected for mapping, sampling and petrographic analysis (microscopic and XRD). These 2 sites were selected based on the following criteria: i) accessibility, regarding pit walls located near the mine roads; ii) safety: sites were selected which had the lowest risk of rock fall and were located farthest from active mining operations; iii) wall azimuth: mine walls nearly perpendicular to the fault strike; iv) degree of oxidization: sites were chosen where the rock expressed the lowest degree of oxidization, i.e. which had the lowest possible hematite and limonite content; and v) representativeness: architectural fault which can be found in most faults observed around the mine.

The internal structure of the selected faults has been characterized from maps of the mine walls at different scales (some cm to tens of meters). These maps were produced in the field, as scaled sketch-maps and then digitally re-drawn on photo-mosaics. This mapping was carried out by grouping rock volumes to define units, according to their macroscopic petrographic properties, such as colour, microstructure, fabric, and observable mineralogy. At least one sample was taken from each unit for subsequent microscopic and mineralogical description.

III.2.2. Internal Structure (Outcrop Scale)

The rocks observed in the mine walls have been grouped into 5 units, based on their mineralogic content, microstructure and spatial relation with the faults (Figure II-2): Black Cataclasite-Gouge, Quartz Vein, White Proto-cataclasite, Clay-altered Granite and Pyrite Breccia. Although other rock bodies with different mineralogy and nature are present within the mine walls (e.g. <2mm thick veinlets, and massive bodies of undeformed fine-grained pyrite), these have not been grouped into units because they represent only a small proportion of the deposit.

The most conspicuous characteristic of the faults in RT is their black fault core, which contrasts with the surrounding white clay-rich haloes. Almost all the observed faults in RT exhibit this feature, and as such are referred to as black faults. These faults are crosscut obliquely by some younger NW-SE-trending faults. The black material is found with diverse levels of cohesion, from highly cohesive to uncohesive (dispersible with the fingers). All those varieties are grouped into a Black Cataclasite-Gouge unit, which is distributed in irregular layers with a highly variable thickness of between 1 mm and 1 m which are always spatially related to quartz veins (Figure II-3 a and Figure II-4 a). These fault-related quartz veins exhibit different levels of macroscopic brittle deformation, ranging from continuous tabular bodies (Figure III-3 b, d), to multiple angular blocks surrounded by black cataclasite-gouge (Figure III-4 b). The continuous quartz veins are 3 to 50 cm in thickness, and meters to tens of meters in length. They have sinuous shapes with smooth curvatures of metric wave-lengths. Internally, the veins are primarily composed of millimetre-scale quartz crystals, which are slightly elongated perpendicular to the walls and distributed in tens of parallel layers with thicknesses of millimetres to centimetres in thickness. Although some quartz veins occur away from any faults, most of them are spatially related to faults. The Quartz Vein unit includes all of the banded quartz veins, both those spatially related to and unrelated to faults (Figure III-3 a, c), as well as all the fragments of veins included within fault zones (Figure III-4 b). Locally, adjacent to the Black Cataclasite-Gouge faults, irregular bodies rich in coarse fragments of pyrite are present. These bodies are grouped into the Pyrite Breccia unit. (Figure III-3 b). Pyrite breccia is distributed in discontinuous and irregular layers, 5-50 cm in thickness and metric lengths. Surrounded by the layers of black cataclasite-gouge and pyrite breccia, highly altered rock bodies are present which vary from millimetre-scale lenses to meter-scale regions between fault branches (Figure III-4 a, c). These bodies present strong alteration to clay and quartz, very low deformation intensity and low matrix content, and are hence termed protocataclasite (after Sibson 1977). Their composition varies from quartz-rich (hard) to clay-rich (soft), all grouped into

the White proto-cataclasite unit. Surrounding all the mentioned units, there are irregular volumes of rock, between 1 and 10 meters in thickness, which are richer in clay, quartz and pyrite than the surrounding protolith (although poorer in these minerals than the white proto-cataclasite unit). These zones will be referred to here as green-white fault haloes and are grouped in the Clay-altered granite unit. Distribution of quartz and clay within these haloes is very variable and heterogeneous. In most regions, only minor amounts of clay are selectively distributed in the plagioclase and orthoclase crystals. In other regions, the plagioclase is fully replaced by clay minerals forming macroscopic tabular aggregates of clay.

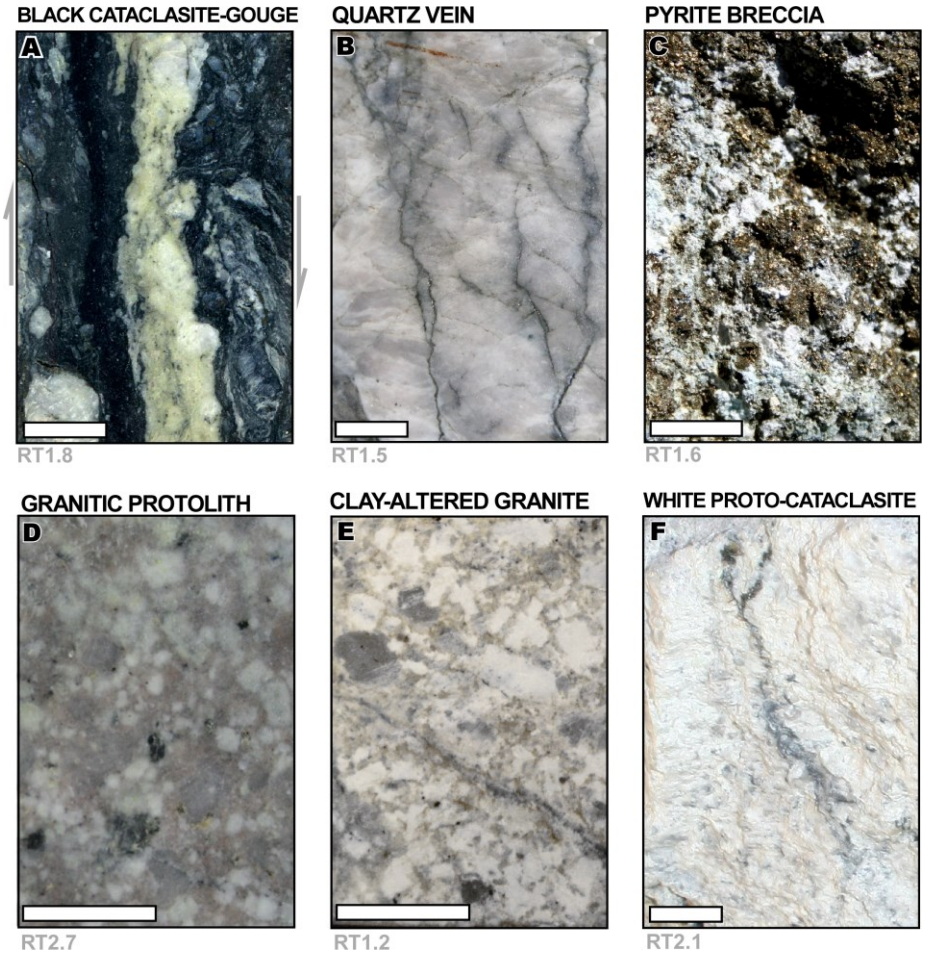

Figure III-2. Mesoscopic photos of the 6 rock units.
White bars are 10mm length. A, B, D and E are saw-cut faces; C and F are fresh fracture faces. A: Black Cataclasite with sigmoid-shape features and a white band of white protocataclasite in the middle (Sample RT1.8). B: Quartz Vein, with irregular thin bands of molybdenite (Sample RT2.5). C: Coarse Pyrite Breccia (Sample 1.6). D: Protolith rock, crystals of biotite and plagioclases are supported by a mass of microscopic k-feldspar (Sample RT2.7). E: Section of a typical clay-altered granite found in the white haloes around the faults. The white tabular pseudo-crystals are only kaolinite-smectite (Sample RT1.2). F: Protocataclasite highly altered to kaolinite and quartz. The oblique grey band is an altered sulphide veinlet with no shear across it. (Sample RT2.1).

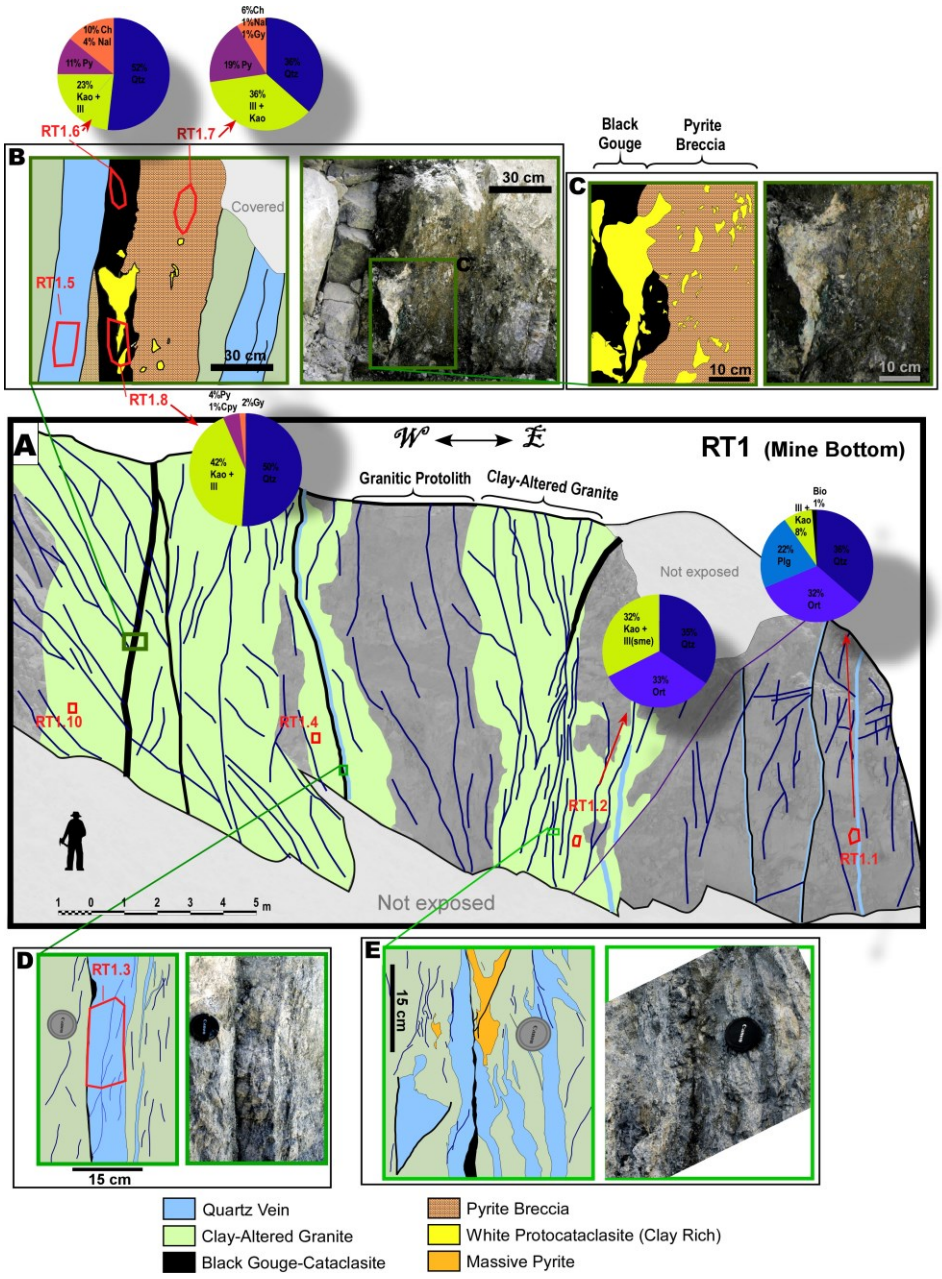

Figure III-3. Outcrop maps RT-1.
Outcrop-maps of exposed faults in a South-facing bench, perpendicular to the fault strike, at the bottom of Radomiro Tomic Mine (ca. 370 m depth in October 2009). The grey background represents the granitic protolith. Pie plots show semi-quantitative XRD analysis. Qz: Quartz, Plg: Plagioclase, Ort: Orthoclase, Kao: Kaolinite, Ill: Illite, Sme: Smectite, Py: Pyrite, Cpy: Chalcopyrite, Ch: Chalcanthite, Gy: Gypsum, Al: Alunite, Nal: Natroalunite, Bio: Biotite. A: General view of the mine wall. Showing the presence of a larger fault at west and two smaller ones towards the east, the three faults have white-green haloes and an adjacent quartz vein. B: Internal structure of the westernmost fault, consisting of thick bands of pyrite breccia and black gouge containing fragments of highly altered protocataclasite. C: Zoom windows from B. D: Middle fault, is a thin fringe of black gouge adjacent an obliquely fractured quartz vein. E: Easternmost fault, is a thin band of black cataclasite cutting through an irregular arrangement of ductility deformed quartz veins. In orange is a volume of fine-grained massive pyrite.

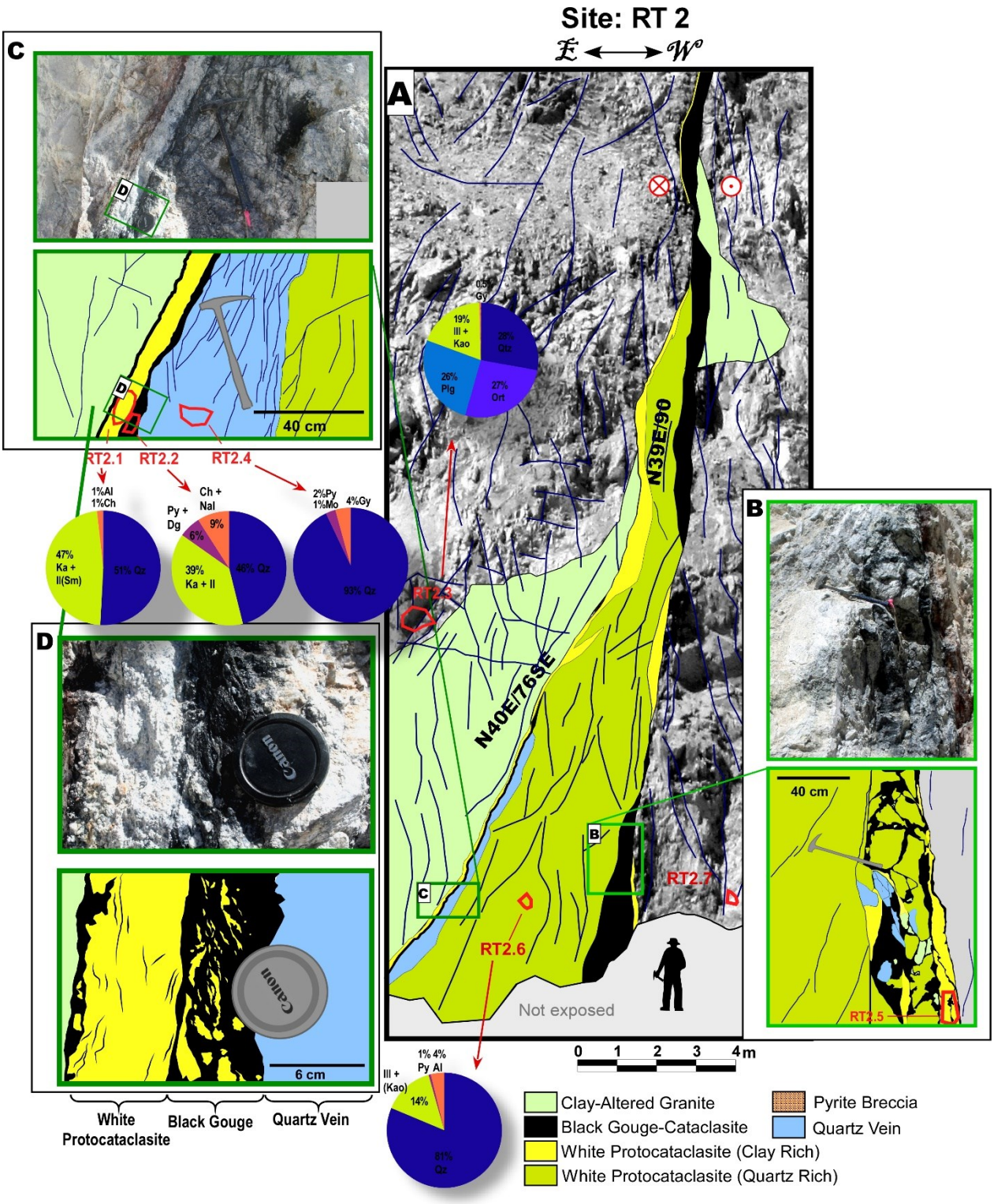

Figure III-4. Outcrop maps RT-2.
Internal structure outcrop maps of a fault exposed in the southernmost wall of the Radomiro Tomic Mine, at ca. 290m depth. Pie plots show semi-quantitative XRD analysis Tabla VII-1. Dg: Digenite, Qz: Quartz, Pl: Plagioclase, Or: Orthoclase, Ka: Kaolinite, Il: Illite, Sm: Smectite, Py: Pyrite, Cp: Chalcopyrite, Ch: Chalcanthite, Gy: Gypsum, Al: Alunite, Nal: Natroalunite, Bi: Biotite A: General wall view, looking

southwards. Note that two NE trending splay faults connect upwards, in an A-shape. B C and D: Zoom windows detailing the internal structure in the two branches.

III.2.3. Petrography of the Fault-Related Units

The petrographic analysis performed on the 5 fault-related units is presented in detail below. For each unit, we describe field occurrence, distribution, and the mineralogical content and microscopic properties of the most abundant minerals. A more comprehensive list of petrographic and mineralogical characteristics, with a systematic record of the same features for all the major minerals in each unit, is given in the table S6 of the section III.6 “Supplementary Information” of the present Thesis. Here we highlight and explain the most conspicuous features, which are later used to infer the genetic conditions and processes of deformation.

III.2.3.1. Granitic Protolith

All the granitic rocks in the RT deposit outside the green-white fault haloes are considered into the granitic protolith unit. Although these are not fault-rocks, they are described in the same terms to allow comparisons and interpretations. At deposit scale, all the plutonic rocks show a porphyritic texture with variable contents of quartz (25 - 40% vol.), K-feldspar (25 - 35% vol.), plagioclase (20 - 30% vol.) and minor biotite (>5% vol.), which replace amphibole as pseudomorphs. Phenocrysts represent more than 50% of the rock volume, vary in size from 1 mm to 3 cm and are set in a crystalline groundmass (0.01-0.4 mm grain size), which varies from grey aphanitic to white phaneritic. Quartz is mainly present in the groundmass, but also rarely as small phenocrysts (< 5mm in size), and in both cases is anhedral in shape, exhibiting sub-grains (Figure III-5 a), and undulose extinction. K-feldspar is also present in the groundmass, though the phenocrysts are larger than the quartz (up to 3 cm in length). Plagioclase is only present as phenocrysts (up to 10 mm in length). Both types of feldspar show homogenous extinction and are absent of sub-grains or any evidence of plastic deformation. They exhibit a clear concentric zoning, with smaller euhedral crystals of quartz enclosed in their outer zones. A systematic description of minerals and other microphotographs of this unit is given in the Text S3 and Figure S1 of the section III.6 “Supplementary Information” in the present Thesis.

III.2.3.2. Clay-Altered Granite (Green-White Haloes))

This unit includes granitic rocks with more quartz and clay than its protolith, irregularly distributed around the black faults, in green-white haloes. The haloes are 1- 10 meters in width and gradually fade against the surrounding granitic protolith. The only evidence of brittle deformation in these rocks are heterogeneously distributed tensile cracks and minor shear bands. These rocks are composed of quartz (30 – 40 % vol.), K-feldspar (25 – 35 % vol.), clay (25 – 35 % vol. / illite > kaolinite), pyrite (< 1 % vol.), and alunite (0 – 4 % vol.). A notable characteristic is the total absence of plagioclase, which is replaced by quartz and clay, producing pseudomorphism. By contrast, k-feldspar is preserved, with only partial clay replacement. Texturally, these rocks still preserve the porphyritic texture of the protolith, with phenocrysts of quartz and k-feldspar, however the tabular plagioclase crystals are replaced by clay mineral aggregates (pseudomorphism). Microscopically, quartz exhibits irregular sub-grains and bulged boundaries both in the phenocrysts and in the groundmass crystals. In contrast, sub-grains of K-feldspar are only present in the groundmass (Figure III-5 b); phenocrysts are anhedral, but without sub-grains. A systematic description of minerals and microphotographs of this unit can be found in the, Text S4, Figure S2 of the section III.6 “Supplementary Information” in the present Thesis.

III.2.3.3. White Proto-cataclasites

This unit includes rocks exhibiting very high levels of mineralogical alteration with respect to the protolith, indicated by the higher relative content of quartz and clay minerals. These rocks exhibit much fewer fractures and rock fragments than the black cataclasite-gouge unit, reflecting their lower brittle deformation intensity. In the field, they show a white colour with pearly brightness, crossed by some thin veinlets (1-2 mm thick) of black-to-grey colour. This is the least common unit and is always delimited by black cataclasite-gouge layers. The white protocataclasite is distributed in millimetre- to centimetre-size lenses and bands within larger cataclasites layers, or in meter-sized regions between fault branches. Mineralogically, these protocataclasites are almost entirely composed of quartz (50 – 80% vol.) and clay (15 – 50% vol., illite > kaolinite > smectite), plus minor amounts of pyrite, chalcanthite and alunite (< 1% vol.), as determined by XRD (Tabla VII-1 of the present PhD Thesis). The main texture is porphyritic, with quartz phenocrysts and clay-quartz pseudomorphs of feldspar set within a strongly altered groundmass composed of massive clay and irregular patches of quartz. By contrast, the zones of higher strain consist of quartz-rich fragments set within a clay-rich matrix (Figure III-5 c). These rocks show a very variable degree of cohesion, depending on their relative quartz content, ranging from very weak clay-rich rocks (ca. 50% clay and 50% quartz), which are dispersible with the fingers or water, to strongly silicified

rocks (ca. 20% clay and 80% quartz), which are resistant to the hammer impact. Locally, shear textures and fragmented material are found in this unit. The veinlets in these rocks are rarely disrupted with offsets, evidencing that the shear deformation affecting this unit is very low. The clay minerals present are illite, kaolinite and some minor smectite, mainly distributed in the altered groundmass as pseudomorphs of feldspar (0.1-3cm size), and minorly in the fragmental matrix and within veinlets (<10-micron size). In the cases where altered proto-cataclasite is surrounded by fault cores in structural traps (Figure III-4), the unit exhibits a higher quartz content (ca. 80%) and the clay is highly crystalline, varying in composition from illite to muscovite. This gives the unit a greenish and slightly translucent appearance (Figure III-4, Sample RT2.6). A systematic description of minerals and microphotographs of this unit is presented in Text S5, Figure S3 of the section III.6 “Supplementary Information” in the present Thesis.

III.2.3.4. Quartz Vein

This unit includes all the bodies of banded quartz veins (including minor amounts of metallic sulphides), regardless of their shape or deformation state. In the field, these veins exhibit a translucent purplish grey colour with millimetre- to centimetre-scale bands (parallel to their walls) composed of quartz crystals of variable size. Most quartz veins have sinuous tabular shapes, are found adjacent to the black faults (Figure III-3 c) and persist along several meters. However, there also are quartz veins in small discontinuous bodies, with irregular and lensoidal shapes (Figure III-3 d). Quartz veins are found with different degrees of brittle damage, from continuous tabular bodies (fractured and filled with metallic sulphides) to centimetre-scale blocks surrounded by a black matrix of fine pyrite. Mineralogically, the veins are mainly composed of quartz (~95%), with minor bands of pyrite and molybdenite. Traces of illite, chalcocite, chalcopyrite, covellite, digenite, and bornite are also observed. Quartz is distributed in parallel bands, 1mm to 1cm in thickness, composed of (1mm to 1cm) euhedral-to-anhedral crystals with different internal microstructure. The largest quartz crystals (0.5 – 1 mm in size) occur away from the molybdenite bands and show strong patchy extinction and small sub-grains (30-50 microns in size) along main crystal boundaries (Figure III-5 d). Molybdenite, pyrite, and other minor minerals are distributed in irregular and discontinuous bands, formed by intercrystalline spaces between quartz crystals. Unlike molybdenite, Fe and Cu sulphides (e.g. pyrite, chalcopyrite) are also found in fractures, oblique to the main banding. The boundary relationships indicate the following sequence of precipitation: quartz, molybdenite, pyrite and chalcopyrite (subsequently replaced by secondary sulphides). Molybdenite bands are commonly strongly striated, even in quartz-veins with very low

brittle deformation. A systematic description of minerals and microphotographs of this unit is presented in, Text S6, Figure S4 of the section III.6 “Supplementary Information” in the present Thesis.

III.2.3.5. Black Cataclasite/Gouge

This unit includes the fault rocks composed of more than 50% matrix, regardless of their cohesion (including cataclasites and gouges). These rocks have a characteristic black to dark grey colour, with some white spots, bands and lenses. Under direct sunlight, they show a gentle golden brightness. These rocks are typically distributed in 1 mm - 1 m thick layers, varying from thin ultracataclasite layers to thicker zones of cataclasites or gouge. The cohesion of these rocks is highly variable, ranging from strong and well cemented rocks which deform in sharp fractures upon impact with a hammer) (i.e. cataclasites), to poorly cemented, dusty rocks (in dry conditions) which are characterized by a muddy aspect in wet conditions are disperse when submerged in water (i.e. gouge). Macroscopically, the texture of black cataclasites consists of fragmented, angular white blocks or porphyroclasts (0.5 - 10 mm in size) set in a fine black matrix (ca. 0.1 mm grain size) of very variable proportions (50 - 90% matrix), which is primarily composed of clay, quartz and fine grains of pyrite. Porphyroclasts are fragments of quartz veins, quartz crystals from the granitic protolith and irregular lenses of massive clay (white proto-cataclasites). Some cataclasites show sub-horizontal right-lateral kinematics, evidenced by subvertical shear foliations oriented between 0 to 30 degrees counterclockwise with respect to synkinematic shear bands. Black cataclasite is commonly interlayered with <1cm-thick fringes of white rock resulting in a banded microstructure. Mineralogically, black cataclasite gouges are very similar to the white protocataclasite, being mainly composed of quartz (40-50 vol.%) and clay (20-45 vol.%; consisting of kaolinite, illite, and traces of smectite. However, black cataclasite gouges have important amounts of metallic sulphides (5 - 10 vol.%), of which pyrite is the most abundant, followed by chalcopyrite, digenite, molybdenite and minor covellite.

Quartz porphyroclasts are 0.1mm to 5cm in size, and under optical microscope two types are identified: Type I: Angular to sub-angular polycrystalline fragments, exhibiting internal fabric varying from diffuse patchy extinction to sub-grains with clear boundaries (Figure III-5 e). Boundaries between the sub-grains are irregular and bulged, suggesting dynamic recrystallization; Type II: Monocrystalline fragments, with continuous internal fabric (homogeneous and fast extinction). These porphyroclasts are sub-rounded with bulged external boundaries, surrounded by several smaller fragments (Figure III-5 f). Optical cathodoluminescence microscopy

reveals that the bulged boundaries are composed of smaller quartz fragments (bright pink) cemented with newly-formed (dark purple) quartz, forming aggregated clusters. Type I are more abundant in the darker portion of the cataclasites and type II are only found in the white bands.

III.2.3.6. Pyrite Breccia

This unit includes fault rocks containing larger fragments of pyrite and less matrix (30 - 50 vol.%) than the black cataclasite-gouge. In the field, they exhibit very low cohesion (being easy to disintegrate with the hand) and present a combination of grey and dark-golden colours, with some centimetre-scale white bands and lenses. They are present only in some of the faults and are distributed in discontinuous bodies adjacent to the layers of black cataclasite-gouge unit. This unit is mainly composed of quartz (30 - 40 vol.%), clay (30 – 40 vol.%; composed of illite > kaolinite) and pyrite (10 - 20 vol.%), with minor amounts of sulphates (< 10 vol.%; composed of gypsum, chalcanthite and natroalunite) filling pore spaces. Rarely, relict feldspar is found under microscopic analysis (although was not detected with XRD, Tabla VII-1 of the present PhD Thesis). Texturally, this feldspar has an isotropic fragmental microstructure, consisting of large porphyroclasts (0.1-10 mm in size), set in an isotropic matrix of fine fragments of clay, quartz, and traces of pyrite (0.01-0.1 mm in size). Four types of porphyroclasts are recognized: 1) Fractured euhedral crystals of pyrite; 2) angular quartz fragments (mono and poly-crystalline); 3) sub-tabular blocks of clay (plagioclase pseudomorphism); and 4) elongated fragments of foliated gouge (composed of much finer fragments of quartz and clay). In contrast to the black cataclasite-gouge unit, these breccias exhibit textural characteristics corresponding to low shear strain, namely: Larger grain-size, very poor foliations and an absence of sigmoidal bodies.

Figure III-5. Optical microphotographs of the 6 Rock Units
They are all are presented on polarized light (left) and with crossed polars (Centre), in some cases a zoom box or a cathodoluminescence (CL) picture is included (right). (A) GRANITIC PROTOLITH: Quartz phenocryst showing irregular boundaries and large subgrains, set on a matrix of K-feldspar and quartz. (B) CLAY-ALTERED GRANITE: Quartz + k-feldspar + clay assemblage in the groundmass around a quartz veinlet. Plagioclase phenocryst are fully replaced by a clay and quartz. K-feldspar is altered to clay, but its internal texture (with large subgrains) is still observable. (C) WHITE PROTOCATACLASITE: Texture of a quartz rich sheared portion of the protocataclasite. The fractures around a polycrystalline quartz are filled by a fragmental matrix of clay and quartz. (D) BLACK CATACLASITE: Type I quartz porphyroclast on the dark portion of a cataclasite. The quartz fragment is composed of several very small subgrains. The shear bands are pyrite rich. (D) BLACK CATACLASITE: Type II porphyroclasts on a white band of a cataclasite. The quartz fragments are mainly monocrystalline, but some of them are composed of several homogeneous fragments. The optical cathodoluminescence picture (to the right), show that the fragments are cemented with a younger darker generation of quartz.

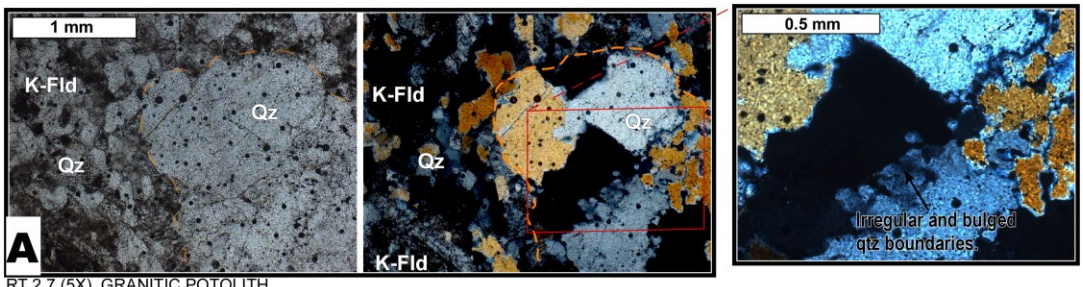

RT 2.7 (5X). GRANITIC POTOLITH

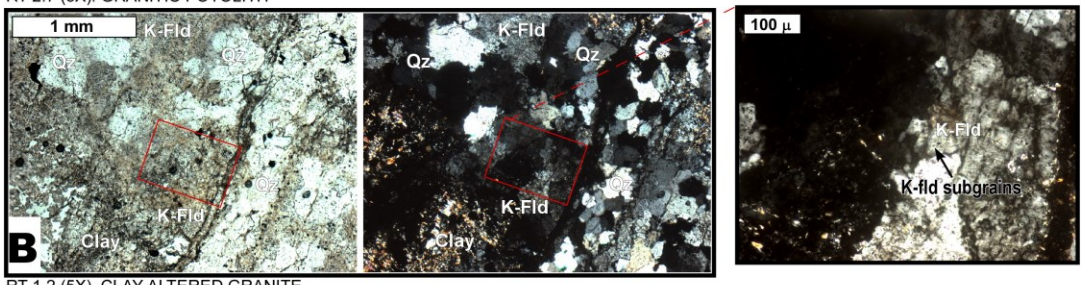

RT 1.2 (5X). CLAY-ALTERED GRANITE

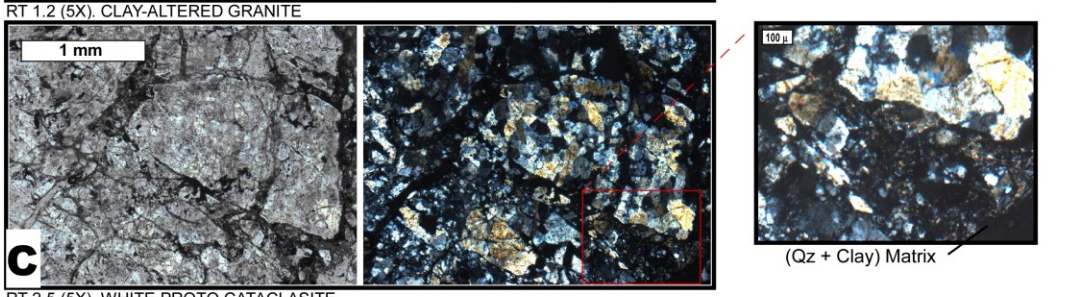

RT 2.5 (5X). WHITE PROTO CATACLASITE

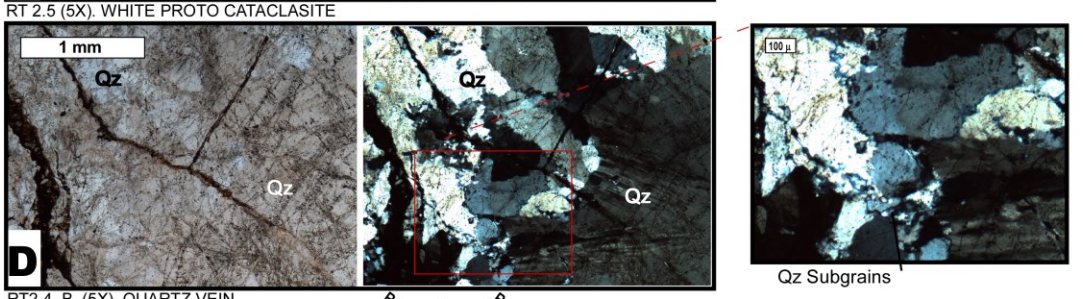

RT2.4_B (5X). QUARTZ VEIN

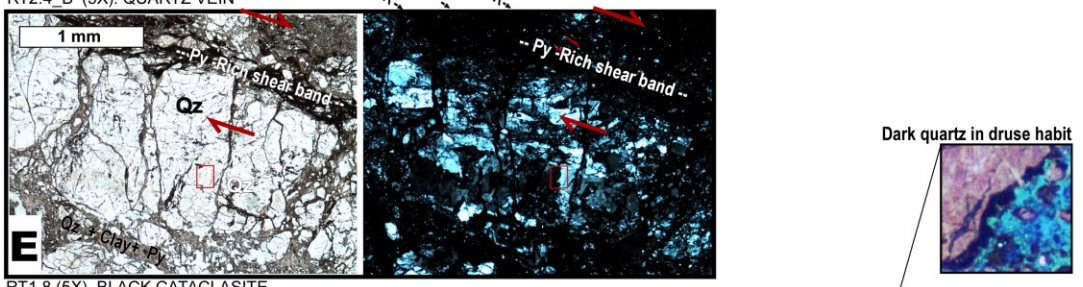

RT1.8 (5X). BLACK CATACLASITE

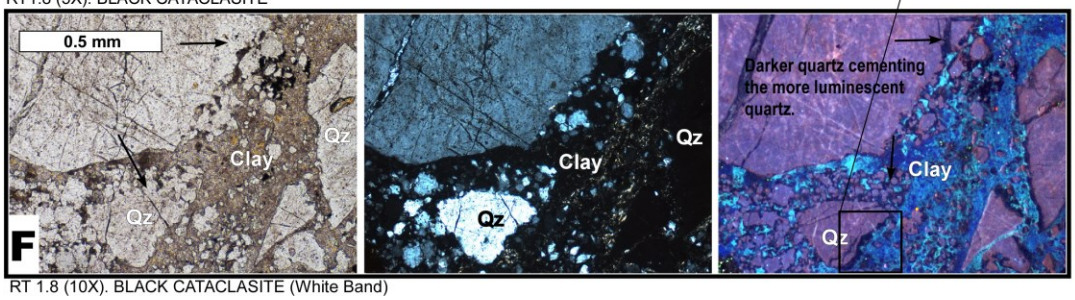

RT 1.8 (10X). BLACK CATACLASITE (White Band)

III.3. DISCUSSION

The final state of the described rocks is a consequence of the successive modification of their petrographic properties by the chemical and physical effects of pore fluids and deformation processes. The processes by which those modifications occur will be referred to here as "petrogenetic processes" (

Figure III-6). These processes are inferred from the petrographic properties of the rocks, described in section 3 and discussed in section 4.1. The mineralogical effects of the fluids on the fault-related rocks are deduced from mineralogical assemblages (determined via XRD, Tabla VII-1 of the present PhD Thesis), mineral occurrence and distribution (determined via mapping), crystal shape and their spatial relationships (determined via optical microscopy). In turn, the mechanical effects of deformation on the fault rocks are deduced from their macro- and microscopic structure, i.e. fragment size, foliations, shape of the crystal boundaries and intra-crystalline structure (e.g. crystal plastic textures). After a discussion of the petrogenetic processes of each unit, their distribution within the fault structure and their time sequence are analysed in sections 4.2 and 4.3 respectively.

The abundance of clay in the faults (cores and haloes), is a consequence of the hydrolytic breakdown of the feldspar and a robust evidence that fluids played a key role in the formation of fault-related rocks. Chemically active fluids tend to change the mineralogy of faults and hence their petrographic properties. However, there are also other process controlling the petrography of the faults; for example, the accommodation of deformation within faults also directly controls the resulting textural properties (e.g. fragmental textures and grain-size reduction).

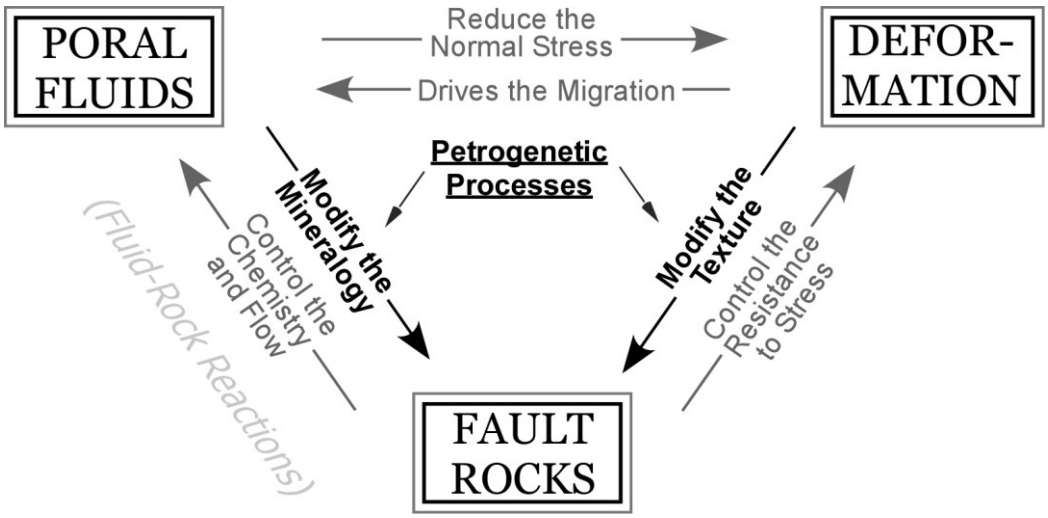

Figure III-6. Fluid-Rock-deformation interaction in faults.
Black arrows represent the processes that control the mentioned property or condition. Effects of deformation and poral fluids on the fault rocks, indicated as petrogenetic processes, are the focus of this article.

III.3.1. Petrogenetic Processes

III.3.1.1. Granitic Protolith

These rocks represent the initial stage of the studied magmatic system and are correlated with the East Porphyry Unit (Cuadra & Rojas, 2001). The porphyritic texture of these rocks suggests at least two main stages of cooling and crystallization. The grain size of the crystalline groundmass suggests a second cooling stage at sub-volcanic depths. The k-feldspar megacrysts enclosing quartz in their outer rings (Figure S1) were probably formed during a late magmatic stage (Farina *et al.,* 2010). In turn, the amphibole transformation to biotite (pseudomorphic replacement) requires the addition of potassium to its structure and the release of calcium, sodium and/or magnesium, and temperatures between 300 to 500°C (Brimhall *et al.,* 1985), suggesting post magmatic hydrothermal alteration. Neither biotite pseudomorphism or K-feldspar megacrysts are distributed related to the faults planes, instead they are homogeneously distributed in the deposit. (Figure III-7). Both features have been considered as part of an "Early Background Potassic Alteration" of 32.7 Ma (Cuadra *et al.*, 1997), which occurs throughout all the deposit. The microstructure of the quartz phenocrystals and groundmass (undulose extinction, sub-grains, bulged boundaries, triple points) suggests recrystallization at a low strain rate (Drury & Urai, 1990), probably induced by post-magmatic heating events.

III.3.1.2. Clay-Altered Granite (Green-White Fault Haloes)

The distribution of alteration minerals in haloes indicates that fluid flowed through the fault damage zones which formed during the propagation and evolution of the faults (Mitchell & Faulkner 2009). The absence of plagioclase, which has been replaced by phyllic and argillic assemblages (as illite, kaolinite and smectite), indicates that the circulating fluids produced plagioclase hydrolysis, also called hydrogen metasomatism (Hemley & Jones, 1964; Dolejs & Wagner, 2007). The preservation of the plagioclase pseudomorphs of clay indicates that this hydrolytic alteration terminated under static conditions and that the rocks have not been significantly deformed since then. The presence of illite, kaolinite and smectite has been related

to the "Quartz/sericite alteration" hydrothermal events of 31.8 ± 0.3 Ma and "Argillic Alteration" of younger relative age (Cuadra *et al.*, 1997).

III.3.1.3. White Protocataclasites

The complete replacement by clay of all the feldspars and their distribution surrounded by black cataclasite (or gouge) layers, suggest that these rocks were mainly formed by the intense chemical alteration of protolith rocks, enhanced by hydrologic compartmentalization between low-permeability fault rocks. The absence of plagioclase and k-feldspar indicates that fluid-rock interaction was so strong that all the feldspar was destroyed by hydrolysis (Figure III-7), creating clay and quartz. As in the rocks of the clay-altered granite unit, the preservation of plagioclase pseudomorphs indicates that static conditions persisted during and after the feldspar hydrolysis. The clay formation in this unit can be related both to the “Argillic” and “Quartz/Sericitic” alteration stages (Diaz *et al.*, 2009).

III.3.1.4. Quartz-veins

No fragment of wall-rock was found within the veins, indicating that abrasive wear by shearing did not occur either before or during the precipitation of the veins. This suggests that these structures initially formed as tensile fractures (mode I) sealed by quartz to become the first tabular bodies or structural anisotropy across the protolith. Later, abrasive shearing and faulting would have initiated after the formation of the veins. The sinuous shapes of the veins could be a consequence of ductile deformation. The intracrystalline features of the quartz (*i.e.* sub-grains and extinction patterns) indicate that such deformation was conducted by dynamic recrystallization of quartz at very low strains rates.

The banded microstructure of the quartz veins indicates episodic pulses of fluid flow. The euhedral crystals of quartz suggest that fluid pressure was high enough to keep the fracture walls away from each other. All these characteristics are consistent with the formation of veins by hydrofracturing during episodic transient periods of brittle deformation, which disrupted a longer-term and slower plastic deformation. This phenomenon has been supported by the dependence of the deformation mechanisms to the strain rate and fluid pressure (Fournier, 1999; Weis, 2012). In turn, the distribution and shape of the sulphides which occur between euhedral quartz crystals indicates the following sequence of precipitation: Quartz, molybdenite, pyrite and chalcocite. The striation on the molybdenite bands indicates that the veins were sheared after their formation.

III.3.1.5. Black Cataclasite-Gouge

The fragmented texture of these rocks is evidence of comminution and frictional wear of pre-existing minerals. In turn, the distribution of clay along shear bands and in the matrix of the rocks is evidence of cataclastic flow lubricated by clay. However, the intercrystalline structure the quartz porphyroclasts indicates that crystal-plastic deformation occurred before the cataclasis. Bulged boundaries of quartz (Figure S5_A) is evidence of low strain recrystallization and the presence of smaller sub-grains (Figure S5_C) indicates dynamic recrystallization by sub-grain rotation SGR) (Drury and Urai 1990). The total absence of feldspar indicates the chemical destruction of all the feldspar by hydrolysis. The presence of smaller quartz crystals, growing around older quartz fragments and cementing the rock, indicates that faults where cemented and sealed after the cataclastic flow, by one or multiple pulses of fluids with dissolved silica. The origin of this late cementing silica is unclear, however the fact that it is crystalline, instead of banded amorphous, suggests a hot hypogene origin. Three possible sources of quartz are suggested: (1) as a product of the latest stage of the “Quartz/Sericitic alteration”, after an earlier main stage involving the alteration of plagioclase to illite. Stoichiometrically, the formation of illite from plagioclase results in dissolved silica, which could slowly accumulate during ongoing deformation until the concentration increases to a level sufficient to precipitate silica; (2) An external pulse of silica-rich fluid after the phyllic stage, totally independent to it;(3) Lower temperature argillic alteration. Alteration of feldspar to kaolinite also generates dissolved silica that can precipitate when concentrations reach sufficient levels. It is worthy of mention that quartz is not the only mineral that cements the fault rocks: minor amounts of pyrite are also found in the intercrystalline spaces of larger fragments of quartz, precipitated in pore spaces.

The described characteristics of black cataclasite-gouge indicate that these rocks were formed by episodic alternations of precipitation of pyrite and quartz, and intense brittle shearing, causing frictional wear and comminution.

III.3.1.6. Pyrite Breccia

These rocks have a very similar mineralogy to the rocks in the black cataclasite-gouge unit, but with differences in fragment size and shape. The pyrite breccias have a much larger fragments and are comprised of less deformed pyrite crystals. These textural features indicate that the comminution and frictional wear (induced by shear strain) acted on these rocks less effectively

than in the Black cataclasite-gouge. Instead, most of the pyrite blocks have a non-sheared, “jigsaw puzzle” texture (Woodcock *et al.*, 2006), indicating that dilatation was the final deformation process and no significant shear strain occurred after it. The described textural and mineralogical characteristics of the pyrite breccia suggest a high precipitation rate during relatively slow brittle shearing, probably at the final stage of the shear deformation that formed the black gouge and cataclasites.

III.3.2. Distribution of Processes Across the Fault Structure

The characterization of the internal structure of faults around the world has consistently shown that their components can be internally separated into several tabular zones or layers with different intensities of deformation and petrographic properties (Chester *et al.*, 1993, 2004; Faulkner *et al.*, 2003; Smith *et al.*, 2013; Kim *et al.*, 2016).

Here, in order to analyse the petrogenetic processes, and to understand the zones within the faults where they may be expected, the units are separated into fault-core and damage-zone zones (Figure III-7). This separation is made according to the deformation intensity and the distribution of the units (according to Chester *et al.*, 2004; Chester *et al.*, 1993). In this regard, the black cataclasite-gouge and pyrite breccia are considered to represent the fault-cores of the studied faults. In turn, the damage-zone is represented by the white proto-cataclasite and the clay altered granite haloes, as they show less deformation intensity than the rocks in the fault-core (although more than the background protolith). Following the same criteria, quartz veins are also considered as part of the fault-core, as they record the most intense deformation. Considering this classification, it can be stated that: (1) not all the petrogenetic processes are related to the faults; and (2) the fault-related processes do not take place across all internal structure of the faults. In detail:

- *Recrystallization of Quartz*: Evidences for this process are found both surrounding faults (in the protolith rocks) and within the fault zones (core and damage zone). suggesting that crystal plasticity was not restricted to the faults. Assuming a progressive cooling scenario, quartz recrystallization should be expected at the earliest stages of the development of the hydrothermal system. However, there is a lesser possibility that this recrystallization took place at a later stage, following the onset of brittle deformation, as a consequence of hot fluid pulses passing through the faults.

- ***Recrystallization of K-Feldspar:*** Indicative textures of this process are only found in the fault damages zones, forming mineral haloes. Indicating that the temperature needed to activate the plastic deformation mechanisms of k-feldspar was reached in the vicinity of the faults. This petrogenetic process is related to higher heat transfer by fluid flow channelled by faults. It is also expected to occur into the fault core, however, there is not feldspar left to observe textures.

-Destruction of Feldspars by Hydrolysis: Full replacement of plagioclase by clay is spatially related to the fault and observed throughout the entire fault zone (core and damage zone). In turn, the k-feldspar is only fully replaced by clay in the fault-core and in blocks of damage zone (protocataclasite) surrounded by fault-core rocks (black cataclasites). This suggest that the hydrolysis is more efficient in the cores than in the damage zones but is enhanced when the rocks are hydrologically compartmentalized.

***-Frictional Wear and Comminution*:** These processes took place only in the fault core. This finding is consistent with published research (Chester *et al.*, 1993; Sibson 1977) and evidences strain concentration by recurrent fault activation. The localized thin bands of small fragmented rocks, resulting from this localization, provide low-permeability barriers to the hydrothermal system, leading to hydrologic compartmentalization.

***-Cementation by Quartz Precipitation ("silicification")*:** This process and the consequent rock hardening are also restricted to the fault-core (Cataclasite and Quartz Veins). The high cohesion of the black cataclasite contrasts with ductile microstructure, indicating cataclastic ductile flow. This can only be achieved if the rocks are cemented after the cataclasis by mineral precipitation. The microstructure of the quartz veins also indicates mineral precipitation and cementation of fractures, when the deformation was dominated by dilation. Quartz crystals grow on the fractures walls, sealing the open spaces, in the same way that they do at smaller scales around fragments within gouges (becoming cataclasite).

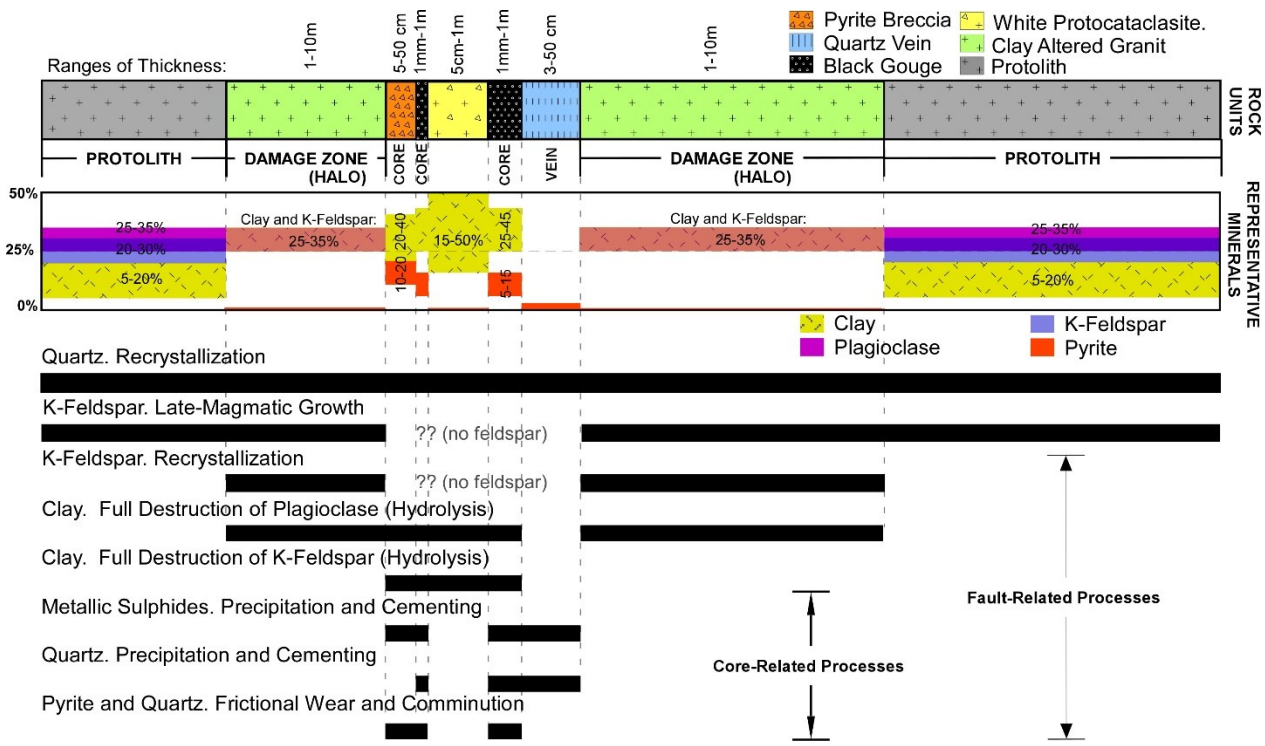

Figure III-7. Schematic section representing the internal structure faults in Radomiro Tomic. Uppermost bar (column) represent the distribution of rock-units. Coloured bars in the centre, represent the typical distribution of the minerals within them (ranges of volumetric percentage). The black bars in the bottom indicate the process deduced to form the rock units, and their distribution.

III.3.3. Fault Evolution (Mineralogy and Texture)

According to the distribution of and relationships between the rock units, the petrogenetic processes can be arranged into a logical time sequence, representing the textural and mineralogical evolution of the faults in RT. The first two processes were the late-magmatic feldspar growth and the replacement of amphibole by biotite, which were probably related to the early background potassic alteration (Cuadra *et al.*, 1997). During this stage, temperatures can be expected to have reached up to 450-550°C (Sillitoe, 2010), allowing crystal-plasticity of quartz and subsequently ductile creep by crystal plasticity at relatively slow strain rates. This plastic deformation is responsible for the recrystallization textures observed in the host rocks as well as the sinuous shapes of the quartz veins.

The repetitive brittle dilation, as evidenced by the separation of the quartz veins into multiple bands, is a consequence of repeated pulses of ascending fluids, which suddenly increased fluid-

pressure and strain-rate. These conditions likely favoured brittle fracturing over longer-term plastic flow, at the same temperature (Fournier 1999; Weis, 2012). This stage is illustrated in Figure III-8A.

In the quartz vein, the euhedral crystals of quartz and the open inter-crystalline spaces, evidence precipitation under fluid pressure that was sufficient to prevent the walls yielding under the lithostatic pressure. The inter-crystalline spaces are aligned parallel to the walls, providing the highest permeability direction. Some of the spaces were filled with euhedral crystals of molybdenite and chalcopyrite before the onset of shearing strain and subsequent striation and fracturing (Illustrated in Figure III-8B). Striations on molybdenite crystals and the abundant fragments of quartz veins in the black cataclasite-gouge both evidence brittle faulting after vein formation. Most of the shear bands of black cataclasite-gouge are located adjacent to quartz veins or else contain fragments of quartz-vein. This indicates that the structures started as opening fractures (Mode I) and subsequently were sheared to become faults (Figure III-8C). This is consistent with the deformation of a mechanically anisotropic rock mass, given by the relatively strong veins crossing a weaker altered rock (shearing across the veins requires more energy than along their walls). At the time when the fractures started to form along the vein walls, hydrothermal fluids were channelled along them, considerably increasing the process of mineral alteration and precipitation, resulting in the formation of the alteration haloes and massive bodies of pyrite. Pyrite is mainly distributed along fractures and shear bands, suggesting that sulphide-rich hydrothermal fluids penetrated the system when brittle deformation started. The phyllic alteration minerals are also spatially related to the faulted veins. Illite is concentrated in the fault-vein haloes and within the fault cores, suggesting that illite formation was associated to the brittle deformation and it was subsequently deformed by cataclastic flow.

Considering the spatial relationship between illite and pyrite, and their state of deformation, these minerals are considered to be syngenetic: They formed after quartz vein precipitation, during brittle deformation. The relationship between pyrite precipitation and quartz-sericitic alteration is consistent with previous research based on petrographic observations and geochemical analysis. These processes are grouped in a single stage named "Phyllic Alteration" (Beaufort and Meunier 1983; Hemley et al 1980). The onset of fracture propagation, the subsequent formation of a quartz-sericitic halo and the precipitation of pyrite within fractures, are represented in Figure III-8D. The state of deformation that illite and pyrite exhibit within cataclasites indicates that the shear deformation along veins continued to be an important process after the influence of phyllic fluids.

Along with the accumulation of shear strain, gouge is formed in the faults, progressively reducing their grain size and re-distributing the quartz, pyrite and clay along parallel bands. The period of gouge formation is when most dextral displacement was accommodated by the faults

and is represented by Figure III-8E. During (and possibly also subsequent to) the final portion of this shearing stage, pyrite and other sulphides were precipitated in significant quantities, forming sulphide-rich bodies, which were subsequently sheared to different degrees, forming the pyrite breccia.

Following the formation of the black gouge and pyrite breccia units, no further deformation affected the faults, however they still experienced two important mineralogical modifications: Silicification of the fault gouge (becoming cataclasite) and the formation of kaolinite from feldspar and illite. The observation under optical cathodoluminescence microscope of small crystals of quartz, surrounding and joining quartz fragments, indicates cementation of the gouge by crystalline quartz, forming cataclasites under hydrothermal conditions (represented in Figure III-8G). In turn, the occurrence of kaolinite-rich haloes, forming around weak but undeformed rocks, suggests a final alteration event, in which kaolinite was formed from feldspar after the cessation of deformation (Figure III-8h).

According to the published models of the evolution of ore-forming hydrothermal systems, this type of argillic alteration can occur during the entire lifetime of a hydrothermal system, via the chemical action of ascending low-temperature, low-salinity and low-pH vapours. Such alteration is nearly always found in the uppermost zone of the hydrothermal system (close to the surface) and is frequently imposed over other alteration zones (e.g. potassic and sericitic alteration) when the surface is degraded. (Sillitoe, 2010).

In terms of rock-forming minerals, the mineralogy of the studied faults evolved from the stability of k-feldspar, illite and then kaolinite. This sequence indicates an evolution of the hydrothermal system from high-temperature and intermediately-acidic (dominated by K+ cations) to a medium-to-low temperature and highly-acidic system (dominated by H+ cations). (Meunier, 2005; Utada, 1980).

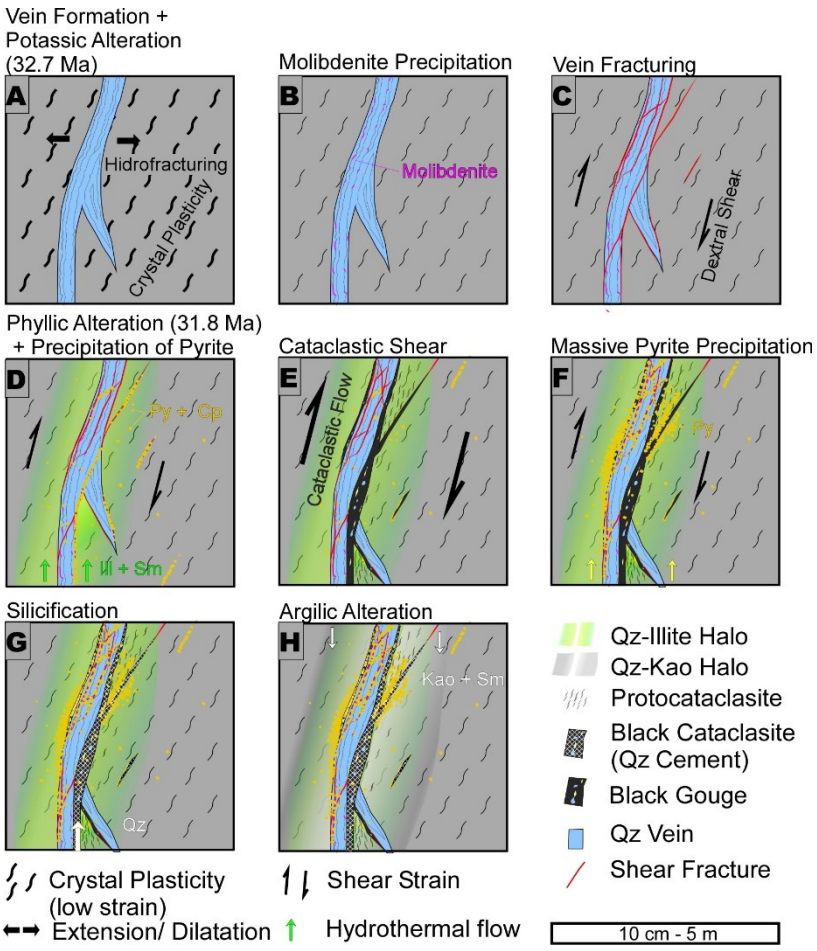

Figure III-8. Sequential evolution of the faults in Radomiro Tomic
Deduced from the petrographic characteristics and relationships observed under microscope and in the mine walls. Schematic maps in plain view representing scales from millimetres to several meters.

III.3.4. Insights Into the Mechanical Effects on a Developing Fault

Understanding the processes involved in fluid-fault interaction is important for the comprehension of the mechanical changes that a fault will experience during its development under the effect of hydrothermal fluids.

The precipitation of new minerals (*e.g.* quartz, metallic sulphides, sulphates, salt) requires open spaces (pores) in the host material. In geological faults, the core is the zone where most spaces are created during slip; whether because of the irregularities in the slipping plane (*e.g.* dilatational jogs) or extension induced by the general stress conditions (*i.e.* hybrid fractures). Consequently, the fault core is where most precipitation should be expected, as shown by the faults in RT (Figure III-7). This process will result in the "replacement" of pore spaces by minerals, which implies more chemical bonds to break, in order to propagate new fractures or reactivate old ones. Then, it should be expected that the cooling hydrothermal fluids will strengthen the fault cores, proportionally to the strength of the precipitated minerals.

Moreover, the hydrothermal fluids passing through a fault will also alter the minerals within and around the faults. The mechanical effect of such alteration on the faults will depend on the strength difference between the existing and replacing minerals. In our case study, magmatic feldspars (both k-feldspar and plagioclase) are replaced by hydrothermal clays, which are weaker than feldspar, both in the fault cores and damage zones (mineral haloes).

The chemical reaction responsible for the replacement of feldspars by clays is hydrolysis, also called hydrogen metasomatism (Hemley & Jones, 1964; Dolejs & Wagner, 2007). The hydrolytic destruction of feldspar, forming clay rich alteration zones, is common in hydrothermal systems related to porphyry copper, including epithermal environments (Sillitoe, 2010), especially during their latest stages and in their uppermost zone, modifying all earlier mineral assemblages. However, hydrolysis is also a significantly common reaction during the weathering of granitic rocks (Clayton, 1988).

In light of the current observations and interpretation, we hypothesise that the effects of the hydrothermal fluids on the mechanics of a fault can be summarized as the combination of: (1) weakening by alteration; and (2) hardening by precipitation. Both processes can occur either in the fault core or in the damage zone. However, process (2) is expected to be much more localized in the fault core than process (1), promoting the formation of faults that locally have a strong core surrounded by a relatively weaker damage zone.

However, regardless of the level of strengthening that the fault core locally reaches by cementation, the total strength of a fault (considering its entire internal structure) will be reduced

or weakened by the aforementioned combination of processes. Because the failure of the fault will be controlled by the strength of the weaker component. So, the action of a hydrothermal system related to a porphyry copper deposit during the development of a fault system should be considered to weaken the faults, decreasing their capacity to accumulate stress.

III.4. CONCLUSION

- The black faults in RT were formed by shear strain acting along banded quartz (and molybdenum) veins, after the fluid pressure was reduced and hydrofracturing ceased. All the faults are adjacent to quartz veins or contain fragments of quartz veins in their cores. In contrast, not all the veins are faulted, and some non-sheared quartz veins are found in the mine walls. The distribution and microstructures of minerals indicate that the hydrothermal system was channelled by faults since the onset of phyllic alteration.
- Hydrolytic destruction of feldspar is the main effect of the hydrothermal fluids on the rocks in RT around the faults. Plagioclase is fully replaced by clay, both in the cores and haloes of faults. In turn, K-feldspar is still preserved in the fault haloes (damage zone) but is fully replaced by clay in the fault cores and in the blocks of damage zone trapped by gouge layers.
- Fluids that caused phyllic alteration have been channelled by fractures along the quartz veins, weakening the rocks around them, and enhancing deformation and fault development. This created more permeable channels and increased the mineralogical alteration in a positive feedback between alteration fluids and brittle deformation processes.
- Fault cores are characterized by frictional wear and comminution, but also by the abundant precipitation of minerals, mainly quartz and pyrite, in contrast to the mineral haloes in the damage zone. This precipitation tends to cement the faults cores and recover their cohesion, probably strengthening them with respect to their previous states, and possibly even with respect to the surrounding rocks.
- Although fault cores tend to be strengthened by precipitation, the total strength of the fault is at the same time weakened, since the hydrothermal fluids also replace most of the feldspar with clay, in surrounding the damage zones.

III.5. REFERENCES

Arancibia G., Fujita K., Hoshino K., Mitchell T., Cembrano J., Gomila R., Morata D., Faulkner D. & Rempe M. (2014) Hydrothermal alteration in an exhumed crustal fault zone: Testing geochemical mobility in the Caleta Coloso Fault, Atacama Fault System, Northern Chile. Tectonophysics 623, 147-168

Bos, B. & Spiers, C. J. (2002). Frictional-viscous flow of phyllosilicate-bearing fault rock: Microphysical model and implications for crustal strength profiles. Journal of Geophysical Research: Solid Earth 107(B2), ECV 1-1-ECV 1-13.

Braathen, A., Tveranger, J., Fossen, H., Skar, T., Cardozo, N., Semshaug, S. E., Bastesen, E. & Sverdrup, E. (2009). Fault facies and its application to sandstone reservoirs. AAPG Bulletin 93(7), 891-917.

Briceno, C. & Rubio, X. (2012). Caracterización y Distribución de Arcillas en el yacimiento Radomiro Tomic y sus Implicancias en Procesos Metalúrgicos. In: VIII Congreso Geologico Chileno (edited by departamentoo de Ciencias Geologicas, U. C. d. N.), Antofagasta.

Caine, J. S., Evans, J. P. & Forster, C. B. (1996). Fault zone architecture and permeability structure. Geology 24(11), 1025-1028.

Carrasco, M., Skarmeta, J., (2007). Informe Modelo Estructural Radomiro Tomic: Fase I. Reporte Interno. Codelco, Calama, 51p.

Carrasco, M., Skarmeta, J., (2009). Informe Modelo Estructural Radomiro Tomic: Fase II, Reporte Interno. Codelco, Calama, 34p.

Charrier, R., Pinto, L. & Rodrigues, M. (2007). Tectonostratigraphic evolution of the Andean Orogen in Chile. In: The Geology of Chile (edited by Moreno, T. & Gibbons, W.). The Geological Society, London, 21–114.

Cheary, R. W. & Coelho, A. (1992). A fundamental parameters approach to X-ray line-profile fitting.

Chester, F. M. & Chester, J. S. (1998). Ultracataclasite structure and friction processes of the Punchbowl fault, San Andreas system, California. Tectonophysics 295, 199-221.

Chester, F. M., Chester, J. S., Kirschner, D. L., Schulz, S. E. & Evans, J. P. (2004). Structure of large-displacement, strike-slip fault zones in the brittle continental crust. In: Rheology and deformation in the Lithosphere at Continental Margins (edited by Karner, G. D., Taylor, B., Driscoll, N. W. & Kohlstedt, D. L.). Columbia Univ. Press, New York.

Chester, F. M., Evans, J. P. & Biegel, R. L. (1993). Internal Structure and Weakening Mechanisms of the San-Andreas Fault. Journal of Geophysical Research-Solid Earth 98(B1), 771-786.

Cuadra, P. & Rojas, G. (2001). Oxide Mineralization at the Radomiro Tomic Porphyry Copper deposit, Northern Chile. Economic Geology 96(2), 387-400.

Cuadra, P., Zentilli, M. P., A. & Tidy, E. (1997). Dataciones radiometricas recientes en Radomiro Tomic. In: VIII Congreso Geologico Chileno Antofagasta.

Curewitz, D. & Karson, J. A. (1997). Structural settings of hydrothermal outflow: Fracture permeability maintained by fault propagation and interaction. Journal of Volcanology and Geothermal Research 79(34), 149-168.

Diaz, J., Boric, R. & Riquelme, R. (2009). Geologia de los sulfuros de Radomiro Tomic (RT), Nuevos Antecedentes. In: XII Congreso Geologico Chileno, Santiago.

Dilles, J.H., Tomlinson, H., Garcia, M. & Alcota, H., (2011). The geology of the Fortuna Granodiorite Complex, Chuquicamata district, Northern Chile: relation to porphyry copper deposits. SGA (2011).

Dolejs, D. & Wagner, T. (2007). Thermodynamic modelling of non-ideal mineral–fluid equilibria in the system Si–Al–Fe–Mg–Ca–Na–K–H–O–Cl at elevated temperatures and pressures: Implications for hydrothermal mass transfer in granitic rocks. *Geochimica and Cosmochimica Acta.* 72(2), 526-553

Eisenlohr, B. N., Groves, D. & Partington, G. A. (1989). Crustal-scale shear zones and their significance to Archaean gold mineralization in Western Australia. Mineralium deposita 24(1), 1-8.

Evans, J. P. & Chester, F. M. (1995). Fluid-rock interaction in faults of the San Andreas system: Inferences from San Gabriel fault rock geochemistry and microstructures. Journal of Geophysical Research: Solid Earth 100(B7), 13007-13020.

Faulkner, D. R., Lewis, A. C. & Rutter, E. H. (2003). On the internal structure and mechanics of large strike-slip fault zones: field observations of the Carboneras fault in southeastern Spain. Tectonophysics 367(3-4), 235-251.

Farina, F., Andrea, D., Innocenti, F., Roschi, S. & Westerman, D. (2010). Rapid incremental assembly of the Monte Capanne pluton (Elba Island, Tuscany) by downward stacking of magma sheets. GSA Bulletin 122(9/10), 1463-1479. Doi: 10.1130/B30112.1.

Fournier, R. O. (1999). Hydrothermal processes related to movement of fluid from plastic into brittle rock in the magmatic-epithermal environment. Economic Geology 94(8), 1193-1211.

Goddard, J. V. & Evans, J. P. (1995). Chemical changes and fluid-rock interaction in faults of crystalline thrust sheets, northwestern Wyoming, U.S.A. Journal of Structural Geology 17(4), 533-547.

Gratier, J. P., & Gueydan, F. (2007). Effect of Fracturing and Fluid–Rock Interaction on Seismic Cycles. *Tectonic Faults: Agents of Change on a Dynamic Earth*, *95*, 319e356.

Hemley, J. J., Jones, W. R. (1964). Chemical aspects of hydrothermal alteration with emphasis on hydrogen metasomatism. *Economic Geology*, 59 (4): 538–569.

Hoffmann-Rothe, A., Kukowsky, N., Dresen, D., Helmut, E., Oncken, O., Jurgen, K., Scheuber, E. & Kellner, A. (2006). Oblique Convergence along the Chilean Margin: Partitioning, Margin-Parallel Faulting and Force Interaction at the Plate Interface. In: The Andes: Active Subduction Orogeny (edited by Oncken, O., Gotze, H., Chong, G., Ramos, V., Franz, G., Strecker, M., Giese, P. & Wigger, P.). Springer London, Limited.

ICDD. (2010). PDF-4+ 2010 (Database) (edited by Kabekkodu, S.). International Centre for Diffraction Data, Newtown Square, PA, USA

Janssen, C., Hoffmann-Rothe, A., Tauber, S. & Wilke, H. (2002). Internal structure of the Precordilleran fault system (Chile) - insights from structural and geophysical observations. Journal of Structural Geology 24(1), 123-143.

Janssen, C., Lüders, V. & Hoffmann-Rothe, A. (2004). Contrasting styles of fluid-rock interaction within the West Fissure Zone in northern Chile. Geological Society, London, Special Publications 224(1), 141-160.

Jensen, E., Cembrano, J., Faulkner, D., Veloso, E., Arancibia, G., (2011). development of a self-similar strike-slip duplex system in the Atacama Fault system, Chile. Journal of Structural Geology. 33, 1611–1626.

Kim, CM., Han, R., Jeong, G.Y. Jonh, OJ., Moon, S., (2016): Internal structure and materials of the Yangsan fault, Bogyeongsa area, Pohang, South Korea. Geoscience Journal., 20(6), 759-773. DOI 10.1007/s12303-016-0019-8

Lindsay, D., Zentilli, M. & Rojas, J. (1995). Evolution of an Active Ductile to Brittle Shear System Controlling Mineralization at the Chuquicamata Porphyry Copper deposit, Northern Chile. International Geology Review 37, 14.

López, D. L. & Smith, L. (1996). Fluid flow in fault zones: Influence of hydraulic anisotropy and heterogeneity on the fluid flow and heat transfer regime. Water Resources Research 32(10), 3227-3235.

Maksaev, V. & Zentilli, M. (1999). Fission track thermochronology of the Domeyko Cordillera, northern Chile: Implications for Andead tectonics and porphyry copper metallogenesis. Exploration and Mining Geology, Special Issue on Latin American Mineral deposits 6, 24.

Maksaev, V. (1978). Cuadrangulo Chitigua y sector oriental del Cuadrangulo Cerro Palpana, Region de Antofagasta. In: Carta Geologica de Chile escala 1:50000. Instituto de Investigaciones Geologicas, Santiago, Chile.

Meunier, A. (2005). Clays. (book) Springer.

Mitchell, T. M. & Faulkner, D. R. (2009). The nature and origin of off-fault damage surrounding strike-slip fault zones with a wide range of displacements: A field study from the Atacama fault system, northern Chile. Journal of Structural Geology 31(8), 802-816.

Moore, D. M. & Reynolds, R. C. (1989). X-ray Diffraction and the Identification and Analysis of Clay Minerals. Oxford University Press (OUP).

Ossandon, G., Freraut, R., Gustafson, L. B., Lindsay, D. D. & Zentilli, M. (2001). Geology of the Chuquicamata Mine: A Progress Report. Economic Geology 96(2), 249-270.

Reutter, K.-J., Scheuber, E., Chong, G. (1996). The Precordilleran fault system of Chuquicamata, Northern Chile: evidence for reversals along arc-parallel strike-slip faults. Tectonophysics 259(13), 213-228.

Smith, S., Bistacchi, A., Mitchell, T., Mittempergher S., Di Toro, G. (2013). The structure of an exhumed intraplate seismogenic fault in crystalline basement, Tectonophysics, Vol. 599, 29-44. https://doi.org/10.1016/j.tecto.(2013).03.031.

Schulz, S. E. & Evans, J. P. (1998). Spatial variability in microscopic deformation and composition of the Punchbowl fault, southern California: implications for mechanisms, fluid-rock interaction, and fault morphology. Tectonophysics 295(1-2), 223-244.

Sibson, R. H. (1977). Fault rocks and fault mechanisms. J. Geol. Soc. London 133, 22.

Sillitoe, R. H. (2010). Porphyry Copper Systems. Economic Geology 105, 38.

Utada, M. (1980). Hydrothermal alterations related to igneous activity in Cretaceous and Neogene formations of Japan. Mining Geol., Spec. Issue 8, 67-83.

Weis, P., Driesner, T., & Heinrich, C. A. (2012). Porphyry-copper ore shells form at stable pressure-temperature fronts within dynamic fluid plumes. Science, 338(6114), 1613-1616.

Wibberley, C. A. J. & Shimamoto, T. (2003). Internal structure and permeability of major strike-slip fault zones: The Median Tectonic Line in Mie Prefecture, Southwest Japan. Journal of Structural Geology 25(1), 59-78.

Wintsch, R. P., Christoffersen, R. & Kronenberg, A. K. (1995). Fluid-rock reaction weakening of fault zones. Journal of Geophysical Research: Solid Earth 100(B7), 13021-13032.

Woodcock, N., Omma, J. & Dickson, J. (2006). Chaotic breccia along the dent Fault, NW England: implosion or collapse of a fault void? Journal of the Geological Society 2006; v. 163; p. 431-446. Doi: 10.1144/0016-764905-067

Yang, J.-H., Wu, F.-Y. & Wilde, S. A. (2003). A review of the geodynamic setting of large-scale Late Mesozoic gold mineralization in the North China Craton: an association with lithospheric thinning. Ore Geology Reviews 23(3-4), 125-152.

Zapettini, E., Godeas, M., Seggiaro, R., Korzeniewski, L., Ribiolo, D., Miranda, V., Uribe, H. & Heuschmidt, B. (2001). Mapa metalogenico de la region fronteriza entre Argentina, Bolivia, Chile y Peru [14°S-28°S]. Servicio Nacional de Geología y Minería.

III.6. SUPPLEMENTARY INFORMATION

In this document we support complementary data to support the petrographic descriptions given in the main text of this article. This data consists of microscopic descriptions, tables, and microphotographs. Furthermore, a brief explanation of the methods used is given in texts S1 and S2.

Text S1: (Methodology) Identification of Minerals with X-Ray Diffraction:

All XRD analysis were conducted in the "Laboratorio de Difracción de Rayos X" of the "Universidad Católica del Norte, Antofagasta" with an Automated Siemens D5000 Diffractometer, using a vertical Bragg-Bretano Goniometer and a X-Ray generator tube of copper emitting radiation of Cu Ka1 (l = 1,5406 Å) of 40Kv. Two different procedures of sample preparation and scanning were carried out, designed for targeting different mineral-groups: "Whole-Rock Mineralogy" and "Clay Mineralogy".

Whole-Rock Mineralogy XRD procedure was aimed to identify and quantify the concentration of major mineral components (>1% volume), however, this method also provides the concentration of minor components (0.3-1% vol.) as a secondary product. The rock samples were first crushed into a motorized jaw-crusher down to 6mm and then pulverized in a tungsten carbide ring-and-puck grinder. The resultant powder was sieved in a 270 Tyler mesh, from which the coarser part was ground again with an agate mortar and pestle until grain size <54 microns (270 Tyler mesh). The final powder was put into a cylindrical sample holder and rotated with coarse-polished glass to randomize the crystal orientation. The mounted samples were scanned with the diffractometer from 3 to 70° (2θ), in 0.02° steps of 1 second to obtain diffractograms. Mineral species were identified and quantified fitting the diffractograms to standard profiles from the ICDD database (ICDD 2010), using Fundamental Parameters Approach (Cheary & Coelho; 1992) in the DIFFRACplus TOPAS software.

Clay Mineralogy XRD Identification procedure is designed for the identification of minerals on the phyllosilicate group. depending on their cohesion the rock samples were first jaw-crushed or hand-crushed and then submerged in triple distilled water in order to disperse it. After strong stirring and 15 minutes of ultrasonic bath, this water turned into a small-particle suspension (<sand size), composed of any particle able float for some seconds in the distilled water, that was extracted for its use. In order to decrease high ionic content of the aqueous phase, the extracted suspensions were consecutively centrifuged at maximum speed for 10 minutes, drained and refilled with water, until obtain a "clean suspension". Then, in order to keep only clay-size particles, the suspensions were separated by decantation, extracting subsamples at constant depth/time after stirring following the Stokes Law. Sodium hexametaphosphate or "Calgon-S" was used as dispersant agent in this separation. The final "clay-size suspension" was concentrated by

centrifugation and poured over a glass slide. Finally, the slides were dried at 40°C, resulting in a thin clay rich layer with platy crystals oriented parallel to the surface, called "Oriented Aggregate Mount". The Oriented Aggregate Mounts were scanned in the diffractometer within a range from 2 to 34° (2θ), in 0.02° steps of 0.3 second. The clay species were identified following the procedure of glycolation and observation of shape, distribution and intensity of basal (00l) reflection peaks (Moore & Reynolds 1989).

ROCK UNIT	SAMPLE	FAULT ZONE	SPECIMEN	Quartz *SiO2*	K-Feldpar *KAlSi3O8*	Plagioclase *NaAlSi3O8*	QZ+FLDS
Site RT1							
PROTOLITH	0610RT1.1	Protolith	D-9	36,12	32,13	21,50	**89,75**
QUARTZ VEIN	0610RT1.1	Core	D-8	99,40	0,00	0,00	**99,40**
CLAY ALTERED GRANIT	0610RT1.2	Damage Zone	D-7	34,64	32,94	0,00	**67,58**
BLACK GOUGE/CATCLASITE	0710RT1.6	Core	D-10	51,76	0,00	0,00	**51,76**
BLACK GOUGE/CATCLASITE	0810RT1.8	Core	D-12	50,42	0,00	0,00	**50,42**
PYRITE BRECCIA	0710RT1.7	Core	D-11	36,44	0,00	0,00	**36,44**
Site RT2							
BLACK GOUGE/CATCLASITE	0710RT2.2	Core	D-14	46,06	0,00	0,00	**46,06**
WHITE PROTOCATACLISTE	0710RT2.1	Damage Zone	D-13	50,84	0,00	0,00	**50,84**
QUARTZ VEIN	0710RT2.4	Core	D-15	92,96	0,00	0,00	**92,96**
WHITE PROTOCATACLISTE	0810RT2.6	Damage Zone	D-16	81,35	0,00	0,00	**81,35**
PROTOLITH	0710RT2.3	Proto+	D-17	28,06	26,76	26,38	**81,20**

Table S2. XRD % volume of Rock Forming Minerals. Only the quartz and feldspar part of the *Total XRD Table* (Tabla VII-1) is shown here.

ROCK UNIT	SAMPLE	FAULT ZONE	SPECIMEN	Illite-2M1 *(K,H3O)Al2Si3 AlO10(OH)2*	Muscovite-2M1 *KAl2(Si3Al)O10(OH,F)2*	Kaolinite-1A *Al2Si2O5(OH)4*	Smectite-18A *Na0.3(AlMg)2Si4O 10OH2·6H2O*	Saponite-15A *Ca0.2Mg3(Si,Al)4 O10(OH)2·4H2O*	Nontronite-15A *Ca0.1Fe2(Si,Al)4O10 (OH)2·4H2O*	TOTAL CLAY
Site RT1										
PROTOLITH	0610RT1.1	Protolith	D-9	6,84	0,00	1,37	0,00	0,00	0,00	**8,21**
QUARTZ VEIN	0610RT1.1	Core	D-8	0,00	0,00	0,00	0,00	0,00	0,00	**0,00**
CLAY ALTERED GRANIT	0610RT1.2	Damage Zone	D-7	14,02	0,00	18,27	0,00	0,00	0,00	**32,29**
BLACK GOUGE/CATCLASITE	0710RT1.6	Core	D-10	9,40	0,00	13,16	0,00	0,00	0,66	**23,22**
BLACK GOUGE/CATCLASITE	0810RT1.8	Core	D-12	12,79	0,00	29,28	0,00	0,00	0,00	**42,07**
PYRITE BRECCIA	0710RT1.7	Core	D-11	28,87	0,00	6,23	0,85	0,00	0,00	**35,95**
Site RT2										
BLACK GOUGE/CATCLASITE	0710RT2.2	Core	D-14	16,82	0,00	21,13	0,00	0,80	0,00	**38,75**
WHITE PROTOCATACLISTE	0710RT2.1	Damage Zone	D-13	29,78	0,00	17,69	0,00	0,00	0,00	**47,47**
QUARTZ VEIN	0710RT2.4	Core	D-15	0,00	0,00	0,00	0,00	0,00	0,00	**0,00**
WHITE PROTOCATACLISTE	0810RT2.6	Damage Zone	D-16	0,00	14,24	0,00	0,00	0,00	0,00	**14,24**
PROTOLITH	0710RT2.3	Proto+	D-17	12,18	0,00	6,92	0,00	0,00	0,00	**19,10**

Table S3. XRD % volume of Clay Minerals. From *Total XRD Table* (Tabla VII-1).

ROCK UNIT	SAMPLE	FAULT ZONE	SPECIMEN	Biotite-2M1 *KMg3(Si3Al)O1 0(OH)2*	Pyrite *FeS2*	Chalcopyrite *CuFeS2*	Digenite *Cu9S5*	Chalcosine *Cu2S*	Molibdenite *MoS2*	Coveline *CuS*	TOTAL SULPHIDES
Site RT1											
PROTOLITH	0610RT1.1	Protolith	D-9	1,38	0,00	0,00	0,00	0,00	0,00	0,00	**0,00**
QUARTZ VEIN	0610RT1.1	Core	D-8	0,00	0,00	0,00	0,00	0,60	0,00	0,00	**0,60**
CLAY ALTERED GRANIT	0610RT1.2	Damage Zone	D-7	0,00	0,00	0,00	0,13	0,00	0,00	0,00	**0,13**
BLACK GOUGE/CATCLASITE	0710RT1.6	Core	D-10	0,00	10,28	0,00	0,31	0,00	0,25	0,00	**10,84**
BLACK GOUGE/CATCLASITE	0810RT1.8	Core	D-12	0,00	3,41	1,19	0,00	0,00	0,10	0,00	**4,70**
PYRITE BRECCIA	0710RT1.7	Core	D-11	0,00	18,62	0,00	0,00	0,00	0,00	0,00	**18,62**
Site RT2											
BLACK GOUGE/CATCLASITE	0710RT2.2	Core	D-14	0,00	3,30	0,00	2,60	0,00	0,00	0,30	**6,20**
WHITE PROTOCATACLISTE	0710RT2.1	Damage Zone	D-13	0,00	0,00	0,00	0,00	0,00	0,00	0,00	**0,00**
QUARTZ VEIN	0710RT2.4	Core	D-15	0,00	1,58	0,00	0,00	0,00	1,18	0,00	**2,76**
WHITE PROTOCATACLISTE	0810RT2.6	Damage Zone	D-16	0,00	0,66	0,00	0,00	0,00	0,00	0,00	**0,66**
PROTOLITH	0710RT2.3	Proto+	D-17	0,00	0,00	0,00	0,00	0,00	0,00	0,00	**0,00**

Table S4. XRD % volume of Sulphide Minerals. Part of the *Total XRD Table* (Tabla VII-1).

ROCK UNIT	SAMPLE	INTERNAL STRUCTURE	XRD SPECIMEN	Pyrite *FeS2*	Chalcopyrite *CuFeS2*	Digenite *Cu9S5*	Chalcosine *Cu2S*	Molibdenite *MoS2*	Coveline *CuS*	TOTAL SULPHIDES
	Site RT1									
PROTOLITH	0610RT1.1	Protolith	D-9	0.00	0.00	0.00	0.00	0.00	0.00	**0.00**
QUARTZ VEIN	0610RT1.1	Core	D-8	0.00	0.00	0.00	0.60	0.00	0.00	**0.60**
CLAY ALTERED GRANIT	0610RT1.2	Damage Zone	D-7	0.00	0.00	0.13	0.00	0.00	0.00	**0.13**
BLACK GOUGE/CATACLASITE	0710RT1.6	Core	D-10	10.30	0.00	0.30	0.00	0.30	0.00	**10.90**
BLACK GOUGE/CATACLASITE	0810RT1.8	Core	D-12	3.40	1.20	0.00	0.00	0.40	0.00	**5.00**
PYRITE BRECCIA	0710RT1.7	Core	D-11	18.62	0.00	0.00	0.00	0.00	0.00	**18.62**
	Site RT2									
BLACK GOUGE/CATACLASITE	0710RT2.2	Core	D-14	3.30	0.00	2.60	0.00	0.00	0.30	**6.20**
WHITE PROTOCATACLISTE	0710RT2.1	Damage Zone	D-13	0.00	0.00	0.00	0.00	0.00	0.00	**0.00**
QUARTZ VEIN	0710RT2.4	Core	D-15	1.58	0.00	0.00	0.00	1.18	0.00	**2.76**
WHITE PROTOCATACLASITE	0810RT2.6	Damage Zone	D-16	0.66	0.00	0.00	0.00	0.00	0.00	**0.66**
PROTOLITH	0710RT2.3	Protolith	D-17	0.00	0.00	0.00	0.00	0.00	0.00	**0.00**

Table S5. XRD % volume of Oxide and Sulphate Minerals. Part of the *Total XRD Table (*Tabla VII-1*)*.

Text S2: (Methodology) Microscopic Petrographic descriptions

In order to recognize mineral assemblages and crystallographic textures to deduce petrographic processes during the faults life-time; 11 thin sections were analysed under optical microscope (reflected and transmitted light).

The microscopic petrography of the Rock Units is based on the systematic description of each mayor mineral. describing their mineral size, distribution, shape, orientation, intra-crystalline structure (extinction pattern) and crystal boundaries. (detailed results in Table S6). Complementary, one sample of Black Cataclasite was analysed also under a scanning electronic microscope and optical cathode-luminescence microscope. The SEM was used to observe fabric of fine grain matrix, and the O-CL to identify quartz precipitation from fragment dissolution.

Text S3. (Data) Micro-petrography of the main components of Granitic Protolith:

QUARTZ: Is between 25 and 40 % volume, present in the groundmass and phenocrysts. (1) In the groundmass, there are several quartz crystals of a wide range of sizes (10 to 400 microns) and range of crystallinity (from euhedral crystals with triple points to anhedral) distributed around the phenocrysts. (2) Quartz phenocrysts are anhedral, 1-5mm size and with well-developed subgrains. The subgrains have very irregular boundaries with bulges and triple points, suggesting dynamic and static recrystallization.

K-FELDSPAR is in amounts between 25 and 35% volume, present in the groundmass and phenocrysts. (1) In the groundmass, k-feldspar crystals are from 50 to 250 microns size, monocrystalline and showing homogeneous extinction (no sub-grains). (2) K-feldspar phenocrysts are sub-tabular to anhedral, 2 mm to 3 cm size, also with homogeneous extinction without subgrains. Both at macro- and microscopic scale, these phenocrysts are enclosing euhedral crystals of quartz and plagioclase (*Figure S1, C and D*)

PLAGIOCLASE: Is between 20 and 30 % volume, as 0.5- 10 cm size tabular phenocrysts. Internally, they have polysynthetic twins and concentric zoning. In their outer most zones, smaller euhedral crystals of quartz are enclosed by the plagioclase.

CLAY: Is between 5 and 20 % volume. Homogenously distributed within the feldspars (mainly in plagioclase) and in <0.5 mm thin veinlets. Clay Mineralogy XRD analysis identifies it as Illite and kaolinite. The clay crystals are 10 - 50 mm sheets with undulose extinction forming radial patterns.

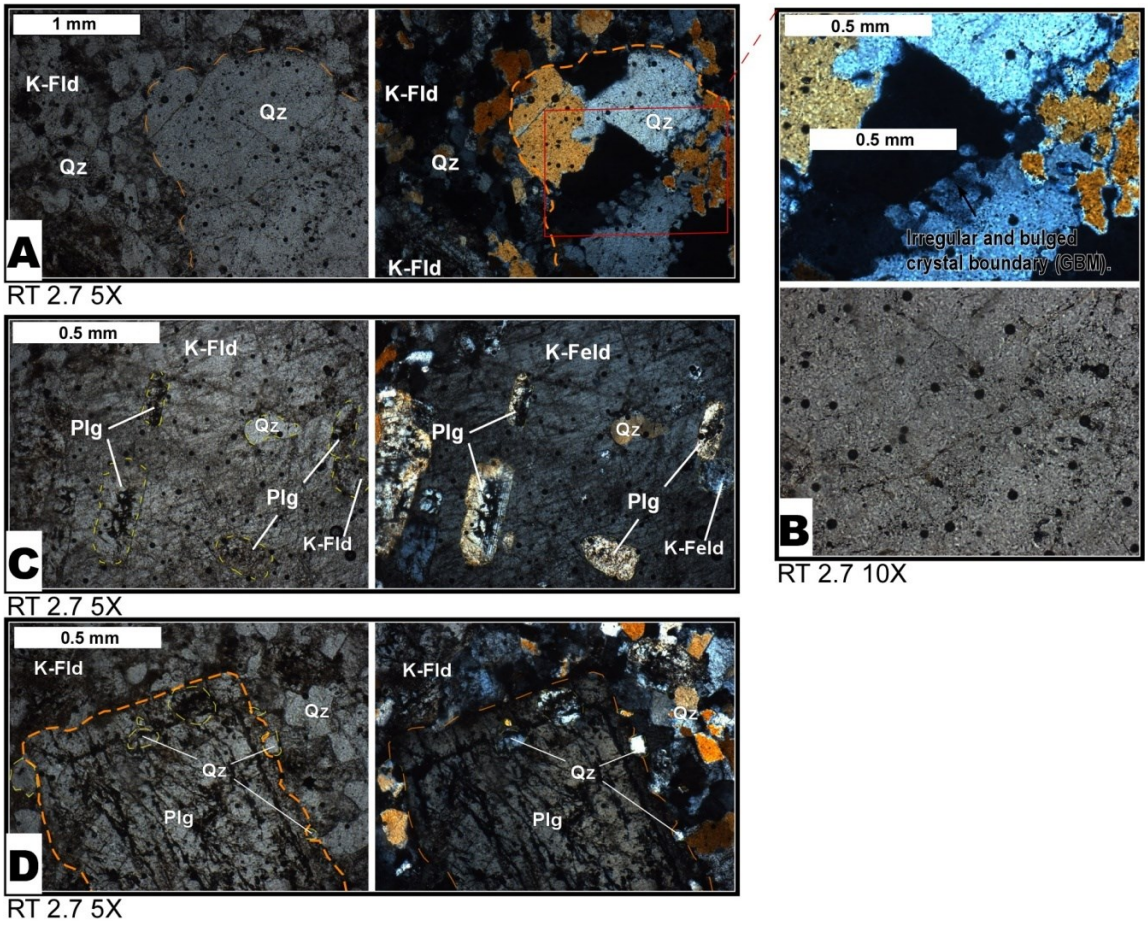

Figure S 1. Optical microphotographs of the granitic Protolith (polished thin sections).
All pictures are presented in pairs: with and without crossed polar. A: (5x) Quartz phenocryst (boundaries highlighted with orange segmented line) surrounded by smaller groundmass composed of Qtz + K-Feld. B: (10X) Zoom inset in image A, shows the sub-grains within quartz phenocryst. C: (5X) K-Feldspar phenocryst, slightly replaced by clay, enclosing smaller crystals of plagioclase and quartz. (highlighted with yellow segmented line) D: (5X) Zoned plagioclase phenocryst, enclosing quartz crystals in its outermost zone. Surrounded by a Qtz + K-Feld groundmass

Text S4. (Data) Micro-petrography of the main components of Clay Altered Granite:

QUARTZ: Is between 30 and 40 % volume, present in the groundmass and as phenocrysts. (1) Similar to its protolith, quartz crystals in the groundmass have a wide range of sizes, but a bit larger (20 to 700 microns) and a wide range of crystallinity (from euhedral crystals with triple points to anhedral with irregular boundaries). (2) Quartz phenocrysts, are equal to the protolith: Anhedral, 1-5mm size and well-developed sub-grains.

K-FELDSPAR: Is between 25 and 35% volume, present in the groundmass and the phenocrysts. (1) In the groundmass, the crystals are anhedral, 200 microns to 1 mm size (one order of magnitude larger than the protolith) and have well developed sub-grains, with very irregular (bulged) boundaries suggesting dynamic recrystallization (*Figure S2, B*). and (2), the phenocrysts are identical to the protolith in size and shape but altered to clay.

CLAY: Is between 25 and 35 % volume, replacing feldspars in different degrees. Clay Mineralogy XRD analysis identifies it as Illite and kaolinite. (1) Plagioclase phenocrysts are completely replaced by clay forming tabular pseudomorphs of massive clay, 0.5 to 10 mm size. (1) Clay within the K feldspar crystals is very fine (10 -100 microns) and homogeneously distributed, giving a brown dirty aspect to the k-feldspar. (3) A smaller portion of the clays is also distributed within thin veinlets crossing quartz and feldspar.

METALLIC SUPHIDES: Less than 1% vol. Pyrite > chalcocite > digenite are mainly in veinlets and filling intercrystalline spaces. Pyrite is also in patches of fine-grained aggregates with massive clay.

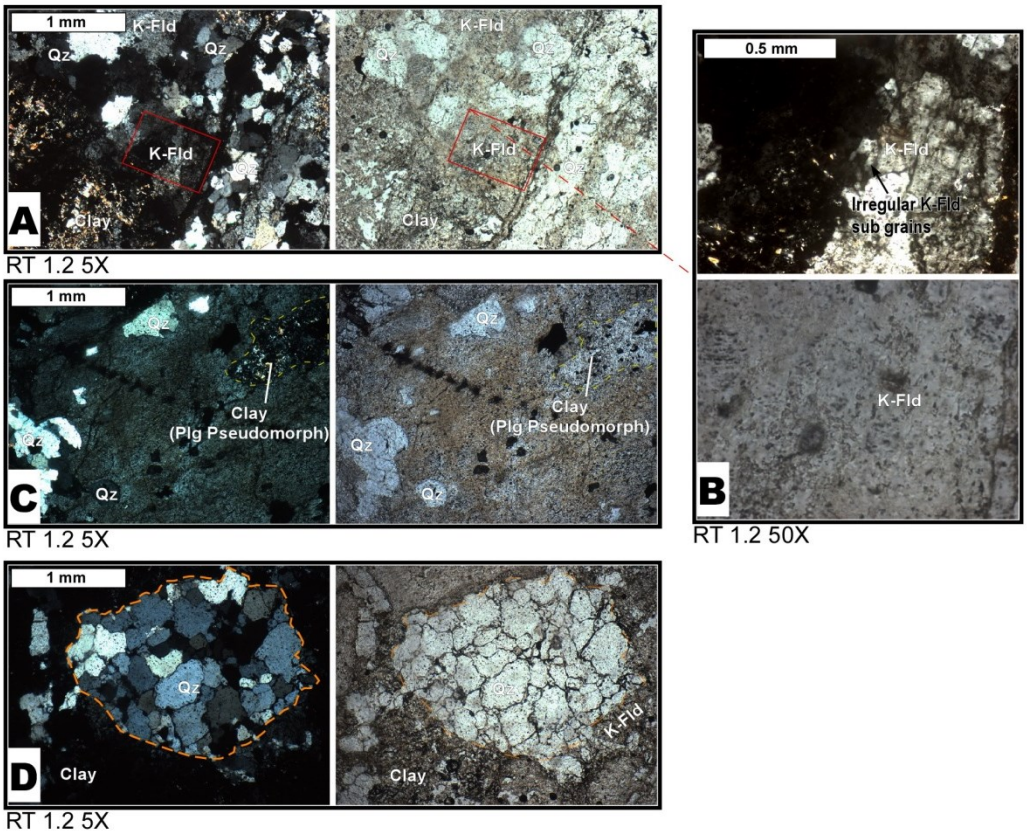

Figure S 2. Optical microphotographs of Clay Altered Granite (polished thin sections).
All pictures are presented with and without crossed polar. A: (5x) Quartz + k-feldspar + clay assemblage in the groundmass. K-feldspar is altered to clay but still recognizable. B: (20x) Zoom to the k-feldspar showing ca. 0.1 mm sub-grains. C: (5x) Large k-feldspar phenocryst, partially altered to clay, enclosing a plagioclase pseudomorph (replaced by clay and pyrite). D: Anhedral quartz phenocryst showing well developed sub-grains, set on a groundmass made of clay + quartz + k-feldspar.

Text S5. (Data) Micro-petrography of the main components of White Protocataclasite:

QUARTZ: Is in amounts between 50 and 80 % volume. Macroscopically, very heterogeneously distributed in irregular translucent patches. When the weaker samples are dispersed in water, the resulting particles of quartz are very irregular up to 1cm size.

Microscopically, quartz is observed in three modes of occurrence: (1) In the groundmass, as several crystals of a wide range of sizes (10 microns - 1mm) and crystallinity (from euhedral crystals with triple points to anhedral sub-grains), distributed in very irregular patches (1 - 10cm). (2) Euhedral phenocrysts, 1-5mm size, with full developed sub grains. (3) In skeletal tabular structures mixed with clay (Feldspar replacement).

CLAY: Is in amounts between 15 and 50 % volume. According to Clay Mineral XRD analysis is a mix of illite, kaolinite and smectite. Macroscopically the clay can be observed as a dusty white powder, as pearly white patches and as translucent green tabular blocks. Microscopically, clay is observed in two modes of

occurrence (1) In the groundmass, as randomly oriented sheets (10 to 200 microns size) distributed in large (1-10cm) irregular zones with minor recrystallized quartz. (2) As pseudomorphs of phenocrysts, sub-tabular blocks (0.1-3cm size) of only randomly oriented sheets. (3) A minor portion of the clay is also distributed within thin veinlets (<10 microns thick) crosscutting the quartz in the groundmass.

PYRITE: Is in less than 1% vol. Mainly in macroscopic and microscopic veinlets (0.2-2mm thick). These veinlets have irregular shapes and are composed of several microscopic crystals of pyrite, plus some small amount of quartz. Pyrite is lowly deformed, with few fractures and no offsets.

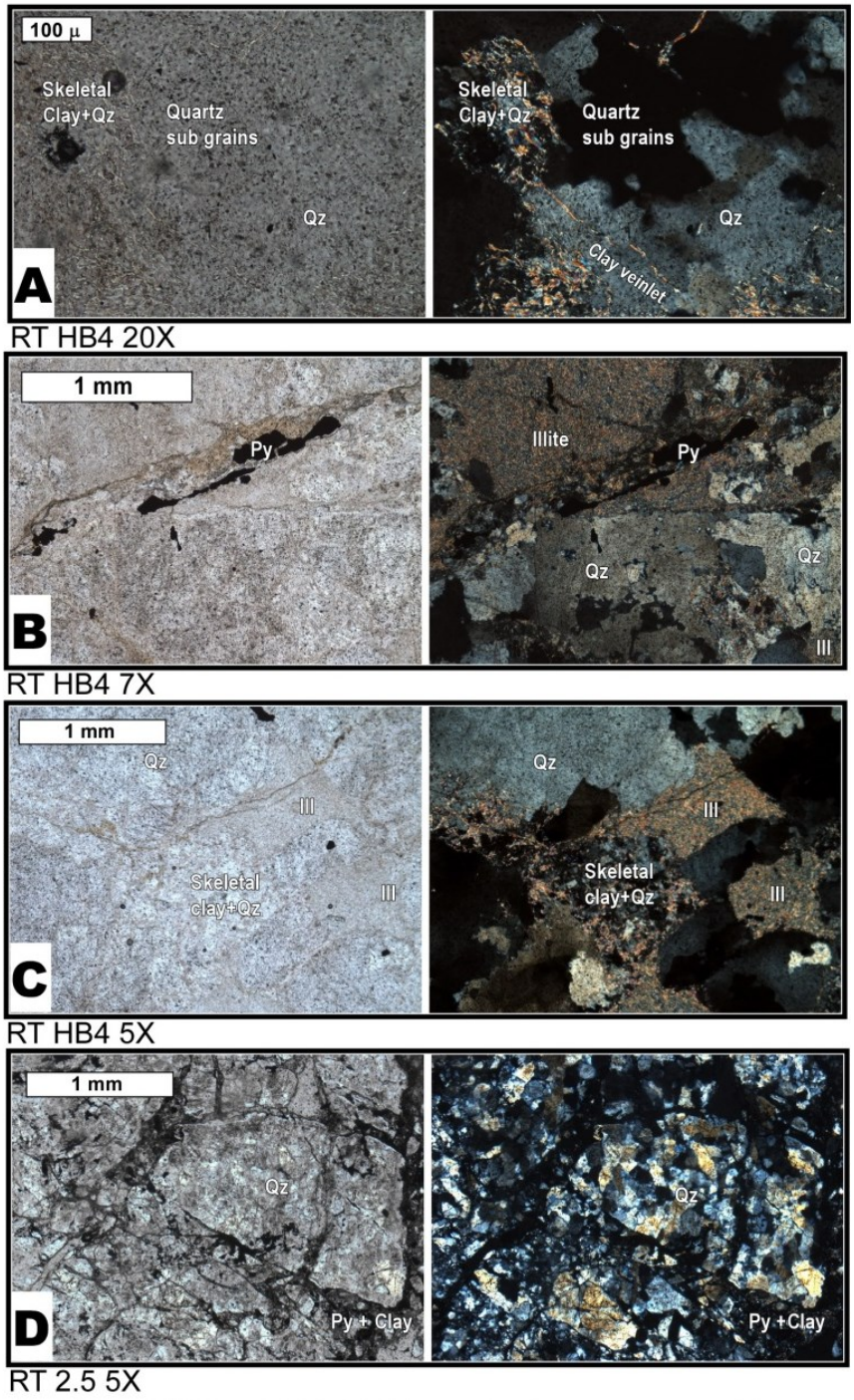

Figure S 3. Optical microphotographs of White Protocataclasite (polished thin sections).
All pictures are presented in pairs: with and without crossed polaroid. A: Texture of quartz and clays in quartz rich and low-shear zone. B: Pyrite + quartz + clay veinlet crossing massive illite and quartz. C: Tabular blocks of massive illite, quartz-illite assemblage and irregular quartz. D: Texture of a sheared zone of the protocataclasite. The fragment of quartz is surrounded by pyrite and clay matrix.

Text S6. (Data) Micro-petrography of the main components of Quartz Vein:

QUARTZ: Is distributed in tens of 1mm to 1cm parallel bands, formed by euhedral crystals elongated sub-perpendicular to the walls. The crystal size varies from 0.1 mm to 1 mm. Larger crystals show strong patchy extinction under crossed polar and several porphyritic.

Microscopically, fractures in the quartz are observed to be tensional and shear-tensional (< 1mm offset). Some of the fractures are crowded with rounded quartz sub-grains, suggesting fluid-aided crack healing (*Figure S4,* C). Also, spatially associated with fractures are the illite, pyrite and covellite.

PYRITE: Is up to 3% volume, as crystals up to 5 mm size. Mostly distributed along fractures and in poral spaces between euhedral quartz, but some of them (a trace amounts) are sub-microscopic (~1 micron) crystals disseminated in quartz crystals. Most crystals are fully anhedral (adopting the shape of the pore), however, some are only anhedral against the quartz and molybdenite, but euhedral against chalcocite and gypsum (*Figure S4*). Suggesting that pyrite is posterior to quartz and molybdenite, but previous to chalcocite and gypsum. Pyrite crystal show very low brittle deformation or fragmentation.

MOLYBDENITE: Is up to 2% volume, distributed along fractures and within intercrystalline spaces between euhedral quartz (*Figure S4,* B). Intercrystalline molybdenite is distributed in very irregular layers (millimetres thick, tens of centimetres long) parallel to the vein walls. Macroscopically, sub-horizontal striation is observed on molybdenite.

Molybdenite crystal are euhedral against all other minerals except quartz, indicating it is posterior to quartz, but previous to pyrite, chalcocite and gypsum).

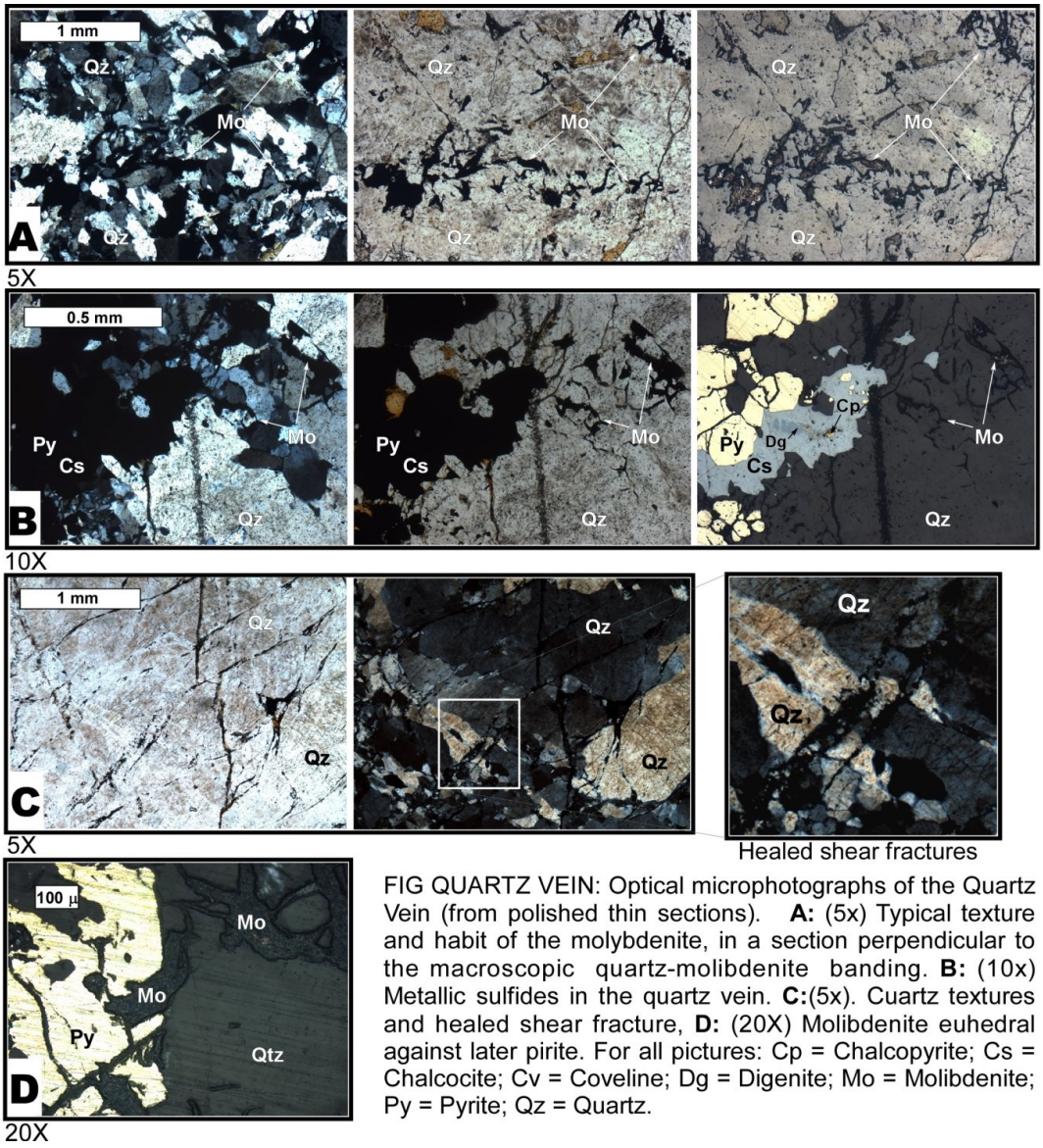

FIG QUARTZ VEIN: Optical microphotographs of the Quartz Vein (from polished thin sections). **A:** (5x) Typical texture and habit of the molybdenite, in a section perpendicular to the macroscopic quartz-molibdenite banding. **B:** (10x) Metallic sulfides in the quartz vein. **C:**(5x). Cuartz textures and healed shear fracture, **D:** (20X) Molibdenite euhedral against later pirite. For all pictures: Cp = Chalcopyrite; Cs = Chalcocite; Cv = Coveline; Dg = Digenite; Mo = Molibdenite; Py = Pyrite; Qz = Quartz.

Figure S 4. Optical microphotographs of Quartz Vein (polished thin sections).
A: (5x) Typical texture and habit of the molybdenite, in a section perpendicular to the macroscopic quartz-molybdenite banding. B: (10x) Metallic sulphides in the quartz vein. C: (5x). Quartz textures and healed shear fracture, D: (20X) Molybdenite euhedral against later pyrite. For all pictures: Cp = Chalcopyrite; Cs = Chalcocite; Cv = Covelline; Dg = Digenite; Mo = Molybdenite; Py = Pyrite; Qz = Quartz.

Text S7. Micro-petrography of the main components of Black Gouge/Cataclasite.

QUARTZ: Is 40- 50% vol. of the rock, distributed in three modes:

(1) The quartz porphyroclasts (0.1mm to 5cm size), have a milky white colour and are often accompanied by clay and pyrite. Under optical microscope two types are identified:

-Type I: Are angular to sub-angular polycrystalline fragments, exhibiting internal fabric varying from diffuse patchy extinction to sub-grains with clear boundaries. (*Figure S5*, B). Boundaries between the sub-grains are irregular and bulged, suggesting dynamic recrystallization.

-Type II: Are monocrystalline fragments, exhibiting continuous internal fabric (homogeneous with fast extinction). They are sub-rounded with serrated external boundaries, surrounded by bulges and several smaller fragments (*Figure S5*, D). Optical cathodoluminescence microscope reveals that the serrated boundaries are many smaller quartz fragments (bright pink) cemented to the large ones with newly formed (dark purple) quartz, forming aggregated colloids.

*Type I is more abundant and distributed in the darker portion of the cataclasites. In contrast, type II is less abundant and found in white fringes of cataclasite.

(2) Matrix quartz is distributed as small fragments (10-100 microns) with irregular to rounded shapes, surrounding larger fragments. Often, they are "welded" and macroscopically look like a single massive patch with irregular boundaries. They are monocrystalline (continuous extinction) and show very scarce internal deformation.

(3) Cementing quartz is only recognized under optical cathodoluminescence microscope, as a much darker quartz than the most abundant luminescent quartz. It is filling cracks (sealing), bounding other quartz fragments and growing as druses from the walls of the more luminescent quartz fragments (<20 microns crystals) (*Figure S5*, D).

CLAY: Is from 20% to 45% volume, distributed in the matrix and the porphyroclasts. Clay Mineralogy XRD analysis identifies it as kaolinite and illite with some traces of smectite

In the matrix clay is distributed as platy crystals (10 - 50 microns) oriented in foliations and in random aggregates. In the porphyroclasts, clays are filling cracks or in intercrystalline spaces.

PYRITE AND CHALCOPYIRITE: Are in amounts between 5 to 10 % volume. Pyrite is the most abundant (3% to 10% vol.), and chalcopyrite is minor (0-3% vol.). Microscopically both minerals are found in two ways: In quartz porphyroclasts and into the matrix. In the first, the occurrence of these minerals is in veinlets up to 1 mm thick. These veinlets are formed by multiple small (10 microns) euhedral crystals. In the matrix, they are in angular fragments roughly aligned along shear bands (<0.05 mm). These shear bands are both parallel and oblique (~30°) to the main shear plane, often growing from larger porphyroclast and, in times, forming asymmetrical patterns, similar to pressure shadows. (*Figure S5*, E)

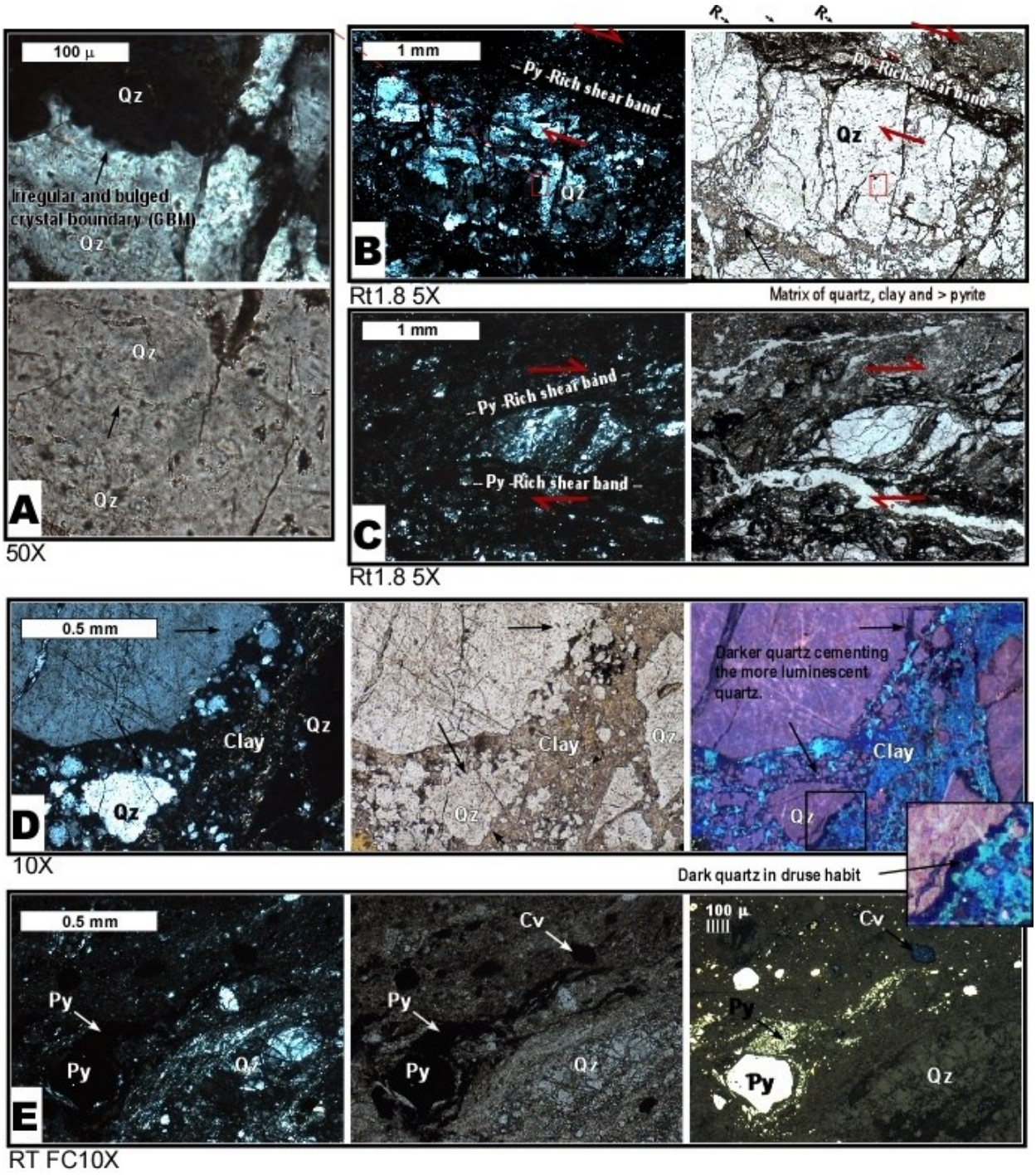

Figure S 5. Optical microphotographs of Black Cataclasite (polished thin sections).
All pictures are presented in pairs: with and without crossed polaroid. In addition, for D there is an extra optical cathode-luminescence image and for E there a reflected light image. A: (50x) Shape of the boundary between sub-grain within an heterogenous quartz porphyroclast ("Type I"). It is irregular and bulged, indicating crystal-plastic deformation (grain boundary migration). B: (5x) Heterogeneous ("Type I") quartz porphyroclast adjacent to a black shear band. The subgrains within the quartz porphyroclast indicate sub grain rotation. The shear band is composed of mainly sigmoid quartz and pyrite micro fragments. Secondary (smaller) shear bands are oriented in Riedel position. The thin section was made sub horizontal and indicates right-lateral shearing. C: (5x) Sigmoid shape quartz fragment from a small grain size and dark band of the

black gouge. The shape and thin-section orientation (sub-horizontal) indicate right lateral shearing. D: (10x) Very irregular homogeneous quartz fragment surrounded by clay+quartz, from a white band of the Black Gouge. Aggregated clusters of smaller fragments are observed with the crossed polaroid (left). The optical-CL image reveals two types of quartz: fragments of light pink quartz and darker blue quartz cementing them and growing in druse habit (inset). E: (10x) Larger pyrite crystal with an smaller grain pyrite halo with a pattern of pressure shadow. For all pictures: Cp = Chalcopyrite; Cs = Chalcocite; Cv = Covelline; Dg = Digenite; Il: Illite; Mo = Molybdenite; Py = Pyrite; Qz = Quartz.

Text S8. (Data) Micro-petrography of the main components of Pyrite Breccia

QUARTZ: Is between 40 and 50% volume, in fragments up to 1cm size and, in contrast to pyrite, it is equally abundant in the matrix and the porphyroclasts.

(1) Quartz porphyroclasts are 0.1 to 10 mm size, rounded to angular, both polycrystalline and monocrystalline and often very fractured (*Figure S6*, B). (2) In the matrix, quartz fragments are 0.01 to 0.1 size, rounded to sub-rounded and mainly monocrystalline (*Figure S6*, D).

CLAY: Is present in amounts between 30 and 40% volume, distributed in the matrix and the porphyroclasts. Clay Mineralogy XRD analysis identifies it as kaolinite + illite.

(1) In the matrix, is mixed with smallest quartz fragments, surrounding larger fragments of quartz and of pyrite. Platy crystals of clay are in general randomly oriented, but around larger fragments, they are slightly aligned parallel to the fragment boundaries.

(2) The clay porphyroclasts, consist of sub-tabular blocks (0.1-3cm size) composed of only randomly oriented sheets of crystals. Suggesting replacement of feldspar fragments in pseudomorphs.

PYRITE: Is present in amounts from 10% to 20% of volume, in the matrix and the porphyroclast. (1) In the porphyroclasts, pyrite is much more abundant than the matrix, as euhedral crystals and polycrystalline angular to sub-rounded fragments, 0.1 to 5 mm size. They are very fractured, some comminuted and gradually dispersed in the matrix and others cracked in situ forming jigsaw puzzle patterns (*Figure S6*, D). (2) In the matrix, pyrite is isotropically distributed (not in bands) in monocrystalline angular fragments.

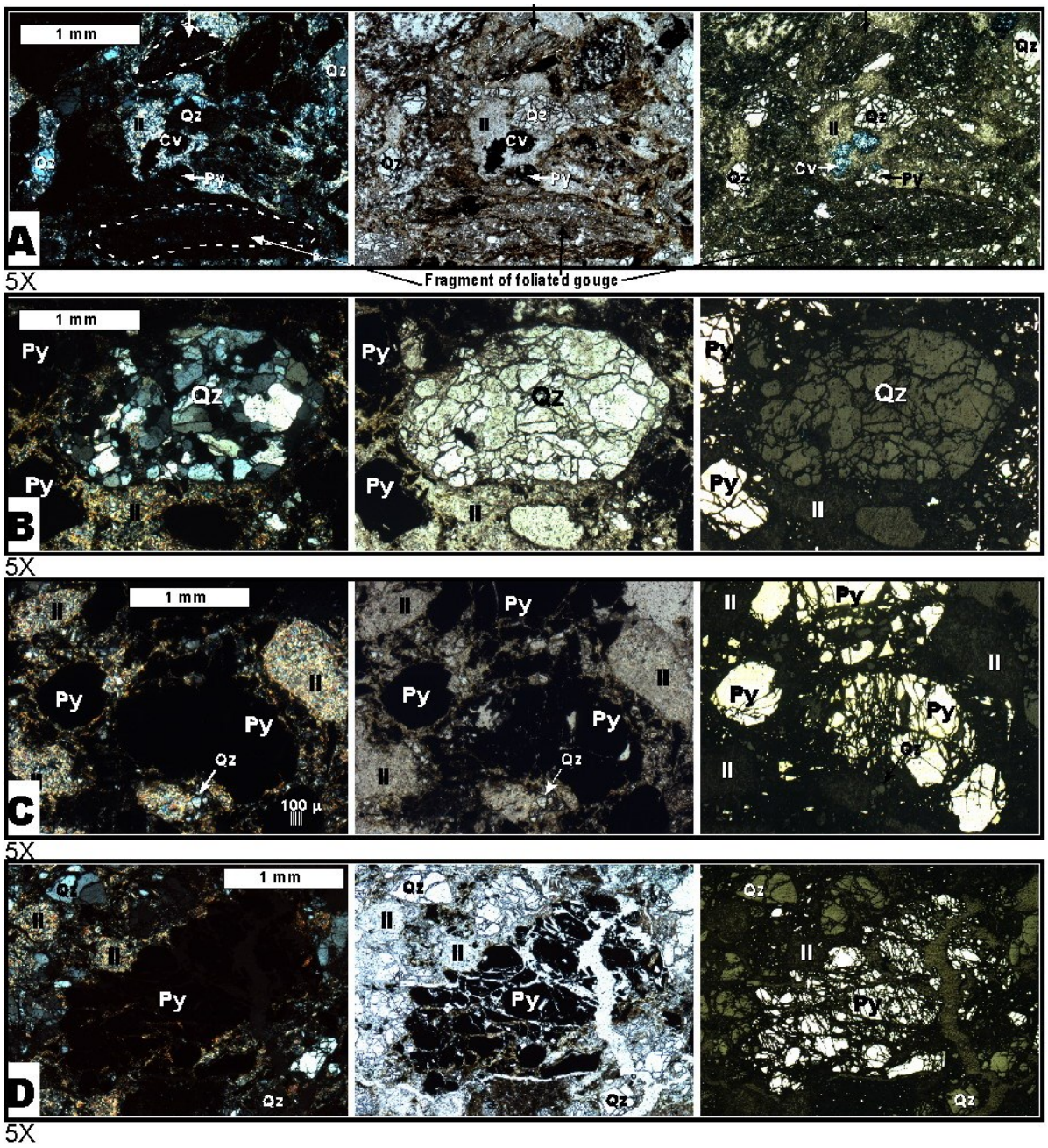

Figure S 6. Optical microphotographs of Pyrite Breccia (polished thin sections).
All presented in groups of three, from left to right: Transmitted polarized light with and without crossed polaroids and reflected polarized light. A: (5x) Zone of small grain-size, where fragments of pyrite and quartz are cemented by illite and some covellite (<1% vol.). Two porphyroclast of foliated gouge are highlighted with arrows. B:(5x) A large rounded porphyroclast of polycrystalline quartz (in the centre) and angular fragments of pyrite, surrounded by a randomly oriented clay matrix. C:(5x) Fragments of fractured pyrite, smaller fragments of homogenous quartz and blocks of illite. The rectangular blocks of fine crystals of illite (10-30 microns), suggest plagioclase replacement. D: (5x) Large fragment of pyrite destroyed by tensile fractures (dilatation) with no shear. For all pictures: Cp = Chalcopyrite; Cs = Chalcocite; Cv = Covellite; Dg = Digenite; Il = Illite; Mo = Molybdenite; Py = Pyrite; Qz = Quartz.

IV. QUANTIFYING THE MECANICAL EFFECTS OF HYDORTHERMAL ALTERATION ON THE FAULTS AND WALL ROCKS OF A PORPHYRY COPPER DEPOSIT

IV.1. INTRODUCTION

If the earth's crust were homogeneous and continuous, its brittle strength would be determined by the necessary stress to propagate cracks and bring it to failure. However, the crust holds important discontinuities called faults which control the crust's rheology by their frictional properties, when are favourably oriented (*e.g.:* Kohlstedt *et al.,* 1995; Townend & Zoback,, 2000).

In addition to be mechanical weaknesses, faults also provide first order control on the flow of fluids through the crust. Therefore, they commonly record a complex history of fluid-rock interaction with subsequent chemical and mineralogical changes (*e.g.:* Evans & Chester 1995; Goddard & Evans 1995; Schulz & Evans, 1998). Understanding such fluid-induced mineralogical changes is highly important for understanding the mechanical behaviour of the faults, hence of the crust. In this context, measuring the mechanical properties of fault-related rocks in structural systems mineralogically altered by hydrothermal fluids is fundamental for predicting the mechanical behaviour of the crust.

Research based in laboratory experiments conclude that the frictional properties of most abundant rocks in the crust commonly fall in the range between 0.65 and 0.8 (Byerlee 1978). However, those experiments also show that phyllosilicates minerals, less abundant in the crust but very common in faults, have much lower friction coefficient than most common rock-forming minerals (*i.e.:* quartz, feldspar, amphibole) and show a different response to the variations of pore pressure and sliding velocity (*e.g.:* Ikari *et al.,* 2011; Ikari *et al.,* 2009; Moore & Lockner 2004).

Here, to understand how hydrothermal fluids can change the mechanical behaviour of rocks and faults through their mineralogical modification, the mechanical properties of granitic rocks from a porphyry copper deposit are systematically measured. We selected this deposit as a study case because it exhibits strong spatial relation between alteration minerals and faults in granitic rock as a protolith, which is the most abundant type of rock in the earth´s crust. Furthermore, the location of the faults, within a large-scale hydrothermal deposit, makes it possible to unravel the relationship between faulting and hydrothermal activity. Finally, the open pit mining activity which

takes place in RT provides direct access to faults for sampling and mapping at deep structural levels, below the water table and away from the atmospheric weathering zone.

Direct shear and indirect tension ("Brazilian") tests were performed to measure the coefficient of friction, slip-rate dependence (earthquake stability) and the tensional strength on altered wall rocks and fault-core rocks. This strategy allows a quantitative estimation of the permanent changes of mechanical properties induced by hydrothermal alteration related to flow of fluids along faults (*i.e.* Increase of clay by hydrolysis of feldspars and precipitation of minerals in the core rocks).The quantification obtained in this way is intended to (1) Adjust numerical models of propagation of fractures based on Coulomb criteria (e.g.: Zhang et al., 2008; Jaeger and Cook; 1979). (2) Understand the seismogenic potential of fault systems hosting hydrothermal ore deposits. (3) Analyse stability of slopes and mine designs.

The samples used here were collected from Radomiro Tomic, a porphyry copper deposit operated by the Chilean state (CODELCO) as an open-pit mine, which was selected as case of study for exhibiting close relationships between faulting and mineral alteration. The alteration minerals in this deposit are mostly localized in haloes around the faults and veins, indicating that the fluids were channelled by faults. The alteration mineralogy of RT is relatively simple, in comparison with other porphyry deposits like Chuquicamata (its closest neighbour). Furthermore, RT has a single granitic protolith, relatively homogeneous and widely distributed at district scale, which keeps the research away from uncertainties about the original mineralogy.

We document the coefficient of friction and cohesion of a granitoid at 4 levels of hydrothermal alteration and a fault rock developed from it. The samples were selected for being formed from the same protolith and representing a progression in the mineralogical alteration induced by hydrothermal fluid circulation along faults and fractures. These relative stages of alteration were recognized in the field from changes in texture, relative hardness and colour, where the whitest and softest rocks represent the highest level of alteration. X-Ray Diffraction shows that the clay content in the samples increases with the increasing alteration level.

IV.2. GEOLOGICAL BACKGROUND

IV.2.1. Regional Tectonic Setting

RT is located in the Central Andes Forearc in a trench parallel fault system called Domeyko Fault System (it is also called Precordilleran Fault System, and here will be referred as DFS). DFS is composed of several traces passing along the axis of the Domeyko Range that can be traced

for more than six hundred kilometres. Both the range and fault-system were formed during the Incaic phase in the Eocene (Maksaev, 1978, Maksaev & Zentilli, 1999; Reutter *et. al* 1996)

This fault system has a very strong and important connection with hydrothermal fault-controlled fluid flow, as it is the host of the most important base metal deposits found in the Northern Chile that can be found all along his trace (e.g.: Hoffmann-Rothe *et al.,* 2006; Ossandon *et al.,* 2001; Zapettini *et al.,* 2001).

IV.2.2. Lithologic and Mineralogic Background

The RT Cu-deposit is hosted by a granodioritic to monzogranite intrusive rock with medium- to coarse-grained phenocrystals set in a fine grain groundmass, termed East Porphyry Unit (Cuadra & Rojas, 2001; Diaz *et al.,* 2009). Three hypogene hydrothermal events, altering the described protolith, have been documented in the literature (*e.g.*: Cuadra & Rojas, 2001; Diaz *et al.,* 2009):

1. An early “K-Silicate Alteration” or “Background Potassic Alteration”, which is widespread throughout all the deposit and is represented by biotite crystals replacing hornblende phenocrystals and by veinlets of quartz/K-feldspar (early A-type veinlets).
2. “Quartz/Sericite Alteration” overprints the early potassic alteration and is markedly spatially associated to sub-vertical faults. It is represented by distributed fine quartz (silicification) and Illite and it is distributed in haloes, around and between B-type quartz veins and black faults.
3. “Argillic Alteration” was the last to occur, imposed over both previous alteration zones and genetically related to ground water as it is represented by the abundance of clay minerals from the kaolinite and smectite groups. (Diaz *et al.,* 2009).

In the shallower part of the deposit (over *ca*. 2750 m.a.s.l.), argillic alteration minerals are mainly from the smectite group with some kaolinite bearing vertical bands. In the deeper part, in turn, clays are mainly from the kaolinite group. (Briceno & Rubio, 2012).

Because of the above-mentioned hydrothermal events, the deposit exhibits a marked vertical mineralogical anisotropy. However, in the uppermost 400 meters there is a leaching cap resulting from a later oxidation processes, called “supergene enrichment” (Cuadra & Rojas, 2001). This leaching cap is mainly given by the distribution and oxidation state of mobile elements and has been separated in two: Oxide Zone (Above) and Secondary Enrichment Zone (bellow). The Oxide Zone is divided in “Upper” and “Lower” according to the atacamite content and the Secondary Enrichment Zone, in turn, is divided in “Strong” and “Weak” according to the sulphide content.

In order to avoid heterogeneities caused by this horizontal anisotropy, the samples were taken only from the Weak Sulphide Secondary Enrichment Zone.

IV.2.3. The Black Faults

The structure of Radomiro Tomic mainly consists of subvertical fault-veins striking N30-60E. According to internal reports in Radomiro Tomic mine (Carrasco 2007), the largest faults (hundreds of meters long and tens of centimetres thick) of this system are the ones striking N30-40E, and the smaller and thinner trend N40-60E.

Petrographically, these faults are characterized by dark fault-cores of pyrite rich gouges (and cataclasites) surrounded by contrasting white haloes. Both cores and haloes have mineralogic compositions resulting from the hydrothermal alteration of the granitic host-rock. Such alteration processes are mainly (1) Hydrolysis, breaking down the feldspars (plagioclase and k-feldspar) into quartz + clay (kaolinite, illite and minor smectite) and (2) the addition of highly variable amounts of iron sulphide (mainly pyrite and chalcopyrite).

Clay content in the studied rocks is inversely proportional to the content of feldspars and they exhibit textural features suggesting replacement of feldspars in various stages of evolution. The most probable process capable to produce this progressive replacement is the hydrolysis of feldspars, which is expected to occur in any hydrothermal system, where its cooling destabilizes K+ and stabilizes H+ (Utada 1980). Detailed petrographic descriptions, maps and interpretations of the rocks related to the studied faults are provided in the previous chapter of the present thesis.

IV.3. EXPERIMENTAL METHODS

IV.3.1. Sample Selection (Definition of Alteration Levels)

As is discussed in detail in the previous chapter, for the case study, the main processes of causing mineralogical alteration by hydrothermal fluids are: (1) Hydrolysis of the feldspars, plagioclase (across the fault) and orthoclase (only in the fault core). (2) Precipitation of quartz and metallic sulphides, mainly in the fault core. Both are spatially related to faults and occurred after a homogenously distributed (not structurally controlled) potassic metasomatism. These two mineralogical reactions are expected to occur in all the porphyry cooper systems, changing the mechanical behaviour of the involved faults.

To quantify those mechanical changes, 4 samples of altered wall were selected in order to form a sequence that mineralogically represent 4 levels (AL) of a progressive process of hydrothermal alteration. They were selected from the samples petrographically described and mineralogically analysed in the previous chapter and are named AL1, AL2, AL3 and AL4 (**Figure IV-1).** Progressively, from 1 to 4, the samples have increasing amounts of kaolinite and Illite (% vol., measured with XRD), and decreasing amounts of feldspars.

With this strategy, we are dealing with the effects caused by argillic and quartz-sericitic alteration induced by hydrothermal fluids in faults. Potassic alteration is a pre-existing bulk alteration, not considered in the analysis.

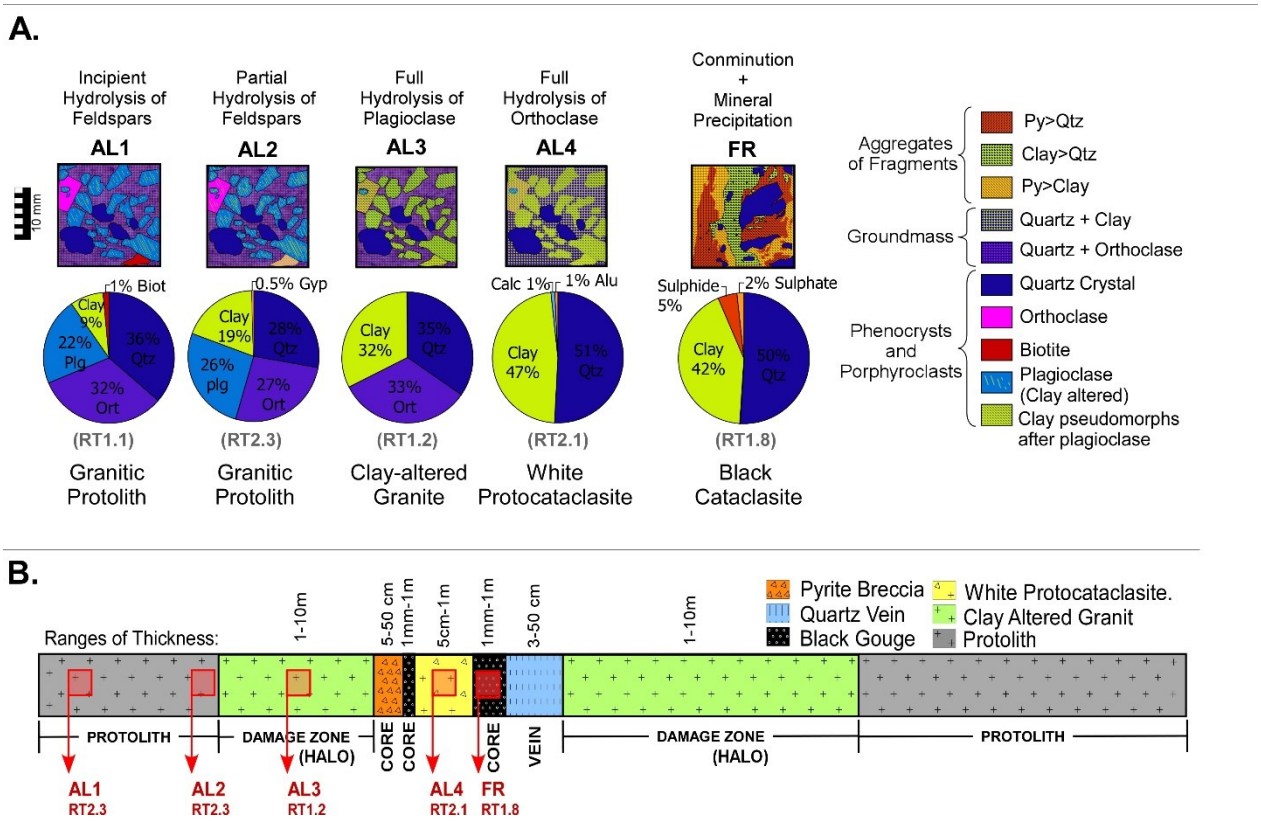

Figure IV-1. Alteration levels.

A. Schematic micromaps representing the most important petrographic features of the samples here selected to measure. The pie plots show the XRD mineralogy of each sample. The pie plots are taken from **Figure III-3**, **Figure III-4** of the previous chapter and data to made them is presented in **Tabla VII-1** (Anexos). Plg: Plagioclase, Qtz: Quartz, Clay: Kaolinite + Illite, Ort: Orthoclase, Biot: Biotite, Gyp: Gypsum, Calc: Calcite, Alu: Alunite, Sulphides: Sum of all metallic sulphides, Pyrite > Chalcopyrite > Molybdenite. Sulphate: Gypsum > Natroalunite.

B. Schematic cross-column representing the relative position of the samples with respect to the typical internal structure of the faults in the case of study**.**

AL1: Sample of granitic protolith (Labelled RT1.1). It is the least altered sample of wall rock collected in the mine. Composed of quartz (36%), orthoclase (32%) and plagioclase (22%), with a minor amount of clay (8%) and some biotite (1%). It is a compact rock and maintain its cohesion when it is submerged in water. 50- 60% of its volume consist of phenocryst of plagioclase, quartz and orthoclase (1 mm to 3 cm in size) which are set within a fine groundmass of quartz and orthoclase (0.01-0.4 mm size).

AL2: Sample of Granitic Protolith Unit with some alteration to clay, taken some centimetres out of the halo (Labelled RT2.3). It has a very similar mineral composition to the AL1 but with larger amounts of clay (19%) and no biotite. In both AL1 and AL2 the clays are found inside the plagioclase crystals and preferentially around quartz veinlets. At these alteration levels the rock is still not dispersible in water and scarce loss of material occurs when washed in water

AL3: Sample of Clay-Altered Granite unit, taken from a white halo (Labelled RT1.2). It has orthoclase but no plagioclase, instead, it exhibits a larger amount of clay (32%). This clay can also be found resembling plagioclase crystals (*i.e.* Pseudomorphism). At this alteration level, the rock is partially dispersible in water and a big loss of material occur when is washed (preventing wet coring but allowing particle size measuring).

AL4: Sample of white protocataclasite taken from a strongly altered block of rock wrapped around by 2 gouge layers (Labelled RT2.1). It is the most altered rock of the sequence and does not have any plagioclase nor orthoclase. It is composed mainly by clay (47%) and quartz (51%). Alunite also can be found in minor amounts (< 1%). At this level, the rock is extremely weak, and the original texture completely obliterated. This alteration level is closely related to faults and only found in lenses of fractured rock surrounded by fault rock.

None of the samples exhibit shear textures and all of them have some quartz veinlets of mm-scale thickness showing low shear strain (less than one mm offset per each cm of rock). So, the rock sequence represents the hydrolytic alteration of a granitic rock with low shear strain.

The whole-rock properties of their cylindric specimens (explained in section 3.2.1) will be used for understanding the potential evolution of the wall-rocks around faults. In turn, the frictional properties of the powder specimens obtained from the same samples will be used to represent the mechanical evolution of a hypothetical fault developing under hydrolytic alteration. In it this way, other mineralogical changes related to the fault-cores (associated with mineral precipitation) can be kept out of the analysis.

Furthermore, in order to also understand the mechanical changes induced by the accumulation of all the mineralogical processes that affected the fault-cores, a sample of black cataclasite was also used for lab testing. The mechanical properties of this sample provide insights

about the fault mechanics after the hydrolysis of the feldspars, the comminution by wear and the adhesion by silicification(See previous chapter of this thesis).

The fault-core sample **FR** (*i.e.* fault rock) is a black cataclasite, cohesive under dry conditions, but partially dispersible when submerged into water (80°C distilled water). Its cohesion is given by the quartz, pyrite and gypsum precipitated between fragments. The main mineralogical difference between this sample with the most altered wall rock (AL4) is the presence of metallic sulphides (*>5%* pyrite, chalcopyrite and trace molybdenite) and sulphates (*ca.* 1% gypsum and trace natroalunite).

IV.3.2. Whole-Rock Mechanical Properties

IV.3.2.1. Specimen Preparation

The specimens used for whole-rock mechanical properties were cylindrical pieces of rock, prepared by drilling, cutting and rectification of the less fractured pieces of each sample. Two types of cylindrical specimens were obtained: **Long Cylinders** (20 mm diameter and 35 to 56 mm length), made to perform Triaxial and Uniaxial Tests, identified with “LC” in their specimen names. **Flat Cylinders** or “rock coins” (20 mm diameter and 4 to 9 mm length), made to perform Brazilian Tests (indirect tension) and Porosity Tests, identified with “FC” in their specimen names.

In order to avoid influence of the specimen shape in the strength measurements, also called “*l/d effect*” (Hawkes & Mellor, 1970; Paterson, 2005) the Long Cylinders were prepared with length/diameter > 2.5 . The Flat Cylinders were prepared with length to diameter ratios between 0.2 and 0.75, according to the ASTM standard for tests of indirect tensile strength (ASTM, 2016). After cutting the samples with these dimensions, they were squared in a rotational grinding machine to a strict tolerance of ±0.02 mm. The number of long cylinders that were possible to obtain from each sample, is related their resistance to be drilled. From sample AL1, 5 specimens were obtained; from AL2, 3 specimens, from AL3, 1 specimen and from AL4, zero specimen.

IV.3.2.2. Porosity

Porosity was measured to get a quantitative value of the textural properties of the measured samples. Flat cylinders specimens were used to measure the sample porosity. This value was calculated from the net specimen volume provided by a pycnometer. This device provides the net volume of the specimen measuring the pressure of an inert gas (helium) that is injected into a

camera of known volume, which is containing the specimen. The difference between this “net volume” and their “total specimen volume” (volume of the cylinder) correspond to the porosity of the sample.

IV.3.2.3. Brazilian (indirect tension) and Uniaxial Compressive Tests

These experiments were performed to measure the whole rock mechanical properties of naturally altered rocks. Both types of tests were performed in the same standard steel frame, equipped with a manually controlled air pump to compress the specimens between a rigid plate and a moving piston. Axial force was measured with a load cell which was constantly sending raw data to a data logger connected to a recording laptop. The raw consist in analogue values in millivolts (mV), that were corrected to digital values (also mV) adding 0.6. Then the digital values (mV) were converted or calibrated to Force values (kN), applying empirically obtained conversion (multiplying by 2.94). This Force values must be “zeroed” subtracting the background value, which is measured as an average of the pre-load values.

To determine both indirect tensile strength (brazilian test) and uniaxial strength, the maximum pre-failure or “Ultimate Force” value is recorded (kN). To convert this force into a material strength (MPa) equations based on the specimen are applied: For Brazilian Test (Indirect Tension) the equation 1 and for Uniaxial Compressive Test the equation 2.

$$\text{Tensile Strength} = (2 * \text{Ultimate Force}) / (\pi * \text{Diameter} * \text{Length}) \quad \text{(Eq. 1)}$$

$$\text{Uniaxial Strength} = (\text{Ultimate Force}) / (\text{Basal Area of the Cylinder}) \quad \text{(Eq. 2)}$$

IV.3.2.4. Triaxial Compressive Tests

The triaxial strength of the long cylinders was tested in a Triaxial deformation Apparatus designed and constructed in the Rock deformation Laboratory, University of Liverpool to achieve axisymmetric stress conditions (S1 > S2 = S3). It consists of a sealed cylindrical steel vessel that allows the application of hydrostatic confining pressure (S2 = S3) manually pumping silicon oil and automatically control it with a servo motor, connected in a feedback loop to a pressure gauge. The axial pressure (S1), in turn, is provided by means of a ball-screw piston driven by a gear train and another servo motor. The net axial force is measured by means of an internal force gauge (consisting of a cylindrical steel frame, of known elasticity, containing an internal LVDT device to

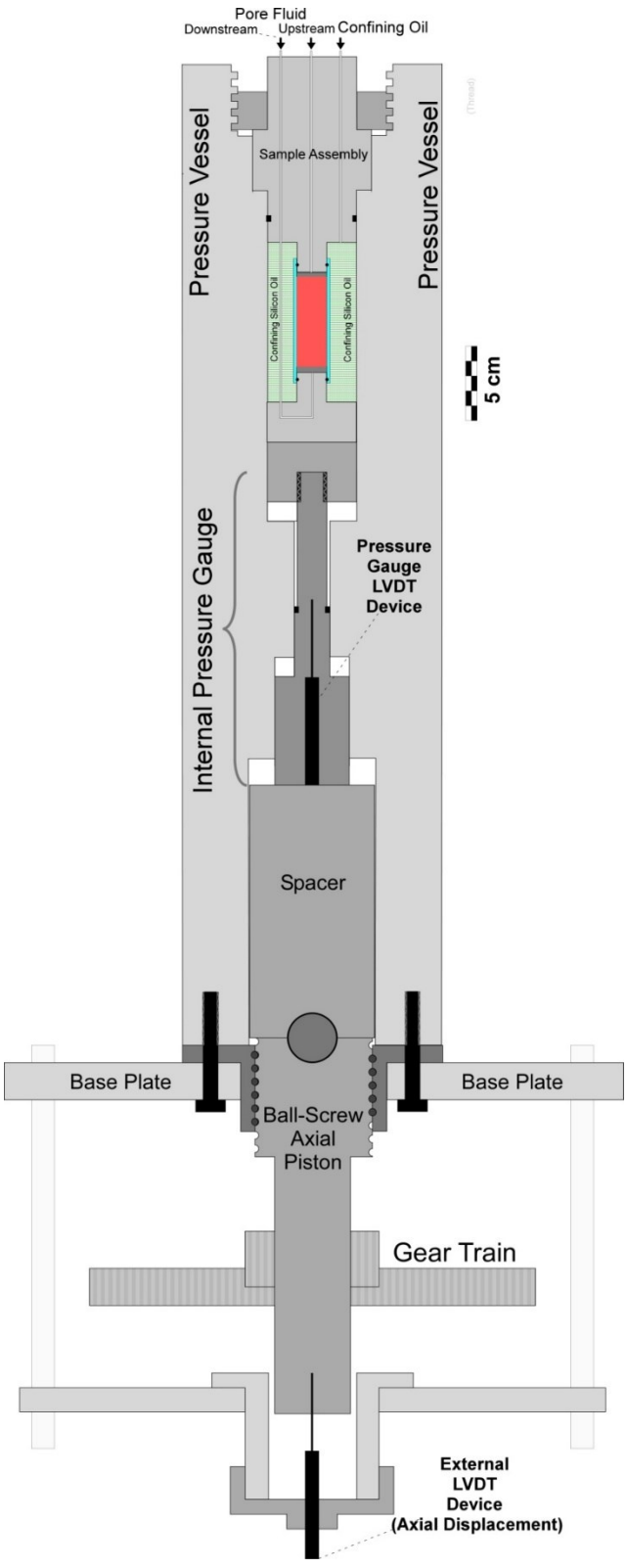

record its deformation) with accuracy of 0.1 kN, equivalent to 0.1 - 5% of the axial forces used in our tests. The axial displacement, in turn, is measured with an external LVDT device, fixed to the external rig frame and connected to the ball-screw piston. The pore fluid (deionized water) gets to the sample through a micrometric bore steel pipe and can be controlled whether by a servo pump or a manual wheel pump. A map of the apparatus is shown in **Figure IV-2**.

The procedure started by manually increasing the confining pressure, pumping in the silicon oil with an air compressor, and then the activation of the automated servo control (when the objective pressure was reached). Vacuum impregnation of specimens and pore fluid injection were not necessary, as the triaxial tests were performed in “dry” conditions. After confining pressure was set, the axial force was increased at a constant rate of 3.5 μm/s until failure. The maximum pre-failure force was then recorded (in kN), corrected (zeroed) subtracting the background force before hit-point and, finally, converted to Axial Stress (MPa) dividing the force by the basal area of the cylinder.

Figure IV-2. Triaxial Rig Map.
Sectional map of the Triaxial deformation Apparatus, used in this research. designed and built in the Rock deformation Laboratory, Liverpool. The red rectangle represents the space for the cylindrical specimens (triaxial test) or the sliding blocks (for direct shear test). The green area represents the confining medium (silicon oil).

IV.3.3. Frictional Properties

IV.3.3.1. Specimen preparation

Specimens for frictional experiments are gouges or “powders” with particle size < 150, keeping the mineralogy of their respective source samples. In order to perform the tests, the specimens are mounted as layers 1.3 (±.2) mm thick layers (i.e.: at least 8 particles across each layer). Considering the highly variable cohesive strength of the 5 samples, two different procedures were conducted to obtain the powders:

Hard samples, AL1 and AL2, are not dispersible in water. So, to prepare the powders specimens, the samples were directly ground down into a vibratory ring pulveriser machine. To avoid overgrinding, the softer minerals (while the harder and coarser particles are protected by the surrounding clay) the process was conducted in periods of 20 seconds. After each period, the < 150 µm part was kept and the coarser part was ground again. Until 98% weight of the particles were < 150 µm. The specimens prepared in this way have a synthetic granulometry but keep same mineralogy than the source sample, that is why they have the word “FULL” within the specimen name.

Dispersible samples, FR, AL3 and AL4, are clay rich (>30%) rocks, cohesive but dispersible in water. Then, in order to prepare specimens without modifying the granulometry, the samples were impregnated with distilled water in a vacuum chamber and dispersed combining agitation with a stirring rod and ultrasound bath. For the fault rock FR, hot water (ca. 80degC) was added to dissolve cementing minerals enhance the dispersion. When the dispersion was visually complete (*i.e.* most of the visible particles consist of single crystals or single fragment but not aggregates) their granulometry or statistical particle size distribution was measured. In order to do so, the dispersed material was separated into a fine and a coarse fraction (Limit: 62 µm). Coarse fraction was sieved in dry conditions, and the fine fraction was “sieved” under water measuring settling times. Following the classical sieve and pipette technique (Gee & Bauder, 1986).

After sieving, the fine fraction was dried under frozen conditions in a vacuum drying machine (“freeze drying”), in order to avoid slumping, hard crusts and heterogeneous sub-sampling. The wet samples were rapidly frozen with liquid nitrogen just after stirring, to overtake the gravitational settling and get a random particle size spatial distribution. Finally, in order to get powder specimens with a particle size <150 µm and, at the same time, keeping the mineralogy of the original sample, each coarse fraction was ground down to 150 µm (in 20 seconds periods) and

mixed with the freeze-dried fine fraction. The specimens prepared in this way have the word “MIX” in their names.

IV.3.3.2. Direct Shear in a Triaxial Apparatus

Direct shear tests were conducted to measure the frictional properties of the powder specimens, representing the evolution of a hypothetical fault progressively experiencing mineralogical alteration induced by hydrothermal fluids (mainly hydrolysis). In order to also measure how the hydrothermal alteration impacts in the potential of faults to propagate earthquakes, the rate dependence of friction was represented by means of the a-b parameter (Dieterich, 1979; Scholz, 1998).

These friction tests were performed in the same Triaxial Deformation Apparatus described above (**Figure IV-2**), however the cylindrical specimen of rock is replaced with two steel forcing blocks, to produce direct shear conditions, similar to the configuration used by . Powder specimens layer was compressed between the two steel blocks of steel, in a 69-configuration, covered with a 3.3 mm-thick jacket of flexible PVC. To fill the “deformation space” needed to slide the blocks, two 10mm-thick plugs of acetoxy silicone and two 0.5mm semi-circular PTFE layers were used (as shown in **Figure IV-3**¡Error! No se encuentra el origen de la referencia.). The layers had uncompacted thicknesses between 1.2 and 1.4 mm previous to the test, and final thickness between 0.9 and 1 mm, after the test were run.

The pore fluid is supplied into the sample trough 0.5 mm holes in the sliding area of each block that continue as conduits within the sliding blocks. These conduits were filled with bulk alumina fibre, to stop the sample to intrude. Above and below the blocks, two spacers of highly porous steel are placed to dissipate the fluid flow and to connect the pore fluid conduits during movement. Furthermore, two couples of PTFE shims (with their corresponding conduit slots) were used to reduce any friction between sample assembly and the sliding blocks during the tests. After each use, the sliding blocks and porous spacers were cleaned with an ultrasound bath of distilled water.

With this sample assembly, the “normal stress” is directly provided by the confining pressure, and it can be measured without the need of a continuum vector decomposition, as the classical oblique jigsaw blocks. The “shear stress”, in turn, is directly calculated by the axial force (load) divided by the sliding area. Which is initially 32mm x 20mm, and progressively increases during the test performance.

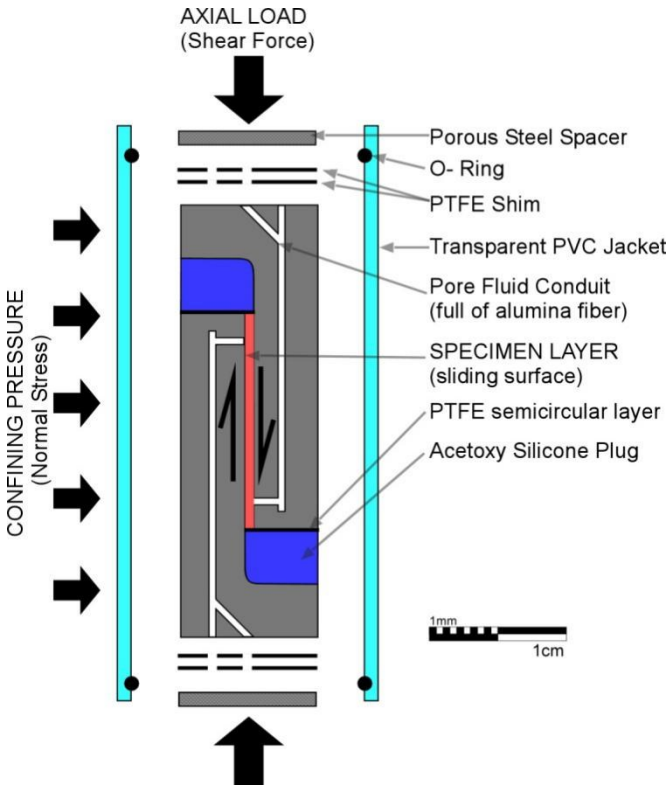

Figure IV-3. Sample assembly.
Longitudinal section showing the sliding blocks with a "69" configuration. The red layer represents the specimen (powder). The cyan layers represent a tubular PVC jacket, which is tightly fit around the sliders but separated only for the sketch. The dark blue silicone plugs and semi-circular PTFE layers are essential to keep the specimen from escaping to this space.

The friction tests were all performed at constant room temperature (*i.e.*: 23°C), at 4 different constant confining pressure: 60, 110, 160 and 210 MPa, saturated with water at a constant 10MPa pore pressure. These conditions correspond to 50, 100, 150 and 200 MPa of effective confining pressure and effective normal stress (in the sliding plane) and are equivalent to the effective pressures expected at 2.5 km, 5 km , 7.5 km and 10 km in depth, respectively.

To reach such conditions with success, a procedure of 3 stages was carried out before running each test: (1) Confining pressure was manually raised up to the target effective pressure (50, 100 or 150MPa). (2) Pore fluid pipes were connected, the pore fluid was manually pumped up in discrete steps of 1MPa, up to 10MPa and then automatically controlled by the computer (until the end of the test). (3) The confining pressure was automatically controlled by the servo motor, being gently raised up to 60, 110 or 160MPa (at a rate of 0.01MPa/s) (Moore and Lockner 2004). This procedure was conducted to keep the specimen in the proper position and avoid spreading it around the blocks. When the confining chamber was pressurised after the saturation of the gouge layer liquefaction and extrusion of the gouge occurred.

In order to analyse dependence of the dynamic friction to the slip rate, the axial piston was moved in 3 velocity steps during each test. The velocity of the piston (or slip-rate) was automatically controlled by the main servo motor, gear-train and external LVDT device. However, the velocity changes were executed manually, observing the distance from the hit-point (which

slightly vary for each test). The piston started away from the assembly, with a rate of 2 μm/s. The moment when it touches the assembly and started pushing it is called “Hit-Point” and is detected by an axial load increase. The slip rate was kept in 2 μm/s until approximately 1.5 mm after the hit-point (from here will be called “mm ahp”). At ca. 1.5mm ahp the rate was drastically reduced to 0.2 μm/s. At around 2.5 mm ahp the rate was increased back to 2 μm/s until 4 - 5 mm when the test is finished. The slip rates used here fall in the range of fault creeping during post seismic and interseismic periods (*e.g.*: Perfettini *et al*., 2004; Perfettini *et al*., 2010).

The dynamic coefficient of friction μ_d was then calculated dividing shear stress / effective normal stress and plotted against the slip distance after the hit point . For each test, the result is a friction curve similar to the ones shown in the **Figure IV-4**. Then, 3 values of μ_d were extracted from each curve, calculated as average in intervals of 50μm length to deal with the noise these are (the blue rectangles in **Figure IV-4**) which are:

μ_{4000}: Dynamic coefficient of friction at 2 μm/s, obtained at 4000 μm ahp, (*i.e*. 4mm of slip). Considering the initial thickness of the specimens, 1.3±.2 mm, this ahp distance corresponds to a shear strain between 3.6 and 3.6. However, considering their final thickness, after running the tests, 0.8 - 1 mm this distance corresponds shear strain 4 to 5.

μ_{SLOW} and **μ_{FAST}**: Dynamic coefficients of friction at 0.2 μm/s and 2 μm/s, respectively. The ahp distance at which each value is measured depends on the distance at which the acceleration was manually executed and on the distance of stabilization after the piston acceleration stated (when the curve reaches a steady state with constant slope). These two values are used to calculate the frictional stability of the specimens, using the friction rate parameter a – b (Dieterich, 1979; Scholz, 1998), defined as:

$$a - b = \Delta\mu_d / \ln(V/V_0) \qquad \text{(Eq. 3)}$$

$\Delta\mu_d$ is the change in coefficient of friction after reaching steady state (here, μ_{FAST} - μ_{SLOW}), upon an instantaneous change in sliding velocity, from Vo to V (0.2 and 2 μm/s, respectively) When the a – b parameter is positive the material is said to be “Velocity-strengthening” and considered to be seismically stable. When the parameter is negative, the material is said to be “Velocity-weakening” and is a requirement for the occurrence of unstable fault slip that result in earthquake nucleation (Dieterich, 1979; Marone, 1998; Scholz, 2002; Ikari, 2011).

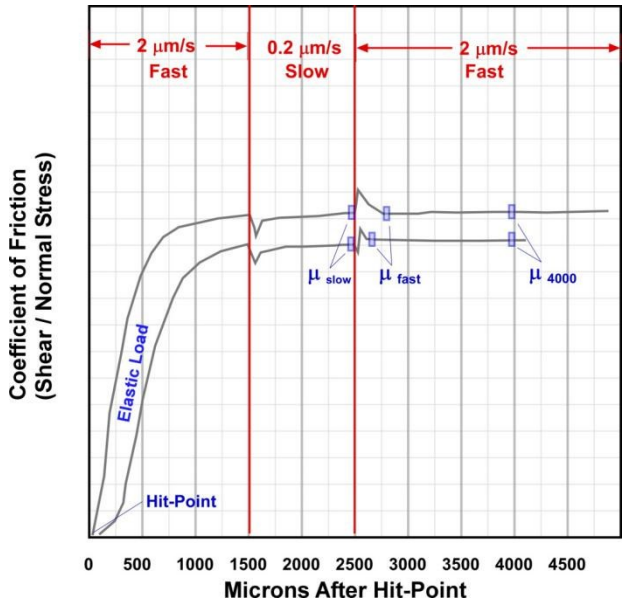

Figure IV-4. Frictional test curves.
Example of curves resulting from 2 frictional tests. Blue squares show the 50μm intervals where the 3 values of μ were obtained.

IV.4. EXPERIMENTAL RESULTS

IV.4.1. Tensile Strength and Porosity

The tensile strength values, obtained from the Brazilian tests performed on flat cylinder specimens, are summarized in the table 1 and **Figure IV-5**. To simplify, they are analysed in terms of their central tendency measures, mean (Avg) and standard deviation (Stdv) shown in the table 4.

In general, a strength reduction with the alteration level of alteration can be observed. The average values of T are reduced from AL1 to AL3, but the two most altered rocks (AL3 and AL4) show very similar average tensile strength (around 5 MPa). In turn, the cataclasite sample (FR) has a slightly larger mean value of tensile strength (6.23 MPa).

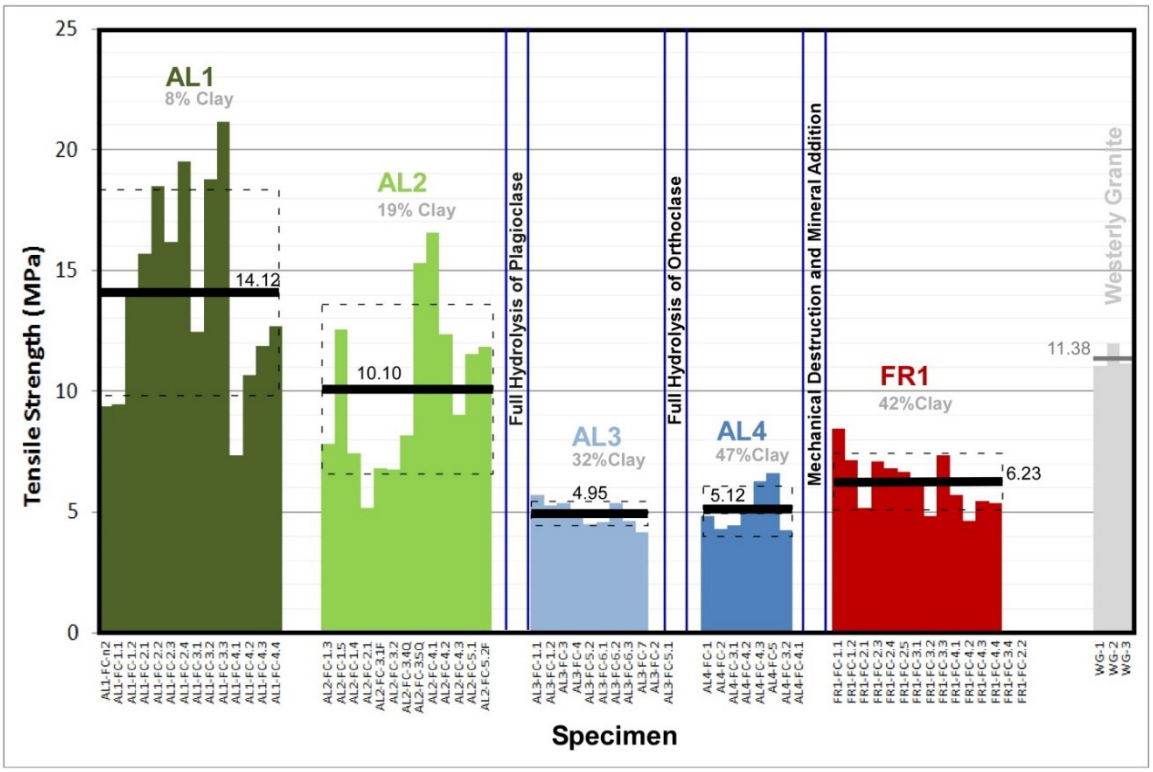

Figure IV-5. Histogram of tensile strength.
Histogram of tensile strength measured with the brazilian tests to the flat cylinder specimens. The source data is presented in the table S3 (Section IV.8 "SUPPLEMENTARY INFORMATION" of the Present Thesis). Black horizontal bars represent their average (mean) and the segmented squares their standard deviation, indicated in table 1. Westerly granite (in grey bars)

Tensile Strength (MPa)

	AVG	STDV	% Change
AL1	14.12	4.27	
AL2	10.10	3.51	-28%
AL3	4.95	0.51	-51%
AL4	5.12	0.95	3%
FR	6.23	1.14	22%

Table 1. Tensile strength. Central tendency values.
Average (Mean) value and standard deviation of the tensile strength data from flat cylinder specimens, presented in Table S3. The values in the column "% Change" are the proportional differences with respect to the previous sample

Porosity values measured with the pycnometer are summarized in the table 2 and **Figure** IV-6. They are analysed in terms of their central tendency measures: mean (Avg) and standard deviation (Stdv).

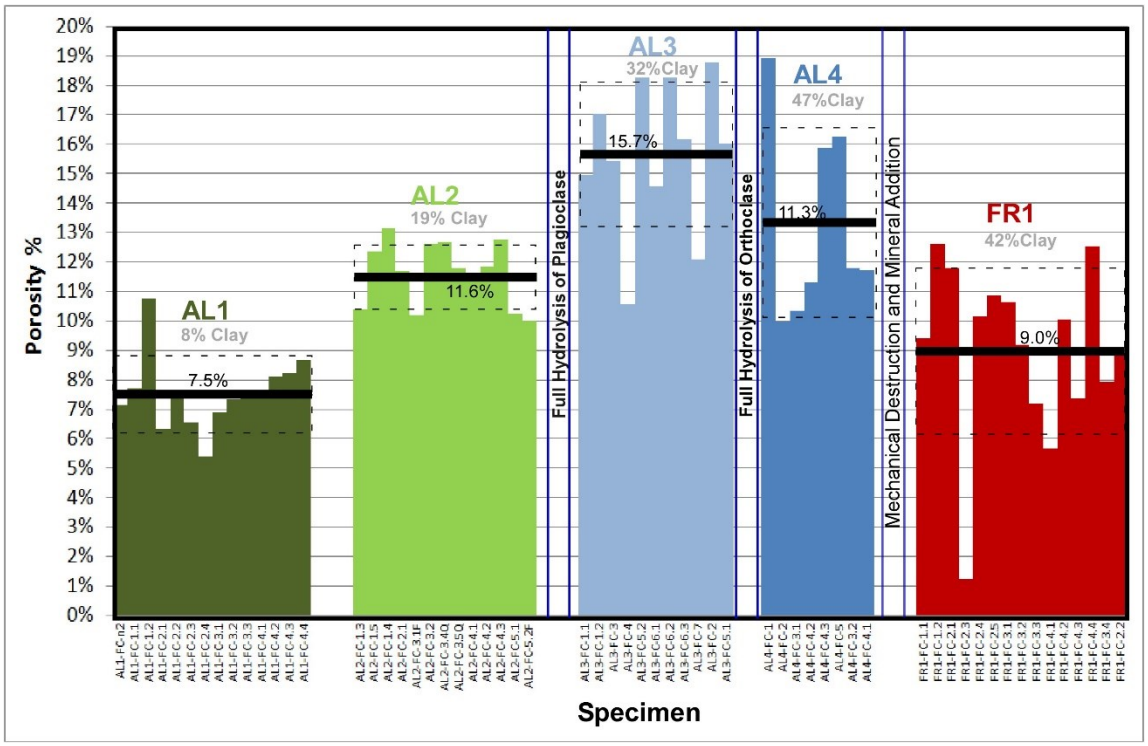

Figure IV-6. Histogram of porosity.
Histogram of porosity measured with the pycnometer to the Flat Cylinders Specimens. The source data is presented in the table S3. Black horizontal bars represent their average (mean) and the segmented squares

their standard deviation, indicated in table 2. Black horizontal bars represent their average, the segmented squares the standard deviation.

Porosity (Effective)

	AVG	STDV	% Change
AL1	7.5%	1.3%	
AL2	11.6%	1.1%	55%
AL3	15.7%	2.5%	35%
AL4	13.3%	3.3%	-15%
FR	9.0%	2.9%	-33%

Table 2. Tensile strength. Central tendency values.
Average (Mean) value and standard deviation of the porosity data from the flat cylinder specimens table S3 (Section IV.8 "Supplementary Information" of the Present Thesis). The values in the column"% Change" are the proportional differences with respect to the previous sample.

Similar to tensile strength, porosity show a correlation to the alteration level. In the firsts 3 levels (from AL1 to AL3) porosity increases with the progression of alteration. However, the most altered rock AL4 have a mean value (13.3%) slightly lower than the specimens of the previous level AL3 (15.7%), apparently reversing the correlation (**Figure IV-6**). However, considering the large scatter (standard deviation) found in those two samples (probably arising from the heterogeneity of the samples), they must be considered to have the same porosity. In contrast with the tensile strength, the fault rock shows a mean porosity lower than most of the specimens from the altered wall rock.

IV.4.2. Whole Rock Compressive Strength

The data obtained from uniaxial and triaxial compressive tests performed in this work is presented in the Table 1. Using these results, combined with the average values of cohesion (C), Mohr-Coulomb are estimated as a "best-fit" for AL1, AL2 and AL3 shown in **Figure IV-7**. The cohesion, C, was calculated from tensile strength, T, measured from brazilian tests, using the equation C = 2T (Griffith, 1921; Brace, 1960).

The internal friction "μ", correspond to the slope of the envelope of fracture, therefore it is a fracturing parameter. As the tensile strength, this parameter evidences strong weakening with increasing alteration level. Therefore, it is near twice as hard to propagate fractures in an AL1 rock than in an AL3 rock.

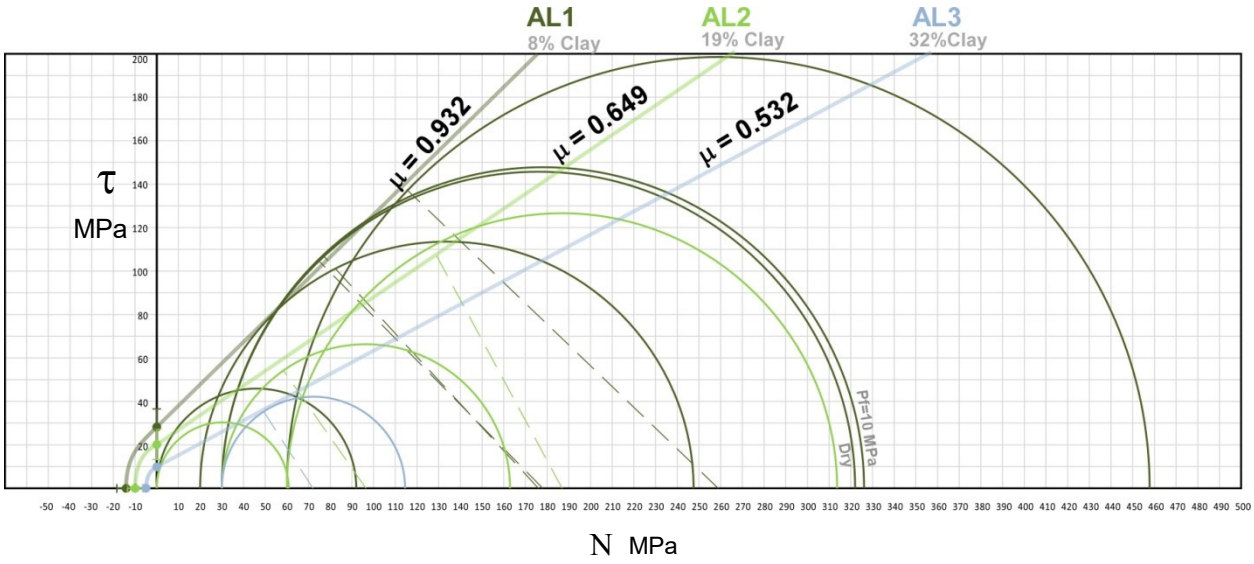

Figure IV-7. Mohr Diagrams.
Mohr diagram, Shear vs. Normal Stress for 3 samples of altered wall rock, constructed from the triaxial and uniaxial compressive tests performed to the Long Cylinders Specimens. Semi Circles are constructed from the ultimate stress and confining pressure listed in the Table S1 (Section IV.8 "Supplementary Information" of the Present Thesis). The envelopes (straight and coarser lines) are the fracture Griffith-coulomb envelopes (*e.g.*: Griffith, 1921; Brace, 1960) best fitting to the available circles. The given μ values correspond to the "internal friction" of the whole rocks, therefore they are fracturing parameters.

IV.4.3. Coefficient of Friction

Direct shear tests were performed on 23 powder specimens (or synthetic gouges) taken from the 5 samples. Three values of the dynamic friction coefficient were obtained from each test, performed under 4 different coffining pressures: 50, 100, 150 and 200 MPa.

Similar to the previous parameters, the data show an inverse correlation between alteration level and friction coefficient of simulated gouges, under all the confining pressures. In general, the least altered gouges (AL1) are near twice stronger than the most altered one (AL4). This effect is more remarkable under lower than higher confining pressure (= normal stress). Contrasting with the whole rock mechanical properties, where the AL3 and AL4 show very similar values, the friction coefficient of AL4 is lower than AL3, following the weakening trend coming from AL1 to AL3.

In turn, the fault rock specimens, show higher friction coefficients than AL4 under all confining pressures.

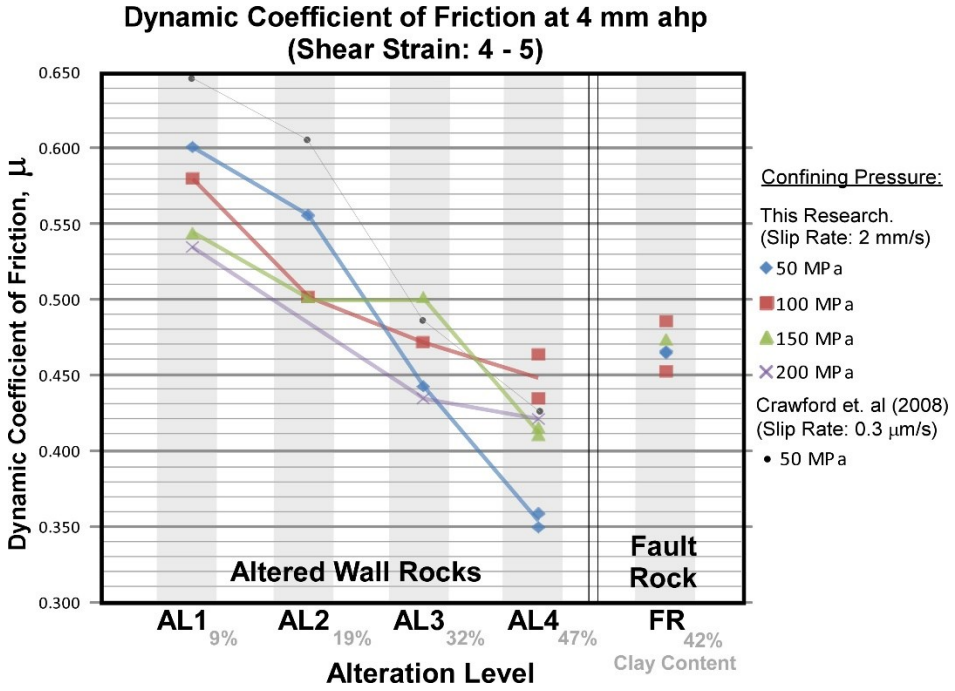

Figure IV-8. Scatter plot of dynamic friction.
Plot of dynamic friction μ-4000 of the 6 samples, measured in 23 specimens. Assorted colours represent different confining pressures. Gouge from the most altered rock (AL4) are 45%-30% weaker than gouge from the less altered rock (AL1). Gouge from the fault rocks have friction coefficient equivalent to the AL3 and AL4 sample. For the complete mineralogical content of the samples see Figure. Black dots show the frictional coefficient from synthetic gouges of pure quartz and clay (Crawford et al, 2008).

All the tested specimens show only positive values of a – b parameter (Table 2 and **Figure IV-9**). This means that all our gouges tend to increase their resistance to slip when the rate increases, called velocity strengthening. Furthermore, despite the scatter, a general tendency to increase friction with alteration levels can be observed. AL4 becomes twice stronger with the acceleration than AL1.

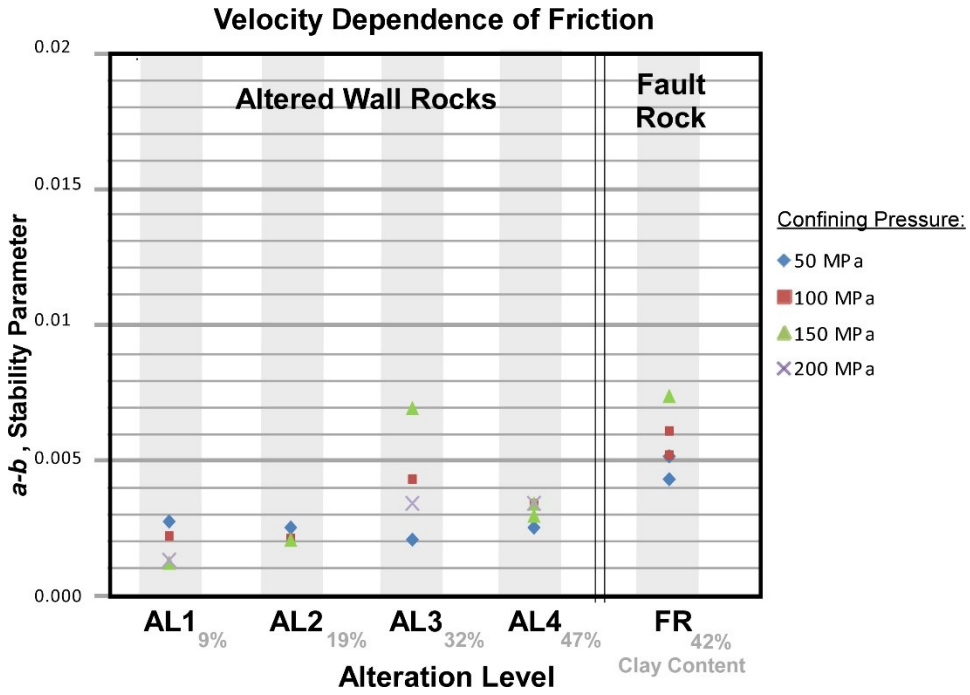

Figure IV-9. Scatter plot of Velocity Dependence a – b Parameter.
Velocity dependence calculated for the same 23 specimens shown in Figure IV-8. Values correspond to the differences between the friction coefficient before and after de slip rate acceleration (from 0.2 to 2 μ/s), in proportion to the former. This represent the effect of the slip rate on the frictional coefficient. The colours represent different confining pressures.

IV.5. DISCUSSION

IV.5.1. Analysis of the Data

IV.5.1.1. Whole-rock properties of AL1-AL2-AL3-AL4

As a series, these samples represent the progressive evolution of a granitic rock hosting a hydrothermal system, especially around faults, considering their channelling effect on fluids (Caine *et al.*, 1996; López & Smith, 1996; Wibberley & Shimamoto, 2003). However, individually, they also represent the current final state of the rocks in the case of study, RT.

Data suggests that whole rock mechanical properties tend correlate with the alteration level, hence clay content (**Figure IV-5** and **Figure** IV-6 and **Figure IV-7**). For the 3 first levels (from AL1 to AL3) the clay content increases at the expense of plagioclase reduction, then tensile and compressive strength are dramatically reduced. The rocks lose 60% of their tensile strength and *ca*. 40% of their triaxial compressive strength. Furthermore, the porosity is proportionally increased in *ca*. 100% of the original value.

Contrastingly, when the alteration progresses to the next level (AL3 to AL4), the clay minerals are only formed at the expense of the orthoclase breakdown. There, the tensile strength of AL4 is not reduced, and the porosity is not increased with respect to AL3 (**Figure IV-5** and **Figure** IV-6). The mean values of tensile strength and porosity show an apparent reverse of the trend observed from AL1 to AL3. However, this cannot be fully proven, since the standard deviation boxes show an important overlap between AL3 and AL4.

Such differences between the consequences of the plagioclase hydrolysis and the orthoclase hydrolysis can be explained by the original texture of the granitic protolith. The phenocrysts are more than 50% of the rock volume and are touching each other, suggesting that the mechanical support of the rock is provided by them. Originally, these phenocrysts are mainly composed of tabular plagioclase crystals (and minor orthoclase megacrysts). Then, when they are dissolved and replaced by clay the rock their support is removed. In contrast, orthoclase is mostly present in the microcrystalline groundmass together with quartz plus some phenocrysts which are minor in volume (see microamps in **Figure IV-**).

The increase of the porosity related to hydrolysis of plagioclase (and not orthoclase) is interpreted to be consequence of the dissolution of those interconnected phenocrysts, providing interconnected pores and effective porosity.

IV.5.1.2. Whole-rock Properties of the Fault Rock

They represent the final state of a fault after experiencing hydrolysis, mechanical comminution, cataclasis, and precipitation of new cementing minerals (quartz, sulphides and sulphates). The data indicate that the mineralogical processes related to the fault-core tend to strongly reduce the porosity of the fault rocks. Getting to make fault rocks even less porous than the original protolith (See **Figure** IV-6).

The tensile strength (T) and consequently the cohesion (C = 2T) of the fault rocks also increase with the precipitation of minerals in the core. The whole-rock tests show that some specimens can have tensile strength up to 8 MPa (*i.e.* cohesion up to 16 MPa) which means that some fault rocks can get to be more cohesive than the wall rocks (**Figure IV-6**, **Figure IV-10**). Then, considering that the fragmental fault rocks were completely uncohesive during its formation (brittle conditions), such values of cohesion mean an important fault-core strengthening by the action of hydrothermal fluids. The petrographic observations of the fault rocks, at outcrop-scale and microscopic-scale (Previous chapter of this thesis), indicate that the strengthening is consequence of the precipitation of minerals between the fragments. The most abundant minerals precipitating in the cores are pyrite, quartz and gypsum, from which quartz is the strongest but is distributed heterogeneously along the faults. Therefore, the strengthening of faults is also expected to be heterogenous along them.

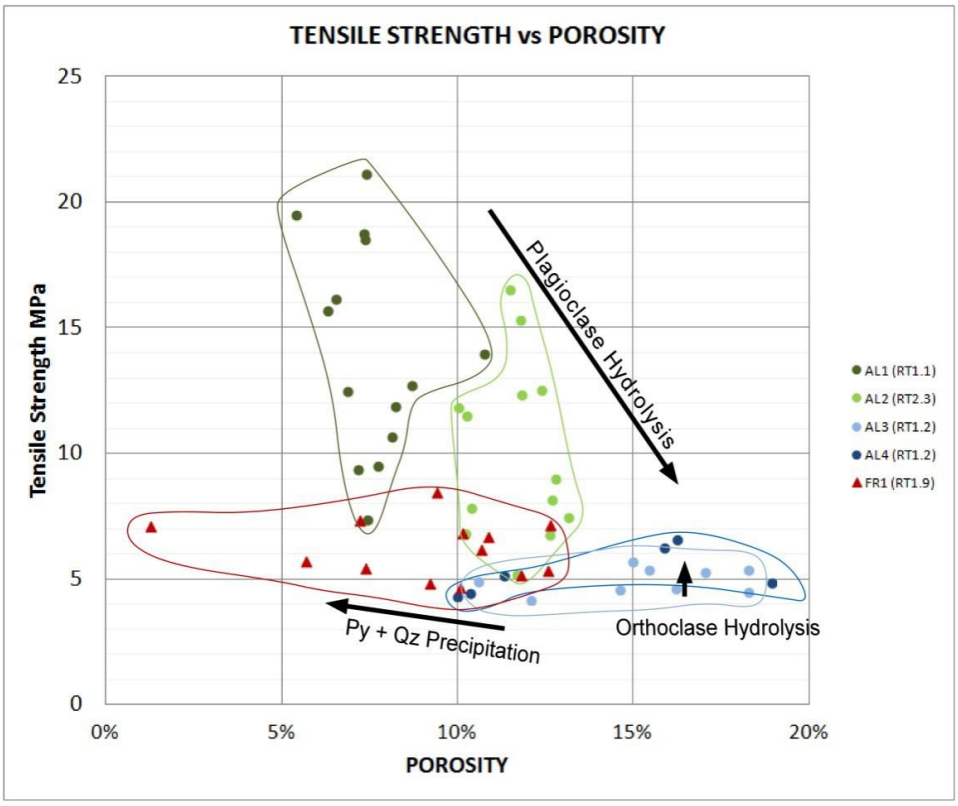

Figure IV-10. Tensile strength vs. porosity, measured in the flat cylinder specimens.

IV.5.1.3. Friction of Gouges from AL1-AL2-AL3-AL4

As a series, the frictional properties of the powder specimens from altered wall-rock represent the mechanical evolution of a hypothetical fault experiencing only hydrolysis of their feldspars, without precipitation of quartz or any new mineral. They show a decrease of dynamic friction coefficient μ_d with the alteration level, which indicates that the frictional strength of the faults is reduced with hydrolysis of the feldspars. Unlike in whole-rock properties, this relationship is here continuous from the first to the last alteration level (AL1 to AL4).

The dynamic friction coefficient is clearly reduced with the increase of clay, under all the confining pressures (**Figure IV-10**). The most altered rock (47% clay) have friction coefficients between 0.3 to 1.3 smaller than the least altered one (9% clay), which means they are 30-45% weaker. Our data show the same weakening trend of μ_d (when increasing % clay) and total loss of fiction coefficient than synthetic mixtures of pure quartz and pure clay previously measured in oblique sliding blocks (Crawford *et al.,* 2008; Tembe *et al.,* 2010). This confirms that the content of clay in gouges is the most important parameter controlling their friction coefficient, regardless the mineralogy of the other components (like orthoclase or quartz).

The velocity dependence of the friction coefficient is also related to the hydrothermal mineral alteration. Despite the scatter, proportional velocity-strengthening parameter shows a general increment with respect to the increasing alteration level (AL1-AL4) and clay content (9 to 47 % vol). This suggest that the hydrothermal fluids tend to make the faults more stable and less likely to be seismically active.

IV.5.1.4. Friction of Gouges from the Fault Rock

The frictional properties of powder specimens from the fault rock sample represent final state of a hypothetical fault experiencing all the mineralogical modifications related to the fault core (hydrolysis of feldspar and addition of quartz and metallic sulphides). However, without the mechanical effect of sealing and cementation, since the specimen preparation includes disaggregation, grinding and dissolution of the most soluble minerals (distilled water at 80°C).

Frictional data shows that mineralogical modifications of the fault core induce strengthening. The powder specimens made from the fault rock (FR) have higher friction coefficient than the powders made from the wall-rock sample AL4. In average the friction coefficient values for FR are 17% higher than AL4 but these differences are smaller for higher confining pressures. This two samples have near the same clay/quartz content; however, FR has 5% of metallic sulphides (mainly pyrite and minor chalcopyrite) that is absent in AL4. This finding suggests that the presence of metallic sulphides in the fault tend to increase its frictional strength.

Furthermore, the fault roc (FR) show higher a – b parameters than their equivalents from altered wall rock (AL4). Suggesting that the metallic sulphide makes faults stronger but at the same time more stable and less probable to slip seismically.

IV.5.2. Mechanical Effect of Feldspar Hydrolysis

According to field and microscopy observations (see Section IV page 116), the hydrolysis caused by hydrothermal fluids is a mineralogical process that can be expected to occur in and around faults, in the fault core and the damage zone (as a mineral halo). It can affect any intact rock but is favoured by the permeability provided by fractures. This process destroys the feldspar and creates clays from them.

The mechanical data presented here indicates that this mineralogical change produce important weakening to granitic rocks (wall-rock) and gouges (fault-core), modifying their envelopes of fracture and reactivation (**Figure IV-11**). In granitic rocks the hydrolysis can produce

a loss of tensile strength up to 60% and loss of compressive triaxial strength (internal friction) up to 40%. Additionally, it can increase the porosity in up to 100%. In fault gouges the hydrolysis of feldspar produces loss of frictional coefficient up to 45% and reduces their potential to slip seismically, increasing their stability.

According to this, we can hypothesize that if a fault system is penetrated by hydrothermal fluids that are able to hydrolyse feldspars, the surrounding rocks would become weaker, more prone to fail for the stress and propagate more fractures. However, simultaneously, the faults also would become weaker, slipping easier and not allowing the stress field to grow enough to bring the surrounding altered rocks to failure. Also, the fault system would be able to accommodate more crustal strain and less prone to be seismically active.

IV.5.3. Mechanical Effect of Mineral Precipitation

Precipitation of new minerals is the most important process in the formation of any ore deposits. There is a large number of minerals that can precipitate in the rocks from hydrothermal fluids, however in the case of the present study the precipitating minerals are quartz, sulphides (mainly pyrite and chalcopyrite) and sulphates (mainly gypsum). The precipitation of these minerals is spatially related to faults, some occur in fractures of the damage zone, but most occur in the fault cores. In the cores, those minerals precipitate in the available space between particles of rocks and minerals fragmented by frictional wear.

According with the observations made to the data here obtained, the mechanical effect that the mineral precipitation has on the faults can be separated in. (1) Cohesion of fault rocks. Any mineral precipitating in a porous rock would replace open spaces by new minerals, increasing its strength proportionally to the strength of the new precipitated mineral. For the case of study, the final effect of the precipitation of all the minerals combined is an increase of tensile strength from 0 to an average of 6.2 MPa (maximum 9MPa). Locally, getting to form some fault rocks even stronger than some altered wall rocks. This change is also reflected in the porosity of the fault rock, which can by reduced down to values even lower than some wall rocks. (2) Modification of friction by mineralogical modification. In a larger scale of time, if the precipitation cannot supply enough cohesion to stop the frictional wear, the new minerals are going to be comminuted to form part of the new fault gouges. So, they could modify the frictional properties of the fault gouges. From the case of study, it can be deduced that if pyrite is added to the gouges (previously composed only by clay and quartz) the coefficient of friction is increased. This increment could be only a consequence of the proportional reduction of clay content that the addition of any mineral

would involve. However, more research on the frictional properties of metallic sulphides (absent in the published literature) is necessary. According to our data, the addition of pyrite would also increase the velocity strengthening making faults more stable and less seismic.

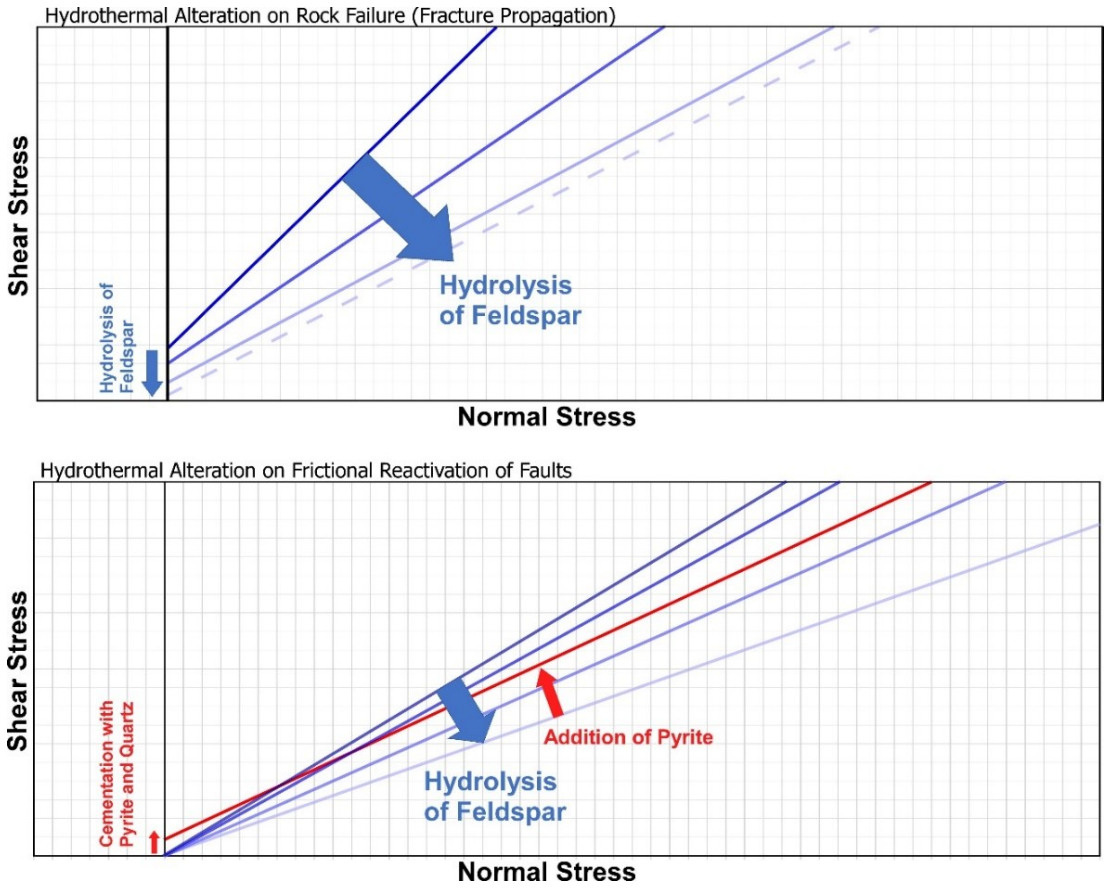

Figure IV-11. Effects of mineral alteration and precipitation on the fracture and reactivation envelope. Shear vs normal stress plots, with schematic fracture and reactivation envelopes showing the changes expected after hydrolysis and precipitation of minerals (above) and fault gouges (below).

IV.6. CONCLUSION

The hydrothermal fluids related to porphyry copper environments modify the mechanical properties fault cores and both wall rocks, by the hydrolysis of feldspars (replacing them with clays) and the precipitation new minerals.

The hydrolysis of the feldspars produces an important decrease of tensile and compressive strength (and increase of porosity) of the granitic rocks in the wall rocks. The magnitude of these changes depends on the mineral being hydrolysed. The hydrolysis of the plagioclase phenocrysts, in the first levels of alteration, is highly more influent than the later hydrolysis of the orthoclase, left in the ground mass.

In fault gouges, the hydrolysis produces decrease of coefficient of friction only by the pure addition of clay content (independent of the feldspar being hydrolysed). In contrast, the precipitation of minerals in the same fault cores make them stronger, increasing both the cohesion and the frictional coefficient.

Both hydrolysis of feldspar and precipitation of pyrite have shown to enhance velocity strengthening of the gouges, making faults more seismically stable.

In general, the fluid-rock interaction related to fault, produces a competition between processes weakening the rocks and processes strengthening the fault rocks. The dominant process along the life of a fault will define its final mechanical behaviour. In hydrothermal systems related to porphyry copper deposit, it can be expected that the fluids make the entire faults weaker (faults and damage zones) and less prone to be seismically active.

IV.7. REFERENCES

ASTM International. (2016). ASTM D3967-16 Standard Test Method for Splitting Tensile Strength of Intact Rock Core Specimens. West Conshohocken, PA. https://doi.org/10.1520/D3967-16.

Brace, W. F. (1960). An extension of the Griffith theory of fracture to rocks. Journal of Geophysical Research 65(10), 3477-3480.

Briceño, C. & Rubio, X. 2012. Caracterización y Distribución de Arcillas en el yacimiento Radomiro Tomic y sus Implicancias en Procesos Metalúrgicos. In: VIII Congreso Geológico Chileno (edited by departamento de Ciencias Geológicas, U. C. d. N.), Antofagasta.

Byerlee, J. 1978. Friction of rocks. pure and applied geophysics 116(4-5), 615-626.

Caine, J. S., Evans, J. P. & Forster, C. B. (1996). Fault zone architecture and permeability structure. Geology 24(11), 1025-1028.

Carrasco, M. S., J. (2007). Informe Modelo Estructural Radomiro Tomic: Fase I. In: Reporte Interno. Codelco Calama, 51.

Crawford, B. R., Faulkner, D. R. & Rutter, E. H. (2008). Strength, porosity, and permeability development during hydrostatic and shear loading of synthetic quartz-clay fault gouge. Journal of Geophysical Research-Solid Earth 113(B3).

Cuadra, P. & Rojas, G. (2001). Oxide Mineralization at the Radomiro Tomic Porphyry Copper deposit, Northern Chile. Economic Geology 96(2), 387-400.

Cuadra, P., Zentilli, M., Puig, A. & Tidy, E. 1997. Dataciones radiometricas recientes en Radomiro Tomic. In: VIII Congreso Geologico Chileno Antofagasta.

Charrier, R., Pinto, L. & Rodrigues, M. (2007). Tectonostratigraphic evolution of the Andean Orogen in Chile. In: The Geology of Chile (edited by Moreno, T. & Gibbons, W.). The Geological Society, London, 21–114.

Diaz, J., Boric, R. & Riquelme, R. (2009). Geologia de los sulfuros de Radomiro Tomic (RT), Nuevos Antecedentes. In: XII Congreso Geologico Chileno, Santiago.

Evans, J. P. & Chester, F. M. (1995). Fluid-rock interaction in faults of the San Andreas system: Inferences from San Gabriel fault rock geochemistry and microstructures. Journal of Geophysical Research: Solid Earth 100(B7), 13007-13020.

Gee, G. W., & Bauder, J. W. (1986). Particle-size analysis1. Methods of soil analysis: Part 1—Physical and mineralogical methods, (methodsofsoilan1), 383-411.Goddard, J. V. & Evans, J. P. (1995). Chemical changes and fluid-rock interaction in faults of crystalline thrust sheets, northwestern Wyoming, U.S.A. Journal of Structural Geology 17(4), 533-547.

Hawkes, I. & Mellor, M. (1970). Uniaxial testing in rock mechanics laboratories. Engineering Geology 4(3), 179-285.

Hoffmann-Rothe, A., Kukowsky, N., Dresen, D., Helmut, E., Oncken, O., Jurgen, K., Scheuber, E. & Kellner, A. (2006). Oblique Convergence along the Chilean Margin: Partitioning, Margin-Parallel Faulting and Force Interaction at the Plate Interface. In: The Andes: Active Subduction Orogeny (edited by Oncken, O., Gotze, H., Chong, G., Ramos, V., Franz, G., Strecker, M., Giese, P. & Wigger, P.). Springer London, Limited.

Ikari, M. J., Marone, C. & Saffer, D. M. (2011). On the relation between fault strength and frictional stability. Geology 39(1), 83-86.

Ikari, M. J., Saffer, D. M. & Marone, C. C. B. (2009). Frictional and hydrologic properties of clay-rich fault gouge. Journal of Geophysical Research: Solid Earth 114(B5).

Jaeger, J. & Cook, N. (1979). Fundamentals of Rock Mechanics. 3rd edition.. London: Chapman and Hall. ISBN 0 412 220105.

Janssen, C., Lüders, V. & Hoffmann-Rothe, A. (2004). Contrasting styles of fluid-rock interaction within the West Fissure Zone in northern Chile. Geological Society, London, Special Publications 224(1), 141-160.

Kohlstedt, D. L., Evans, B. & Mackwell, S. J. (1995). Strength of the lithosphere: Constraints imposed by laboratory experiments. Journal of Geophysical Research: Solid Earth 100(B9), 17587-17602.

López, D. L. & Smith, L. (1996). Fluid flow in fault zones: Influence of hydraulic anisotropy and heterogeneity on the fluid flow and heat transfer regime. Water Resources Research 32(10), 3227-3235.

Moore, D. E. & Lockner, D. A. (2004). Crystallographic controls on the frictional behaviour of dry and water-saturated sheet structure minerals. Journal of Geophysical Research B: Solid Earth 109(3).

Ossandon C, G., Freraut C, R., Gustafson, L. B., Lindsay, D. D. & Zentilli, M. (2001). Geology of the Chuquicamata Mine: A Progress Report. Economic Geology 96(2), 249-270.

Paterson, M. & Wong, T. (2005). Experimental rock deformation-the brittle field. Springer Science & Business Media.

Perfettini, H. & Avouac, J. P. (2004). Postseismic relaxation driven by brittle creep: A possible mechanism to reconcile geodetic measurements and the decay rate of aftershocks, application to the Chi-Chi earthquake, Taiwan. Journal of Geophysical Research: Solid Earth 109(B2).

Perfettini, H., Avouac, J.-P., Tavera, H., Kositsky, A., Nocquet, J.-M., Bondoux, F., Chlieh, M., Sladen, A., Audin, L., Farber, D. L. & Soler, P., (2010). Seismic and aseismic slip on the Central Peru megathrust. Nature 465, 78.

Schulz, S. E. & Evans, J. P. (1998). Spatial variability in microscopic deformation and composition of the Punchbowl fault, southern California: implications for mechanisms, fluid-rock interaction, and fault morphology. Tectonophysics 295(1-2), 223-244.

Scholz, C. H. (1998). Earthquakes and friction laws. *Nature* 391(6662), 37-42.

Scholz, C. (2002). The Mechanics of Earthquakes and Faulting. Cambridge: Cambridge University Press. doi:10.1017/CBO9780511818516

Tembe, S., Lockner, D. A. & Wong, T.-F. C. B. (2010). Effect of clay content and mineralogy on frictional sliding behaviour of simulated gouges: Binary and ternary mixtures of quartz, illite, and montmorillonite. Journal of Geophysical Research: Solid Earth 115(B3).

Townend, J. & Zoback, M. D. (2000). How faulting keeps the crust strong. Geology 28(5), 399-402.

Utada, M. (1980). Hydrothermal alterations related to igneous activity in Cretaceous and Neogene formations of Japan. Mining Geol., Spec. Issue 8, 67-83.

Wibberley, C. A. J. & Shimamoto, T. (2003). Internal structure and permeability of major strike-slip fault zones: The Median Tectonic Line in Mie Prefecture, Southwest Japan. Journal of Structural Geology 25(1), 59-78.

Zapettini, E., Godeas, M., Seggiaro, R., Korzeniewski, L., Ribiolo, D., Miranda, V., Uribe, H. & Heuschmidt, B. (2001). Mapa metalogenico de la region fronteriza entre Argentina, Bolivia, Chile y Peru [14°S-28°S]. Servicio Nacional de Geología y Minería.

Zhang, Y., Schaubs, P. M., Zhao, C., Ord, A., Hobbs, B. E. & Barnicoat, A. C. (2008). Fault-related dilation, permeability enhancement, fluid flow and mineral precipitation patterns: numerical models. Geological Society, London, Special Publications 299(1), 239.

IV.8. SUPPLEMENTARY INFORMATION

TEST/ SPECIMEN NAME	Length (mm)	Diameter (mm)	Confinning Pressure	Fluid Pressure	Effective Confinning Pressure	Ultimate Strenght (Mpa)	Ultimate Force KN	Alfa Angle
AL1_LC_1 UNIAXIAL	49.30	20	0 MPa	0 MPa	0 MPa	92.04	28.90	Not Preserved
AL1_LC_2 TRI_30Mpa (10Pf)	50.98	20	40 MPa	10 MPa	30 MPa	326.14	103.90	23
AL1_LC_3 TRI_30Mpa (Dry)	50.30	20	30 MPa	0 MPa	30 MPa	322.00	102.58	24
AL1_LC_4 TRI_60Mpa	56.14	20	60 MPa	0 MPa	60 MPa	457.82	145.85	22
AL1_LC_7 TRI_20Mpa ii	46.40	20	20 MPa	0 MPa	20 MPa	247.51	78.85	21
AL2_LC_2 UNIAXIAL	46.13	20	0 MPa	0 MPa	0 MPa	60.83	19.10	Not Preserved
AL2_LC_1 TRI_30Mpa	50.98	20	30 MPa	0 MPa	30 MPa	162.91	51.90	27
AL2_LC_3 TRI_60Mpa	39.82	20	60 MPa	0 MPa	60 MPa	313.74	99.95	31
AL3_LC_2 TRI_30MPa	38.10	20	30 MPa	0 MPa	30 MPa	114.57	36.50	29

Table S1
Compressive strength properties obtained from the Long Cylinders Specimens. Columns show their dimensions, the conditions at which the tests were performed and experimental results. Alfa angle was possible to directly measure for the triaxial tests, because a transparent PVC jacket was used around the cylinders.

ALTERATION LEVEL	SAMPLE	TEST / SPECIMEN NAME	Confinning Pressure	Fluid Pressure	Eff. Normal Stress	μ-SLOW	μ-FAST	μ-4000	a-b Parameter $\Delta\mu_d/\ln(V/V_0)$
AL1	RT1.1	AL1_FULL_1 50	60 MPa	10 MPa	050 MPa	0.602	0.609	0.602	0.003
AL2	RT2.3	AL2_FULL_1 50	60 MPa	10 MPa	050 MPa	0.558	0.564	0.556	0.003
AL3	RT1.2	AL3_MIX_1 50	60 MPa	10 MPa	050 MPa	0.429	0.434	0.443	0.002
AL4	RT2.1	AL4_MIX_1 50 i	60 MPa	10 MPa	050 MPa	0.333	0.339	0.350	0.003
AL4	RT2.1	AL4_MIX_2 50 ii	60 MPa	10 MPa	050 MPa	0.335	0.341	0.359	0.003
FR1	RT1.8	FR1_MIX_2 50 ii	60 MPa	10 MPa	050 MPa	0.440	0.450	0.466	0.004
FR1	RT1.8	FR1_MIX_3 50 iii	60 MPa	10 MPa	050 MPa	0.437	0.449	0.465	0.005
AL1	RT1.1	AL1_FULL_2 100	110 MPa	10 MPa	100 MPa	0.581	0.586	0.580	0.002
AL2	RT2.3	AL2_FULL_2 100	110 MPa	10 MPa	100 MPa	0.509	0.514	0.502	0.002
AL3	RT1.2	AL3_MIX_2 100	110 MPa	10 MPa	100 MPa	0.463	0.473	0.472	0.004
AL4	RT2.1	AL4_MIX_3 100 i	110 MPa	10 MPa	100 MPa	0.438	0.446	0.435	0.003
AL4	RT2.1	AL4_MIX_4 100 ii	110 MPa	10 MPa	100 MPa	0.463	0.471	0.464	0.003
FR1	RT1.8	FR1_MIX_4 100 i	110 MPa	10 MPa	100 MPa	0.464	0.478	0.486	0.006
FR1	RT1.8	FR1_MIX_5 100 ii	110 MPa	10 MPa	100 MPa	0.437	0.449	0.453	0.005
AL1	RT1.1	AL1_FULL_3 150	160 MPa	10 MPa	150 MPa	0.551	0.554	0.545	0.001
AL2	RT2.3	AL2_FULL_4 150 ii	160 MPa	10 MPa	150 MPa	0.501	0.506	0.502	0.002
AL3	RT1.2	AL3_MIX_3 150	160 MPa	10 MPa	150 MPa	0.479	0.495	0.502	0.007
AL4	RT2.1	AL4_MIX_5 150 i	160 MPa	10 MPa	150 MPa	0.390	0.397	0.416	0.003
AL4	RT2.1	AL4_MIX_6 150 ii	160 MPa	10 MPa	150 MPa	0.385	0.393	0.411	0.003
FR1	RT1.8	FR1_MIX_6 150	160 MPa	10 MPa	150 MPa	0.443	0.460	0.474	0.007
AL1	RT1.1	AL1_FULL_6 200	210 MPa	10 MPa	200 MPa	0.548	0.551	0.536	0.001
AL3	RT1.2	AL3_MIX_4 200	210 MPa	10 MPa	200 MPa	0.427	0.435	0.435	0.003
AL4	RT2.1	AL4_MIX_7 200	210 MPa	10 MPa	200 MPa	0.394	0.402	0.420	0.003

Table S2.
Frictional properties obtained from Powder Specimens. Columns show the conditions at which the tests were performed and their experimental results. μ-fast, μ-slow and μ-4000 were obtained as explained in Figure IV-4.

ALTERATION LEVEL	SOURCE SAMPLE	TEST/ SPECIMEN NAME	Length (mm)	Porosity (Effective)	Tensile Strenght	Cohesion (MPa)
AL1	RT1.1	AL1_FC_n2	8.68	7.2%	9.35	18.70
		AL1_FC_1.1	9.26	7.7%	9.49	18.97
		AL1_FC_1.2	9.68	10.8%	13.95	27.90
		AL1_FC_2.1	8.77	6.3%	15.69	31.38
		AL1_FC_2.2	8.96	7.4%	18.51	37.02
		AL1_FC_2.3	9.01	6.5%	16.15	32.31
		AL1_FC_2.4	10.47	5.4%	19.49	38.98
		AL1_FC_3.1	11.49	6.9%	12.47	24.94
		AL1_FC_3.2	7.91	7.3%	18.76	37.53
		AL1_FC_3.3	8.81	7.4%	21.15	42.30
		AL1_FC_4.1	8.98	7.4%	7.34	14.68
		AL1_FC_4.2	7.99	8.1%	10.68	21.37
		AL1_FC_4.3	9.22	8.2%	11.88	23.75
		AL1_FC_4.4	8.35	8.7%	12.70	25.40
AL2	RT2.3	AL2_FC_1.3	8.25	10.4%	7.83	15.65
		AL2_FC_1.5	9.35	12.4%	12.54	25.08
		AL2_FC_1.4	8.10	13.2%	7.45	14.91
	RT2.3b	AL2_FC_2.1	11.78	11.7%	5.18	10.37
		AL2_FC_3.1F	8.30	10.2%	6.81	13.62
		AL2_FC_3.2	10.13	12.6%	6.77	13.55
		AL2_FC_3.4Q	6.88	12.7%	8.15	16.29
		AL2_FC_3.5Q	6.92	11.8%	15.32	30.64
	RT2.3	AL2_FC_4.1	7.72	11.5%	16.55	33.11
		AL2_FC_4.2	8.30	11.8%	12.36	24.72
		AL2_FC_4.3	9.70	12.8%	9.01	18.02
		AL2_FC_5.1	8.49	10.2%	11.52	23.04
		AL2_FC_5.2F	6.90	10.0%	11.82	23.64
AL3	RT1.2	AL3_FC_1.1	9.71	15.0%	5.72	11.44
		AL3_FC_1.2	8.61	17.0%	5.28	10.56
		AL3_FC_2	12.75	18.8%	Not Rec	Not Rec
		AL3_FC_3	9.07	15.4%	5.39	10.77
		AL3_FC_4	11.77	10.6%	4.91	9.81
		AL3_FC_5.1	11.59	16.0%	Not Rec	Not Rec
		AL3_FC_5.2	11.31	18.3%	4.51	9.01
		AL3_FC_6.1	9.76	14.6%	4.58	9.16
		AL3_FC_6.2	6.90	18.3%	5.35	10.70
		AL3_FC_6.3	9.05	16.2%	4.65	9.29
		AL3_FC_7	9.17	12.1%	4.17	8.33
		AL3_FC_8	7.94	16.1%	Noise	Noise
AL3	RT2.1	AL4_FC_1	7.88	18.9%	4.85	9.70
		AL4_FC_2	10.50	10.0%	4.30	8.61
		AL4_FC_3.1	9.08	10.4%	4.44	8.89
		AL4_FC_3.2	8.19	11.8%	4.28	8.56
		AL4_FC_4.1	6.56	11.7%	Not Rec	Not Rec
		AL4_FC_4.2	8.74	11.3%	5.13	10.25
		AL4_FC_4.3	7.76	15.9%	6.27	12.53
		AL4_FC_5	5.44	16.2%	6.60	13.20
FR1	RT1.9	FR1_FC_1.1	6.32	9.4%	8.44	16.88
		FR1_FC_1.2	6.19	12.6%	7.17	14.33
		FR1_FC_2.1	8.54	11.8%	5.18	10.37
		FR1_FC_2.2	8.40	8.8%	Noise	Noise
		FR1_FC_2.3	8.36	1.2%	7.11	14.23
		FR1_FC_2.4	8.55	10.1%	6.84	13.67
		FR1_FC_2.5	7.89	10.9%	6.69	13.38
		FR1_FC_3.1	8.47	10.7%	6.18	12.36
		FR1_FC_3.2	8.88	9.2%	4.83	9.66
		FR1_FC_3.3	8.12	7.2%	7.35	14.69
		FR1_FC_3.4	8.76	7.9%	Not Rec	Not Rec
		FR1_FC_4.1	8.09	5.7%	5.72	11.44
		FR1_FC_4.2	7.87	10.1%	4.66	9.31
		FR1_FC_4.3	7.74	7.4%	5.45	10.91
		FR1_FC_4.4	7.84	12.5%	5.37	10.74

Table S3:
Mechanical and textural properties measured from Flat Cylinders Specimens. All the cylinders were 20 mm in diameter and their length is indicated in mm. Porosity was measured with a pycnometer. Tensile strength was measured with the brazilian tests. Cohesion is calculated as C = 2T.

V. DISCUSIÓN GENERAL

A pesar de haberse desarrollado a partir de rocas graníticas muy parecidas (pórfido granodiorítico y diorita) los dos casos de estudios descritos en esta tesis presentan importantes diferencias en la mineralogía de alteración, en las rocas de fallas y en el espesor de las vetas. Estas diferencias indican diferencias en la composición química y presión de los fluidos que acompañó la deformación frágil en cada caso. Por consiguiente, se pueden esperar diferentes variaciones de las propiedades mecánicas de las fallas y rocas. Además, ambos sistemas de fallas muestran más de un grupo paragenético de minerales, lo que permite deducir la evolución de los sistemas hidrotermales y sus efectos mecánicos en las fallas estudiadas. Por otra parte, los análisis mecánicos de laboratorio han permitido cuantificar algunos de estos efectos (Capitulo IV, página 116).

En este capítulo, "**caso 1**" se usará para referirse a las fallas del Dúplex Caleta Coloso (DCC) del Sistema de Falla Atacama (SFA) y "**caso 2**" a las fallas de Radomiro Tomic (RT) del Sistema de Falla Domeyko (SFD).

Por una parte, las fallas del caso 1 presentan núcleos compuestos de múltiples bandas de rocas cataclásticas (proto- a ultra- cataclasita) principalmente cementadas con clorita, epidota y calcita, acompañados de una franja salbandas ricas en arcillas y hematita (Ver: Figure II-1, perfil F, página 41, Tabla VII-2; Cembrano *et al*., 2005; Faulkner *et al.,* 2008; Jensen *et al*., 2011; Gomila e*t al.,* 2016). Las cataclasitas de clorita y epidota corresponden a la deformación Cretácica del arco volcánico que hoy conforma la Cordillera de la Costa, su desarrollo se puede acotar entre los 125 y 118 Ma (Scheuber & Andriessen, 1990; Cembrano *et al*., 2005) y la mineralogía corresponde a una **alteración propilítica**. Las bandas de salbanda foliada pueden correlacionarse con la reactivación Pliocena del sistema de fallas (Indicada en la Figura I-19) y su mineralogía corresponde a una **alteración argílica**.

Este sistema no presenta evidencia de vetas previas que hayan controlado la propagación de a las grandes zonas de fallas. Las vetas existentes son de algunos centímetros de espesor, se encuentran desplazadas por la deformación frágil y muestran características mineralógicas correspondientes a presiones sub-hidrostáticas (Herrera *et al*., 2005).

La estructura interna de estas fallas, compuesta de múltiples núcleos, es consistente con el endurecimiento (*Hardening*) de las fallas y su subsecuente reactivación cortando el protolito adyacente (Faulkner *et al*., 2008, Arancibia *et al*., 2014). Cabe destacar, que el inicio de la deformación frágil de todo el SFA ha ocurrido justo después de un gran periodo de deformación plástica asociada al desarrollo del arco volcánico (Scheuber *et al*., 1995 y Taylor *et al*., 1998). Y

que las rocas aquí estudiadas muestran evidencias de que el fracturamiento habría ocurrido en un estado frágil-plástico de los feldespatos (Ver Figure II-7, Fotografía B y Sección II.6 **"**CONCLUSIONS**"** , punto 4).

Por otra parte, las fallas del caso 2, presentan núcleos y halos con abundante arcilla (illlita > kaolinita > smectita) y minerales metálicos (sulfuros o sulfatos) con cuarzo hidrotermalmente precipitado entre los fragmentos de las rocas del núcleo. Además, todas las fallas muestran evidencias de haber sido nucleadas a por vetas de cuarzo previamente formadas durante la **alteración potásica** y plasticidad de la roca (Ver Figure III-8, Página 94). Estas grandes vetas de cuarzo, adyacentes a los núcleos y deformadas por los mismos, indican que la deformación frágil inició como fracturas de tensión, por sobrepresurización de fluidos, y subsecuente precipitación de cuarzo. Las texturas de plasticidad intracristlinas (observadas tanto en el protolito como en las vetas) y el remplazo de anfíbol por biotita (indicando temperaturas entre 300 y 500°C) indican que las vetas se formaron durante un periodo de deformación plástica de baja tasa de strain ca. (Fournier, 1999) (Sección III.3.1.1, página 86). Tal hidrofracturamiento bajo condiciones de deformación plásticas es posible a través de eventos transitorios rápidos (*strain rate* > $\mathbf{10^{-12}}\ \boldsymbol{sec^{-1}} = \mathbf{10^{-5}}\ \boldsymbol{year^{-1}} = \mathbf{10}\ \boldsymbol{/\ Ma}$) interrumpiendo un régimen de deformación plástica de menor tasa de strain (ca. $\mathbf{10^{-14}}\ \boldsymbol{sec^{-1}} = \mathbf{10^{-7}}\ \boldsymbol{year^{-1}} = \mathbf{0.1}\boldsymbol{/Ma}$) debido a la dependencia del fracturamiento a la tasa de strain (Fournier, 1999; Weis, 2012). Posterior a su formación, éstas vetas han sido deformadas por cizalle frágil a lo largo ellas, activándolas como fallas (dextrales de rumbo), formando salbandas y cataclasitas foliadas con paragénesis minerales que indican asociación temporal con **alteración fílica** (también llamada cuarzo-sericítica). Finalmente, se encuentran evidencias minerales indicando **alteración argílica** sobre las anteriores, sin deformación registrada (ver Figure III-8, Figura V-1, Tabla VII-1).

De acuerdo con las mineralogías descritas, el caso 1 se ha desarrollado bajo un ambiente químicamente dominado por la actividad de **Calcio + Sodio** y el caso 2 (RT) se ha desarrollado bajo un ambiente dominado por **Potasio** e **Hidrógeno** (además de metasomatismo de azufre y elementos metálicos)**.** Por lo tanto, el caso 1 se puede considerar como un ejemplo de alteración neutral a alcalina producida por el paso de una cantidad moderada de fluidos en "evolución de prograd**o"**, es decir fluidos que se calientan al pasar a través de rocas de mayor temperatura (Giggenbach, 1984; Seedorff, *et al.,* 2005; Seedorff, *et al.,* 2008). El caso 2, se trata de una alteración moderadamente ácida dominada fluidos de alta presión en "evolución de retrogrado", que se enfrían al atravesar rocas de menor temperatura (Giggenbach, 1984; Sillitoe, 2010).

Tales diferencias geoquímicas entre ambos casos son de gran utilidad para comparar el desarrollo de fallas en sistemas hidrotermales de diferente naturaleza y geoquímica.

Considerando el contexto tectónico durante la propagación de las fallas estudiadas (Figura I-18), se puede deducir que las diferencias entre sistemas hidrotermales de ambos casos se deben al efecto que el grosor de la corteza tiene sobre el desarrollo de los magmas que originan los fluidos de alteración. Existe una relación empírica prominente entre el engrosamiento cortical tectónico y la formación de sistemas hidrotermales porfídicos (Sillitoe, 2010) y, por lo tanto, la formación de zonas de alteración potásicas y fílicas, asociadas a sistemas porfídicos.

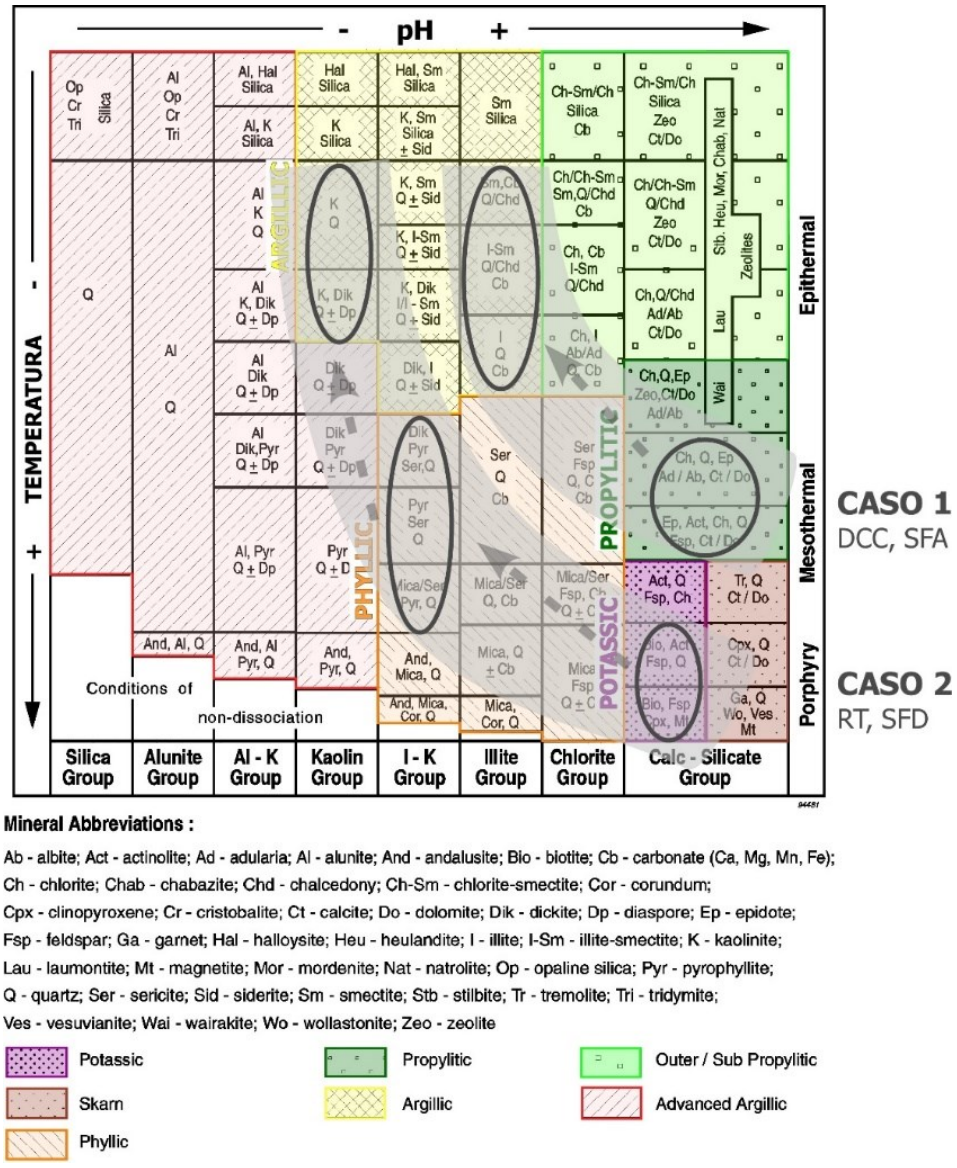

Figura V-1. Evolución mineralógica de ambos casos de estudio.
Diagrama que muestra la evolución de acidez y temperatura de las asociaciones minerales encontradas en los casos de estudios aquí escrito. Ambos tienden a acidificarse mientras se enfrían, pero sus condiciones iniciales son diferentes. Modificado de Corbett and Leach (1998). CASO 1: Fallas del Duplex Caleta Coloso (DCC) perteneciente al Sistema de Fallas Atacama (SFA). CASO 2: Fallas de Radomiro Tomic (RT) pertenecientes al Sistema de Fallas Domeyko (SFD).

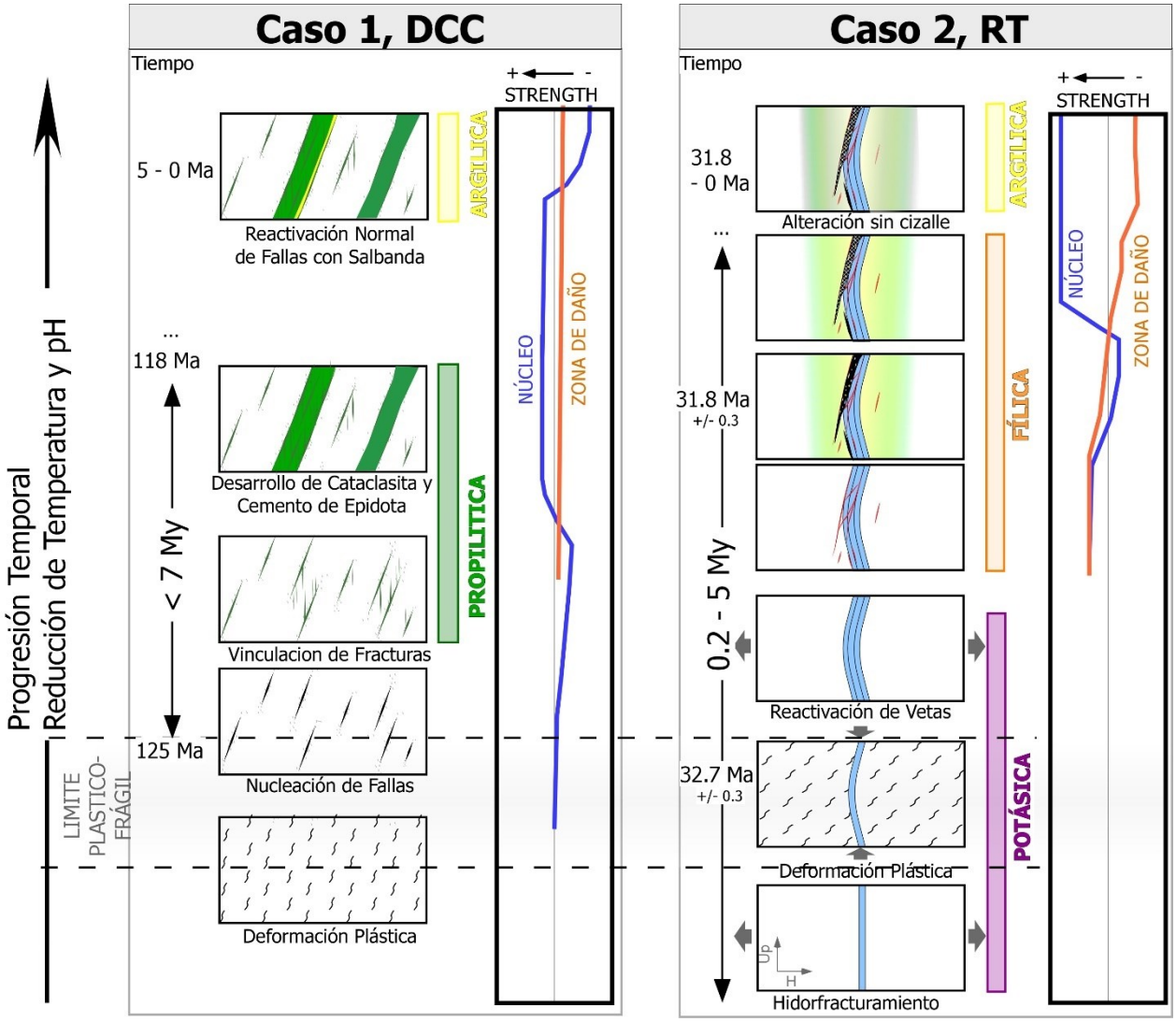

Figura V-2. Evolución de las estructuras de ambos casos de estudio.
Secuencia evolutiva de los casos de estudio descritos en esta tesis. Los rectángulos representan una sección esquemática de cada caso en diferentes momentos de su desarrollo, indicando algunos procesos petrogenéticos. Las franjas de colores indican las alteraciones hidrotermales, deducidas por paragénesis minerales, según Figura V-1. Los gráficos de "Strength" representan las variaciones relativas en fuerza o resistencia al esfuerzo, esperables para las rocas en núcleos (azul) o zonas de daño (naranja) de fallas.

De acuerdo con las mineralogías descritas en los 2 caso de estudio, se puede hacer el siguiente resumen de los efectos que los fluidos hidrotermales en las fallas, asociados a cada tipo de alteración hidrotermal observada, de acuerdo con los términos descritos por Meyer & Hemley (1967), modificada según Rose & Burt (1979).

V.1. ALTERACIÓN POTÁSICA

En general, resulta en minerales alcalinos de alta temperatura y es la primera en ocurrir en ambientes de sistemas hidrotermales porfídicos, por la interacción de fluidos calientes atravesando rocas de menor temperatura. Este tipo de alteración se observa en el caso 2 y por su distribución puede ser considerada como no vinculada a fallas.

La transformación de anfíbol a biotita sugiere temperaturas sobre los 500°C y las texturas intracristlinas de cuarzo indican recristalización dinámica plástica (explicado en la Sección III.3.1.1). Bajo estas condiciones la deformación es dúctil. En áreas con alto strain, se pueden esperar milonitas, sin embargo, el caso 2 muestra deformación de bajo strain (poco desarrollo de subgranos), distribuido en las rocas del depósito. En estas condiciones, la deformación frágil pudo iniciarse como fracturas de extensión por alta presión de fluidos durante periodos de rápida deformación. Estas facturas son selladas por fluidos sobresaturados en sílice, generando vetas de cuarzo. (representado con color celeste en la parte inferior de la Figura V-2). Por lo tanto, se puede esperar que durante esta alteración (alcalina) los fluidos hidrotermales tiendan a sellar las fracturas, inhibiendo la deformación frágil incipiente.

V.2. ALTERACIÓN PROPILÍTICA

También resulta en minerales alcalinos, pero de menor temperatura que la alteración potásica. Ocurre por la circulación de fluidos de temperatura intermedia a través de rocas de mayor temperatura, sobre un sistema magmático (Giggenbach, 1984).

Tras las observaciones petrográficas realizadas en el caso 1 se puede deducir que esta alteración, que transforma anfíboles a clorita, habría ocurrido justo después del límite plástico frágil. Cuando empiezan a nuclearse fracturas distribuidas en todo el cuerpo de roca que se enfría. Progresivamente, algunas estas fracturas se habrían interconectado, para formar las fallas mayores. Según lo observado en el caso 1, los núcleos de estas fallas habrían estado formados por brechas y salbandas de fragmentos de feldespato y/o cuarzo, que posteriormente han sido cementados por epidota (formando núcleos de cataclasitas verdes). Se puede esperar que esta precipitación de epidota entre los fragmentos (y eventualmente calcita y albita) tenga un efecto de fortalecimiento de las rocas de falla y dificultando la deformación frágil.

Entonces, para esta alteración alcalina, también se puede esperar fortalecimiento de las fallas por precipitación con epidota, con tendencia a inhibir la deformación frágil que se empieza a desarrollar, debido a un esperable aumento de la cohesión.

Tanto para esta alteración como la alteración potásica, se puede esperar que la transformación de anfíboles en filosilicatos (clorita o biotita) produzca un debilitamiento de las rocas. Sin embargo, en ambos casos de estudio las rocas de caja son félsicas, por lo que no es un proceso importante. Se hipotetiza que esto sería importante en alteraciones alcalinas en rocas máficas.

V.3. ALTERACIÓN FÍLICA

Los minerales producidos por este tipo de alteración en un sistema porfídico indican condiciones hidrotermales de acidez intermedia y temperatura intermedia (mesotermal), Figura V-1. A partir de lo observado en RT, se puede esperar que este tipo de alteración ocurra una vez que la temperatura haya descendido suficiente para permitir fracturamiento de rocas y/o vetas (Figure III-8. Sequential evolution of the faults in Radomiro Tomic).

Los núcleos de falla tendrán su mayor desarrollo durante esta alteración hidrotermal, debido al debilitamiento de los feldespatos por hidrólisis. El aumento de arcilla, a partir de tal proceso se verá reflejado en texturas de deformación dúctil dentro de salbandas con sulfuros metálicos. A pesar de la precipitación de nuevos minerales metálicos en los espacios porales, mecánicamente esta alteración significará una reducción importante del coeficiente de fricción de las fallas (de hasta un 25% del coeficiente de fricción, Figure IV-8). Por lo tanto, a escala del depósito hidrotermal se puede esperar que las fallas acumulen la mayor cantidad de desplazamiento durante el periodo de alteración fílica.

Sin embargo, durante la última etapa de enfriamiento de los fluidos causantes de esta alteración, se puede esperar que se precipite cuarzo cristalino en los espacios porales. Causando silicificación y fortalecimiento de las rocas en el núcleo de falla, por cohesión.

V.4. ALTERACIÓN ARGÍLICA

Esta alteración ocurre a bajas temperaturas y acidez intermedia a ácida. Puede ocurrir por fluidos meteóricos o una combinación de fluidos meteóricos e hidrotermales. Y se espera que ocurra en la última etapa del sistema hidrotermal. Durante esta alteración, los principales cambios mineralógico son la hidrólisis de feldespatos y la transformación de illita a kaolinita (que incluye

reemplazo de cationes K+ por H+). Por lo tanto, cualquier roca rica en feldespatos se debilitará (perdiendo hasta en 60% de resistencia tensional y un 50% de coeficiente de fricción).

En el caso de fallas que han sufrido previamente alteración fílica con silicificación, no hay feldespato en el núcleo y la alteración argílica solamente afecta a las rocas que rodean las fallas (ver Figura V-2, Caso 2 (RT), rectángulo superior). Esto produciría fallas con núcleos de levemente más resistentes a la deformación que las rocas circundantes (ca. 15% de la resistencia tensional).

Por otra parte, si al momento de iniciarse la alteración argílica, las fallas no hubiesen sido afectadas por otro proceso de alteración que destruya feldespatos, se produciría debilitamiento de los núcleos de falla (por sus fragmentos con feldespato). En este caso se reactivaría el núcleo cuando las condiciones de estrés sean favorables. Como se muestra con amarillo en el rectángulo superior del caso 1(DCC), Figura V-2.

VI. CONCLUSIÓN DE LA TESIS

Respondiendo a la pregunta de investigación: " **¿Cómo afectan los fluidos hidrotermales en la mecánica y desarrollo de fallas en rocas graníticas?**

De acuerdo la información aquí recolectada y arriba discutida, los efectos de los fluidos hidrotermales en las rocas asociadas a fallas se pueden separar en:

VI.1. CAMBIOS MINERALÓGICOS

La interacción química roca-fluido relacionada a fallas, produce una constante competencia entre **procesos de debilitamiento**, como la hidrólisis de las plagioclasas (que disminuyen la resistencia tensional, compresiva y friccional de las rocas, mientras aumentan su porosidad) versus **procesos de fortalecimiento**, como la precipitación de minerales entre fragmentos de rocas (que aumentan la resistencia tensional y friccional de las rocas, mientras disminuyen su porosidad). Los primeros, ocurren a lo ancho de toda la estructura interna (zona de daño y núcleo de falla), pero los segundos, ocurren exclusivamente en el núcleo de falla.

El proceso que domine a lo largo de la vida de una falla definirá el comportamiento mecánico final de esta. Si solo ocurriesen los procesos de debilitamiento, se obtendría una falla débil en todo su ancho, pero un núcleo aún más debilitado por los efectos mecánicos del cizalle. La cual tendría una mínima capacidad de soportar estrés, tendiendo a acomodar la deformación constantemente en la misma zona. Además, tendría una respuesta de alto fortalecimiento frente a la aceleración de deslizamiento, definiendo un comportamiento asísmico.

Si sólo ocurriesen los procesos de fortalecimiento, el resultado final sería una falla cementada, probablemente una falla-veta. Luego, si ésta fuese reactivada, el cizalle ocurriría en una superficie adyacente (entre el núcleo y la zona de daño). Esta falla tendría una alta capacidad de soportar estrés, tanto por su fricción como su cohesión, generando una tendencia a distribuir la futura deformación en la zona de daño (antes de reactivarse como tal). Además, tendría una respuesta de débil fortalecimiento a debilitamiento frente a la aceleración de deslizamiento de superficies, definiendo un comportamiento sísmico (siempre que la presión de fluido se haya perdido).

Si se acumulan **ambos procesos con la misma intensidad**, el resultado sería una falla cementada en su núcleo, pero un halo (en la zona de daño) mucho más débil que éste. Las eventuales reactivaciones también ocurrirían en planos adyacentes al núcleo, cortando por la

zona de daño. Esta falla tendría muy baja capacidad de soportar estrés y acomodaría la deformación progresivamente en el límite entre núcleo y zona de daño. Además, tendría una respuesta de alto fortalecimiento frente a la aceleración de deslizamiento, definiendo un comportamiento asísmico.

Según la información aquí compilada se puede concluir que, para rocas graníticas (félsicas a intermedias). (1) **Fluidos calientes que se enfrían al contacto con las rocas – alteraciones ácidas -** producen tanto debilitamiento como fortalecimiento de las fallas (en distintas magnitudes). (2) **Fluidos que se calientan al contacto con las rocas – alteraciones alcalinas -** fortalecen las fallas, ya que producen mayor precipitación de nuevos minerales que destrucción de los existentes. (distinto sería el caso para rocas máficas o ultramáficas con más anfíboles que feldespato).

Estos procesos de alteración se pueden superponer u ocurrir en diferentes lugares de un sistema de fallas. Por lo tanto, a escala de una falla singular, el resultado final puede ser una combinación de ellos o solo un evento de alteración aislado.

VI.2. LOCALIZACIÓN DE LA DEFORMACIÓN

El aumento de la presión de fluidos (sobre la presión litostática) produce hidrofracturamiento y formación vetas como estado inicial de la deformación frágil (Caso 1). Cuando esto ocurre, dichas vetas localizan la subsecuente deformación a lo largo de ellas (ya que es más fácil que romper a lo ancho de ellas). Además de la reología de la roca (resistencia tensional), este fenómeno depende principalmente de la disponibilidad de fluidos y la baja permeabilidad (para aumentar su presión). Por lo tanto, la cercanía del sistema hidrotermal a fuentes de fluidos (e.g.: magmas en proceso de cristalización) es un factor determinante en la intensidad de la localización en vetas (como ocurre en las fallas de Radomiro Tomic (SFD). Esta localización de la deformación en vetas por hidrofracturamiento, se opone e interrumpe la deformación dúctil que las rocas magmáticas sufren al inicio del proceso de enfriamiento por activación de mecanismos de deformación cristalina plástica.

En contraste, si un cuerpo de roca se enfría y deforma en el límite plástico-frágil bajo condiciones de baja presión de fluidos (sub hidrostática), la deformación frágil se nucleará de forma distribuida antes de localizarse en las fallas principales. Favoreciendo la formación de redes de fracturas autosimilares, como ocurre en el Caso 1 (SFA).

VI.3. REFERENCIAS

Cembrano, J., González, G., Arancibia, G., Ahumada, I., Olivares, V. & Herrera, V. (2005). Fault zone development and strain partitioning in an extensional strike-slip duplex: A case study from the Mesozoic Atacama fault system, Northern Chile. Tectonophysics 400(1-4), 105-125.

Corbett & Leach. (1998). Controls on hydrothermal alteration and mineralization. Society of Economic Geologist. Special Publication No.6, 13.

Faulkner, D. R., Mitchell, T. M., Rutter, E. H. & Cembrano, J. (2008). On the structure and mechanical properties of large strike-slip faults. Geological Society, London, Special Publications 299(1), 139.

Fournier, R. O. (1999). Hydrothermal processes related to movement of fluid from plastic into brittle rock in the magmatic-epithermal environment. Economic Geology 94(8), 1193-1211.

Giggenbach, W. F. 1984. Mass transfer in hydrothermal alteration systems-A conceptual approach. Geochimica et Cosmochimica Acta 48(12), 2693-2711.

Gomila, R., Arancibia, G., M. Mitchell, T., Cembrano, J. & R. Faulkner, D. 2016. Palaeopermeability structure within fault-damage zones: A snap-shot from microfracture analyses in a strike-slip system. Journal of Structural Geology 83, 103-120.

Herrera, V., Cembrano, J., Olivares, V., Kojima, S. & Arancibia, G. 2005. Precipitation by depressurization and boiling in veins hosted in an extensional strike-slip duplex: microstructural and microthermometric evidence. Revista Geologica De Chile 32(2), 207-227

Jensen, E., Cembrano, J., Faulkner, D., Veloso, E. & Arancibia, G. 2011. Development of a self-similar strike-slip duplex system in the Atacama Fault system, Chile. Journal of Structural Geology 33(11), 1611-1626.

Weis, P., Driesner, T., & Heinrich, C. A. (2012). Porphyry-copper ore shells form at stable pressure-temperature fronts within dynamic fluid plumes.Science,338(6114), 1613-1616.

Scheuber, E. & Andriessen, P. A. M. 1990. The kinematic and geodynamic significance of the Atacama fault zone, northern Chile. Journal of Structural Geology 12(2), 243-257.

Seedorff, E., Barton, M. D., Stavast, W. J. A. & Maher, D. J. (2008). Root zones of porphyry systems: Extending the porphyry model to depth. Economic Geology 103(5), 939-956.

Seedorff, E., Dilles, J. H., Proffett, J. M., Einaudi, M. T., Zurcher, L., Stavast, W. J. A., Johnson, D. A. & Barton, M. D. (2005). Porphyry deposits: Characteristics and origin of hypogene features. Economic Geology 100th anniversary volume 29, 251-298.

Sillitoe, R. H. (2010). Porphyry Copper Systems. Economic Geology 105, 38.

VII. ANEXOS

Tabla VII-1. Mineralogía de difracción de RX en 2 fallas de Radomiro Tomic (Caso 1).

ROCK UNIT	SAMPLE	FAULT ZONE	SPECIMEN	Quartz SiO_2	K-Feldpar $KAlSi_3O_8$	Plagioclase $NaAlSi_3O_8$	QZ+FLDS	Illite-2M1 $(K,H_3O)Al_2Si_3AlO_{10}(OH)_2$	Muscovite-2M1 $KAl_2(Si_3Al)O_{10}(OH,F)_2$	Kaolinite-1A $Al_2Si_2O_5(OH)_4$	Smectite-18A $Na_{0.3}(AlMg)_2Si_4O_{10}OH_2{\cdot}6H_2O$	Saponite-15A $Ca_{0.2}Mg_3(Si,Al)_4O_{10}(OH)_2{\cdot}4H_2O$	Nontronite-15A $Ca_{0.1}Fe_2(Si,Al)_4O_{10}(OH)_2{\cdot}4H_2O$	TOTAL CLAY
	Site RT1													
PROTOLITH	0610RT1.1	Protolith	D-9	36.12	32.13	21.50	**89.75**	6.84	0.00	1.37	0.00	0.00	0.00	**8.21**
QUARTZ VEIN	0610RT1.1	Core	D-8	99.40	0.00	0.00	**99.40**	0.00	0.00	0.00	0.00	0.00	0.00	**0.00**
CLAY ALTERED GRANIT	0610RT1.2	Damage Zone	D-7	34.64	32.94	0.00	**67.58**	14.02	0.00	18.27	0.00	0.00	0.00	**32.29**
BLACK GOUGE/CATCLASITE	0710RT1.6	Core	D-10	51.76	0.00	0.00	**51.76**	9.40	0.00	13.16	0.00	0.00	0.66	**23.22**
BLACK GOUGE/CATCLASITE	0810RT1.8	Core	D-12	50.42	0.00	0.00	**50.42**	12.79	0.00	29.28	0.00	0.00	0.00	**42.07**
PYRITE BRECCIA	0710RT1.7	Core	D-11	36.44	0.00	0.00	**36.44**	28.87	0.00	6.23	0.85	0.00	0.00	**35.95**
	Site RT2													
BLACK GOUGE/CATCLASITE	0710RT2.2	Core	D-14	46.06	0.00	0.00	**46.06**	16.82	0.00	21.13	0.00	0.80	0.00	**38.75**
WHITE PROTOCATACLISTE	0710RT2.1	Damage Zone	D-13	50.84	0.00	0.00	**50.84**	29.78	0.00	17.69	0.00	0.00	0.00	**47.47**
QUARTZ VEIN	0710RT2.4	Core	D-15	92.96	0.00	0.00	**92.96**	0.00	0.00	0.00	0.00	0.00	0.00	**0.00**
WHITE PROTOCATACLISTE	0810RT2.6	Damage Zone	D-16	81.35	0.00	0.00	**81.35**	0.00	14.24	0.00	0.00	0.00	0.00	**14.24**
PROTOLITH	0710RT2.3	Proto+	D-17	28.06	26.76	26.38	**81.20**	12.18	0.00	6.92	0.00	0.00	0.00	**19.10**

ROCK UNIT	SAMPLE	FAULT ZONE	SPECIMEN	Biotite-2M1 $KMg_3(Si_3Al)O_{10}(OH)_2$	Pyrite FeS_2	Chalcopyrite $CuFeS_2$	Digenite Cu_9S_5	Chalcosine Cu_2S	Molibdenite MoS_2	Coveline CuS	TOTAL SULPHIDES	Chalcantithe $CuSO_4{\cdot}5H_2O$	Alunite $K(Al_3(SO_4)_2(OH)_6$	Natroalunite $NaAl_3(SO_4)_2(OH)_6$	Gypsum $CaSO_4{\cdot}2H_2O$	Chrisocole $Si_2O_5(OH)_3{\cdot}H_2O$	Credneríte $Cu(Cu_{0.04}Mn_{0.96})O_2$	OXIDES + SULPHATES
	Site RT1																	
PROTOLITH	0610RT1.1	Protolith	D-9	1.38	0.00	0.00	0.00	0.00	0.00	0.00	**0.00**	0.00	0.00	0.00	0.00	0.00	0.00	**0.00**
QUARTZ VEIN	0610RT1.1	Core	D-8	0.00	0.00	0.00	0.00	0.60	0.00	0.00	**0.60**	0.00	0.00	0.00	0.00	0.00	0.00	**0.00**
CLAY ALTERED GRANIT	0610RT1.2	Damage Zone	D-7	0.00	0.00	0.00	0.13	0.00	0.00	0.00	**0.13**	0.00	0.00	0.00	0.00	0.00	0.00	**0.00**
BLACK GOUGE/CATCLASITE	0710RT1.6	Core	D-10	0.00	10.28	0.00	0.31	0.00	0.25	0.00	**10.84**	10.30	0.00	3.88	0.00	0.00	0.00	**14.18**
BLACK GOUGE/CATCLASITE	0810RT1.8	Core	D-12	0.00	3.41	1.19	0.00	0.00	0.10	0.00	**4.70**	0.00	0.00	0.21	1.46	0.00	0.00	**1.67**
PYRITE BRECCIA	0710RT1.7	Core	D-11	0.00	18.62	0.00	0.00	0.00	0.00	0.00	**18.62**	6.03	0.00	1.41	1.18	0.00	0.00	**8.62**
	Site RT2																	
BLACK GOUGE/CATCLASITE	0710RT2.2	Core	D-14	0.00	3.30	0.00	2.60	0.00	0.00	0.30	**6.20**	5.12	0.00	2.76	0.00	0.70	0.41	**8.99**
WHITE PROTOCATACLISTE	0710RT2.1	Damage Zone	D-13	0.00	0.00	0.00	0.00	0.00	0.00	0.00	**0.00**	0.95	0.74	0.00	0.00	0.00	0.00	**1.69**
QUARTZ VEIN	0710RT2.4	Core	D-15	0.00	1.58	0.00	0.00	0.00	1.18	0.00	**2.76**	0.00	0.00	0.00	4.28	0.00	0.00	**4.28**
WHITE PROTOCATACLISTE	0810RT2.6	Damage Zone	D-16	0.00	0.66	0.00	0.00	0.00	0.00	0.00	**0.66**	0.00	3.75	0.00	0.00	0.00	0.00	**3.75**
PROTOLITH	0710RT2.3	Proto+	D-17	0.00	0.00	0.00	0.00	0.00	0.00	0.00	**0.00**	0.00	0.00	0.00	0.42	0.00	0.00	**0.42**

Tabla VII-2. Miineralogía de difracción de rayos X Medida en una falla del Duplex Caleta Coloso (Falla Cristales) (Caso 2)

ROCK UNIT	SAMPLE	FAULT ZONE	XRD SPECIMEN	CUARZO	Ortoclasa $KAlSi_3O_8$	Albita $NaAlSi_3O_8$	Andesina $Na_{0.622}Ca_{0.368}Al_{1.29}Si_{2.71}O_8$	Albita cálcica $(Na,Ca)Al(Si,Al)_3O_8$	FLDESPATO	Actinolita $Ca_2(Mg,Fe)_5Si_8O_{22}(OH)$	Pargasita $(Na,K)Ca_2(Mg,Fe)_4Al(Si_6Al_2)O_{23}$	Tremolita $Ca_2Mg_5Si_8O_{22}(OH)_2$	ANFIBOL
Protolito 1: Cerro Cristales	2304FC1.1	Protolito	D-18	**36.9**	3.7	35.5	0.0	0.0	**39.3**	8.6	0.0	0.0	**8.6**
Salbanda de arcilla morada	2304FC1.3	Núcelo	D-19	**33.5**	0.0	0.0	0.0	18.0	**18.0**	0.0	0.5	0.0	**0.5**
Cataclasita Verde	2304FC1.2	Núcelo	D-21	**37.3**	0.0	28.5	0.0	0.0	**28.5**	0.0	0.0	0.0	**0.0**
Protolito 2: Complejo Bolfín	2304FC1-5	Protolito	D-20	**18.5**	0.0	0.0	50.4	0.0	**50.4**	0.0	0.0	6.7	**6.7**

ROCK UNIT	XRD SPECIMEN	Moscovita $KAl_2Si_3AlO_{10}(OH)_2$	Illita $(K,H_3O)Al_2Si_3AlO_{10}(OH)_2$	Montmorillonita $Na_{0.3}(AlMg)_2Si_4O_{10}OH_2{\cdot}6H_2O$	ARCILLAS	Clorita $(Mg,Fe)_6(Si,Al)_4O_{10}(OH)_8$	Epidota $Ca_2(Al,Fe)_3(Si_2O_7)(SiO_4)(OH)_2$	Halita $NaCl$	Hematita Fe_2O_3	Natrojarosita $NaFe_3(SO_4)_2(OH)_6$	Yeso $CaSO_4{\cdot}2H_2O$	Calcita $CaCO_3$	Witherita $BaCO_3$	CARBONATO
Protolito 1: Cerro Cristales	D-18	0.0	0.0	0.0	0.0	**11.5**	0.0	0.0	0.0	0.0	0.0	3.4	0.3	**3.7**
Salbanda de arcilla morada	D-19	20.4	0.0	0.0	**20.4**	**2.3**	0.0	**5.9**	**5.5**	0.0	4.9	8.9	0.0	**8.9**
Cataclasita Verde	D-21	0.0	15.6	0.0	**15.6**	**8.2**	**2.5**	0.0	**1.4**	0.0	0.0	6.5	0.0	**6.5**
Protolito 2: Complejo Bolfín	D-20	1.8	0.0	3.8	**5.5**	**12.8**	**1.5**	0.0	0.0	0.1	0.0	4.5	0.0	**4.5**

Tabla VII-3. Tabla de características micro-petrográficas.
Texturas y minerales identificados por microscopía óptica en las unidades definidas en Radimiro Tomic.

UNIT	SAMPLES	Distribution	General Texture	Major Minerals	% Vol.	Occurrence	Size (mm)	Shape / distribution	Intracrystal features
Quartz Vein	0610RT1.1 (XRD)	1 -20 cm thick veins with wavy walls and irregular shapes	Homogeneus crystaline texture	Quartz	95	1. Small Crystals	<0,1	Anhedral, difuse grain contacts, distributed in fracture walls	Continuous and homogeneous extinction
	0710RT2.4 (XRD+ TS)	Most have an adyacent layer black gouge (rare cases without)	Both strong-cohesive and fractured outcrops			2. Large Crystals	0.1-10	Euhedral crystals with triple joints Diffuse boundaries crystals	Both Continuous and patchy extinction (subgrains)
			Foliation: 1-10mm thick quartz bands of different crystal sizes with thin molibdenite crystals in between.	Pyrite	3	1. Inter-crystaline space	0.01-5	Anhedral against quartz, euhedral against secondary sulphide	Monocrystaline
				Molibdenite	2	1. Inter-crystaline space	<0,3	In pore spaces between quartz crystals and fractures. Striated.	Normal aspect
				Gypsum	4-5	1. Inter-crystaline space	0.1-2	Anhedral between quartz crystals and fractures	Fibrous
				Chalcocite	0-1	Only detected by XRD	N.O.	Not observed	Not observed
Black Cataclasite/Gouge	RT2.5-L2 (TS)	Distributed in 0.5-1m thick layers .	Large rounded brittle fragments (quartz) surounded by ductile clay-rich matrix.	Quartz	40- 50	1. Porphyroclasts	0.1-50	TYPE I:Angular and fractured fragments. (Black Portion)	Polycrystalline, Subgrains of different sizes (milonitic)
	0810RT1.8 (XRD+TS)	Also surrounding fragments of protolith and quartz vein	Mostly cohesive, but loose in some few outcrops.					TYPE II+I10: Irregular fragments. Found in the white bands .	Continuous and undulose extinction. Cemented to smaller fragments
	0710RT2.2 (XRD)	Allways adyacent to quartz veins or relict fragments it.	0.1-50			2. Matrix Fragments	0.01-0.1	rounded to angular small fragments. "Floating" in clay crystals and cemented in cumuli around large qtz fragments	Continuous and homogeneous extinction
	RT2.5-L1 (TS)	Present in all faults cores				3. Cement Crystals	<0.02	Between quartz matrix fragments and in druse habit around large ones (anhedral agains quartz and euhedral against clay).	Continuous and homogeneous extinction
	0710RT1.6 (XRD+TS)			Clay (Kao>Ill)	20-45	1. Matrix Crystals	0.01-0.05	Euhedral platty crystals randombly oriented in fracures and beween large fragments.	Undulose extinction , foliated and radial
				Pyrite	3-10	1. Porphyroclasts	0.01-0.2	Large fragments of only pyrite and fragments of polydrystalline quartz(milonitic)+pyirite filling intercrsytaline spaces.	Polycristaline and monocrystaline fragments
						2. Matrix Fragments	0.001-0.01	Both angular and irregular fragments . Distributed in shear bands.	Mono- and Poly-cristaline fragments, dissolution patterns (missing mass).
				Chalcopyirte	0-3	1. Porphyroclasts	0.01-0.2	Large fragments of only pyrite and fragments of polydrystalline quartz(milonitic)+pyirite filling intercrsytaline spaces.	Polycristaline and monocrystaline fragments
						2. Matrix Fragments	0.001-0.01	Both angular and irregular fragments . Distributed in shear bands.	Mono- and Poly-cristaline fragments, dissolution patterns (missing mass).
				Digenite	0-3	Only detected by XRD	N.O.	Not observed	Not observed
				Chalcanthite	0-10	1. Coating pyrite	<0.01	Thin layer coating pyrite fragments	Not found under microscope
				Natroalunite	0-4	Only detected by XRD	N.O.	Not observed	Not observed
				Gypsum	0-2	1. Poral space filling	0.1-1	Anhedral crystals, in fractures	Fibrous
				Chrysocolla	0-1	Only detected by XRD	N.O.	Not observed	Not observed
Pyrite Brechia	0710RT1.7 (XRD+TS)	Distributed in irregular 10-40cm thick layers .	Large briittle fragments (quartz and pyrite) surrounded by ductile matrix	Quartz	30-40	1. Porphyroclasts	0.1-10	Rounded to angular fragments, with both tensional and shear fractures.	Very fractured. Both polycristaline and monocrystaline fragments.
		Adyacent to to black gouge layers	Highly uncohesive and crumbly			2. Matrix Fragments	0.01-0.1	Rounded to sub rounded fragments distributed homogeneosly in small amounts	Monocrystaline fragments. Continuous and homogeneous extinction
		Only present in some faults	Scarce foliations	Clay (Ill>Kao)	30-40	1. Porphyroclasts pheudomorph (RT1.7)	0.1-3	Blocks of massive fine clay (feldspar fragments psuedomorph)	Undulose extinction , foliated and radial
						2. Matrix Crystals	0.01-0.05	Euhedral platty crystals randombly oriented in fracures and beween large fragments.	Undulose extinction , foliated .
				Pyrite	10-20	1. Porphyroclasts	0.1-5	Angular to irregular fragments. Very cracked and some dissolved.	Policristaline fragments, dissolution patterns (missing mass).
						2. Matrix Fragments	0.01-0.1	Both angular and irregular fragments . Distributed isotropically.	Monocrystaline fragments
				Chalcanthite	0-10	Only detected by XRD	N.O.	Not observed	Not observed
				Natroalunite	0-4	Only detected by XRD	N.O.	Not observed	Not observed
White Proto-Cataclasite	0710RT2.1 (XRD)	Distributed in uncontinuous 1-10cm thick bands and lenses.	Pervasive white clay and brittely fractured quartz fragments	Quartz	50-80	1 Groundmass	0.01-1	Large irregular zones composed by quartz crystals of different sizes and crystalinity.	Well developed subgrains in patchy extinction. Triple points
	0810RT2.6 (XRD)	Both adyacent or within the black gouge layers	Very low cohesion. Dispersable with water and dry.			2 Phenocrysts	1-5	Euhedral but with irregular boundaries.	Undulose extinction, poor developed subgrains
	HB1.4	Also in blocks of damage zone between fault branches.	Isotropic	Clay (Ill>Kao>Sm)	15-50	1. Groundmass	0.01-0.2	Large sheets of clay randomnly oriented . Distributed in veinlets and in massive irregular zones with some quartz	Undulose extinction , foliated and radial
	RT2.5-L2					2. Phenocrysts pheudomorph	0.5-2	Massive clay distributed in sub-tabular shapes (pheudomorph of plagioclase)	Undulose extinction , foliated and radial
				Pyrite	~ 1	1. Veinlets	0.2-2	Uncontinuous veinlets of py and quartz. Little to no offsets.	Monocrystaline
						2. Intercrsystaline space	0.02-0.8	Very irregular to euhedral crystals of pyrite within intercristaline spaces.	Monocrystaline
				Chalcantihite	~ 1	Only detected by XRD	N.O.	Not observed	Not observed
				Alunite	~ 1	Only detected by XRD	N.O.	Not observed	Not observed
Clay-Altered Granite	0610RT1.2 (XRD + TS)	Distributed around faults		Quartz	30-40	1. Groundmass	0.02-0.7	Anhedral and euhedral with triple points.	From undulose - patchy extinction to fully developed subgrains.
						2. Phenocrysts	1-5	Anhedral	Patchy exctintion, large subgrains with bulged boundaries.
				K-Feldspar	25-35	1. Groundmass	0.2-1	Anhedral	Patchy exctintion, subgrains with bulged boundaries.
						2. Phenocrysts	2-30	Sub-tabular to anhedral, overgrown.	Enclosing euhedral crystals of quartz and plagioclase pseudomorphs of clay
				Clay (Ill>Kao)	25-35	1. Phenocrysts pheudomorph	0.5-10	Massive clay distributed in sub-tabular shapes (pheudomorph of plagioclase)	Undulose extinction , foliated and radial
						2. Replacing K-feldspar (phenocryst and groundmas)	0.01-0.1	Radial and random sheets, homogeneosly ditributed within feldspar crystals	Undulose extinction , acicular
						3. Veinlets	0.01-0.3		Undulose extinction , acicular
				Pyrite	0-1	Veinlets and intercrystalline spaces	<0.5	Anhedral to euhedral crystals .	Not observed
				Alunite	0-4	Only detected by XRD	N.O.	Not observed	Not observed
Granitic Porphiry (Protolith)	0610RT1.1 (XRD)		Porphiric ingneous texture	Quartz	25-40	1. Groundmass	0.01-0.4	Anhedral and euhedral with triple points .	From undulose - patchy extinction to fully developed subgrains.
	0710RT2.3 (XRD)	Widespread all around de RT deposit, away from faults.	Large crystals of feldspar in a microcristaline groundmass			2. Phenocrysts	1-5	Anhedral	Patchy exctintion, large subgrains with bulged boundaries.
	RT1.10(L6)			K-Feldspar	25-35	1. Groundmass	0.05-0.25	Anhedral	Monocrystaline , homogeneus extinction.
	RT2.7(L7)					2. Phenocrysts	2-30	Sub-tabular to anhedral, overgrowth.	Zoned, enclosing euhedral crystals of quartz and plagioclase.
	RT1.1(L2)			Plagioclase	20-30	1. Phenocrysts	0.5-10	Tabular elongated	Polysintethic twins, zoned and enclosing quartz
				Clay (Ill>Kao>Sme)	5-20	1. Whitin feldspars	~0.01	Radial and random sheets, homogeneosly ditributed within feldspar crystals	Undulose extinction , foliated and radial
						2. Filling microcracks	~0.05	Parallel oriented sheets in microfractures	Undulose extinction , foliated.
				Biotite	0-5	Phenocrysts	0.5-4	Layered amphiboles pseudomorphs. Some are plastically deformed	Foliated with undulose extinction